UNIVERSITY OF SOUTHAMPTON

A Numerical Investigation of Noise Mitigation for Railway Track

by

Hongseok Jeong

A thesis submitted for the degree of
Doctor of Philosophy

in the
Faculty of Engineering and Physical Sciences
Institute of Sound and Vibration Research

November 2018

UNIVERSITY OF SOUTHAMPTON

ABSTRACT

FACULTY OF ENGINEERING AND PHYSICAL SCIENCES
INSTITUTE OF SOUND AND VIBRATION RESEARCH

Doctor of Philosophy

A NUMERICAL INVESTIGATION OF NOISE MITIGATION FOR RAILWAY TRACK

by Hongseok Jeong

Railways are considered to be environmentally friendly, but the noise and vibration from railways is an obstacle to the promotion of railways. The main source of railway noise is rolling noise, which is caused by the interaction between the rail and wheel irregularities. For the mitigation of rolling noise, various control methods at source have been developed and used, as they are more cost–effective than conventional noise barriers. A promising technique is to use sound absorbing materials to improve the performance further. To be able to predict their performance accurately, it is necessary to understand how sound absorbing materials behave as a part of noise mitigation measures.

To address this issue a 2.5D finite element model for poro–elastic media has been developed and implemented in an existing in-house finite element/boundary element model. The developed model has been validated, highlighting differences between the poro–rigid model and the poro–elastic model.

The input parameters, which are introduced by the Biot-Allard model, are also presented and ways to determine each parameter have been shown. A melamine foam has been characterised and used in the validation of the numerical model. The flow resistivity has been measured directly, and the other fluid parameters have been inferred from the measured absorption coefficient and impedance. The frame properties have also been identified using a dynamic stiffness measurement and associated simulation.

The acoustic absorption of railway ballast has been investigated, comparing a locally–reacting formulation with the current extended reaction model. Three cases from previous studies are revisited: the sound absorption of the ballast layer, the effects of the ballast on the sleeper noise radiation and the effects on the rail noise radiation. It was found that the extended reaction model shows a better agreement with the measurements, although some discrepancies still exist. In addition, the noise radiation from the ballast vibration has been calculated using a 3D finite element model in COMSOL. The results showed that the ballast can radiate as much noise as the sleepers below 200 Hz, although the sound power of the ballast will be overestimated due to the limitation of the model. The ground stiffness affects the noise level at low frequencies below 200 Hz, but the relative contribution of the ballast to the sleeper noise is unaffected. The dynamic stiffness of the ballast for use in the track dynamic models has also been calculated, showing good agreement with a previous measurement.

Measurements were conducted in an anechoic chamber to study the effect of absorptive panels laid on the track. A 1:5 scale ballasted track was used, and the insertion loss of the panels was measured reciprocally. A low–height noise barrier was also used for comparison. It was found that the noise barrier is more effective than the absorptive panels. In most cases the combination of the two showed the best performance. A comparison with results from the numerical model showed moderate agreement.

The effects of a noise barrier with a porous lining and absorptive blocks placed on a slab track have been studied separately. The materials for the lining have been characterised from impedance tube measurements. It was found that the barrier with the porous lining becomes more effective in the presence of a car body, due to increased reflections. Noise from the slab has also been calculated, and found to have an impact only on the low frequency noise. The effects on rolling noise of absorptive blocks made of porous rubber have been calculated. From a study of the blocks of the same geometry but with different absorbing properties, it was found that the shielding effect is dominant. This was improved when the blocks were absorptive, compared with the case of the rigid blocks, by up to 2 dB(A) for the selected configuration and material. In total, an overall reduction of 4 dB(A) was found in the rolling noise from the numerical calculation by application of the absorptive blocks.

Contents

List of Figures

List of Tables

List of symbols

c	Speed of sound
c_0	Speed of sound in air
c_p	Compressional wave speed
c_s	Shear wave speed
f	Frequency
f_r	Resonance frequency
h	Thickness
i	$\sqrt{-1}$
k	Wavenumber
k_0	Acoustic wavenumber
k_e	Equivalent wavenumber
k_x	Wavenumber in x direction
$\mathbf{n}$	Unit normal vector
p	Sound pressure
$\tilde{\mathbf{p}}$	Nodal pressure vector in space domain, 3D
$\hat{\mathbf{p}}$	Nodal pressure vector in space domain, 2D
$\bar{\mathbf{p}}$	Nodal pressure vector in wavenumber domain
q_0	Permeability
q_0'	Thermal permeability
r	Roughness
s_p, s_b	Stiffnesses of upper and lower springs in track model
t	Time
$\mathbf{u}$	Displacement vector
$\mathbf{u}^s$	Solid displacement vector
$\mathbf{u}^f$	Fluid displacement vector
u_n	Normal displacement
u, v, w	Displacements in Cartesian coordinates
v	Particle velocity
v_n	Normal velocity

x, y, z	Cartesian coordinates
A	Area
A_1, A_2, B_1, B_2	Coefficients for plane waves
$\tilde{\mathbf{C}}_s, \tilde{\mathbf{C}}_f$	Coupling matrices for poro–elastic model
$\mathbf{D}$	Stress–strain relation matrix
E	Young's modulus
F	Force
$\mathbf{H}_a, \mathbf{G}_a$	Matrices for acoustic boundary elements
K_c	P–wave modulus
K_e	Equivalent bulk modulus
K_m	Measured dynamic stiffness
$\mathbf{K}_{s2}, \mathbf{K}_{s1}, \mathbf{K}_{s0}$	Stiffness matrices for solid phase
$\mathbf{K}_{f2}, \mathbf{K}_{f0}$	Stiffness matrices for fluid phase
$\mathbf{M}_s, \mathbf{M}_f$	Mass matrices for solid and fluid phase
$\mathbf{N}$	Shape function
$\mathbf{N}_s$	Shape function for solid
$\mathbf{N}_f$	Shape function for fluid
P_0	Ambient pressure
P, Q, R, S	Biot's coefficients
V	Volume
W	Sound power
Y_r, Y_w, Y_c	Mobilities of rail, wheel and contact
Z_c	Characteristic acoustic impedance
Z_s	Surface impedance
α	Absorption coefficient
α_θ	Absorption coefficient for oblique incidence
α_d	Diffuse field absorption coefficient
α_∞	Tortuosity
γ	Ratio of specific heats
$\tilde{\gamma}$	Coupling coefficient for poro–elastic model
$\boldsymbol{\epsilon}$	Strain vector
η	Loss factor
θ	Angle
θ_d	Dilatation
κ	Wavenumber in x direction
λ	Wavelength
λ_i	Lagrangian multiplier
λ_L	Lamé first coefficient
μ_L	Lamé second coefficient

ν	Poissn’s ratio
ν_k	Kinematic viscosity
ν'	Thermal viscosity
ρ	Density
ρ_e	Equivalent density
ρ_1	Density of frame
$\tilde{\rho}$, $\tilde{\rho}_{11}$, $\tilde{\rho}_{12}$, $\tilde{\rho}_{21}$, $\tilde{\rho}_{22}$	Effective densities for poro–elastic model
σ	Flow resistivity
σ_{rad}	Radiation ratio
$\boldsymbol{\sigma}$	Stress tensor
$\hat{\boldsymbol{\sigma}}^s$	Effective stress tensor
τ	Ratio of displacements
ϕ	Porosity
ξ	Local coordinate
ψ_a	Velocity potential
ψ	Azimuthal angle
ω	Angular frequency
Γ_θ	Angle dependence in impedance
Λ	Viscous characteristic length
Λ'	Thermal characteristic length
Ω	Boundary
$^{\mathrm{T}}$	Transpose
$^{\mathrm{H}}$	Hermitian transpose

Acronyms

2D	Two dimensional
2.5D	Two and a half dimensional
3D	Three dimensional
BE	Boundary Element
BEM	Boundary Element Method
dB	Decibel
DB	Delany–Bazley
DBM	Delany–Bazley–Miki
FE	Finite Element
IL	Insertion Loss
ISVR	Institute of Sound and Vibration Research
JAC	Johnson–Allard–Champoux
KRRI	Korean Railroad Research Institute
RMS	Root Mean Square
SEA	Statistical Energy Analysis
SNR	Signal to Noise Ratio
SPL	Sound Pressure Level
TMM	Transfer Matrix Method
TSI	Technical Specifications for Interoperability
TWINS	Track–Wheel Interaction Noise Software
WANDS	WAveNumber Domain Software

Declaration of Authorship

I, Hongseok Jeong, declare that this thesis entitled A Numerical Investigation of Noise Mitigation for Railway Track and the work presented in it are my own and has been generated by me as the result of my own original research.

I confirm that:

1. This work was done wholly or mainly while in candidature for a research degree at this University;
2. Where any part of this thesis has previously been submitted for a degree or any other qualification at this University or any other institution, this has been clearly stated;
3. Where I have consulted the published work of others, this is always clearly attributed;
4. Where I have quoted from the work of others, the source is always given. With the exception of such quotations, this thesis is entirely my own work;
5. I have acknowledged all main sources of help;
6. Where the thesis is based on work done by myself jointly with others, I have made clear exactly what was done by others and what I have contributed myself;
7. Parts of this work have been published as:
    - H. Jeong, G. Squicciarini, D. J. Thompson, J. Ryue, Development of a model to assess acoustic treatments to reduce railway noise, International Conference on Recent Advances in Structural Dynamics, Southampton, 2016.
    - H. Jeong, G. Squicciarini, X. Zhang, D. J. Thompson, J. Ryue, Acoustic modelling of railway ballast, International Conference on Rail Transportation, Chengdu, 2017.

- X. Zhang, D. J. Thompson, H. Jeong, G. Squicciarini, The effects of ballast on sound radiation from railway track, Journal of Sound and Vibration, 2017.

.

Signed:

Date:

Acknowledgements

Completing a PhD is a challenging journey for me, and I would not have been able to complete this journey without the help and support from many people.

Firstly, I would like to express my sincere gratitude to my first supervisor Prof. David Thompson, for his guidance, support, insight and advice he has provided throughout my study. Whenever I faced a problem in my research, he always guided me to the right direction. He also provided details so that I could solve the problem easily. Through this experience I learned a lot from him about research and also English writing. It has been truly wonderful being his student.

I am also extremely grateful to my second supervisor Dr. Giacomo Squicciarini, for his help and guidance in my research. He has helped all of my measurements during my study, from setting up the equipment to carrying out the measurements. He has also been encouraging and motivating, with a sense of humour. Discussions with him have always been useful and enjoyable.

I would like to acknowledge the help of other people with the measurements and the code. Dr. Xiaowan Liu and Hui Li helped me with the measurements in the anechoic chamber. Hui Li also helped me with cross–checking the half space formulation in the BEM code. I appreciate the discussions with Prof. Jungsoo Ryue, who kindly answered my questions and helped me understand the structure of WANDS. Thanks must go to Dr. Evangelos Ntotsios for helping me with using COMSOL and also the project. Also, many thanks to Dr. Xianying Zhang and Dr. Martin Toward for sharing their measurement results.

I wish to thank my colleagues in the Dynamics Group, espesically Boniface Hima, Bo Ding, Kolade Olanipekun and Jin Zhang for their help and support. The discussions with them were precious, which made me realise how little I know. It has been a real pleasure to be with them.

Sincere gratitude to my parents and my sister for their continuous love and support. I would also like to thank my girl friend, Dalrae Jin, for all her love and support. They are the most important people to me, and I dedicate my thesis to them.

I would also like to express my gratitude for all those who I did not mention explicitly.

Finally, I appreciate the financial support from KRRI through the project "Theoretical modelling for the development of an optimized low–noise track". Especially, I would like to thank Dr. Jiyoung Hong who provided this opportunity to me.

Chapter 1

Introduction

1.1 Background

Railways are considered to be environmentally friendly, so that their role has been expanded in recent years in the carriage of freight and in long-distance travel as well as metro systems in cities. Trains of higher speed and higher capacity are being developed to remedy the increasing road traffic, and new railway lines are under construction to support this. However, the noise and vibration from railways has become an obstacle to their promotion and development. It is often a concern for residents living nearby, which can result in the opposition to the construction of new railway lines. As the noise issues have grown, consideration of the noise and vibration has been required in many countries. For example, regulations such as TSI (Technical Specifications for Interoperability) Noise regulations in Europe or Railroad Noise Emission Compliance Regulations in the U.S. are in place to regulate the noise levels emitted by railway vehicles. Consequently it is hardly possible to introduce high speed trains unless their noise is reduced to an acceptable level. A simple solution to this would be to use noise barriers, which have been widely used for roads. However, noise barriers are usually expensive to install and visually intrusive. For these reasons, a range of measures have also been developed to be applied at the noise source which can effectively reduce the railway noise. To make use of these measures efficiently, it is necessary to understand how they work and how to improve their performance.

It is known that the dominant source of railway noise in most situations is rolling noise. This is caused by the vibration of wheels, rails and sleepers excited by surface roughness at the wheel/rail contact. Both wheels and track contribute to the total noise, with the latter being generally the dominant source below 2 kHz [1]. Research has been conducted since the 1970s to model the rolling noise. Early work on the theoretical modelling can be found in the papers by Remington [2, 3]. This was improved by the same author [4, 5], by introducing some advances in each part of the model: inclusion of the contact stiffness, inclusion of ground effects and improvements to the wheel and rail vibration models. Later a more comprehensive model was established by Thompson [6–10] based on which a rolling noise prediction software called TWINS ("Track-Wheel Interaction Noise Software") was developed by Thompson et al. [11, 12]. A schematic diagram of the rolling noise generation mechanism is shown in Figure 1.1. The software has been widely used in Europe and elsewhere as a tool for the prediction of railway noise.

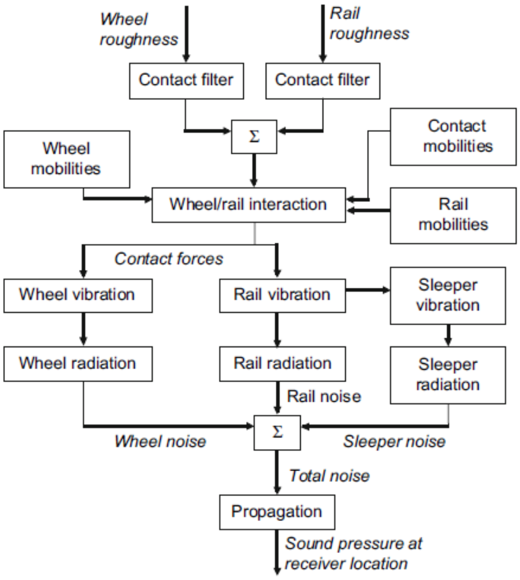

Figure 1.1. Schematic diagram of rolling noise generation mechanism [1]

As the track is the dominant source in an important part of the frequency range, there is an increase of interest in controlling and reducing the noise radiated from the track. This can be achieved by controlling the noise at the source or by reducing it in the transmission path. In the former case attention is focused on controlling roughness levels or modifying rail and wheel vibration properties. For example, reducing the roughness of either the wheel or the rail by using disc brakes or by rail grinding can result in noise reduction. Also optimized rail pads, dynamic absorbers and rail shape optimisation can also be adopted [1]. To affect the transmission path, absorptive or shielding treatments may be used in proximity to the track to reduce noise levels at the receiver. Noise barriers are one of the common solutions. The performance of a barrier is basically affected by its height, and particularly for railway applications it could be improved by adding a layer of absorbent material on the inner face. However, barriers are visually intrusive and expensive. This can be overcome if one considers low–height trackside barriers close to the rails. The basic principle is the same as that of conventional noise barriers but low–height noise barriers are more cost–effective and not visually intrusive. Furthermore, absorptive blocks or panels on the surface of a slab track can be placed closer to the source, as shown in Figure 1.2. Not only do they absorb noise, they can also act as a small noise barrier due to their geometry, although the effect would be limited.

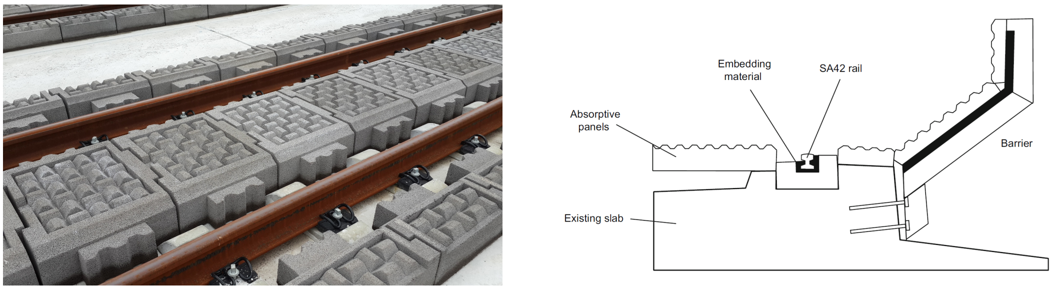

(a) (b)

Figure 1.2. Noise mitigation measures with absorptive materials: (a) porous concrete blocks (own photograph) and (b) absorptive panels and a low–height barrier [1]

In order to provide an effective solution, it is necessary to understand how these measures affect the noise radiation from the track. The main focus of this research is to investigate this problem, particularly for the measures including absorptive materials. For example, an interesting aspect regarding absorptive treatments is to study their behaviour when they are mounted in close proximity to the track. Generally it is expected that if they are placed closer to the track their performance would be improved. However, in this case, there can also be radiation of noise from vibration of the absorptive materials themselves, which would weaken their overall effectiveness. Structural vibration due to the train pass–by can propagate into the absorptive materials which in turn can radiate noise. This is illustrated in Figure 1.3. Thus noise radiated from the track components can be absorbed by the absorptive treatments, but also structural vibration from the track can be transmitted into the absorptive treatments, and this can radiate noise. An understanding of the relative effects of the absorption and the radiation is still an open question.

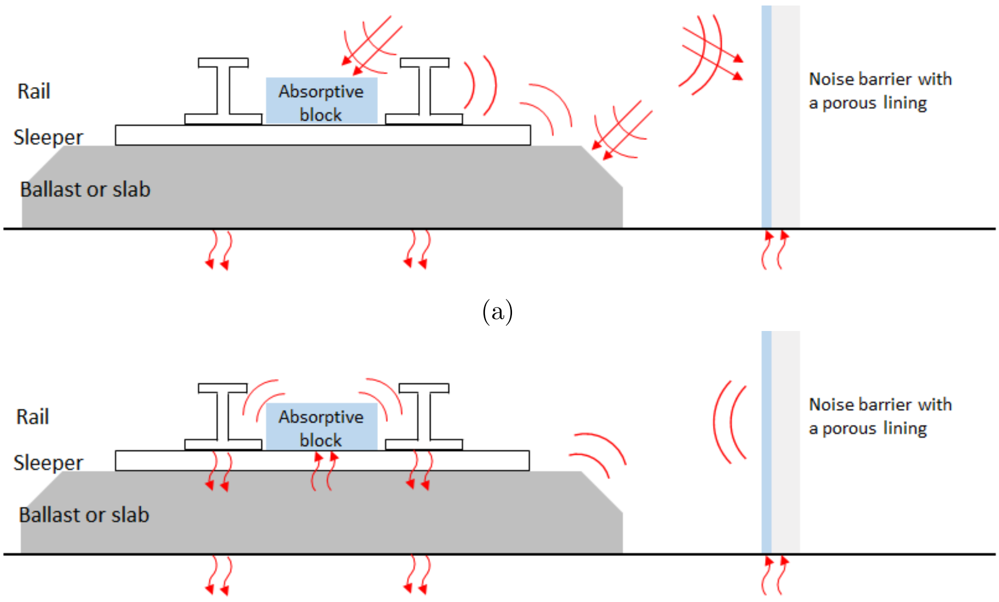

(a)

(b)

Figure 1.3. Absorption and radiation of noise by absorptive treatments: (a) absorption and (b) radiation

In the case of absorptive blocks placed above the ballast or slab, the radiation is likely to be significant, as they are directly connected to the track. However, it is less obvious if this is also the case for noise barriers because they are relatively far from the source.

An additional open question related to absorption and radiation close to the track is the role of railway ballast. This can also be considered as an absorptive medium from an acoustic point of view. One of the issues related to the ballast absorption is that one should consider sound propagation inside the ballast, i.e., using an extended reaction model. However, in the analysis of track radiation using boundary element methods, ballast is usually modelled as an impedance plane, and thus the sound propagation inside the ballast is not taken into account. If this is considered, its effect can be analysed with more realistic assumptions. Furthermore ballast itself vibrates during the train pass–by and can also potentially contribute to the noise radiation [13]. This effect has not yet been fully addressed and clarified in the railway noise literature.

In terms of numerical predictions, the boundary element method is often used to investigate these effects, by modelling absorptive surfaces as an impedance boundary. However, this may not represent absorptive materials correctly as it cannot model wave propagation inside the medium, which might be important in the above cases. Therefore a finite element model for porous media is required, to address these issues. A simple model for porous materials would be an equivalent fluid model, which considers the dynamics of fluid inside the pores. As the pores are assumed to be rigid, this is also called the poro–rigid model. It allows for wave propagation inside the medium, hence extended reaction can be modelled. However, it still cannot capture the structural vibration of porous materials. This can be achieved with the poro–elastic model. In fact, the poro–rigid model can be regarded as a simpler version of the poro–elastic model. Thus by using the poro–elastic model one can study the effect of the structural vibration as well as the wave propagation inside the medium.

1.2 Aim and objectives

The main aim of this research is to evaluate and quantify the effect of absorptive treatments on the exterior noise radiation from a railway track. The type of treatments will include absorptive concrete blocks located between the rails and low-height barriers mounted beside the track (see Figure 1.2).

A numerical model to analyse the effect of absorptive treatments will be developed. A poro–elastic finite element model should be able to capture the characteristics of absorptive treatments. Also, the model needs to be combined with an acoustic boundary element model to be used in calculating the track noise radiation. This model will provide a more accurate prediction of the track noise radiation with absorptive treatments. As railway track has a two–dimensional geometry with the third dimension of infinite extent, a 2.5 dimensional (2.5D) approach is appropriate [14–17]. To achieve this, the following objectives are set for the thesis:

- To develop a 2.5 dimensional (2.5D) finite element model for poro–elastic media,
- To characterise the properties of poro–elastic materials for use in this model,
- To couple the poro–elastic model with an existing 2.5D FE/BE model,
- To apply the model to a track with absorptive treatments,
- To carry out measurements in a laboratory for comparison with the numerical model.

1.3 Original contributions

The original contributions of this thesis are:

- extension of a published 2D $\mathbf{u}-p$ finite element model for poro–elastic materials to a 2.5D model: the $\mathbf{u}-p$ finite element model has been formulated for 2.5D problems,
- prediction of effects of railway ballast in the radiation of sleepers and rails: acoustical effects of ballast on the rail and the sleeper noise radiation have been studied with a local reaction model and an extended reaction model,
- prediction of the relative contribution of the ballast and sleeper noise: noise from the ballast has been compared with that of the sleepers to quantify the effect of the ballast noise at low frequencies,
- prediction of the frequency–dependent stiffness of ballast and ground for use in rolling noise calculations: previous measured data have been reviewed and compared with results from a numerical model,
- measurement and comparison of shielding and absorbing noise mitigation measures: an experimental study has been carried out to study shielding and absorbing measures, which can also be used for validation of the numerical model,
- prediction of effects of porous materials on the track noise radiation, including noise barriers and absorptive blocks: noise barriers with absorptive linings and absorptive blocks have been assessed using the developed model,
- prediction of the contribution of the slab noise to the rolling noise: noise from the slab has been calculated up to 1 kHz, where the slab would have an impact on the overall noise.

1.4 Structure of the thesis

The thesis is structured as follows. First, previous work on the subject is reviewed in Chapter 2. This includes noise barriers and absorptive blocks used in railways, the acoustical effects of ballast, numerical modelling of porous materials and properties of porous materials.

In Chapter 3 the properties that are introduced by the Biot-Allard model are presented. There are nine frequency-independent macroscopic parameters: porosity, flow resistivity, tortuosity, viscous and thermal characteristic lengths, frame density, Young's modulus, Poisson's ratio and loss factor. These can be obtained by measurements and associated simulations. The flow resistivity can be directly measured using a standard ISO method [18]. The porosity, tortuosity and characteristic lengths can be determined by curve fitting from impedance tube measurements. The Young's modulus, Poisson's ratio and loss factor can be obtained from a combination of dynamic stiffness measurement and a numerical simulation, which is also one of the standard methods [19]. A melamine foam has been characterised using these methods.

To make use of the Biot-Allard model, a finite element model for poro–elastic media has been implemented. To take account of the infinite characteristic of railways, a 2.5D formulation is developed and implemented in the code. The developed model has been coupled with an existing 2.5D finite element/boundary element software called WANDS (WAveNumber Domain Software for solids and fluids) [20, 21]. The coupled code is validated against data from a previous 2D study. A summary of the theory and the formulation is given in Chapter 4.

Chapter 5 deals with ballast as a porous material. For the ballast absorption problem, comparisons are made between the developed model and a conventional boundary element model with an impedance plane for the ballast. To study differences between the two models, three cases from previous research for which measurement data are available are revisited with the developed model. These are: the absorption coefficient of ballast in a diffuse field and both rail radiation and sleeper radiation in the presence of ballast. The effects of sound propagation inside the medium on the absorption coefficient and the radiation efficiency are discussed. The sound radiation from the ballast vibration is also investigated, in comparison with that of sleepers. With the parameters obtained from the radiation case, the stiffness of the ballast is calculated. The calculated stiffness is compared with a previously measured result.

A laboratory measurement has been carried out with a 1:5 scale track in an anechoic chamber and the results are presented in Chapter 6. As direct measurement methods would have practical problems, a reciprocal method was used in the measurement; the vibration of the track was measured due to excitation by a loudspeaker. The performance of a low–height noise barrier and absorptive rubber panels was measured and these were compared in terms of insertion loss. Results from the numerical model are also shown, and are compared with the measured results.

Simulations of sound radiation of a slab track are presented in Chapter 7. The sound radiation of a rail in the presence of a noise barrier with porous linings is studied, with and without a car body. The effects of absorptive blocks on the slab track have also been investigated. The noise from the slab is calculated, and the shielding and absorbing effects of the absorptive blocks on the rail noise are discussed. A way to make use of the developed model to calculate the sound radiation of the track substructure caused by the wheel–rail interaction is also proposed.

Finally, conclusions and recommendations for further work are given in Chapter 8.

Chapter 2

Literature review

This literature review consists of four parts. The first section is about noise barriers and absorptive treatments for railways. The acoustical effect of ballast is reviewed in the second part. Modelling porous materials, which is essential to analyse the absorptive treatments, is introduced next. Properties that are required for the modelling are discussed and ways to obtain them are presented in the final part.

2.1 Noise mitigation in the transmission path

2.1.1 Noise barriers

Noise barriers are one of the most common noise reduction methods used in railways. However, conventional barriers are known to be less cost-effective compared to control measures at the source [22]. This can be improved when they are installed in close proximity to the track, for which the height of the barrier can be lower. Therefore the overall cost for the installation will decrease. In terms of performance, it can be further improved when combined with other measures.

Jolibois et al. [23] carried out a field measurement for a prototype low–height noise barrier made of pressed wood. The measurement setup is shown in Figure 2.1. The height of the barrier was 0.95 m and the inner surface of the barrier was lined with a layer of fiberglass of 80 mm thickness. The results were presented in terms of insertion loss, for various speeds of tram pass-by and receiver positions. It was shown that the effect of the low barrier is 4–7 dB(A) for trams on the far track and 9–15 dB(A) for trams on the near track, depending on the receiver position. From a frequency analysis it was shown that the barrier provides attenuation in the region 200–2500 Hz. The measured results were compared with results from a 2D boundary element model, showing moderate agreement.

Figure 2.1. Measurement setup for low–height noise barrier: close tram on the left hand side and far tram on the right hand side [23]

Koussa et al. [24] investigated the acoustic performance of a gabion barrier (see Figure 2.2) using a loudspeaker source. A 2D boundary element model was used for prediction and good agreement was found with measured data from a 1:10 scale measurement. From the numerical analysis it was shown that different gabion configurations did not help reduce the noise more than a rigid barrier of the same shape. The difference was up to 3 dB(A) in the overall insertion loss, mainly due to a good performance of the rigid barrier at low frequencies. It should also be noted that the information of the boundary conditions for the gabion barrier was not clear. Only the porosity of the gabion was presented, which was 0.4.

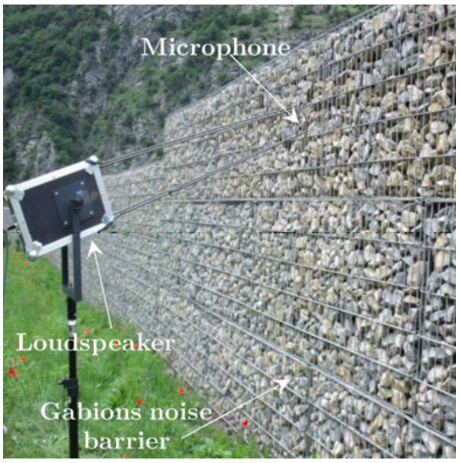

Figure 2.2. Gabion noise barrier [24]

Jones et al. [25] investigated the effect of low noise barriers combined with bogie shrouds (see Figure 2.3). From the field tests it was shown that a reduction of typically 8 dB(A) could be achieved at 145 km/h for both tread–braked and disc–braked rolling stock. Also the results implied the reduction would be greater at higher speeds. Later a numerical model for a system including low noise barriers and bogie shrouds was developed by the same author [26]. The results were calculated by using a combination of statistical energy analysis (SEA) and the boundary element method (BEM). The results from the prediction model showed a reasonable agreement with those from the measurements.

Figure 2.3. Experimental system of shrouds and barriers [25]

An experimental investigation of the effects of various configurations of bogie shield and barrier was carried out by Frid [27]. A 1/4 scale mock-up of the German BR185 locomotive was used, and the sound source was imitated by loudspeakers, with the source strength obtained from TWINS [11, 12]. From the result it was shown that the skirt with the barrier had an insertion loss of 10 dB(A), while the skirt by itself had an insertion loss of only 3 dB(A).

As shown in the above cases, the boundary element method is often employed in the prediction of the effect of barriers and ground. There are also analytical models for barriers [28–32], but these cannot deal with complex geometries. The use of a standard boundary element formulation was described by Seznec [33] for calculating sound diffraction around a barrier. The numerical results were compared with the ones from analytical formulae, and they showed better agreement as the distance from the barrier increased. It was shown that six elements per wavelength would be sufficient for linear elements, although 8–10 elements per wavelength were used in the study.

An investigation was performed by Morgan et al. [34] to analyse the effect of the shape and of the absorption of the barrier. Based on a two–dimensional boundary element model, a comparison of performance predictions was made for different types of barrier. A 2 m high straight barrier 1.4 m from the nearest rail was used as a reference and from the comparison the mean insertion loss for the barriers ranged from 7.1 to 13.5 dB.

The screening effect was improved by 2.9 – 6.0 dB when the track–facing surface of the barrier was lined with an absorbent material.

A variational form of the boundary element method was used by Jean [35]. In this paper a range of barrier shapes were compared in terms of their insertion loss. It was shown that a T–shaped barrier was the most efficient among the examples considered for a given height, and the addition of absorbent treatments showed a gain of about 4 dB for a straight barrier. Using this approach, the effect of elastic vibration of the barrier was investigated by the same author [36]. Due to the inclusion of the structural vibration, the bending modes of the barrier could be captured from the result. It was shown that the vibration of a thin paraglass barrier can influence the noise reduction typically by more than 5 dB at around 200 Hz, with dependence on the geometry and the configuration. This effect occurred at the frequencies where the rigid barrier showed the minimum attenuation at the receiver position. It was also shown that adding an absorbent layer onto the barrier results in a change of the spectrum pattern in magnitude, depending on the elasticity of the barrier.

The above studies used the 2D boundary element method. This is because in general noise barriers can be thought of as infinitely long in one direction. However, in the 2D method the source is a line source so the response to a point source cannot be obtained. The point source problem was addressed in [37], where the measured insertion loss for a point source was compared to a result from the 2D boundary element method. This gave good agreement for source and receiver in the same plane. The case where the source and the receiver are not in the same plane cannot be resolved by the 2D model. Duhamel [38] proposed a way of solving this 3D problem using the 2D model for a geometry that is uniform in one direction. This was called the Fourier–BEM (also known as 2.5D). It reduces the computational cost compared with 3D models, despite the increase of time required to find solutions of Bessel functions. The formulation enables incoherent point sources to be used and for a moving source the time history of the signal at a receiver position can be obtained by Fourier transformation. Recently, a quasi–periodic boundary element method for the 3D problem was presented by Fard et al. [39]. This reduces the length of the barrier to a finite value, depending on the convergence results of the boundary length. The results were compared with those from a finite element model, showing good agreement.

2.1.2 Absorptive blocks

Absorptive blocks are usually installed on ballastless track, as the surface of the track is flat. To some extent, they have similar characteristics to low noise barriers because they shroud some part of the source region. There are few studies on the effect of absorptive blocks. Shin et al. [40] measured equivalent sound pressure levels for an hour in the day and the night, with and without absorbing blocks (see Figure 2.4). The measurement was conducted at different positions, and it was shown that the insertion loss is up to 5 dB at a point near the track. However, no details were provided about the exact measurement positions or the blocks.

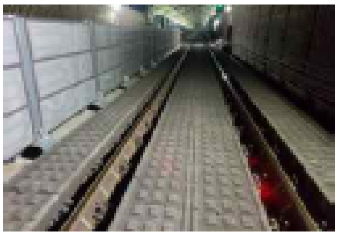

Figure 2.4. Track with absorbent blocks for the measurement [40]

Zhao et al. [41] developed a sound absorbing porous concrete slab. During the development, it was found that out of three candidate materials (expanded perlite, slag and clay ceramsite) the expanded perlite had the best absorption property. It was also shown that an aggregate gradation of 1–3 mm would give much higher absorption, compared to the values of 0–2 mm. A field measurement was carried out to measure the effect of the developed blocks, and from the result it was observed that around 2.5–4.0 dB reduction could be achieved at 7.5 m from the centre of the track and 1.5 m above the rail head, for train speeds between 80 km/h and 200 km/h. From the frequency band analysis an increase of the level was seen below 125 Hz, as shown in Figure 2.5. The reason for this was not addressed.

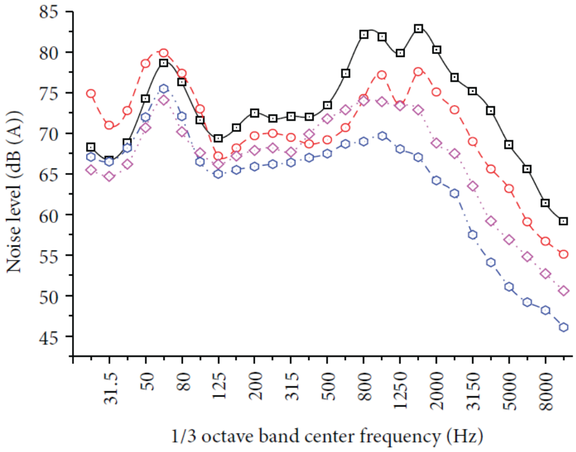

Figure 2.5. Noise absorbing effect from absorptive concrete slabs at a train speed of 140 km/h [41]: red and black – position 1, with and without the blocks; blue and purple – position 2, with and without the blocks.

Kim and Kim [42] studied a noise absorbing block on a slab track. A numerical simulation using finite elements showed a noise reduction of around 3 dB(A) at 3 m away from the centre of the track. A field measurement was also conducted, for which the configuration and the measurement setup are shown in Figures 2.6 and 2.7. From the measurement it was shown that the noise level was reduced by more than 3 dB(A) at 3.3 m away from the centre of the track. In the frequency spectrum the reduction was achieved at frequencies from 300 Hz to 1250 Hz.

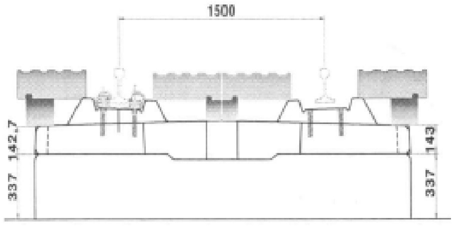

Figure 2.6. Configuration of the absorbing blocks on the track (dimensions in mm) from [42]

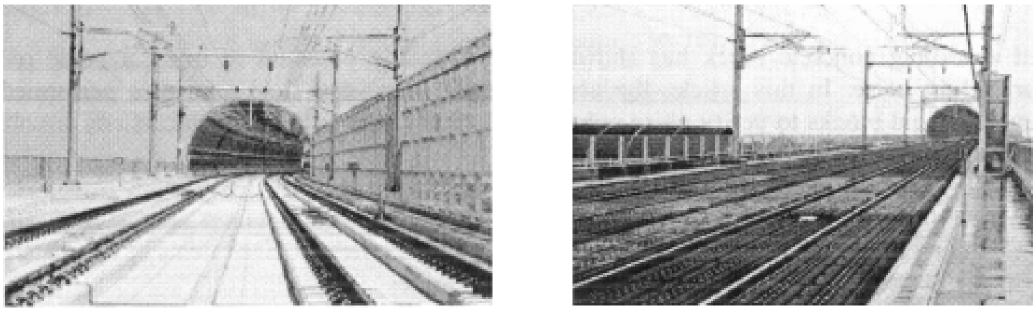

(a) (b)

Figure 2.7. (a) Track without absorbing blocks and (b) with absorbing blocks from [42]

A similar concept would be absorptive panels that cover the whole track (see Figure 2.8). An investigation by Diehl et al. [43] showed a layer of absorptive material covering the whole track including a part of the rails gave reduction of around 3 dB. This was improved when combined with shielding and a noise barrier, giving a reduction of around 6 dB.

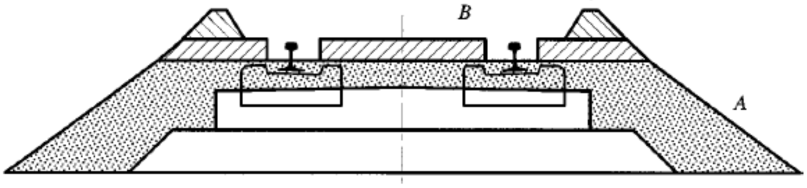

Figure 2.8. A cross–section of slab track with absorptive treatments: A – absorptive panel, B – shielding and C – low barrier [43]

Bryne [44] measured noise reduction by absorbing rubber mats on slab track in Dublin. For the measurement, the rubber mats were installed on the track over 100 m (see Figure 2.9). Two locations were chosen for the measurement (denoted by A and B), and three events were undertaken with three tram passes for each event. A noise reduction of up to 4.8 dB(A) was found, and the acoustic attenuation was seen at frequencies above 400 Hz (see Figure 2.10). However, the locations of the measurements, the type of the tram and tram speed were not provided.

Figure 2.9. Absorbing mats installed on slab track [44]

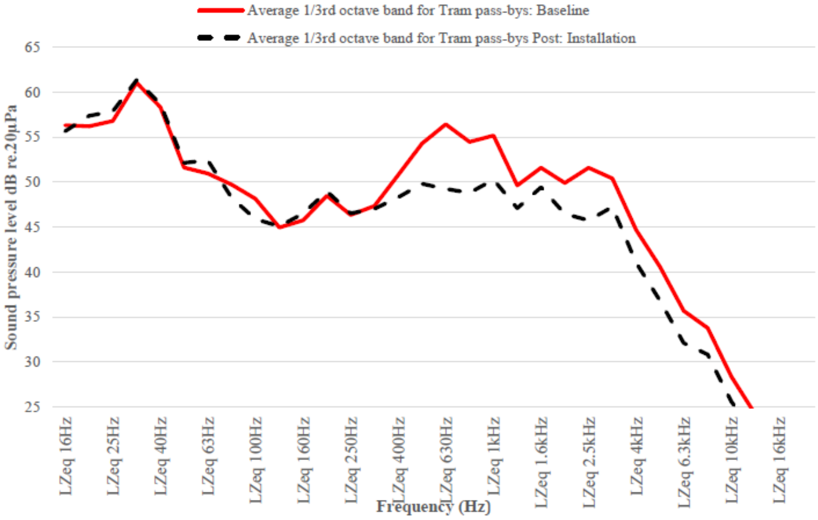

Figure 2.10. Comparison of sound pressure level with and without the rubber mats, at location B (outbound direction) [44]

2.2 Acoustical behaviour of railway ballast

Ballast is an important part of the track structure which also affects its dynamic properties. From a dynamical point of view, its stiffness and damping affect the sleeper vibration and the vibration transmitted to the ground. On the other hand, ballast is also a sound absorbing material which has an influence on the noise radiation from the track. The ballast is often modelled as a locally reacting surface, for example in boundary element methods. A flow resistivity of 50 kNs/m^4 is recommended for use with local reaction models [45].

However, it has been pointed out that the flow resistivity of the ballast would be lower than 50 kNs/m^4, so that the use of the local reaction model might not be appropriate. This is because there could sound propagation inside the medium, for materials with a very low flow resistivity [46–49]. Attenborough et al. [47] studied the influence of ballast and porous concrete on the rail noise. This was investigated using a two–dimensional boundary element method. In their work the flow resistivity of the ballast was measured, giving a value of 200 Ns/m^4. The stone density and the porosity were also measured, which were 2710 kg/m^3 and 0.491 respectively. The tortuosity and the viscous characteristic length were obtained indirectly from impedance tube measurements. The characteristic impedance was calculated from those parameters, using the Johnson–Allard–Umnova model [50]. With the parameters obtained the ballast was modelled using an extended reaction model, assuming that its thickness is 0.3 m. As the impedance would change with the incidence angle, impedance of the elements representing the ballast was calculated separately. The angle dependence of the impedance was given by [47]

$$\Gamma_\theta = \frac{1}{-\mathrm{i}\frac{\rho_0}{\rho_b}\tan\left(k_0 l\sqrt{\frac{k_1^2}{k_0^2}-\sin^2\theta}\right)\sqrt{\frac{k_1^2}{k_0^2}-\sin^2\theta}} \tag{2.1}$$

where $k_0 = \omega/c_0$ (with ω the circular frequency and c_0 the speed of sound in air) and k_1 are the propagation constants in air and ballast, l is the depth of the layer, ρ_0 is the density of air, ρ_b is the density of the ballast (complex) and θ is the incidence angle.

Heutschi [46] also studied sound propagation over ballast surfaces. An electrical network model was proposed to represent a layer of ballast with spherical cavities, as shown in Figure 2.11. This was further simplified to a electrical line network by assuming that there is no acoustical energy flux in a horizontal plane. A field measurement was carried out to adjust the geometrical parameters in the model. The results were compared in terms of insertion loss of the ground (ballast). The model showed good agreement with the measurement at various locations, especially at low and mid frequencies. A result from a local reaction model with a flow resistivity of 50 kNs/m^4 was also presented, which showed poor agreement with the measurement. From the comparison it was indicated that an extended–reaction approach was needed to consider the sound reflection over a ballast bed, as the thickness of the ballast bed had a significant effect.

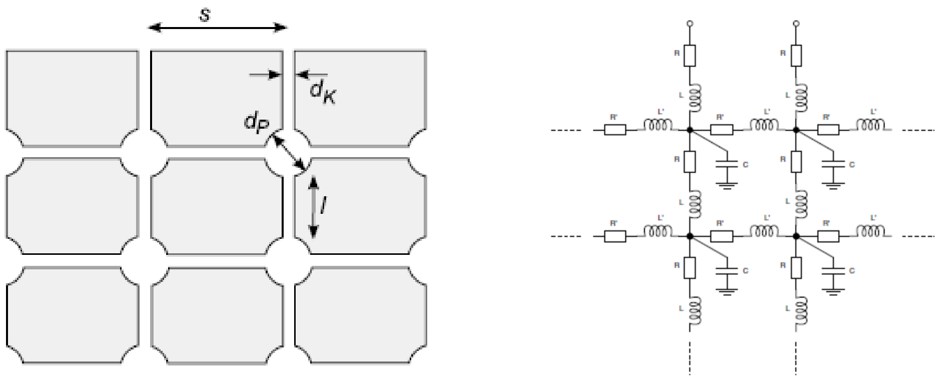

(a) (b)

Figure 2.11. (a) Simplified model of ballast and (b) an electrical network representation [46]

Similarly, the material properties of the ballast were obtained from acoustic properties by Broadbent et al. [51]. A sound absorption measurement in a diffuse field was conducted in a reverberant chamber of which the volume is 342 m^3. The measurement setup is shown in Figure 2.12. A transfer matrix approach was used to calculate the diffuse field absorption coefficient. The results were matched to the measurement by curve fitting, and good agreement was found when the ballast layer was divided into three regions. The top and the bottom layer were assigned the same properties, with the flow resistivity of 25 kNs/m^4. The flow resistivity of the middle layer was 51 kNs/m^4, which is close to the one used in [45]. The parameters obtained were used to calculate the excess attenuation in a free field assuming the ballast to be a locally reacting surface. A comparison with a free field measurement at different source and receiver positions showed good agreement below 3 kHz.

Figure 2.12. Measurement setup in a reverberant chamber [51]

An attempt to study the effects of ballast on the track noise radiation was made by Zhang et al. [52]. In this study comparisons between a local reaction model and an extended reaction model for the ballast was made for different cases. The results showed that the use of the extended model gives better predictions than the local one, in the cases of the radiation from a sleeper embedded in ballast and the radiation of a rail above ballast[1]. The vibration of the ballast was also measured, with a 1:5 scale track with the rails attached to three sleepers (see Figure 2.13). An impact hammer was used to excite the rail at the middle sleeper, and the vibration level was measured by a scanning laser vibrometer. From the results it was shown that the vibration of the ballast is much lower than that of the sleepers in general, but the area close to the excitation showed a comparable vibration level at low frequencies. The sound radiation of the ballast was also calculated using the Rayleigh integral, which showed an increase in the noise level of up to around 5 dB at 20–300 Hz in full scale frequency.

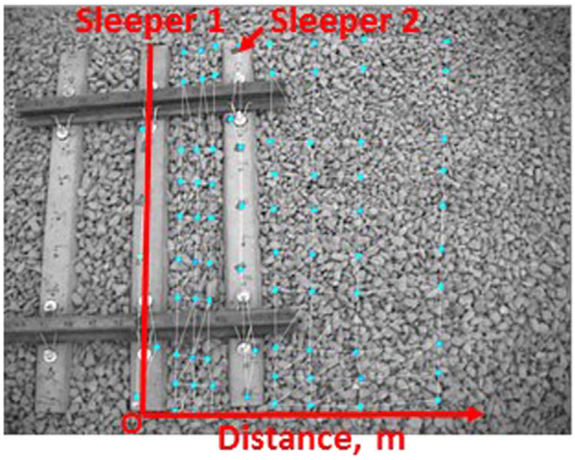

Figure 2.13. Grid for ballast vibration measurement [52]

Hannema et al. [53] carried out a measurement of noise radiation of a full scale track. Both vertical and lateral excitations were considered using a shaker, and the sound pressure was measured using a semicircular array of microphones above the rail. The vibration of the ballast was also measured using a laser vibrometer, and was used as an input to a 3D finite element simulation. From the comparison between the measurement and the simulation, it was shown that the difference in the sound pressure level was less than 4 dB, depending on the position. However, the details about the numerical model and frequency spectra of noise were not presented.

2.3 Modelling porous materials

2.3.1 Semi-empirical models

In order to analyse the track radiation in the presence of absorbent treatments, one has to consider how to model porous materials. The simplest model is an empirical model developed by Delany and Bazley [54], which requires only one variable. According to this

---

[1] Note that some of the results in the thesis were presented in this study

model, for a material with flow resistivity σ, the empirical expressions for the complex wavenumber k and characteristic impedance Z_c are given by

$$k = \frac{\omega}{c_0}\left[1 + 10.8\left(10^3\frac{f}{\sigma}\right)^{-0.70} - 10.3\mathrm{i}\left(10^3\frac{f}{\sigma}\right)^{-0.59}\right] \tag{2.2}$$

$$Z_c = \rho_0 c_0\left[1 + 9.08\left(10^3\frac{f}{\sigma}\right)^{-0.75} - 11.9\mathrm{i}\left(10^3\frac{f}{\sigma}\right)^{-0.73}\right] \tag{2.3}$$

where ω is angular frequency, c_0 is the speed of sound in air, ρ_0 is the density of air, f is frequency and σ is the flow resistivity of the material. It was suggested by the authors that the model is valid in the range $0.01 \leq f/\sigma \leq 1.00$ (m^3/kg). Also, the materials used in the study were all highly porous (porosity close to 1), thus the model may not work well for low porosity materials. Miki [55] modified the values used in the derivation of the formula to ensure that the impedance function satisfies the positive-real property. The modified formulas are given by

$$k = \frac{\omega}{c_0}\left[1 + 7.81\left(10^3\frac{f}{\sigma}\right)^{-0.618} - 11.41\mathrm{i}\left(10^3\frac{f}{\sigma}\right)^{-0.618}\right] \tag{2.4}$$

$$Z_c = \rho_0 c_0\left[1 + 5.50\left(10^3\frac{f}{\sigma}\right)^{-0.632} - 8.43\mathrm{i}\left(10^3\frac{f}{\sigma}\right)^{-0.632}\right] \tag{2.5}$$

Later an attempt was made by Taraldsen [56] to produce a theoretical model similar to the Delany–Bazley model. He presented a way to derive the admittance of a porous material from Darcy's law, which requires three variables (porosity, flow resistivity and tortuosity). It was shown that the numerical difference between the two models was very small, which may give a theoretical background to the Delany–Bazley model.

An empirical model for granular media was developed by Voronina et al. [57]. Acoustical properties obtained from impedance tube measurements were used to deduce the coefficients of the real and imaginary parts of the characteristic impedance and the propagation constant, with knowledge of the characteristic particle dimension, porosity, tortuosity and the specific density of the grains. Different granular materials were used, and the predicted results showed good agreement with the measurements. The flow resistivity was also obtained from the low frequency limit of the impedance, which showed good agreement with the experimental data.

2.3.2 Modelling sound propagation in porous media having a rigid frame

When sound propagates through a porous medium, it loses energy due to viscous and thermal dissipation. In order to take this into account, it is first necessary to define parameters to determine the characteristics of porous materials. However, due to their inherent geometric complexity, it is difficult to describe porous materials analytically. For this reason, most research on porous materials has been based on phenomenological descriptions on a large scale. In addition, a frequency domain analysis is often employed with a series of physical parameters used to clarify their physical nature. The analysis starts from evaluating the velocity and the pressure in the pores.

A simplified model in which viscous and thermal effects are included separately was derived by Zwikker and Kosten [58] for porous materials having pores with circular cross–sections. The model was validated and also the thermal exchange effects were related to the viscous effects by Stinson [59]. The theory was extended to include pores of arbitrary shape. Berengier et al. [60] modified the Zwikker and Kosten model to allow a frequency-dependent thermal behaviour.

Attenborough [61] developed a five–parameter model based on the material properties (flow resistivity, porosity, tortuosity, dynamic shape factor and steady-flow shape factor) to predict the acoustic impedance of ground surfaces at low frequencies. Due to the limited range of the empirical formulae, $0.01 \leq f/\sigma \leq 1.00$ (m^3/kg), a theoretical approach was used with the five parameters. After deriving the formulation, the relationship between porosity, tortuosity and flow resistivity and the range of the two shape factors were discussed. From the analysis it was found that predicted impedance is sensitive to the ratio of the two shape factors, thus it was suggested that these values should be deduced first. It was also pointed out that for granular materials, the imaginary part predicted by the empirical formulae is greater than the real part over a considerable range, which was contradictory to the developed model and some measurements.

Wilson [62] viewed the viscous and thermal diffusion as relaxational processes. For identical uniform pores simple forms were obtained that give reasonably accurate results over a wide frequency range. The Delany–Bazley model can be deduced from this by approximating the thermodynamic and aerodynamic characteristic times, but the model is valid beyond the range in which the Delany–Bazley model holds [63].

The Johnson and Allard model [64–66], which also considers five parameters, has become a widely used model of porous media having a rigid frame. Briefly, the model describes the porous material as an equivalent fluid having an effective density and an effective bulk modulus. The dynamic tortuosity of the effective density and a similar function for the bulk modulus were modified by Pride et al. [67] and Lafarge [68], respectively. Several models for the effective density and the bulk modulus can be found and the validity of these models is discussed in [49]. There are some assumptions which enable the theory to be developed. First, the wavelength should be larger than the characteristic dimensions of the pores. Another assumption is the incompressibility of the fluid in the pores at a microscopic scale.

2.3.3 Modelling sound propagation in porous media having an elastic frame

For many porous materials, the frame can be considered to be almost motionless so that the rigid frame model is applicable. Nonetheless, this is not generally true as the frame vibration can be induced by external vibration as well as by interaction with the fluid in the pores. To analyse sound propagation in poro–elastic media where the frame and the air inside the frame move simultaneously, the comprehensive model developed by Biot has been used [69, 70]. The deformation of the frame is assumed to behave like that of an elastic solid so that the air–frame interaction can be approximated similarly to that of a rigid porous medium. From these assumptions, the wave equations for the solid and the fluid in the pores can be developed.

As the Biot model has two governing equations and additional parameters for the frame, its numerical equations become more complex than that of the rigid frame model. A range of methods has been developed to implement the equations into computer codes. Kang and Bolton [71] developed a model for isotropic porous media, based on a classical displacement formulation. Later Atalla et al. [72] modified the Biot equations and developed a mixed displacement–pressure formulation. This has advantages over the classical model in coupling with air and in terms of computational cost.

Göransson [73] developed a 3D symmetric finite element model for wave propagation in porous materials with five variables: displacements of the frame in three directions, pressure and the fluid displacement potential. This has an advantage over the displacement–displacement formulation as it requires fewer variables. Due to the use of the displacement potential for the fluid, the fluid in the pores is assumed to be irrotational. The model was used to study sound transmission through a double panel with a porous filling with different boundary conditions.

Easwaran et al. [74] applied a waveguide finite element method (i.e. 2.5D) to poro–elastic media, to address spurious modes that occur from the displacement–based formulation. The results were validated against an analytical solution in terms of dispersion curves (or eigenvalues of the system matrix). From the eigenvalue problem it was shown that spurious modes occur due to neglecting the irrotationality of the fluid in the formulation. It should be noted that in the formulation the density and stiffness matrices were considered to be frequency-independent, as the fluid is assumed to be nonviscous. Therefore the system matrix was also frequency–independent. This approach cannot be used in formulations with viscous and thermal effects, for which the system matrix is dependent on frequency.

For a layered system that is laterally infinite, an analytical solution can be obtained for both poro–rigid and poro–elastic models. This is useful when calculating acoustic properties of a porous layer. Also, when a porous layer is coupled to other media, the Transfer Matrix Method (TMM) can be employed to consider the coupled system. Details about the method and the analytic solution for a poro–elastic layer is shown in Appendix A.

2.4 Characterisation of porous materials

There are nine properties that must be quantified to use a numerical model based on Biot's theory with the viscous and thermal effects: for the fluid these are porosity, flow resistivity, tortuosity, viscous characteristic length and thermal characteristic length and for the frame they are bulk density, Young's modulus, Poisson's ratio and damping loss factor. A range of methods have been developed either to measure these properties or to determine them inversely.

2.4.1 Properties of saturated fluid

Porosity

The porosity of a porous material is the volume fraction of fluid within the material. It can be directly measured by a porosimeter, or, when possible, simply calculated by comparing its weight before and after it is saturated with liquids, with the accuracy depending on measurement system. Beranek [75] introduced a U–shaped manometer with a known cross-sectional area to measure the porosity. Leonard [76] presented a dynamic method that exploits the compliance of the air in the pores. Compared with the previous method it showed less dependence on the temperature and took less time for a single measurement. Champoux et al. [77] proposed a porosity measurement system, which made use of air instead of liquids. An electronic pressure transducer and a piston made it possible to measure the change of pressure and the change in volume. Leclaire et al. [78] made an improvement to Beranek's method, by adding a reference chamber to the U–tube manometer. As the method uses two chambers the thermal effects were minimised. Different types of samples of low porosity were tested, showing an error of around 5%. A method by Salissou and Panneton [79] is based on the measurement of mass at different static pressures and uses the perfect gas assumption ($PV = mRT$). The measurement setup is shown in Figure 2.14. Four different configurations (low and high pressure and with and without the material) can determine the solid volume proportion V_s of a porous material. This is calculated by

$$V_s = \left(\frac{M_2 - M_1}{P_2 - P_1} - \frac{M_4 - M_3}{P_4 - P_3} \right) RT \tag{2.6}$$

where M are the measured masses, P are the measured pressures, R is the gas constant and T is the temperature. The porosity is then calculated by

$$\phi = 1 - \frac{V_s}{V_t} \tag{2.7}$$

where V_t is the total volume of the material.

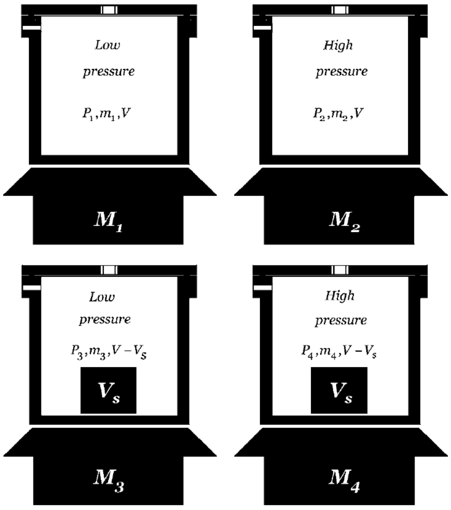

Figure 2.14. Four different conditions for the measurement [79]

Flow resistivity

The flow resistivity is defined as the ratio of the pressure drop to the flow velocity through a sample of the material of unit thickness. It is a measure of how much flow is resisted through the material. A direct measurement method exists following ISO 9053 [3]. There are also indirect methods based on impedance tube measurements [80, 81]. For example Picard et al. [82] measured the specific acoustic impedance at the front and the rear surfaces of a sample in an impedance tube. By subtracting one from the other, the flow resistivity can be obtained by dividing it by the thickness of the test sample. Doutres et al. [81] proposed a three-microphone impedance tube method shown in Figure 2.15 to characterise acoustic and non-acoustic properties. It requires a knowledge of the porosity to determine the other properties. A method that uses only the standard two microphone impedance tube was proposed by Tao et al. [80]. The procedure consists of four steps. First the impedance is measured on the front surface of the sample with and without a cavity at the back. Second the impedance at the back surface of the sample is calculated theoretically. The calculation of the propagation constant and the characteristic impedance based on the impedance transfer function follows next to determine the flow resistivity as in [81].

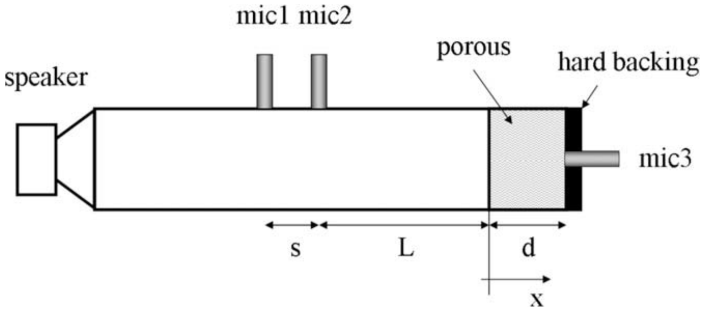

Figure 2.15. Standing wave tube with three microphones [81]

Tortuosity and characteristic lengths

The tortuosity and the two characteristic lengths are related to the structure of the material and control the high–frequency behaviour. Tortuosity is defined as the ratio of the average of the squared velocity and the square of the averaged velocity in the homogenised volume [49]. This is given by

$$\alpha_\infty = \frac{\frac{1}{V}\int_V v^2 \mathrm{d}V}{\left(\frac{1}{V}\int_V v \mathrm{d}V\right)^2} \tag{2.8}$$

where α_∞ is the tortuosity, V is a representative volume and v is the particle velocity at high frequencies where the viscous boundary layer is small in the pores. It describes the structural disorder of the material. For example, if the material has straight cylindrical pores in the direction of wave incidence then the tortuosity is 1.

The viscous characteristic length was introduced by Johnson et al. [64] to replace the hydraulic radius of the pore, making the analysis more accurate. Similarly, Champoux and Allard [65] proposed the thermal characteristic length to consider temperature effects. The viscous characteristic length Λ and the thermal characteristic length Λ' are given by

$$\frac{2}{\Lambda} = \frac{\int_A v^2 \mathrm{d}A}{\int_V v^2 \mathrm{d}V} \tag{2.9}$$

$$\frac{2}{\Lambda'} = \frac{\int_A \mathrm{d}A}{\int_V \mathrm{d}V} \tag{2.10}$$

where A and V are the area and the volume of the pores and v is the velocity of the inviscid fluid. Depending on the geometry, the thermal characteristic length falls in a range between Λ and 2Λ.

These three variables can be measured in various ways. For example, Leclaire et al. [83] presented an ultrasonic attenuation measurement to obtain the viscous characteristic length. Henry et al. [84] showed that the standard Brunauer, Emmett and Teller method (BET) could help to obtain the thermal characteristic length. Fellah et al. [85] measured the porosity and the tortuosity simultaneously by measuring reflected ultrasonic waves at oblique incidence.

On the other hand, a range of indirect methods has been developed to characterise those parameters from acoustic properties. This is basically an optimisation process performed by adjusting each parameter while comparing measured acoustic properties with calculations. For example, Atalla and Panneton [86] proposed an optimisation method based on impedance tube measurements. This used the differential evolution optimisation algorithm to characterise these three parameters of the Johnson–Allard–Champoux (JAC) model, which are difficult to measure. To eliminate the effect of the frame the measurement was done in a frequency range above the decoupling frequency, so that the frame can be considered motionless. A review of acoustical methods for characterisation of porous materials is presented by Horoshenkov [87]. The author presented the characteristics of different types of porous material (foams and fibrous materials, granular materials and sandy soils). Also, some examples were given with corresponding properties. One of the examples was the properties of gravels, for which the properties were: $\sigma = 218$ Pa·s/m^2, $\phi = 0.424$, $\alpha_\infty = 1.51$ and $\Lambda = \Lambda' = 1.24$ mm. These could be used a reference for the ballast properties, in terms of magnitude.

2.4.2 Elastic properties

The frame of porous materials can be regarded as viscoelastic, the behaviour of which is between that of the pure elastic solid and the ideal viscous fluid. As, for acoustical purposes, most of them do not undergo large deformations, studies have been confined to the region of linear viscoelasticity. Also, anisotropy and inhomogeneity have barely been taken into account due to the complexity of the problem. Based on these assumptions, a number of methods have been proposed to obtain the elastic parameters [88].

Mariez et al. [89] measured dynamic mechanical properties of anisotropic open-cell foams using a cubic sample. When a certain dynamic displacement is imposed on the sample by a shaker, a dynamic compressional stiffness can be obtained by measuring the force and the imposed displacement. The Poisson's ratio can be obtained by measuring the induced transverse displacement with a laser vibrometer. This was done at a low frequency in order to avoid any resonances from the measurement setup or the sample. By keeping the strain rate under a certain value, a quasi–static condition was achieved. From a static solid finite element simulation of the measurement, the Young's modulus and Poisson's ratio were expressed in terms of a static compressional stiffness, a static compressional displacement and a static transverse displacement. They were replaced with the quasi–static compressional stiffness and the measured displacements, which allowed the Young's modulus and the Poisson's ratio of the cell to be found. Tarnow [90] proposed analytical expressions for the variables used in the measurement. This was valid only for glass wool, where the Poisson's ratio is assumed to be zero. A method by Langlois et al. [91] modified the measurement by using a cylindrical sample. Based on the isotropic assumption, two samples of different sizes were used and, from precomputed results of the static measurement, the complex Young's modulus and the Poisson's ratio were estimated. A similar setup but using a different approach was presented by Etchessahar et al. [92]. This used a rotor to generate torsion on the sample surface. The torque and the angular displacement were measured to estimate the complex shear modulus.

Apart from the direct measurement methods, indirect methods based on an acoustical excitation or a phase-velocity measurement have also been considered. For example, a method by Allard et al. [93] used an omnidirectional compact acoustic source to excite a thin porous sample with a grazing incidence. This induces a shear mode of the structure, and this mode is related to the frequency at which the thickness of the sample is equal one quarter of the wavelength of the shear wave. Using an iterative method, a complex angle of incidence θ_p was obtained at which the reflection coefficient becomes zero. It was shown that $\cos\theta_p$ had fast variations where the shear resonance occurs. By fitting the measured $\cos\theta_p$ with a predicted one, the shear modulus was obtained. Hong [94] made a full optimisation for nine parameters including the rigid frame parameters. This was done with two acoustic properties measured from an impedance tube: absorption coefficient and transmission loss. An axisymmetric finite element model was used for simulation. To reduce the number of constraints, principal component analysis was employed. This produces nine vectors that have nine variables as components, which are nearly independent from each other. Then by reducing the less effective vectors, identified from a sensitivity analysis, this will lead to a reduction of the computational cost. Sim and Kim [95] made use of a transmissibility measurement of a cylindrical sample to obtain an apparent Young's modulus. This is then used to calculate the Poisson's ratio from a static finite element simulation of the sample. To check the value the obtained Poisson's ratio is again put into the simulation to produce another value of the Poisson's ratio. The process is iterated until the Poisson's ratio converges.

2.5 Summary

In this chapter it is shown that when absorptive treatments are considered in the track, the acoustic boundary element method has often been used with impedance (or admittance) boundary conditions. In some research on the ballast it was indicated that the sound propagation within the ballast should be considered, yet few investigations have considered this. Also, the sound radiation from the ballast has not been highlighted due to the complexity in modelling. Therefore the contribution to the rolling noise is still an open question.

The elasticity of porous materials has not been considered in the analysis of the radiation of the track. This may be important when the absorptive treatments are excited by the vibration transmitted from the rail as well as the acoustical excitation radiated from the rail. This would be the case for absorptive blocks, as they are installed on the track. However, most of the research about absorptive blocks was based on experiments. To understand the mechanism and provide a better solution, an appropriate prediction model is required. The numerical model presented in this thesis will address these aspects.

Chapter 3

Characterisation of porous materials

In the Biot-Allard model [49], the properties of porous materials can be divided into two categories. One consists of the properties of saturated fluid (porosity ϕ, flow resistivity σ, tortuosity α_∞, viscous characteristic length Λ and thermal characteristic length Λ') and the other of the elastic properties of the frame (density ρ_1, Young's modulus E, loss factor η and Poisson's ratio ν). These are discussed separately in the following sections, and example results are shown for a melamine foam.

3.1 Properties of saturated fluid

In this section the flow resistivity measurement in the laboratory and the procedure for the inverse characterisation are described. The inverse characterisation for a melamine foam has been conducted to obtain the fluid parameters.

3.1.1 Flow resistivity measurement

The flow resistivity of a layer of porous material having thickness h is given by

$$\sigma = \frac{\Delta p}{vh} \tag{3.1}$$

Here, Δp is the pressure drop across the sample and v is the mean flow velocity passing through the material. The measurement setup adopted is shown in Figure 3.1. Air is blown through a small tube from a compressed air reservoir. Its volume flow rate is measured by a flow meter and as the flow passes through the cone area, it is distributed uniformly over the cross-section. After the flow is stabilised in the cylinder, the pressure drop across the sample is measured by a manometer (model fco 510 by Furness Controls). A 1.5 mm thick perforated steel plate with a perforation ratio of 0.31 is used at the bottom of the cylinder to hold the sample and to ensure the flow exits smoothly at the back of the sample. The diameter of the perforation is 3 mm. It is recommended that the velocity of the flow is between 5×10^{-4} and 5×10^{-2} m/s [18]. Also, in reality it is not possible to cut the sample to fit exactly in the cylinder. Thus there could be a gap between the sample and the cylinder, which could lead to leakage around the edge of the sample. To prevent this, samples have been cut to have a slightly larger diameter ($\geq$ 101 mm) than that of the cylinder (100 mm). It was possible to squeeze the sample into the cylinder as the material was soft. This might not be the case for harder materials. It should be noted that squeezing the sample might affect the result as well as the gap, which was not taken into account in this study.

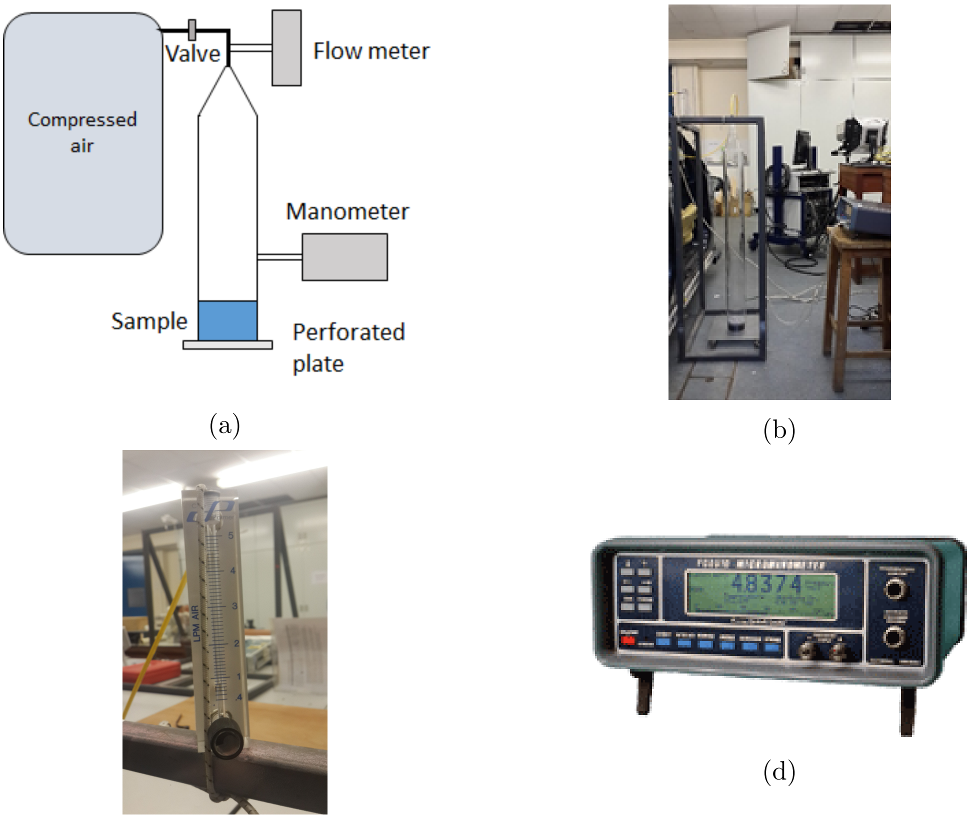

(a) (b) (c) (d)

Figure 3.1. Flow resistivity measurement setup: (a) diagram, (b) setup in the laboratory, (c) flow meter and (d) manometer

In the current setup, a 1 m long cylinder with a diameter of 100 mm has been used. To check the validity of the setup, the measurement has been carried out with three different flow rates for two different sample thicknesses. For each flow rate, the measurement was repeated three times and the sample was removed and reassembled for each measurement. The melamine foam samples and the results are shown in Figure 3.2 and Figure 3.3, respectively. The error bars in Figure 3.3 are the range of the three measured values. The measured flow resistivity has some deviations but in general the values are within a reasonable range. In this case a value of 11000 ± 500 Ns/m^4 has been identified for the flow resistivity. From the result it can be said that the set up can be used for other porous materials.

(a) (b)

Figure 3.2. Foam samples for the flow resistivity measurement: (a) 17 mm and (b) 34 mm

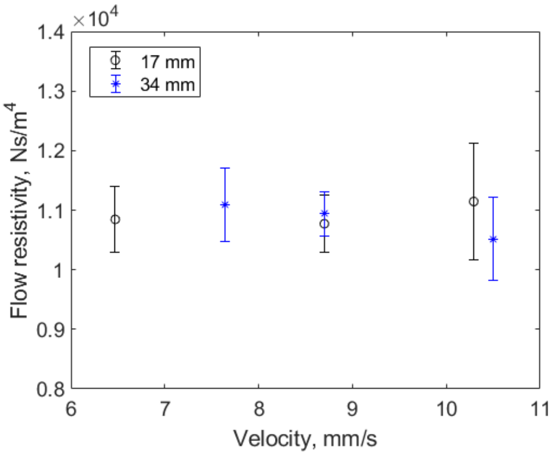

Figure 3.3. Measured flow resistivity for different thicknesses; — 17 mm sample, — 34 mm sample; range obtained from three repeated measurements

3.1.2 Inverse characterisation from acoustic properties

In this section a method to obtain the remaining properties of saturated fluid is presented. Basically one should find the most influential parameter first and the others next according to priority. To set the priority of each variable a sensitivity analysis has been conducted for a material with known properties. Glass wool, for which all the properties of saturated fluid are known [72], has been chosen to show how sensitive the result is to each parameter. Later the method has been applied to the melamine foam.

3.1.2.1 Sensitivity analysis

As mentioned above, only the flow resistivity has been measured and the other parameters have been obtained inversely from impedance tube measurements. As a first attempt, a sensitivity analysis has been conducted to see how much the result changes due to the increase/decrease of each variable. The glass wool has been chosen as all properties are known. The fluid parameters are listed in Table 3.1. Note that the elastic parameters are ignored here. For the calculation of the absorption coefficient the transfer matrix method (TMM, see Appendix A) has been employed, which assumes that the domain of interest is a set of layers of infinite area. For modelling the glass wool the Johnson–Allard–Champoux (JAC) model has been used. For a thickness of 100 mm, the results are shown in Figure 3.4.

Table 3.1: Properties of saturated fluid of the glass wool [72]

α_∞	ϕ	σ (Ns/m^4)	Λ (μm)	Λ' (μm)
1.06	0.94	40000	56	110

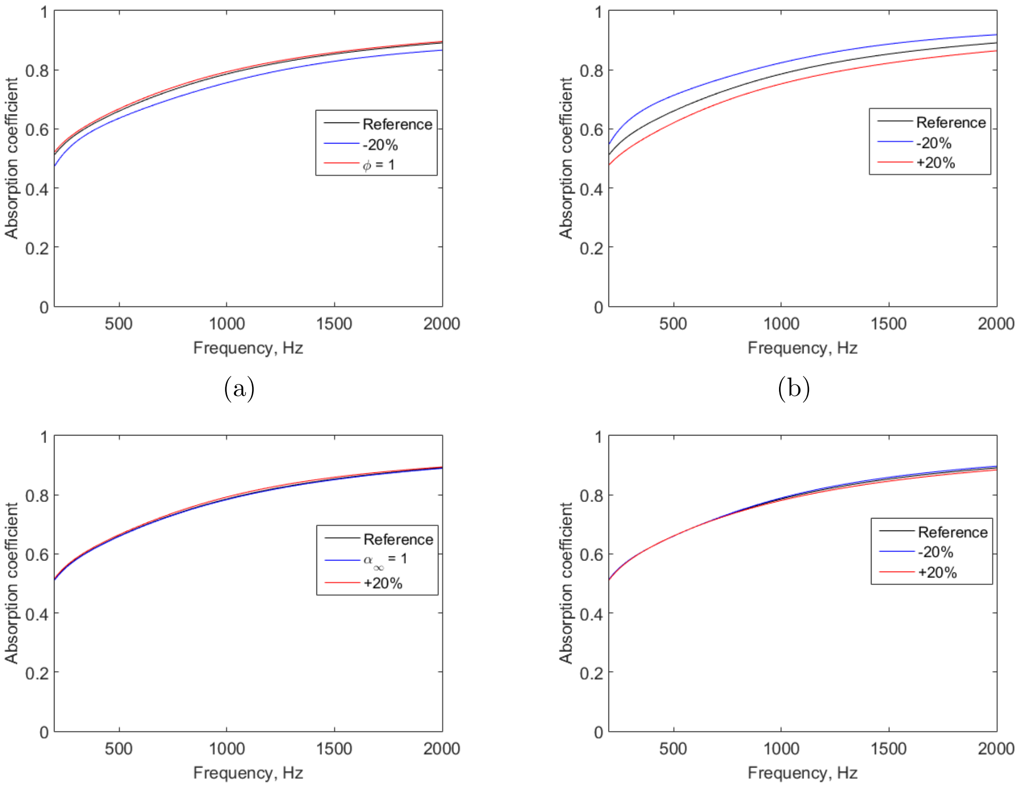

(a) (b) (c) (d)

Figure 3.4. Sensitivity in absorption coefficient for variation in different properties: (a) porosity, (b) flow resistivity, (c) tortuosity and (d) characteristic lengths; — reference, — lower bound, — upper bound

The results show the change in absorption coefficient when each property is changed by ±20%. As there are physical limits for the porosity and tortuosity by definition, their value has been chosen to vary up to the limit when the 20% variation exceeds it. For example the lower limit of 1 is used for the tortuosity as 80% of the reference value is smaller than 1. From the results it can be seen that the flow resistivity and the porosity have the most influence on the result. However, as foams have a high porosity in the range 0.9–1.0 in most cases, the effect of the porosity is not as large as that of the flow resistivity. Thus the flow resistivity should be the first parameter to be fitted. The next most influential parameter is the porosity. The other parameters have little effect on the result. This is mainly because the characteristics are dominated by the flow resistivity when the flow resistivity is high enough. When a material has a low flow resistivity, the effect of the tortuosity and the characteristic lengths would be greater, particularly at high frequencies. This will be shown later for the case of ballast in Chapter 5. Nevertheless, they can be adjusted once the flow resistivity is fixed.

3.1.2.2 Example: properties of saturated fluid of a melamine foam

Figure 3.5 shows the absorption coefficient of the melamine foam of 50 mm thickness measured by Zhang et al. [13]. Based on the measured flow resistivity from Section 3.1.1, the inverse characterisation has been carried out by adjusting each variable. It should be noted that the absorption coefficient is more reliable than the surface impedance, in terms of inverse characterisation. This is because the surface impedance is sensitive to the edge condition. For this reason the absorption coefficient is used throughout this study. Good agreement is seen at low and high frequencies, with a discrepancy between 700 Hz and 1100 Hz. The root mean square error (RMSE, hereafter referred to as RMS error) has been calculated by the following equation:

$$\mathrm{RMSE} = \sqrt{\frac{1}{n}\sum_{1}^{n}(Y_p - Y_m)^2} \tag{3.2}$$

where n is the number of data points, Y_p is the predicted data and Y_m is the measured data. For this case, the predicted data shows an RMS error of 0.02 in the range $f \leq 630$ Hz and $f \geq 1250$ Hz. If the dip region is considered, the RMS error increases to 0.08. The dip in the measured results in this frequency range is due to the elastic properties of the foam, which will be discussed later. Apart from that, the prediction gives reasonable agreement. The adjusted parameters are given in the first row in Table 3.2.

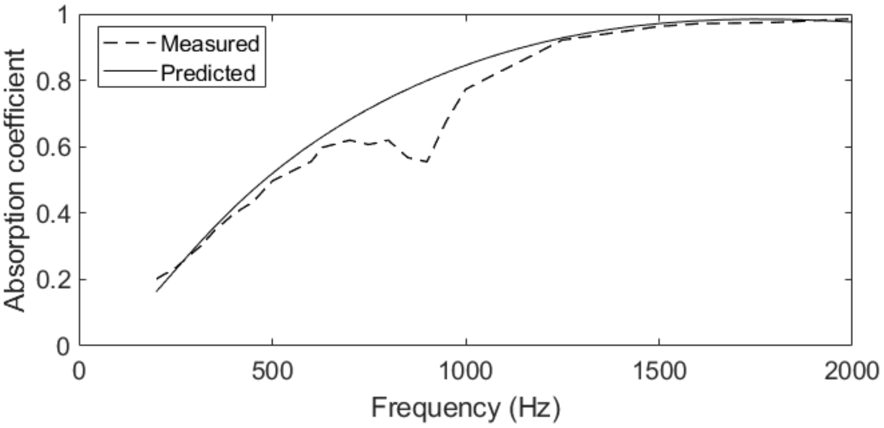

Figure 3.5. Absorption coefficient of the melamine foam; - - - measured, —— predicted using JAC model

TABLE 3.2: Properties of saturated fluid of the foam; (a) obtained by the inverse characterisation and (b) melamine foam used in [96]

	α_∞	ϕ	σ (Ns/m^4)	Λ (μm)	Λ' (μm)
(a)	1.06	0.97	11000	150	200
(b)	1.01	0.99	11000	120	240

For comparison, the properties of saturated fluid of a melamine foam, used in [96], are also shown in the second row in Table 3.2. Little difference is seen, although the samples are not the same. This shows that the properties in Table 3.2 are in a reasonable range.

3.2 Elastic properties

While the properties of saturated fluid affect the general tendency in the absorption coefficient curve, the elastic properties determine the dips (or peaks) in the absorption coefficient, which are related to resonances of the frame. This is shown in Figure 3.6, which shows two results from the poro–elastic model described in Appendix A. The dip at around 900 Hz represents the resonance of the frame, which could not be obtained from the rigid frame model. The position of the dip is largely influenced by the P–wave modulus, which is related to the Young's modulus and the Poisson's ratio of the frame. It is given by

$$K_c = \frac{E(1-\nu)}{(1+\nu)(1-2\nu)} \tag{3.3}$$

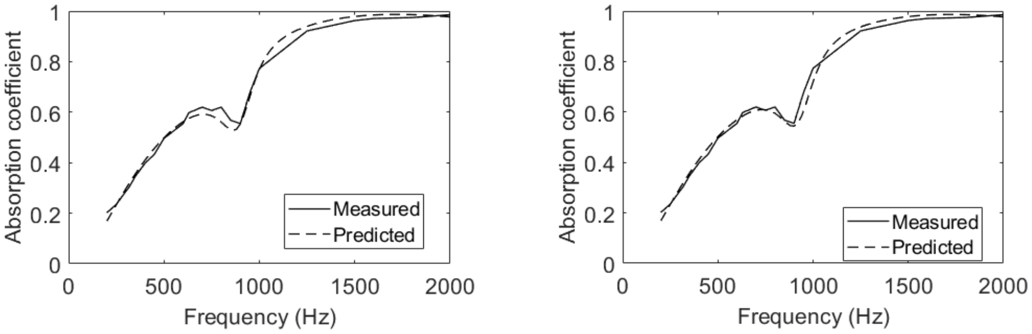

(a) (b)

Figure 3.6. Comparison with the measured absorption coefficient: (a) E = 300 kPa, $\nu = 0.2$ and (b) E = 94 kPa, $\nu = 0.45$; ━ measured, - - - predicted using poro–elastic model

In this example the elastic properties were chosen to match the measurement. From Figure 3.6 it can be seen that two completely different combinations of the elastic parameters could lead to very similar results. Although the P-wave modulus is the same in each case, one cannot rely solely on this factor as it has a strong dependence on the edge condition when measured in the impedance tube [94]. To resolve this problem, a method in the ISO standard [19] has been used. It consists of a dynamic stiffness measurement and a finite element simulation of the measurement for the static case. From the measurement, the dynamic stiffness and the loss factor of the material can be obtained. On the other hand, a polynomial relation between the Young's modulus and the Poisson's ratio can be derived from the static simulation. By combining these one can find the Young's modulus as a function of the Poisson's ratio. Taking two samples with a different shape gives two different Young's modulus curves, the intersection of which allows a unique combination of the Young's modulus and the Poisson's ratio to be found. The term representing the size is called the shape factor, which is the ratio between the diameter and the thickness of the sample.

3.2.1 Dynamic stiffness measurement

The dynamic stiffness of the melamine foam used in the previous section has been measured according to the procedure described in [91]. The measurement setup is depicted in Figure 3.7. It consists of a disc-shaped sample of the porous material placed between two stiff aluminium plates, for which the properties are shown in Table 3.3. A large steel mass (31 kg) is located at the bottom to provide a blocked termination. An accelerometer is placed on the top plate and a force gauge is located between the lower plate and the mass. The upper surface of the sample is excited by a shaker that is fixed on the holder. Converting the acceleration to displacement, the ratio between two measured values gives the dynamic stiffness of the sample, as a function of angular frequency ω.

$$\frac{F(\omega)}{u(\omega)} = K_m(\omega)\left(1 + \mathrm{i}\eta(\omega)\right) \tag{3.4}$$

Here, $F(\omega)$ and $u(\omega)$ are the force exerted on the sample and the displacement of the sample surface. This can be expressed by using the dynamic stiffness magnitude $K_m(\omega)$ and its loss factor $\eta(\omega)$. The measurement can be regarded as quasi–static if the excitation frequency is well below the resonance frequency of the sample. Also, the strains applied to the sample should be less than 5% to ensure linearity in the sample [91]. Both conditions enable the sample to have *in vacuo*–like behaviour.

Table 3.3: Mechanical properties of the plates

Property	ρ	E	ν	Thickness	Side length	First resonance frequency
	(kg/m^3)	(GPa)		(mm)	(mm)	(Hz)
Value	2700	70	0.33	3	110	850

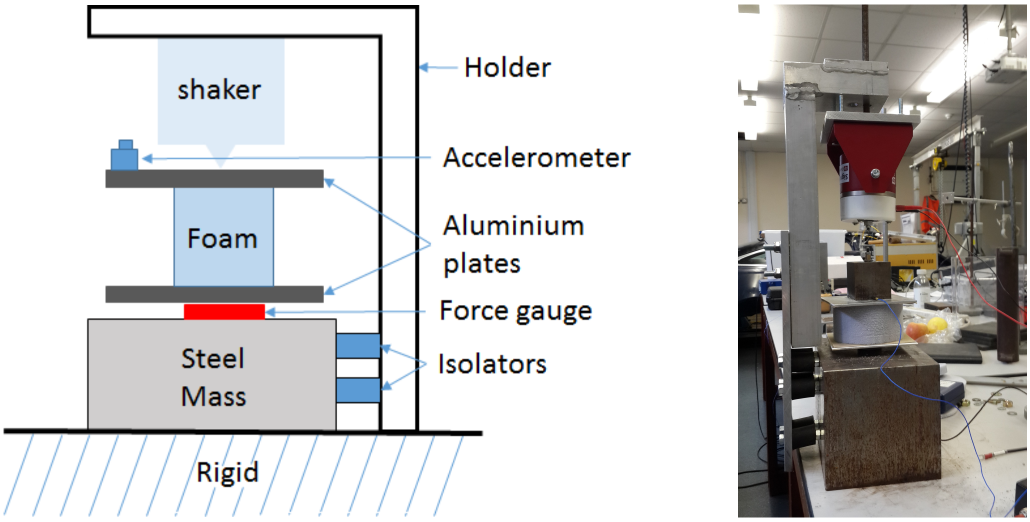

(a) (b)

Figure 3.7. Dynamic stiffness measurement setup: (a) diagram and (b) setup in the laboratory

3.2.2 Finite element simulation

Following the dynamic stiffness measurement, the finite element analysis of the static measurement is needed to extract the relationship between the stiffness and the Poisson's ratio [19]. In the finite element simulation the sample is modelled as a cylindrical solid material with diameter D and length L. For a slender body ($10D < L$) the static compressional stiffness is not affected by the Poisson's ratio, and the Young's modulus is related to the stiffness by

$$K_0 = \frac{EA_s}{L_s} \tag{3.5}$$

where L_s is the length, $A_s = (\frac{D}{2})^2\pi$ is the area and K_0 is the compression stiffness. For a material for which $10D > L$, the compressional stiffness is likely to be affected by the Poisson's ratio. By the same analogy as in Equation (3.5), an apparent Young's modulus E' can be defined as

$$E' = \frac{L_s}{A} K_m(0) \tag{3.6}$$

where $K_m(0)$ is the computed static compression stiffness for a given Young's modulus E from the static FE simulation. Here, 0 in $K_m(0)$ means the angular frequency is zero (i.e., $\omega = 0$). Note that E' is different from E due to the shape factor. Dividing Equation (3.6) by Equation (3.5) yields the normalised ratio of the static compression stiffness.

$$\frac{E'}{E} = \frac{K_m(0)}{K_0} \tag{3.7}$$

Note that the right–hand side of Equation (3.7) is the normalised compressional stiffness, which is independent of the Young's modulus E. In this case, the ratio is only affected by the Poisson's ratio. This can be represented as a function of Poisson's ratio and be approximated as a polynomial function of ν, namely:

$$P_s(\nu) = \frac{K_m(0)}{K_0} = 1 + \sum_{i=1}^{N} D_i^s \nu^i \tag{3.8}$$

where D_i^s is the coefficient obtained by regression analysis. From the quasi–static approximation,

$$K_m(\omega) \to K_m(0) \quad \text{for} \quad \omega \ll \omega_1 \tag{3.9}$$

where ω_1 is the first resonance frequency of the frame. If two different samples s_1 and s_2 are used, the corresponding actual Young's moduli can be calculated in both cases as a function of Poisson's ratio and they should be the same since it is an intrinsic property. From equation (3.7),

$$E = \frac{E'}{K_m(0)/K_0} = \frac{E'}{P_s(\nu)} \tag{3.10}$$

From equations (3.6), (3.8) and (3.10),

$$E = \frac{K_{m,s_1}(\omega) L_{s_1}}{A_{s_1} P_{s_1}(\nu)} \tag{3.11}$$

$$E = \frac{K_{m,s_2}(\omega) L_{s_2}}{A_{s_2} P_{s_2}(\nu)} \tag{3.12}$$

Combining (3.11) and (3.12) yields

$$\frac{K_{m,s_1}(\omega)L_{s_1}}{A_{s_1}P_{s_1}(\nu)} = \frac{K_{m,s_2}(\omega)L_{s_2}}{A_{s_2}P_{s_2}(\nu)} \tag{3.13}$$

By applying the quasi-static condition, equation (3.13) becomes purely an equation for the Poisson's ratio. Solving this polynomial equation gives a unique solution for the Poisson's ratio. Once this is done, then the Young's modulus can also be determined according to the obtained Poisson's ratio using either Equation (3.11) or (3.12).

3.2.3 Example: elastic properties of a melamine foam

The elastic properties of the melamine foam have been investigated as an example. Two samples of the same diameter but with different thickness have been cut and used, which are shown in Figure 3.8. The diameter is 100 mm and the thicknesses are 52 mm and 18 mm, respectively. Again sample (b) has unevenness at the edges, which might affect the result to some degree. The results from the measurement are shown in Figure 3.9. Both results appear to vary to some extent. As it is not easy to choose a single value, a range from the results has been used. Thus $K_m(\omega) = 20 \sim 25$ kN/m for (a) and $K_m(\omega) = 90 \sim 100$ kN/m for (b) have been chosen. The upper and lower limits have been used in the calculation to indicate how much the final result may deviate. The variation in the result comes from several factors. During the measurement it was found that the condition of the sample surfaces was the most crucial factor for the result. The reason for this was that small particles were left on the surface after the sample was cut. Also the sample should be well fixed to the upper plate, as otherwise the upper plate could vibrate separately. To reduce the uncertainty, a small cubic mass has been put on the upper plate to give preload, which will ensure the contact between the sample and the plate is maintained. Sandpaper has been used between the plates and the sample to prevent slip at the interface. The resonance frequency of sample (a) is known to be around 900 Hz, as shown in Figure 3.5. For sample (b) this would be higher as the sample is thinner. Thus the resonance at 50 Hz for (a) and 80 Hz for (b) in the measurement are thought to be due to the test rig frame and can be neglected.

(a) (b)

Figure 3.8. Two melamine foam samples of different shape factors: diameter of 100 mm and thickness of (a) 52 mm and (b) 18 mm

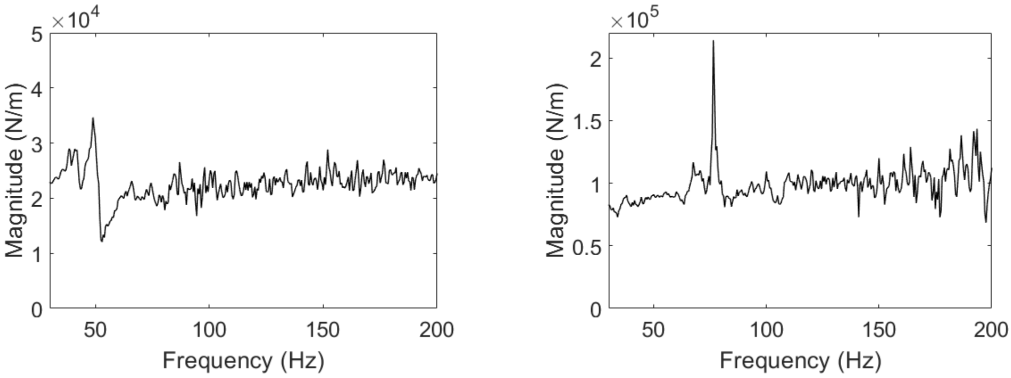

(a) (b)

Figure 3.9. Magnitude of measured dynamic stiffness for each sample: (a) 52 mm and (b) 18 mm

The finite element simulation for each sample has been done by using the commercial software ABAQUS. Results have been obtained at 11 values of Poisson's ratio and functions of the Poisson's ratio curve have been obtained from this and represented by a polynomial. This is illustrated in Figure 3.10.

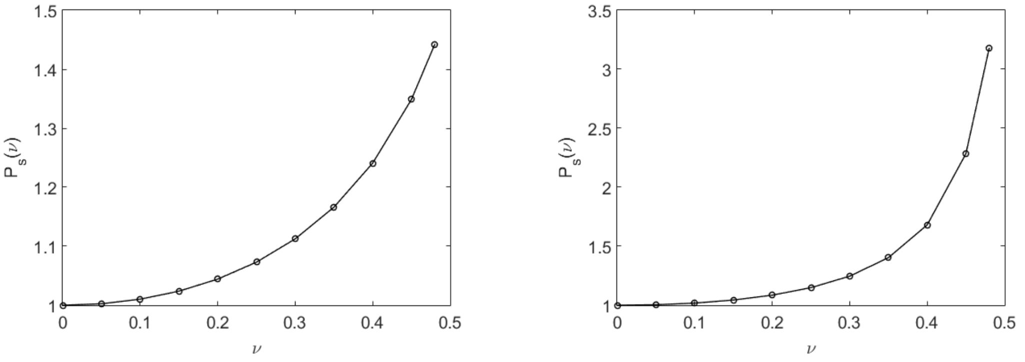

(a) (b)

Figure 3.10. Stiffness ratio as a function of Poisson's ratio for melamine foam of two different thicknesses: (a) 52 mm and (b) 18 mm

The polynomial relation obtained by regression for each sample is

$$P_{sa}(\nu) = 134.2\nu^6 - 153.2\nu^5 + 70.82\nu^4 - 14.24\nu^3 + 2.348\nu^2 - 0.0447\nu + 1 \tag{3.14}$$

$$P_{sb}(\nu) = 1784\nu^6 - 1904\nu^5 + 789.8\nu^4 - 148.7\nu^3 + 14.51\nu^2 - 0.3785\nu + 1 \tag{3.15}$$

Combining the results with equations (3.14) and (3.15), taking the measured dynamic stiffness $K_m(\omega)$ as the input, the Young's modulus curves can be obtained. The result is also given as a range, as shown in Figure 3.11. Each range is calculated from the two limit values of the stiffness measurement for each sample. The intersection between the two ranges gives a region where a set of possible solutions exist. The values in Table 3.4 show the Young's modulus and the Poisson's ratio for each point selected.

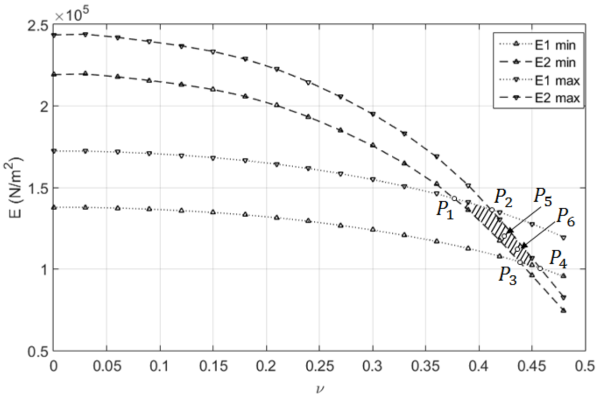

Figure 3.11. Young's modulus curves; ····· thick sample, - - - thin sample. The solution exists in the shaded region.

Table 3.4. (E, ν) for the selected points

	E (kPa)	ν
P_1	143.5	0.377
P_2	137.0	0.412
P_3	104.5	0.438
P_4	101.0	0.458
P_5	122.0	0.425
P_6	110.0	0.441

To see the variance of the solution, the absorption coefficient has been calculated for each point in Table 3.4 using the transfer matrix method with the poro–elastic model for the material. The results are plotted in Figure 3.12 with the measured absorption coefficient. The points at each end, P_1 and P_4, show the range of the results. The other points, which are located in the middle region, show a nearly identical result except P_6, with a dip at around 820 Hz. The result of P_6 is the closest to the measured result in terms of the trend and the resonance frequency. Overall, it can be said that the values in the middle of the shaded zone give acceptable results.

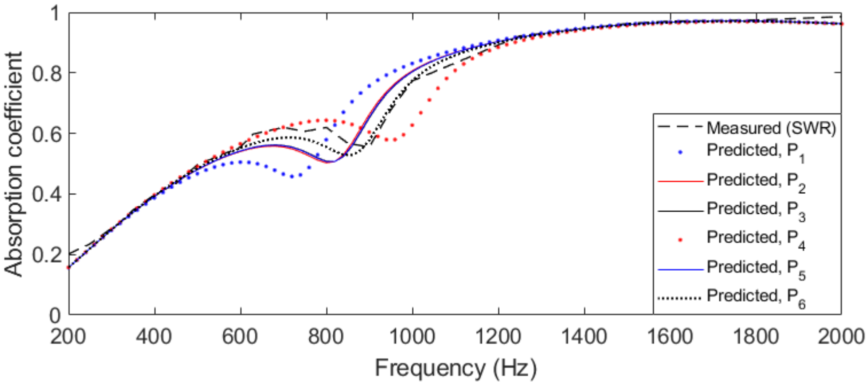

Figure 3.12. Absorption coefficient for the selected points; - - - measured in impedance tube (standing wave ratio method), ⋯⋯ predicted at P_1, ── predicted at P_2, ── predicted at P_3, ⋯⋯ predicted at P_4, ── predicted at P_5, ⋯⋯ predicted at P_6; all predictions are made using poro–elastic model

The loss factor η has been calculated from the ratio of the imaginary part to the real part of the stiffness. This is shown in Figure 3.13 for the two samples. The mean values of the loss factor for the two samples have been calculated using the result from 100 Hz to 200 Hz and these are 0.16 and 0.15 respectively. Therefore the loss factor is expected to be between 0.15 and 0.16.

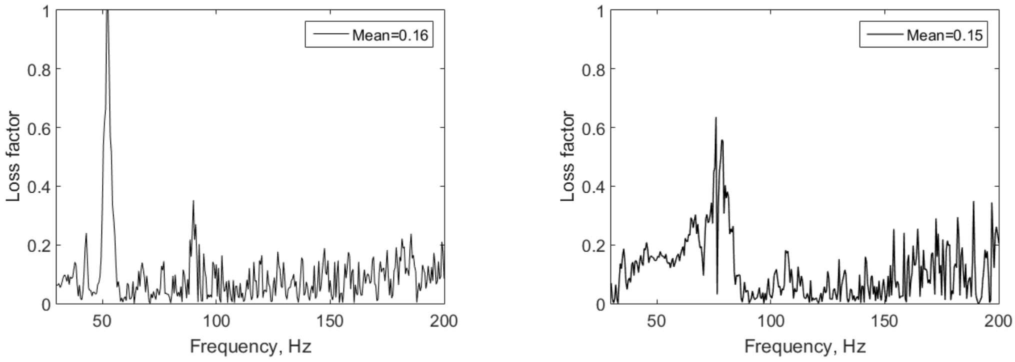

(a) (b)

Figure 3.13. Measured loss factor for each sample: (a) 52 mm and (b) 18 mm ($\eta = \mathrm{Im}\left(K_m(\omega)\right)/\mathrm{Re}\left(K_m(\omega)\right)$)

From these measurements the elastic properties of the foam have been determined with a tolerance and are listed in Table 3.5. Note that the error ranges for the Young's modulus and the Poisson's ratio are determined from the RMS error, using the data points P_1–P_6. For the loss factor the mean value has been taken, and the density was directly measured using a scale.

Table 3.5: Elastic properties of the melamine foam

Property	ρ_1 (kg/m^3)	E (kPa)	η	ν
Value	11	120 ± 16	0.155 ± 0.005	0.42 ± 0.02

3.3 Summary

In this chapter ways to obtain the properties of porous materials required in the Biot-Allard model were presented. It was shown that the porosity and the flow resistivity can be measured directly with ease, whereas the other properties of saturated fluid could be inversely characterised from impedance tube measurements. Measurements are shown for a melamine foam. From the flow resistivity measurement the flow resistivity of 11000 Ns/m^4 was obtained, with a deviation of around 500 Ns/m^4. From the sensitivity analysis it was shown that the porosity and the flow resistivity are the most influential parameters for the given ranges of values. From the impedance tube measurement the other properties of saturated fluid of the melamine foam were determined.

The elastic properties are measured following the ISO standard 18437-5. Melamine foam samples with two different sizes were used to measure the dynamic stiffness. With the assumption of quasi–static behaviour at low frequencies and based on finite element simulations, the complex Young's modulus and the Poisson's ratio were determined.

Chapter 4

Numerical modelling of porous materials

As discussed in Chapter 2, when modelling the sound radiation of a track, the acoustic boundary element method is usually used [33, 35, 97, 15]. In cases where absorptive treatments are involved, they can be modelled as impedance boundaries. The Delany–Bazley model [54] is one example of an impedance model for the absorptive boundaries. This gives a good estimate for absorptive materials with high flow resistivity [47]. However, for absorptive treatments with low flow resistivity or soft frame elasticity, this is not the case. With a low flow resistivity sound waves can propagate inside the medium, rather than being locally reflected at the surface. Moreover, if the material is soft then its frame can vibrate when it is subjected to structural or acoustic excitations. To consider these phenomena, a finite element model is required for modelling sound propagation inside porous materials.

A schematic view of the track with absorptive treatments are shown in Figure 4.1. For a ballasted track with a noise barrier with a porous lining (see Figure 4.1(a)), the ballast and the porous lining can be modelled using poro–elastic finite elements. The rails and the sleeper can be modelled using solid finite elements. The radiation from the track can be calculated from the boundaries of the track and the barrier, which can be modelled using fluid boundary elements. Figure 4.1(b) represents a slab track with an absorptive block. In this case, the slab and the rails can be modelled using solid finite elements and the absorptive blocks can be modelled using poro–elastic finite elements. Also, as the track has a uniform geometry in one direction, a 2.5D approach can be used to reduce the computational cost.

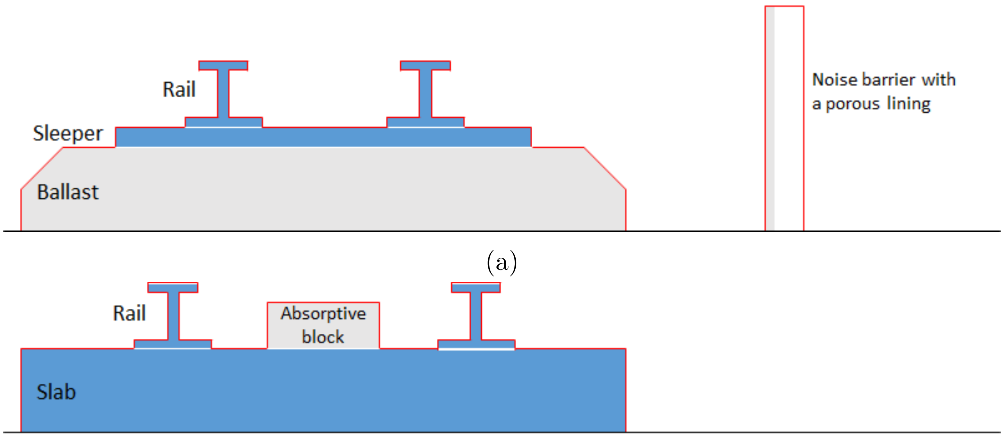

(a)

(b)

Figure 4.1. A schematic view of track with absorptive treatments: (a) ballasted track with noise barrier and (b) slab track with absorptive block; 🟦 solid finite elements, ▨ poro–elastic finite elements, — fluid boundary elements

In fact, there already exists a 2.5D finite element/boundary element software called WANDS (WAveNumber Domain Software) developed in the Institute of Sound and Vibration Research (ISVR), which only leaves the development of a 2.5D poro–elastic finite element model and couplings with the existing models in WANDS. Based on the diagrams in Figure 4.1, a 2.5D mixed displacement–pressure model based on the Biot theory has been developed which can be used to represent the absorptive parts. A formulation is presented, and its verification is carried out with the 2D model.

Couplings between the 2.5D poro–elastic finite element model and the finite element/boundary element models in WANDS are also presented based on the conditions in [98], which have been implemented in WANDS. The theoretical formulations of WANDS models can be found in [20].

4.1 Finite element models for porous materials

In this section, two finite element models for sound propagation in porous materials are introduced. The first one is called a poro–rigid model, in which the frame is assumed to be motionless. Therefore only the fluid behaviour inside the material is of interest. The second is called a poro–elastic model. As the name suggests the frame has elasticity, so that structural waves can occur as well as waves in the fluid. For each part formulation and characteristics are described briefly. For simplicity, the material is assumed to be isotropic.

4.1.1 Sound propagation in porous media having a rigid frame

4.1.1.1 Outline of the theory

The geometrical structure of porous materials is very complicated, thus to consider this accurately in calculation is almost impossible. However, it is still possible to obtain some useful information on the viscous and thermal interaction, by assuming simple geometries. Based on that, phenomenological models have been developed to describe their behaviour in more detail.

By investigating the pressure and velocity of the fluid inside the pores, one may regard the whole volume as an equivalent fluid with modified properties. In this way a classical fluid finite element model can be adopted, for which the governing equation is the Helmholtz Equation.

$$\boldsymbol{\nabla}^2 p + k_e^2 p = 0 \tag{4.1}$$

where $k_e = \omega/c_e$ is the equivalent complex wavenumber with $c_e = \sqrt{K_e/\rho_e}$ being the complex wavespeed and ω is angular frequency. Note that it is assumed that no sources are present within the material as porous materials are not usually in contact with direct excitation. As described in the literature review, the effective density ρ_e and bulk modulus K_e can be written as [49]

$$\rho_e = \rho_0 \left[\alpha_\infty + \frac{\nu_k \phi}{j\omega q_0} G(\omega) \right] \tag{4.2}$$

$$K_e = \gamma P_0 \left[\gamma - \frac{\gamma - 1}{1 + \frac{\nu' \phi}{j\omega q_0'} G'(\omega)} \right] \tag{4.3}$$

where α_∞ is the high–frequency limit of the tortuosity (referred to simply as tortuosity), ν_k is the kinematic viscosity, ϕ is the porosity, q_0 is the static permeability, γ is the ratio of specific heats, P_0 is the ambient pressure, ν' is the thermal viscosity, and q_0' is the static thermal permeability. $G(\omega)$ and $G'(\omega)$ are frequency–dependent functions which can be evaluated by different models. In this work, the models of Johnson et al. [64] and Champoux–Allard [65] have been used for the density and the bulk modulus, respectively. The static permeabilities q_0 and q_0' are given by [64, 68]

$$q_0 = \phi \frac{\Lambda^2}{8\alpha_\infty} \tag{4.4}$$

$$q_0' = \phi \frac{\Lambda'^2}{8} \tag{4.5}$$

where Λ is the viscous characteristic length and Λ' is the thermal characteristic length. The mark $'$ means that the term is related to thermal charcteristics. Note that when the two characteristic lengths are the same, $q_0' = \alpha_\infty q_0$. The flow resistivity, the tortuosity, the viscosity and the viscous characteristic length are related by the following equation [65]:

$$\Lambda = b \left(\frac{8\alpha_\infty \eta}{\sigma\phi} \right)^{1/2} \tag{4.6}$$

where b is a parameter that depends on the geometry of the pores. The value for b usually lies between 1 and 1/4. In this study, $b = 1$ has been chosen and used. Using the relation in Equation (4.6), Equation (4.4) can be rewritten as

$$q_0 = \frac{\eta}{\sigma} \tag{4.7}$$

The equations for $G(\omega)$ and $G'(\omega)$ are [49]

$$G(\omega) = \left[1 + \left(\frac{2\alpha_\infty q_0}{\phi\Lambda} \right) \frac{\mathrm{i}\omega}{\nu_k} \right]^{1/2} \tag{4.8}$$

$$G'(\omega) = \left[1 + \left(\frac{\Lambda'}{4} \right)^2 \frac{\mathrm{i}\omega}{\nu'} \right]^{1/2} \tag{4.9}$$

To utilise this model, five parameters are needed: porosity ϕ, flow resistivity σ, tortuosity α_∞ and the two characteristic lengths, Λ and Λ'. As the rigid frame model has the same governing equation as the acoustic wave equation, its implementation in the FE model does not need a separate validation. The validation of the fluid finite element model is reported in Appendix B.

As it is foreseen from its name, the poro–rigid model is a special case of the poro–elastic model. In fact, by making the frame rigid, the poro–elastic model can represent the poro–rigid model. A comparison between the two models will be shown in the next section.

4.1.2 Sound propagation in porous media having an elastic frame

4.1.2.1 Outline of the theory: the Biot theory

For most cases, the frame of porous materials can be assumed to be rigid. However, when a porous material is excited by a structural vibration, the frame vibration can become important. An example would be sound transmission through a sandwich structure with a porous layer inside. In this case, the frame vibration needs to be considered as well as the fluid in the pores.

The Biot theory [69, 70] provides a model for sound propagation in porous media with an elastic frame. In Biot's model the frame is considered to deform with the fluid in the pores simultaneously. Also, the deformations of the frame which are related to wave propagation are assumed to be similar to those of an elastic solid. The equations of motion for the frame in the absence of external forces forces is given by

$$\rho \frac{\partial^2 \mathbf{u}}{\partial t^2} = (\lambda_L + \mu_L) \boldsymbol{\nabla} \theta_d + \mu_L \boldsymbol{\nabla}^2 \mathbf{u} \tag{4.10}$$

where λ_L and μ_L are the Lamé coefficients and $\theta_d = \boldsymbol{\nabla} \cdot \mathbf{u}$ is the dilatation. After investigating the stress–strain relation and inertial forces in the Biot theory and applying the above equation to the frame and the fluid in the pores, the governing equations can be obtained and are written as

$$-\omega^2 \left(\tilde{\rho}_{11} \mathbf{u}^s + \tilde{\rho}_{12} \mathbf{u}^f \right) = (P - N) \boldsymbol{\nabla} \boldsymbol{\nabla} \cdot \mathbf{u}^s + N \boldsymbol{\nabla}^2 \mathbf{u}^s + Q \boldsymbol{\nabla} \boldsymbol{\nabla} \cdot \mathbf{u}^f \tag{4.11}$$

$$-\omega^2 \left(\tilde{\rho}_{22} \mathbf{u}^f + \tilde{\rho}_{12} \mathbf{u}^s \right) = R \boldsymbol{\nabla} \boldsymbol{\nabla} \cdot \mathbf{u}^f + Q \boldsymbol{\nabla} \boldsymbol{\nabla} \cdot \mathbf{u}^s \tag{4.12}$$

where $\mathbf{u}^s$ and $\mathbf{u}^f$ are the displacements of the solid frame and the fluid in the pores respectively, $\tilde{\rho}$ are the effective densities, and P, Q, R, N are the Biot coefficients derived by Biot et al. [99]. For example, N corresponds to the shear modulus of the material μ_L. A full derivation of the equations is given in [49]. Mathematical expressions for the variables are given in Appendix C.

A conventional way to implement these equations into a finite element code would be to use the Galerkin method based on the displacements. However, using displacements for the fluid phase can lead to a larger computational cost. As an alternative, Atalla et al. [72] developed a mixed displacement-pressure model. This has advantages over the classic displacement formulation. Firstly it is computaionally cheaper as it only requires four variables, whereas the classical formulation has six variables. Also, it is more efficient in coupling with other domains. For these reasons, Atalla's modified formulation has been used throughout the current work. The modified equations are

$$\boldsymbol{\nabla} \cdot \hat{\boldsymbol{\sigma}}^s + \omega^2 \tilde{\rho} \mathbf{u} + \tilde{\gamma} \boldsymbol{\nabla} p = 0 \tag{4.13}$$

$$\boldsymbol{\nabla}^2 p + \omega^2 \frac{\tilde{\rho}_{22}}{R} p - \omega^2 \frac{\tilde{\rho}_{22}}{\phi^2} \tilde{\gamma} \boldsymbol{\nabla} \cdot \mathbf{u} = 0 \tag{4.14}$$

where $\hat{\boldsymbol{\sigma}}^s$ is the modified stress tensor using the Biot coefficients and $\tilde{\gamma}$ is related to the coupling between solid and fluid phases. The definition of $\tilde{\gamma}$ is given in Appendix C. In each equation, the first two terms describe its motion without the effect of the other, and the third term is related to the coupling between the two phases.

4.1.2.2 2.5D numerical implementation

Using the Galerkin method, a weak integral form is obtained by imposing an admissible variation. With two variations of displacement $\delta \mathbf{u}$ and pressure δp, this is given by

$$\int_V \hat{\boldsymbol{\sigma}}^s(\mathbf{u}) : \boldsymbol{\epsilon}(\delta \mathbf{u}) \mathrm{d}V - \omega^2 \int_V \tilde{\rho} \mathbf{u} \cdot \delta \mathbf{u} \mathrm{d}V - \int_V \tilde{\gamma} \boldsymbol{\nabla} p \cdot \delta \mathbf{u} \mathrm{d}V - \int_\Omega [\hat{\boldsymbol{\sigma}}^s \cdot \mathbf{n}] \cdot \delta \mathbf{u} \mathrm{d}\Omega = 0 \tag{4.15}$$

$$\int_V \left[\frac{\phi^2}{\omega^2 \tilde{\rho}_{22}} \boldsymbol{\nabla} p \cdot \boldsymbol{\nabla} \delta p - \frac{\phi^2}{R} p \delta p \right] \mathrm{d}V - \int_V \tilde{\gamma} \boldsymbol{\nabla} \delta p \cdot \mathbf{u} \mathrm{d}V + \int_\Omega \left[\tilde{\gamma} u_n - \frac{\phi^2}{\tilde{\rho}_{22} \omega^2} \frac{\partial p}{\partial n} \right] \delta p \mathrm{d}\Omega = 0 \tag{4.16}$$

where $\mathbf{u}$ is the solid displacement vector and p is the interstitial fluid pressure in the pores. A 2.5D formulation has been applied to each integral in Equations (4.15) and (4.16). As it is assumed that no external forces are directly applied onto the poro–elastic domain, the boundary integrals are considered only in the coupling terms. Assuming a wave type solution in one direction (x), 2D shape functions can be used in the $y - z$ plane. The displacement and the pressure are then expressed as

$$\mathbf{u}(x, y, z) = \mathbf{N}_s(y, z) \tilde{\mathbf{u}}(x, y, z) \tag{4.17}$$

$$p(x, y, z) = \mathbf{N}_f(y, z) \tilde{\mathbf{p}}(x, y, z) \tag{4.18}$$

where $\mathbf{N}_s$ and $\mathbf{N}_f$ are the 2D shape functions for solid and fluid phases and $\tilde{\mathbf{u}}$ and $\tilde{\mathbf{p}}$ are the vectors of nodal displacement and pressure, respectively. As the nodal solutions $\tilde{\mathbf{u}}(x, y, z)$ and $\tilde{\mathbf{p}}(x, y, z)$ are each the sum of waves in the x direction, they can be written for each wave as

$$\tilde{\mathbf{u}}(x,y,z)=\hat{\mathbf{u}}(y,z)e^{-\mathrm{i}k_x x} \tag{4.19}$$

$$\tilde{\mathbf{p}}(x,y,z)=\hat{\mathbf{p}}(y,z)e^{-\mathrm{i}k_x x} \tag{4.20}$$

Equations (4.19) and (4.20) have been used in the following derivation. For the solid phase, the integrand of the first integral in Equation (4.15) can be written as

$$\hat{\boldsymbol{\sigma}}^s(\mathbf{u}):\boldsymbol{\epsilon}(\delta\mathbf{u})=\delta\boldsymbol{\epsilon}^{\mathrm{H}}\mathbf{D}\boldsymbol{\epsilon} \tag{4.21}$$

where $\mathbf{D}$ is the stress–strain relation matrix and $\boldsymbol{\epsilon}$ is the strain vector. They are given by

$$\mathbf{D}=\frac{E}{(1+\nu)(1-2\nu)}\begin{bmatrix} 1-\nu & \nu & \nu & 0 & 0 & 0 \\ \nu & 1-\nu & \nu & 0 & 0 & 0 \\ \nu & \nu & 1-\nu & 0 & 0 & 0 \\ 0 & 0 & 0 & \frac{1-2\nu}{2} & 0 & 0 \\ 0 & 0 & 0 & 0 & \frac{1-2\nu}{2} & 0 \\ 0 & 0 & 0 & 0 & 0 & \frac{1-2\nu}{2} \end{bmatrix} \tag{4.22}$$

$$\boldsymbol{\epsilon}=\begin{Bmatrix} \frac{\partial u}{\partial x} \\ \frac{\partial v}{\partial y} \\ \frac{\partial w}{\partial z} \\ \frac{\partial u}{\partial y}+\frac{\partial v}{\partial x} \\ \frac{\partial u}{\partial z}+\frac{\partial w}{\partial x} \\ \frac{\partial v}{\partial z}+\frac{\partial w}{\partial y} \end{Bmatrix} \tag{4.23}$$

where E and ν are the Young's modulus and the Poisson's ratio and $\mathbf{u}=[u\;\;v\;\;w]^{\mathrm{T}}$ is the displacement vector. The $x-$dependence can be separated in the strain vector, which can be written as

$$\boldsymbol{\epsilon}=\begin{Bmatrix} \frac{\partial u}{\partial x} \\ \frac{\partial v}{\partial y} \\ \frac{\partial w}{\partial z} \\ \frac{\partial u}{\partial y}+\frac{\partial v}{\partial x} \\ \frac{\partial u}{\partial z}+\frac{\partial w}{\partial x} \\ \frac{\partial v}{\partial z}+\frac{\partial w}{\partial y} \end{Bmatrix}=\begin{Bmatrix} 0 \\ \frac{\partial v}{\partial y} \\ \frac{\partial w}{\partial z} \\ \frac{\partial u}{\partial y} \\ \frac{\partial u}{\partial z} \\ \frac{\partial v}{\partial z}+\frac{\partial w}{\partial y} \end{Bmatrix}+\begin{Bmatrix} \frac{\partial u}{\partial x} \\ 0 \\ 0 \\ \frac{\partial v}{\partial x} \\ \frac{\partial w}{\partial x} \\ 0 \end{Bmatrix}=\begin{bmatrix} 0 & 0 & 0 \\ 0 & \frac{\partial}{\partial y} & 0 \\ 0 & 0 & \frac{\partial}{\partial z} \\ \frac{\partial}{\partial y} & 0 & 0 \\ \frac{\partial}{\partial z} & 0 & 0 \\ 0 & \frac{\partial}{\partial z} & \frac{\partial}{\partial y} \end{bmatrix}\mathbf{u}+\frac{\partial}{\partial x}\begin{bmatrix} 1 & 0 & 0 \\ 0 & 0 & 0 \\ 0 & 0 & 0 \\ 0 & 1 & 0 \\ 0 & 0 & 1 \\ 0 & 0 & 0 \end{bmatrix}\mathbf{u}. \tag{4.24}$$

This can be expressed as

$$\boldsymbol{\epsilon} = \left[\mathbf{B}_0 + \frac{\partial}{\partial x}\mathbf{B}_1\right]\mathbf{N}_s(y,z)\tilde{\mathbf{u}}(x,y,z). \tag{4.25}$$

Using Equation (4.25), the integrand can be written as

$$\delta\boldsymbol{\epsilon}^{\mathrm{H}}\mathbf{D}\boldsymbol{\epsilon} = \left\{\left[\mathbf{B}_0\mathbf{N}_s + \frac{\partial}{\partial x}\mathbf{B}_1\mathbf{N}_s\right]\delta\tilde{\mathbf{u}}(x,y,z)\right\}^{\mathrm{H}}\mathbf{D}\left[\mathbf{B}_0\mathbf{N}_s + \frac{\partial}{\partial x}\mathbf{B}_1\mathbf{N}_s\right]\tilde{\mathbf{u}}(x,y,z) \tag{4.26}$$

The integrand of the second integral in Equation (4.15) will be simply

$$\tilde{\rho}\mathbf{u}\cdot\delta\mathbf{u} = \tilde{\rho}\delta\tilde{\mathbf{u}}(x,y,z)^{\mathrm{H}}\mathbf{N}_s^{\mathrm{T}}\mathbf{N}_s\tilde{\mathbf{u}}(x,y,z). \tag{4.27}$$

For the third term the gradient vector $\boldsymbol{\nabla}$ is defined as

$$\boldsymbol{\nabla} = \left[\frac{\partial}{\partial x}\ \frac{\partial}{\partial y}\ \frac{\partial}{\partial z}\right]^{\mathrm{T}} = \left[0\ \frac{\partial}{\partial y}\ \frac{\partial}{\partial z}\right]^{\mathrm{T}} + \frac{\partial}{\partial x}\left[1\ 0\ 0\right]^{\mathrm{T}} = \mathbf{B}_{f0} + \frac{\partial}{\partial x}\mathbf{B}_{f1}. \tag{4.28}$$

Thus the gradient of the pressure can be written as

$$\boldsymbol{\nabla}p = \left[\mathbf{B}_{f0} + \frac{\partial}{\partial x}\mathbf{B}_{f1}\right]\mathbf{N}_f\tilde{\mathbf{p}}. \tag{4.29}$$

With this, the third integrand in Equation (4.15) can be written as

$$\tilde{\gamma}\boldsymbol{\nabla}p\cdot\delta\mathbf{u} = \tilde{\gamma}\delta\tilde{\mathbf{u}}^{\mathrm{H}}\mathbf{N}_s^{\mathrm{T}}\left[\mathbf{B}_{f0}\mathbf{N}_f + \frac{\partial}{\partial x}\mathbf{B}_{f1}\mathbf{N}_f\right]\tilde{\mathbf{p}}. \tag{4.30}$$

Substituting Equations (4.26), (4.27) and (4.30) into Equation (4.15) yields

$$\int_x\left(\sum_{i=0}^{1}\sum_{j=0}^{1}\frac{\partial^i\delta\tilde{\mathbf{u}}^{\mathrm{H}}}{\partial x^i}\mathbf{a}_{ij}\frac{\partial^j\tilde{\mathbf{u}}}{\partial x^j} - \omega^2\delta\tilde{\mathbf{u}}^{\mathrm{H}}\mathbf{M}_s\tilde{\mathbf{u}} - \sum_{j=0}^{1}\delta\tilde{\mathbf{u}}^{\mathrm{H}}\mathbf{C}_j\frac{\partial^j\tilde{\mathbf{p}}}{\partial x^j}\right)\mathrm{d}x = \int_\Omega\left[\hat{\boldsymbol{\sigma}}^s\cdot\mathbf{n}\right]\cdot\delta\mathbf{u}\mathrm{d}\Omega \tag{4.31}$$

where

$$\mathbf{a}_{ij} = \int_S\left[\mathbf{B}_{si}\mathbf{N}_s\right]^{\mathrm{T}}\mathbf{D}\mathbf{B}_{sj}\mathbf{N}_s\mathrm{d}x, \quad i,j = 0,1 \tag{4.32}$$

$$\mathbf{M}_s = \int_S \tilde{\rho}\mathbf{N}_s^{\mathrm{T}}\mathbf{N}_s \mathrm{d}S \tag{4.33}$$

$$\mathbf{C}_j = \int_S \tilde{\gamma}\mathbf{N}_s^{\mathrm{T}}\mathbf{B}_{fj}\mathbf{N}_f \mathrm{d}S, \quad j = 0, 1 \tag{4.34}$$

Applying Equations (4.19) and (4.20) and integrating by parts yields

$$\delta\bar{\mathbf{u}}^{\mathrm{T}}\left[\mathbf{K}_{s2}(-\mathrm{i}k_x)^2 + \mathbf{K}_{s1}(-\mathrm{i}k_x) + \mathbf{K}_{s0} - \omega^2\mathbf{M}_s \quad - \mathbf{C}_0 - \mathbf{C}_1(-\mathrm{i}k_x)\right]\left[\bar{\mathbf{u}}^{\mathrm{T}} \quad \bar{\mathbf{p}}^{\mathrm{T}}\right]^{\mathrm{T}} = \delta\bar{\mathbf{u}}^{\mathrm{T}}\mathbf{F}_s \tag{4.35}$$

where $\mathbf{K}_{s2} = -\mathbf{a}_{11}, \mathbf{K}_{s1} = \mathbf{a}_{01} - \mathbf{a}_{10}$ and $\mathbf{K}_{s0} = \mathbf{a}_{00}$. $\mathbf{F}_s$ represents the boundary integral (external force). $\bar{\mathbf{u}}$ and $\bar{\mathbf{p}}$ are the Fourier transform of $\hat{\mathbf{u}}$ and $\hat{\mathbf{p}}$, respectively, which are defined as

$$\bar{\mathbf{u}} = \int_{-\infty}^{\infty} \hat{\mathbf{u}} e^{-\mathrm{i}k_x x}\mathrm{d}x \tag{4.36}$$

$$\bar{\mathbf{p}} = \int_{-\infty}^{\infty} \hat{\mathbf{p}} e^{-\mathrm{i}k_x x}\mathrm{d}x \tag{4.37}$$

For the fluid phase, the first integrand in Equation (4.16) can be expressed as

$$\frac{\phi^2}{\omega^2\tilde{\rho}_{22}}\boldsymbol{\nabla}\delta p \cdot \boldsymbol{\nabla} p = \frac{\phi^2}{\omega^2\tilde{\rho}_{22}}\left\{\left[\mathbf{B}_{f0}\mathbf{N}_f + \frac{\partial}{\partial x}\mathbf{B}_{f1}\mathbf{N}_f\right]\delta\tilde{\mathbf{p}}\right\}^{\mathrm{H}}\left[\mathbf{B}_{f0}\mathbf{N}_f + \frac{\partial}{\partial x}\mathbf{B}_{f1}\mathbf{N}_f\right]\tilde{\mathbf{p}} \tag{4.38}$$

The second integrand is written as

$$\frac{\phi^2}{R}p\delta p = \frac{\phi^2}{R}\delta\tilde{\mathbf{p}}^{\mathrm{H}}\mathbf{N}_f^{\mathrm{T}}\mathbf{N}_f\tilde{\mathbf{p}} \tag{4.39}$$

The coupling term can be viewed as the transpose of Equation (4.30). However, as the derivative is of the virtual variable, the sign for the derivative changes due to the integration by parts.

$$\tilde{\gamma}\boldsymbol{\nabla}\delta p \cdot \mathbf{u} = \tilde{\gamma}\left\{\left[\mathbf{B}_{f0}\mathbf{N}_f + \frac{\partial}{\partial x}\mathbf{B}_{f1}\mathbf{N}_f\right]\delta\tilde{\mathbf{p}}\right\}^{\mathrm{H}}\mathbf{N}_s\tilde{\mathbf{u}} \tag{4.40}$$

Substituting Equations (4.38), (4.39) and (4.40) into Equation (4.16) yields

$$\begin{aligned}\int_x \left(\frac{1}{\omega^2}\sum_{i=0}^{1}\sum_{j=0}^{1}\frac{\partial^i\delta\tilde{\mathbf{p}}^{\mathrm{H}}}{\partial x^i}\mathbf{b}_{ij}\frac{\partial^j\tilde{\mathbf{p}}}{\partial x^j} - \delta\tilde{\mathbf{p}}^{\mathrm{H}}\mathbf{M}_f\tilde{\mathbf{p}} - \sum_{j=0}^{1}\frac{\partial^j\delta\tilde{\mathbf{p}}}{\partial x^j}^{\mathrm{H}}\mathbf{C}_j^{\mathrm{T}}\tilde{\mathbf{u}}\right)\mathrm{d}x \\ = -\int_\Omega\left(\tilde{\gamma}u_n - \frac{\phi^2}{\tilde{\rho}_{22}\omega^2}\frac{\partial p}{\partial n}\right)\mathrm{d}\Omega\end{aligned} \tag{4.41}$$

where

$$\mathbf{b}_{ij} = \int_S \frac{\phi^2}{\tilde{\rho}_{22}}\left[\mathbf{B}_{fi}\mathbf{N}_f\right]^{\mathrm{T}}\mathbf{B}_{fj}\mathbf{N}_f\mathrm{d}S, \qquad i,j=0,1 \tag{4.42}$$

$$\mathbf{M}_f = \int_S \frac{\phi^2}{R}\mathbf{N}_f^{\mathrm{T}}\mathbf{N}_f\mathrm{d}S \tag{4.43}$$

$$\mathbf{C}_j^{\mathrm{T}} = \int_S \tilde{\gamma}\left[\mathbf{B}_{fj}\mathbf{N}_f\right]^{\mathrm{T}}\mathbf{N}_s\mathrm{d}S, \qquad j=0,1 \tag{4.44}$$

Applying Equations (4.19) and (4.20) and integration by parts yield

$$\delta\bar{\mathbf{p}}^{\mathrm{T}}\left[\mathbf{K}_{f2}(-\mathrm{i}k_x)^2 + \mathbf{K}_{f0} - \omega^2\mathbf{M}_f \quad -\mathbf{C}_0^{\mathrm{T}} + \mathbf{C}_1^{\mathrm{T}}(-\mathrm{i}k_x)\right]\left[\bar{\mathbf{u}}^{\mathrm{T}} \quad \bar{\mathbf{p}}^{\mathrm{T}}\right]^{\mathrm{T}} = \delta\bar{\mathbf{p}}^{\mathrm{T}}\mathbf{F}_f \tag{4.45}$$

where $\mathbf{K}_{f2} = -\mathbf{b}_{11}$ and $\mathbf{K}_{f0} = \mathbf{b}_{00}$. Note that $\mathbf{b}_{01}$ and $\mathbf{b}_{10}$ cancel each other out due to the symmetry. Again $\mathbf{F}_f$ represents the boundary integral (external force). Combining Equations (4.35) and (4.45) completes the formulation:

$$\left[\delta\bar{\mathbf{u}}^{\mathrm{T}} \quad \delta\bar{\mathbf{p}}^{\mathrm{T}}\right]\begin{bmatrix}\mathbf{K}_s - \omega^2\mathbf{M}_s & \tilde{\mathbf{C}}_s \\ \tilde{\mathbf{C}}_f & \frac{1}{\omega^2}\mathbf{K}_f - \mathbf{M}_f\end{bmatrix}\begin{Bmatrix}\bar{\mathbf{u}} \\ \bar{\mathbf{p}}\end{Bmatrix} = \left[\delta\bar{\mathbf{u}}^{\mathrm{T}} \quad \delta\bar{\mathbf{p}}^{\mathrm{T}}\right]\begin{Bmatrix}\mathbf{F}_s \\ \mathbf{F}_f\end{Bmatrix} \tag{4.46}$$

The corresponding matrices are defined as

$$\begin{aligned}
\mathbf{K}_s &= \mathbf{K}_{s2}(-\mathrm{i}k_x)^2 + \mathbf{K}_{s1}(-\mathrm{i}k_x) + \mathbf{K}_{s0} \\
\tilde{\mathbf{C}}_s &= -\mathbf{C}_0 - \mathbf{C}_1(-\mathrm{i}k_x) \\
\tilde{\mathbf{C}}_f &= -\mathbf{C}_0^{\mathrm{T}} + \mathbf{C}_1^{\mathrm{T}}(-\mathrm{i}k_x) \\
\mathbf{K}_f &= \mathbf{K}_{f2}(-\mathrm{i}k_x)^2 + \mathbf{K}_{f0}
\end{aligned} \tag{4.47}$$

By removing the admissible variables the numerical model is obtained:

$$\begin{bmatrix} \mathbf{K}_s - \omega^2\mathbf{M}_s & \tilde{\mathbf{C}}_s \\ \tilde{\mathbf{C}}_f & \frac{1}{\omega^2}\mathbf{K}_f - \mathbf{M}_f \end{bmatrix} \begin{Bmatrix} \bar{\mathbf{u}} \\ \bar{\mathbf{p}} \end{Bmatrix} = \begin{Bmatrix} \mathbf{F}_s \\ \mathbf{F}_f \end{Bmatrix} \tag{4.48}$$

4.1.2.3 Verification of the model

The above equations have been implemented in a Fortran code and the code has been verified against the data published in [72]. The case is shown in Figure 4.2. A single layer of glass wool is excited by a unit pressure on one side, and the other side is backed by a rigid termination. The thickness of the layer h is 100 mm, and the layer is laterally infinite. The material properties for the glass wool can be found in [72] and are given in Table 4.1. The result is compared in terms of input normal impedance, Z_n, which is calculated by the following equation:

$$Z_n = \frac{1}{\mathrm{i}\omega\left(\phi U_n + (1-\phi)u_n\right)} \tag{4.49}$$

Here, U_n is the normal displacement of the internal fluid and u_n is that of the solid frame. U_n can be calculated using the following relation:

$$\mathbf{U} = \frac{\phi}{\tilde{\rho}_{22}\omega^2}\boldsymbol{\nabla} p - \frac{\tilde{\rho}_{12}}{\tilde{\rho}_{22}}\mathbf{u} \tag{4.50}$$

where $\mathbf{U}$ is the displacement of the internal fluid and $\mathbf{u}$ is the displacement of the solid frame.

TABLE 4.1: Physical properties and dimensions of the glass wool [72]

Property	Units	Value
Density of the frame ρ_1	kg/m^3	130
Porosity ϕ	–	0.94
Flow resistivity σ	Ns/m^4	40000
Tortuosity α_∞	–	1.06
Viscous characteristic length Λ	μm	56
Thermal characteristic length Λ'	μm	110
Shear modulus N	kPa	2200
Poisson's ratio ν	–	0
Loss factor η	–	0.1
Thickness h	mm	100

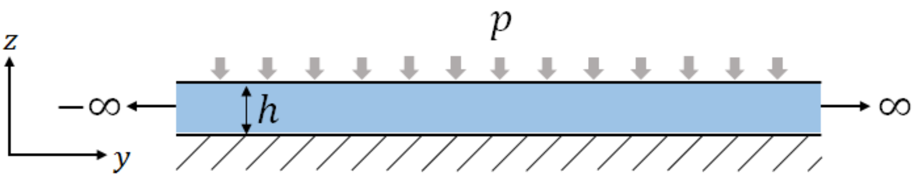

Figure 4.2. Verification case configuration: glass wool layer with rigid termination

For the numerical prediction, a mesh of poro–elastic panel with 100 mm thickness and 2 m width has been made. Linear quadrilateral elements are used, and the size of the elements is 40 mm in y–direction and 5 mm in z–direction. The total number of elements is 1000. Results are shown in Figure 4.3 for both poro–elastic and rigid frame models. It is clear that the result from the developed code shows good agreement with the literature, with a normalised RMS error of around 2%. The dip at 460 Hz occurs at a resonance frequency of the frame, which is not considered in the rigid porous modelling. The resonance frequency f_r is given by

$$f_r \simeq \frac{1}{4h}\sqrt{\frac{\mathrm{Re}\{K_c\}}{\rho_1}} \tag{4.51}$$

where $K_c = \lambda_L + 2\mu_L$ is the P–wave modulus where λ_L and μ_L are the Lamé coefficients. This gives the resonance frequency as $f_r = 460$ Hz. Apart from the resonance, the poro–elastic model shows the same behaviour as the rigid frame model does. Thus, it can be said that the frame vibration should be considered when its resonance frequency is in the range of interest.

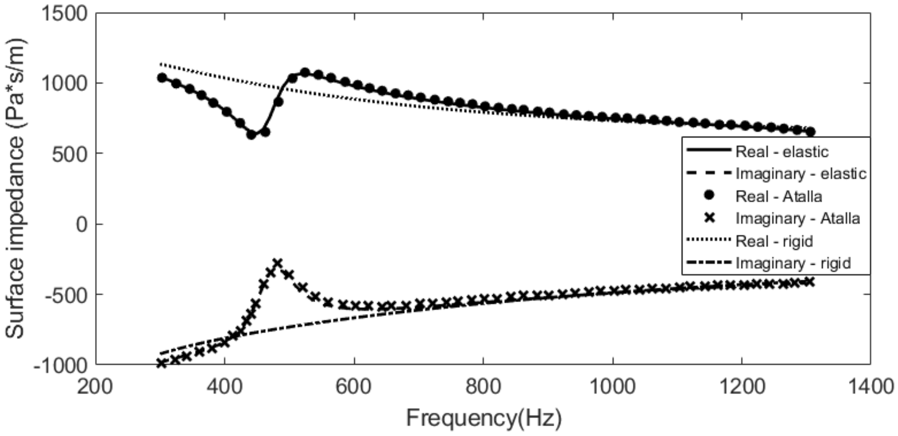

Figure 4.3. Comparison of surface impedance: ── real part (poro–elastic model), - - - imaginary part (poro–elastic model), • real part (Atalla, 1998), × imaginary part (Atalla, 1998), ····· real part (rigid frame model) and -·-· imaginary part (rigid frame model)

4.2 Coupling different domains

The coupling boundary conditions are basically continuity of the normal stress and the displacement and no mass flux at the coupled boundary. These conditions are applied to the boundary integrals in Equations (4.15) and (4.16) combined with the boundary integral of the coupled domain. In this section the coupling with elastic media and fluid media is considered. More boundary conditions can be found in [98]. One should note that the coupling conditions remain unchanged with respect to the Fourier transform.

4.2.1 Boundary integrals

The boundary integrals of the governing equations (Equations (4.15) and (4.16)) are

$$I_1 = -\int_{\Omega} [\hat{\boldsymbol{\sigma}}^s \cdot \mathbf{n}] \cdot \delta \boldsymbol{u} \mathrm{d}\Omega \tag{4.52}$$

$$I_2 = \int_{\Omega} \left[\tilde{\gamma} u_n - \frac{\phi^2}{\tilde{\rho_{22}}\omega^2} \right] \delta p \mathrm{d}\Omega \tag{4.53}$$

The total stress tensor is related to the stress tensor *in vacuo* $\hat{\boldsymbol{\sigma}}^s$ by the following relation:

$$\hat{\boldsymbol{\sigma}}^s(\mathbf{u}) = \boldsymbol{\sigma}^t(\mathbf{u}, \mathbf{U}) + \phi \left(1 + \frac{Q}{R} \right) p \mathbf{I} \tag{4.54}$$

Here $\boldsymbol{\sigma}^t$ is the total stress tensor and $\mathbf{I}$ is the identity matrix. The coupling coefficient $\tilde{\gamma}$ is given by

$$\tilde{\gamma} = \phi\left(\frac{\tilde{\rho}_{12}}{\tilde{\rho}_{22}} - \frac{Q}{R}\right) \tag{4.55}$$

Using above equations I_1 and I_2 can be rewritten as follows.

$$I_1 = -\int_\Omega (\boldsymbol{\sigma}^t \cdot \mathbf{n}) \cdot \delta\mathbf{u} \mathrm{d}\Omega - \int_\Omega \phi\left(1 + \frac{Q}{R}\right) p\delta u_n \mathrm{d}\Omega \tag{4.56}$$

$$I_2 = -\int_\Omega \phi\left(1 + \frac{Q}{R}\right) u_n \delta p \mathrm{d}\Omega - \int_\Omega \phi(U_n - u_n)\delta p \mathrm{d}\Omega \tag{4.57}$$

These expressions will be used in the following coupling formulations.

4.2.2 Poro–elastic media to elastic media

The boundary integral of an elastic medium is given by

$$I^e = -\int_\Omega (\boldsymbol{\sigma}^e \cdot \mathbf{n}^e) \cdot \delta\mathbf{u}^e \mathrm{d}\Omega \tag{4.58}$$

where 'e' denotes the elastic medium. Let I_2 remain unchanged and add this integral to I_1. Then I_1 becomes

$$I_1^e = I_1 + I^e = -\int_\Omega (\boldsymbol{\sigma}^t \cdot \mathbf{n}) \cdot \delta\mathbf{u} \mathrm{d}\Omega - \int_\Omega \phi\left(1 + \frac{Q}{R}\right) p\delta u_n \mathrm{d}\Omega - \int_\Omega (\boldsymbol{\sigma}^e \cdot \mathbf{n}^e) \cdot \delta\mathbf{u}^e \mathrm{d}\Omega \tag{4.59}$$

As the two media have the opposite normal vector, i.e., $\mathbf{n}^e = -\mathbf{n}$, this can be rewritten as

$$I_1^e = -\int_\Omega (\boldsymbol{\sigma}^t \cdot \mathbf{n}) \cdot \delta\mathbf{u} \mathrm{d}\Omega - \int_\Omega \phi\left(1 + \frac{Q}{R}\right) p\delta u_n \mathrm{d}\Omega + \int_\Omega (\boldsymbol{\sigma}^e \cdot \mathbf{n}) \cdot \delta\mathbf{u} \mathrm{d}\Omega \tag{4.60}$$

The coupling conditions are

$$\boldsymbol{\sigma}^t \cdot \mathbf{n} = \boldsymbol{\sigma}^e \cdot \mathbf{n} \tag{4.61}$$

$$U_n - u_n = 0 \tag{4.62}$$

$$\mathbf{u} = \mathbf{u}^e \tag{4.63}$$

The first equation is the continuity of normal stresses. The second one means that there is no relative mass flux and the last is the continuity of the solid displacements. Substituting the coupling conditions into the boundary integrals leads to

$$I_1^e = -\int_\Omega \phi\left(1 + \frac{Q}{R}\right) p\delta u_n \mathrm{d}\Omega \tag{4.64}$$

$$I_2^e = I_2 = -\int_\Omega \phi\left(1 + \frac{Q}{R}\right) u_n \delta p \mathrm{d}\Omega \tag{4.65}$$

In the numerical form these can be expressed as

$$I_1^e = -\int_\Omega \phi\left(1 + \frac{Q}{R}\right) p\delta u_n \mathrm{d}\Omega = \{\delta u_i\}^{\mathrm{T}} \mathbf{I}_{e1} \{p_j\} \tag{4.66}$$

$$I_2^e = -\int_\Omega \phi\left(1 + \frac{Q}{R}\right) u_n \delta p \mathrm{d}\Omega = \{\delta p_i\}^{\mathrm{T}} \mathbf{I}_{e2} \{u_j\} \tag{4.67}$$

where $\mathbf{I}_{e1}$ and $\mathbf{I}_{e2}$ are given by

$$\mathbf{I}_{e1} = -\int_\Omega \phi\left(1 + \frac{Q}{R}\right) \mathbf{N'}_f^{\mathrm{T}} \mathbf{N'}_s \mathrm{d}\Omega \tag{4.68}$$

$$\mathbf{I}_{e2} = -\int_\Omega \phi\left(1 + \frac{Q}{R}\right) \mathbf{N'}_s^{\mathrm{T}} \mathbf{N'}_f \mathrm{d}\Omega. \tag{4.69}$$

Here, $\mathbf{N'}_s$ and $\mathbf{N'}_f$ are one dimensional shape functions at the coupled boundary. For example, a pair of local shape functions for a linear element at the coupled boundary will be given as

$$\mathbf{N'}_s = \begin{bmatrix} \frac{1-\xi}{2} & 0 & 0 & \frac{1+\xi}{2} & 0 & 0 \\ 0 & \frac{1-\xi}{2} & 0 & 0 & \frac{1+\xi}{2} & 0 \\ 0 & 0 & \frac{1-\xi}{2} & 0 & 0 & \frac{1+\xi}{2} \end{bmatrix} \tag{4.70}$$

$$\mathbf{N'}_f = \begin{bmatrix} \frac{1-\xi}{2} & \frac{1+\xi}{2} \end{bmatrix} \tag{4.71}$$

where ξ is the local variable varying from -1 to 1. Note that $\mathbf{I}_{e1}^{\mathrm{T}} = \mathbf{I}_{e2}$. For the third coupling condition, the Lagrange multipliers method is used. The system matrix is then given by

$$\begin{bmatrix} \mathbf{K}_e - \omega^2\mathbf{M}_e & \mathbf{0} & \mathbf{0} & \mathbf{C}_{ss1}^{\mathrm{T}} \\ \mathbf{0} & \mathbf{K}_s - \omega^2\mathbf{M}_s & \tilde{\mathbf{C}}_s + \mathbf{I}_{e1} & \mathbf{C}_{ss2}^{\mathrm{T}} \\ \mathbf{0} & \tilde{\mathbf{C}}_f + \mathbf{I}_{e2} & \frac{1}{\omega^2}\mathbf{K}_f - \mathbf{M}_f & \mathbf{0} \\ \mathbf{C}_{ss1} & \mathbf{C}_{ss2} & \mathbf{0} & \mathbf{0} \end{bmatrix} \begin{Bmatrix} u_{ei} \\ u_{pi} \\ p_{pi} \\ \lambda_i \end{Bmatrix} = \begin{Bmatrix} \mathbf{F}_e \\ \mathbf{F}_{ps} \\ \mathbf{F}_{pf} \\ \mathbf{0} \end{Bmatrix} \tag{4.72}$$

where λ_i are the Lagrange multipliers. $\mathbf{C}_{ss1}$ and $\mathbf{C}_{ss2}$ represent the displacement continuity condition and are calculated as follows. Assume nodes 2 & 3 of the solid domain and nodes 7 & 6 of the poro–elastic domain are coupled correspondingly. A diagram of the coupled boundary is shown in Figure 4.4. Note that the numbers are global node numbers. If local node numbers are used, the connectivity between the local node numbers and the global node numbers should be considered.

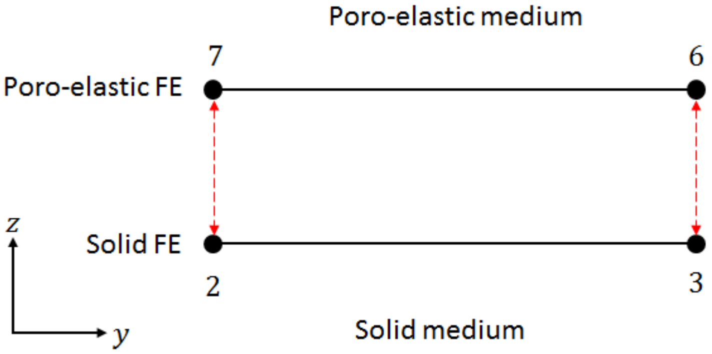

Figure 4.4. An example of coupling between a solid finite element and a poro–elastic finite element

Without constraints, the global degrees of freedom will be 4, 5, 6, 7, 8 and 9 for the coupled solid element and 19, 20, 21, 16, 17 and 18 for the poro–elastic one. The coupling conditions are then given as

$$\begin{aligned} u_{e,4} &= u_{p,19} \\ u_{e,5} &= u_{p,20} \\ u_{e,6} &= u_{p,21} \\ u_{e,7} &= u_{p,16} \\ u_{e,8} &= u_{p,17} \\ u_{e,9} &= u_{p,18} \end{aligned} \tag{4.73}$$

In a matrix form, this can be expressed as

$$\begin{bmatrix} 1 & 0 & 0 & 0 & 0 & 0 & 0 & 0 & 0 & -1 & 0 & 0 \\ 0 & 1 & 0 & 0 & 0 & 0 & 0 & 0 & 0 & 0 & -1 & 0 \\ 0 & 0 & 1 & 0 & 0 & 0 & 0 & 0 & 0 & 0 & 0 & -1 \\ 0 & 0 & 0 & 1 & 0 & 0 & -1 & 0 & 0 & 0 & 0 & 0 \\ 0 & 0 & 0 & 0 & 1 & 0 & 0 & -1 & 0 & 0 & 0 & 0 \\ 0 & 0 & 0 & 0 & 0 & 1 & 0 & 0 & -1 & 0 & 0 & 0 \end{bmatrix} \begin{Bmatrix} u_{e,4} \\ u_{e,5} \\ u_{e,6} \\ u_{e,7} \\ u_{e,8} \\ u_{e,9} \\ u_{p,16} \\ u_{p,17} \\ u_{p,18} \\ u_{p,19} \\ u_{p,20} \\ u_{p,21} \end{Bmatrix} = \mathbf{0} \tag{4.74}$$

In this case, $\mathbf{C}_{ss1}$ and $\mathbf{C}_{ss2}$ are given as

$$C_{ss1,ij} = \begin{cases} 1 & (i,j) = (1,4), (2,5), (3,6), (4,7), (5,8) \text{ and } (6,9) \\ 0 & \text{otherwise} \end{cases} \tag{4.75}$$

$$C_{ss2,ij} = \begin{cases} 1 & (i,j) = (1,19), (2,20), (3,21), (4,16), (5,17) \text{ and } (6,18) \\ 0 & \text{otherwise} \end{cases} \tag{4.76}$$

The number of columns for each matrix corresponds to the number of elastic degrees of freedom.

4.2.3 Poro–elastic media to fluid media

4.2.3.1 Coupling with fluid finite elements

The boundary integral of a fluid medium is given by

$$I^a = -\int_\Omega \frac{1}{\rho_a \omega^2} \frac{\partial p^a}{\partial n^a} \delta p^a \mathrm{d}\Omega \tag{4.77}$$

where 'a' denotes the fluid medium and ρ_a refers to the density of the fluid medium. Again, $\mathbf{n}^a = -\mathbf{n}$. Adding this term to I_2 gives

$$I_2^a = I_2 + I^a = -\int_\Omega \phi\left(1+\frac{Q}{R}\right)u_n\delta p\mathrm{d}\Omega - \int_\Omega \phi(U_n - u_n)\delta p\mathrm{d}\Omega + \int_\Omega \frac{1}{\rho_a\omega^2}\frac{\partial p^a}{\partial n}\delta p^a\mathrm{d}\Omega \quad (4.78)$$

The coupling conditions are given by [98]

$$\boldsymbol{\sigma}^t \cdot \mathbf{n} = -p\mathbf{n} \quad (4.79)$$

$$\frac{1}{\rho_a\omega^2}\frac{\partial p^a}{\partial n} = (1-\phi)u_n + \phi U_n = u_n + \phi(U_n - u_n) \quad (4.80)$$

$$p = p^a \quad (4.81)$$

The first equation is the continuity of normal stresses. The second one means that there is no relative mass flux and the last is the continuity of acoustic pressure. Substituting the coupling conditions into the boundary integrals leads to

$$I_1^a = I_1 = \int_\Omega \left(1-\phi-\phi\frac{Q}{R}\right)p\delta u_n\mathrm{d}\Omega \quad (4.82)$$

$$I_2^a = \int_\Omega \left(1-\phi-\phi\frac{Q}{R}\right)u_n\delta p\mathrm{d}\Omega \quad (4.83)$$

In the numerical form these can be expressed as

$$I_1^a = \int_\Omega \left(1-\phi-\phi\frac{Q}{R}\right)p\delta u_n\mathrm{d}\Omega = \{\delta u_i\}^\mathrm{T}\mathbf{I}_{a1}\{p_j\} \quad (4.84)$$

$$I_2^a = \int_\Omega \left(1-\phi-\phi\frac{Q}{R}\right)u_n\delta p\mathrm{d}\Omega = \{\delta p_i\}^\mathrm{T}\mathbf{I}_{a2}\{u_j\} \quad (4.85)$$

where $\mathbf{I}_{a1}$ and $\mathbf{I}_{a2}$ are given as

$$\mathbf{I}_{a1} = \int_\Omega \left(1-\phi-\phi\frac{Q}{R}\right)\mathbf{N'}_s^\mathrm{T}\mathbf{N'}_f\mathrm{d}\Omega \quad (4.86)$$

$$\mathbf{I}_{a2} = \int_\Omega \left(1-\phi-\phi\frac{Q}{R}\right)\mathbf{N'}_f^\mathrm{T}\mathbf{N'}_s\mathrm{d}\Omega \quad (4.87)$$

Note $\mathbf{I}_{a1}^\mathrm{T} = \mathbf{I}_{a2}$. For the third coupling condition, the Lagrange multipliers method is used. As the FE fluid is formulated with a velocity potential, $\nabla\psi_a = -\mathbf{v}_a$, the coupling condition becomes

$$p = \mathrm{i}\omega\rho_a\psi_a \quad (4.88)$$

The system matrix is then given by

$$\begin{bmatrix} \mathbf{K}_a - \omega^2 \mathbf{M}_a & \mathbf{0} & \mathbf{0} & -\mathrm{i}\omega\rho_a \mathbf{C}_{aa1}^{\mathrm{T}} \\ \mathbf{0} & \mathbf{K}_s - \omega^2 \mathbf{M}_s & \tilde{\mathbf{C}}_s + \mathbf{I}_{a1} & \mathbf{0} \\ \mathbf{0} & \tilde{\mathbf{C}}_f + \mathbf{I}_{a2} & \frac{1}{\omega^2}\mathbf{K}_f - \mathbf{M}_f & \mathbf{C}_{aa2}^{\mathrm{T}} \\ \mathrm{i}\omega\rho_a \mathbf{C}_{aa1} & \mathbf{0} & \mathbf{C}_{aa2} & \mathbf{0} \end{bmatrix} \begin{Bmatrix} \psi_{ai} \\ u_{pi} \\ p_{pi} \\ \lambda_i \end{Bmatrix} = \begin{Bmatrix} \mathbf{F}_a \\ \mathbf{F}_{ps} \\ \mathbf{F}_{pf} \\ \mathbf{0} \end{Bmatrix} \tag{4.89}$$

The matrices $\mathbf{C}_{aa1}$ and $\mathbf{C}_{aa2}$ represent the pressure continuity at the coupled nodes. Therefore the matrix structure is similar to that of the elastic case. The minus sign in front of $\mathbf{C}_{aa1}^{\mathrm{T}}$ is due to the complex conjugate transpose. In the code, scaling factors are introduced for the velocity potential of the fluid $\{\psi_{ai}\}$ and the acoustic pressure in the porous medium $\{p_{pi}\}$. This is to increase the numerical stability of the system matrix.

4.2.3.2 Coupling with fluid boundary elements

The same coupling conditions are used as in the coupling with FE fluid media. In the fluid boundary element method the boundary conditions are given by

$$\mathrm{i}\omega\rho_a \mathbf{C}_a \psi_a + \mathbf{C}_b v_n = \mathbf{C}_c \tag{4.90}$$

Thus the pressure continuity is easily implemented using equation (4.90). Also, Equation (4.77) can be rewritten as

$$I^a = -\int_\Omega \frac{1}{\rho_a \omega^2} \frac{\partial p^a}{\partial n^a} \delta p \mathrm{d}\Omega = -\int_\Omega \frac{1}{\mathrm{i}\omega} v_n \delta p \mathrm{d}\Omega \tag{4.91}$$

Here the Euler equation $\rho_a \frac{\partial \mathbf{v}}{\partial t} = -\boldsymbol{\nabla} p$ is used. Subtracting equation (4.91) from (4.83) gives back the original boundary integral in the poro–elastic medium. Thus the system matrix is written as

$$\begin{bmatrix} \mathbf{H}_a & -\mathbf{G}_a & \mathbf{0} & \mathbf{0} \\ \mathbf{0} & \mathbf{0} & \mathbf{K}_s - \omega^2 \mathbf{M}_s & \tilde{\mathbf{C}}_s + \mathbf{I}_{a1} \\ \mathbf{0} & \mathbf{C}_L & \tilde{\mathbf{C}}_f + \mathbf{I}_{a2} & \frac{1}{\omega^2}\mathbf{K}_f - \mathbf{M}_f \\ \mathrm{i}\omega\rho_a \mathbf{C}_a & \mathbf{C}_b & \mathbf{0} & \mathbf{0} \\ \mathrm{i}\omega\rho_a \mathbf{I}_a & \mathbf{0} & \mathbf{0} & -\mathbf{I}_p \end{bmatrix} \begin{Bmatrix} \psi_{ai} \\ \frac{\partial \psi}{\partial n}{}_{ai} \\ u_{pi} \\ p_{pi} \end{Bmatrix} = \begin{Bmatrix} \frac{\mathbf{p}_a}{i\omega\rho_a} \\ \mathbf{F}_{ps} \\ \mathbf{F}_{pf} \\ \mathbf{C}_c \\ \mathbf{0} \end{Bmatrix} \tag{4.92}$$

where $\mathbf{I}_a$ and $\mathbf{I}_p$ are the pressure coupling matrices that have a component of 1 at the coupled global nodes (columns in the matrix). $\mathbf{C}_L$ is given by

$$\mathbf{C}_L = \frac{1}{\mathrm{i}\omega}\int_{\Omega} \mathbf{N}'^{\mathrm{T}}_f \mathbf{N}_b \mathrm{d}\Omega \tag{4.93}$$

where $\mathbf{N}_b$ is the shape function for the coupled fluid boundary element.

4.2.4 Verification of the coupled model

Verification has been performed for the coupling between the poro–elastic finite elements and fluid finite and boundary elements. A 5.1 m long rigid duct with a porous material (glass wool) at the end has been chosen as a validation case, as shown in Figure 4.5. The red line represents the area filled with air and the blue line is the glass wool. The left–hand end is given a harmonic input velocity of amplitude 1 m/s, and the results are compared in terms of the input impedance, $Z_n = p/v_n$. The right end is a rigid termination. The glass wool has been used for the porous material, as its properties are known. However, its frame is set to be rigid to allow comparison with an analytical solution. The corresponding meshes are shown in Figure 4.6. Quadratic quadrilateral elements have been used, and the element size is 0.1 m for the fluid and 0.01 m for the porous material. The corresponding maximum frequencies are 686 Hz and 2858 Hz. Therefore the mesh will give a reliable result for the given maximum frequency, i.e., 500 Hz.

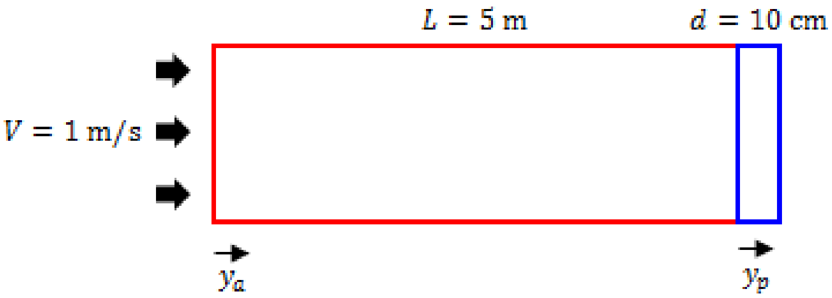

Figure 4.5. Rigid duct with glass wool at the end (not to scale)

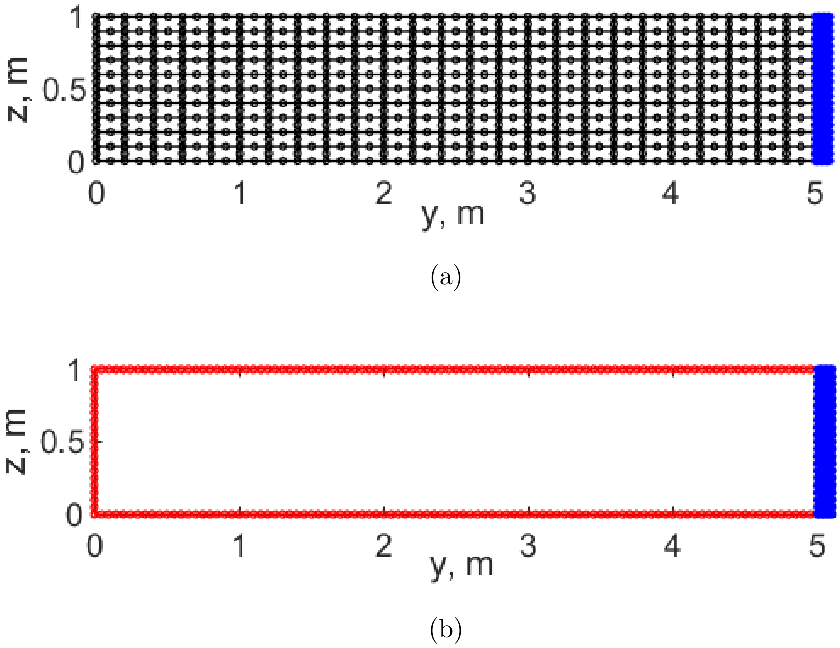

(a)

(b)

Figure 4.6. FE/BE meshes for the validation: (a) fluid FEs (black) and poro–elastic FEs (blue) and (b) fluid BEs (red) and poro–elastic FEs (blue)

With an assumption of 1D sound propagation, the analytical solution is obtained as follows. The form of the solution in each domain is

$$p_a(y_a) = A_a e^{-\mathrm{i}k_a y_a} + B_a e^{\mathrm{i}k_a y_a} \tag{4.94}$$

$$p_p(y_p) = A_p e^{-\mathrm{i}k_p y_p} + B_p e^{\mathrm{i}k_p y_p} \tag{4.95}$$

where the subscripts 'a' and 'p' refer to the air and the porous domains. A and B are the coefficients and k_a and k_p are the wavenumbers. The time dependence ($e^{\mathrm{i}\omega t}$) is suppressed. The boundary conditions are

$$v_a(y_a) = 1 \quad \text{at } y_a = 0 \tag{4.96}$$

$$p_a(y_a) = p_p(y_p) \quad \text{at } y_a = L \;\; (\text{or } y_p = 0) \tag{4.97}$$

$$v_a(y_a) = v_p(y_p) \quad \text{at } y_a = L \;\; (\text{or } y_p = 0) \tag{4.98}$$

$$v_p(y_p) = 0 \quad \text{at } y_p = d \tag{4.99}$$

where L and d correspond to the length of the duct and the thickness of the porous layer, which are 5.0 m and 0.1 m. Solving the above equations for the coefficients gives the solution in each domain.

$$\begin{Bmatrix} A_a \\ B_a \\ A_p \\ B_p \end{Bmatrix} = \begin{bmatrix} \frac{1}{\rho_a c_a} & \frac{-1}{\rho_a c_a} & 0 & 0 \\ \frac{e^{-\mathrm{i}k_a L}}{\rho_a c_a} & \frac{-e^{\mathrm{i}k_a L}}{\rho_a c_a} & \frac{-1}{\rho_p c_p} & \frac{1}{\rho_p c_p} \\ e^{-\mathrm{i}k_a L} & -e^{\mathrm{i}k_a L} & -1 & -1 \\ 0 & 0 & \frac{e^{-\mathrm{i}k_a d}}{\rho_p c_p} & \frac{-e^{\mathrm{i}k_a d}}{\rho_p c_p} \end{bmatrix}^{-1} \begin{Bmatrix} 1 \\ 0 \\ 0 \\ 0 \end{Bmatrix} \tag{4.100}$$

For a unit velocity excitation, the input impedance is $p_a(0) = A_a + B_a$. The magnitude and phase of the impedance at the input side are shown in Figure 4.7 for different models. The black line represents the analytical solution, i.e., $p_a(0)$, the red blue dots represent the result from the fluid finite element and poro–elastic finite element model and the red dots represent the result from the fluid boundary element and poro–elastic finite element model. The air domain is represented either using acoustic finite elements or boundary elements. The results show good agreement with each other and with the analytical result, showing a normalised RMS error of 2% and 1% respectively. Thus it can be said that the coupling is well implemented, at least with fluid finite or boundary elements.

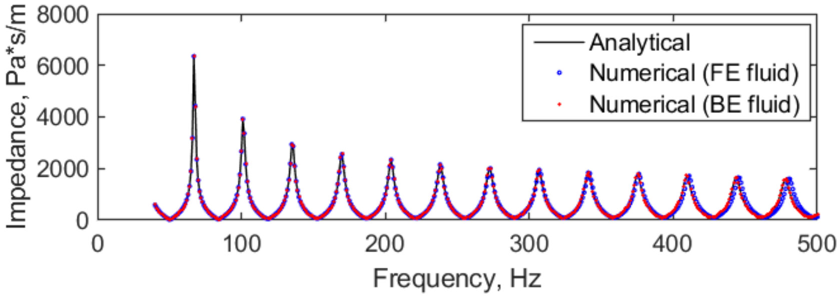

(a)

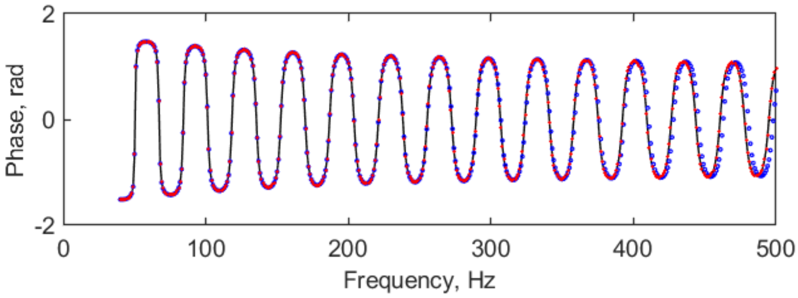

(b)

Figure 4.7. Comparison of input impedance with the rigid frame model for porous materials: (a) magnitude and (b) phase of input impedance; ━ analytical solution, ⋯⋯ predicted using fluid FEs and poro–elastic FEs, ⋯⋯ predicted using BEs and poro–elastic FEs

A comparison has also been made for the poro–elastic case, where all the properties in Table 4.1 are used, and the results are plotted in Figure 4.8. As mentioned in Section 4.1.2.3, the elastic model shows the same behaviour as the rigid model except the region around 460 Hz, where the frame resonance occurs. The coupling with both fluid FE and fluid BE show the same results.

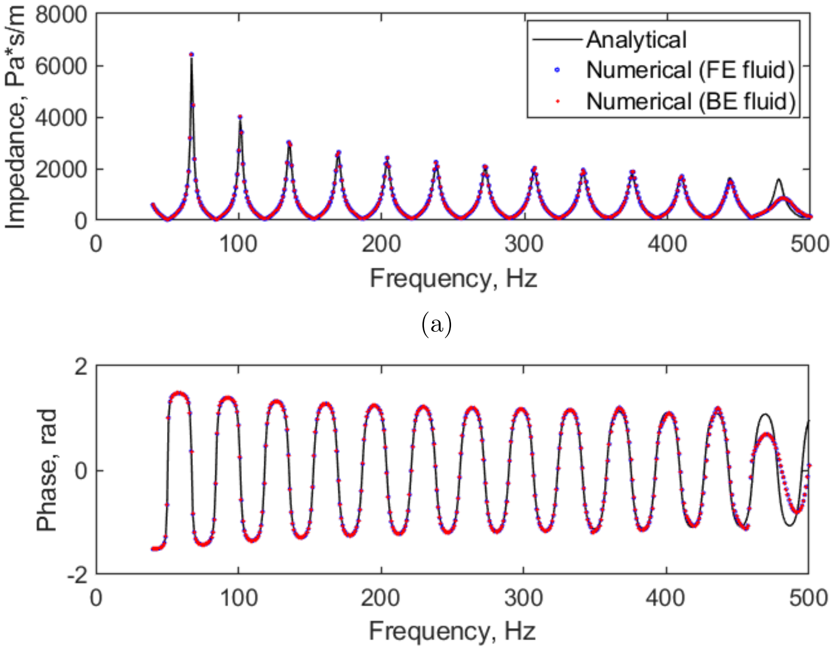

(a)

(b)

Figure 4.8. Comparison of input impedance with the elastic frame model for porous materials: (a) magnitude and (b) phase of input impedance; — analytical solution, ⋯ predicted using fluid FEs and poro–elastic FEs, ⋯ predicted using BEs and poro–elastic FEs

To validate the developed code for an exterior problem with boundary elements, the sound radiation of a 1:5 scale rail above a layer of melamine foam has been chosen, for which measured data are available in [13]. The dimensions of the foam were 2.0 m × 0.4 m × 50 mm and the rail was 2 m long. The measurement setup [13] and the mesh are shown in Figure 4.9. The rail and the boundaries of the foam have been modelled using the boundary elements (blue line in Figure 4.9(b)) and the inside of the foam is modelled using the poro–elastic finite elements (red line in Figure 4.9(b)). The size of an element for the foam is 0.003 m × 0.004 m, with a finer size of 0.002 m × 0.004 m on the part below the rail. This corresponds to the maximum frequency of 7100 Hz. For the rail the element size is around 0.002 m. The ground is represented by a box with a size of 0.6 m × 0.02 m the upper surface of which is at the ground level. The properties of the foam have been obtained by direct measurements and inverse characterisation from impedance tube measurements. The details about the properties are discussed in Chapter 3.

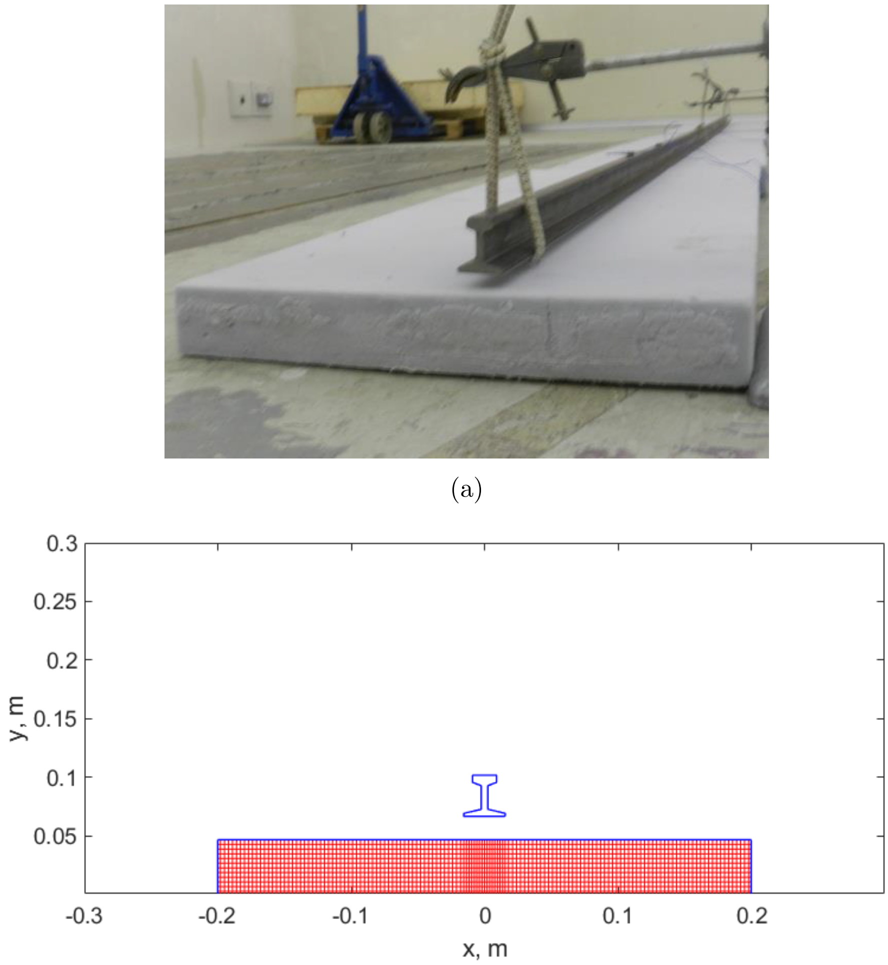

(a)

(b)

Figure 4.9. Validation case for exterior problem: (a) measurement setup [13] and (b) mesh for the calculation (— BEs, — poro–elastic FEs)

A unit vertical velocity is given around the rail and the ground has been assumed to be rigid. The result is compared in terms of the radiation ratio of the rail, which is calculated by the following equation:

$$\sigma_{\text{rad}} = \frac{W}{\rho_0 c_0 S < v_n^2 >} \tag{4.101}$$

where W is the radiated sound power, ρ_0 is the density of air, c_0 is the speed of sound in air, S is the total length of the boundary and $< v_n^2 >$ is the mean square normal velocity of the rail. The sound power is calculated by

$$W = \int_S \frac{1}{2} \text{Re}\{p v_n^*\} \text{d}S \tag{4.102}$$

where p is the pressure and v_n is the velocity normal to the boundary S of the rail.

Figure 4.10 shows the result. The dashed line is the measured radiation ratio, the dotted line is a result from the boundary element model with the surface of the foam modelled as an impedance boundary and the solid line is the result from the boundary element and poro–elastic finite element model. The fluctuating behaviour in the measured data is due to the chamber, for which the Schroeder frequency is around 300 Hz. Thus the measured data below 300 Hz is not reliable. The solid line is from the developed model, which agrees well with the measurement, with an RMS error of 4 dB mainly due to the high frequency components. From Equation (4.51) the frame resonance is expected to occur at $f_r = 863$ Hz for a vertical thickness of 50 mm. This is not seen clearly in the figure, which suggests that the frame of the foam is hardly excited by the acoustic radiation from the rail. A result from a 2D boundary element model with impedance for the foam surface has also been plotted, which is very similar to that from the 2D coupled model. The properties used to calculate the resonance frequency are given in Table 3.5 in Chapter 3.

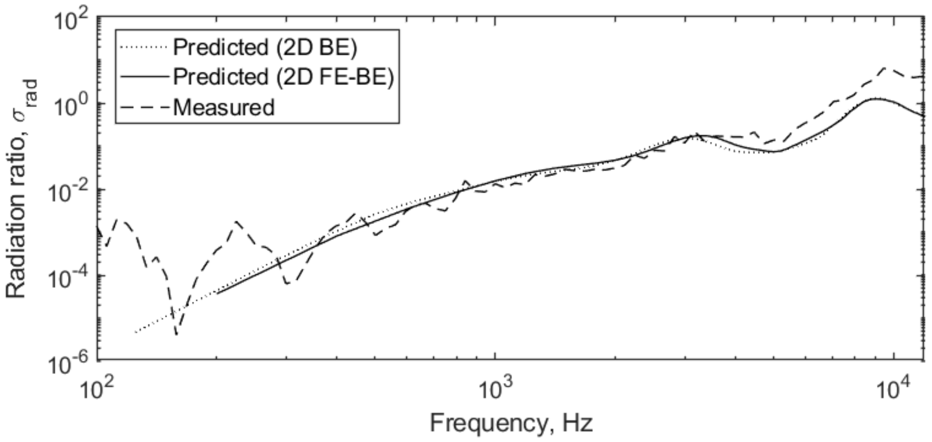

Figure 4.10. Radiation ratio of a 1:5 scale rail above a melamine foam on a rigid ground; - - - measured, ····· predicted using BEs, —— predicted using BEs and poro–elastic FEs

4.3 Summary

A 2.5D finite element model for poro–elastic media has been developed and validated. The developed model has been implemented in an existing 2.5D finite element and boundary element software called WANDS. The coupled model has been validated against an analytical solution in 2D for internal and external problems of the boundary element model. From the validation cases it was shown that the poro–elastic model differs from the poro–rigid model at resonances of the frame. Although the verification for the coupling with elastic media was not shown, it was implemented in the software. The developed program has been used throughout the thesis, i.e., for 2D or 2.5D calculations.

Chapter 5

Effect of railway ballast on track noise

The sources of rolling noise consist of the vibration of wheel, rail and sleeper. The noise can be calculated from the response of each component, which is obtained from a dynamic model of the track and wheel. In the dynamic model of a ballasted track, the rail is modelled as a beam, the rail pad is modelled as a spring, the sleeper is modelled as a mass or a beam and the ballast is modelled as a spring [1]. Therefore, the ballast is not considered in terms of noise radiation because its mass is neglected. However, the ballast at a macroscopic scale also has the characteristics of a porous material. It absorbs the sound radiated by the rail, wheel and sleeper and can also radiate noise itself into the field due to its vibration. Often, impedance plane models are used to model the ballast absorption, sometimes with consideration of its thickness [47, 51, 13]. A more complicated model can also be employed, which allows for wave propagation inside the medium. Graphical illustrations of the two models are shown in Figure 5.1, for a case of a single medium with a rigid termination. In the local reaction model (Figure 5.1(a)) the reflection only occurs at the outer surface of the medium, whereas waves can propagate tangentially in the extended reaction model (Figure 5.1(b)). The two models give similar results when the medium is highly reflective. However, this is not the case for the railway ballast, due to its low flow resistivity [47, 52].

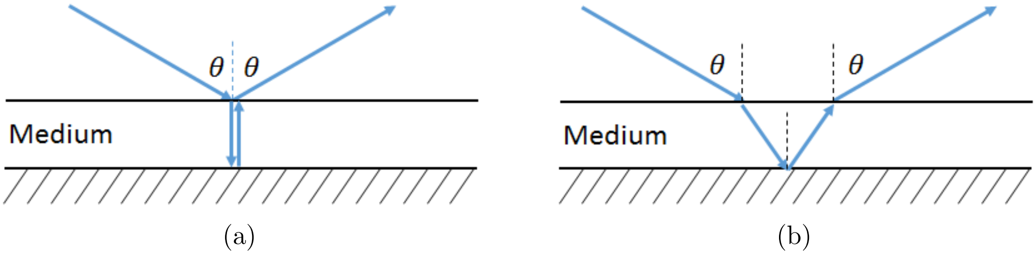

(a) (b)

Figure 5.1. (a) Local reaction and (b) extended reaction models for sound propagation

In this chapter it will be shown how these models give different results in relation to analysing the ballast absorption and radiation. For the absorption, cases from previous studies which used the local reaction model have been considered. These are: the diffuse field absorption coefficient, the sound radiation from a sleeper embedded in ballast and the sound radiation from a rail over ballast.

In terms of noise radiation, the ballast can contribute to the low frequency noise where the sleeper noise is dominant. However, it is difficult to predict the ballast noise radiation due to the complexity in modelling. This includes poro–elastic modelling of the ballast, which requires many input parameters. The properties of saturated fluid can be obtained from acoustic properties such as absorption coefficient, using the inverse characterisation (see Chapter 3). However, the elastic properties are not fully known, thus the sound radiation from the ballast frame (stones) is an open question. This has been investigated in Section 5.4.

Using the elastic properties obtained, the stiffness of the ballast used in the track model has been reviewed. A measurement carried out by Frémion et al. [100] suggested the ballast could be represented as a spring with a frequency–dependent stiffness and damping. This measured stiffness has been used in the rolling noise prediction software TWINS, but it has not been cross–checked. In Section 5.5 a comparison of the stiffness has been made with a numerical prediction. The effect of the underlying ground stiffness on the ballast stiffness will also be dicussed.

5.1 Absorption coefficient in a diffuse field

The absorption coefficient for normal incidence is identical in both local and extended reaction models as can be implied from Figure 5.1. However, they become different at oblique incidence as the extended reaction considers tangential waves within the medium. To check this, a comparison of absorption coefficients has been made for a diffuse field and compared with measurements from [101]. The diffuse field absorption coefficient of ballast was measured by Broadbent et al. [51] in a reverberant chamber.

To calculate the absorption coefficient, for the local reaction case an analytical solution for oblique incidence on a laterally infinite layer with a finite thickness is used. For the extended reaction case the transfer matrix method has been used. The incidence angle is taken from 0° to 78° in steps of 1°. The analytical solution has been obtained by treating the ballast as an equivalent fluid layer. Modified density (ρ_e) and bulk modulus (K_e) from the rigid frame porous model have been calculated from Equations (4.2) and (4.3). The surface impedance Z_s of an equivalent fluid layer with a rigid termination can be written as

$$Z_s = -\mathrm{i} Z_c \cot k_e h \tag{5.1}$$

where $Z_c = \sqrt{\rho_e K_e}$ is the acoustic characteristic impedance of the ballast, $k_e = \omega\sqrt{\rho_e/K_e}$ is the effective wavenumber and h is the thickness of the layer. The reflection coefficient and the absorption coefficient for oblique incidence with angle θ are given by

$$R_\theta = \frac{Z_s \cos\theta - Z_0}{Z_s \cos\theta + Z_0} \tag{5.2}$$

$$\alpha_\theta = 1 - |R_\theta|^2 \tag{5.3}$$

where $Z_0 = \rho_0 c_0$ is the characteristic acoustic impedance of air. For a diffuse field, the absorption coefficient α_d is calculated by

$$\alpha_d = \frac{\int_{\theta_{\min}}^{\theta_{\max}} \alpha_\theta \cos\theta \sin\theta \mathrm{d}\theta}{\int_{\theta_{\min}}^{\theta_{\max}} \cos\theta \sin\theta \mathrm{d}\theta} \tag{5.4}$$

Here, $\theta_{\max}$ and $\theta_{\min}$ are the range of the incidence angle. In this case, $\theta_{\min} = 0°$ and $\theta_{\max} = 78°$ with $\mathrm{d}\theta = 1°$. This range was found to be sufficient to cover the whole range, as the result converged within 1% to the case with a wider angle range.

The ballast has been modelled as a rigid–frame porous material, as the frame will not be affected much by an acoustic excitation. Therefore only the properties of saturated fluid have been considered in the calculation. These are given in Table 5.1. The porosity and the flow resistivity were measured in [13] for a 1:5 scaled ballast. For the full scale ballast, the porosity and the tortuosity remain the same. For the case of flow resistivity, it should be scaled appropriately. However, the scale factor is not clearly defined. Horoshenkov et al. [102] scaled the flow resistivity by the scale factor. However, in this case, the scaled flow resistivity $\sigma = 1400$ Ns/m^4 yields an overestimation of the absorption coefficient at all frequencies by up to 0.2. Also, the flow resistivity used in [47] was 200 Ns/m^4 for full scale ballast, which is close to 280 Ns/m^4. For these reasons, the flow resistivity for the scaled ballast has been used. The other parameters have been determined by curve fitting with the measured absorption coefficient.

TABLE 5.1: Properties of saturated fluid for the full scale ballast, obtained using inverse characterisation

α_∞	ϕ	σ (Ns/m^4)	Λ (μm)	Λ' (μm)
1.3	0.46	280	2800	2800

The results are shown in Figure 5.2 for two different thicknesses of the ballast. The difference between the two models is not large for this case. The extended reaction model shows a higher absorption for the same set of parameters, due to the energy loss in the tangential wave propagation.

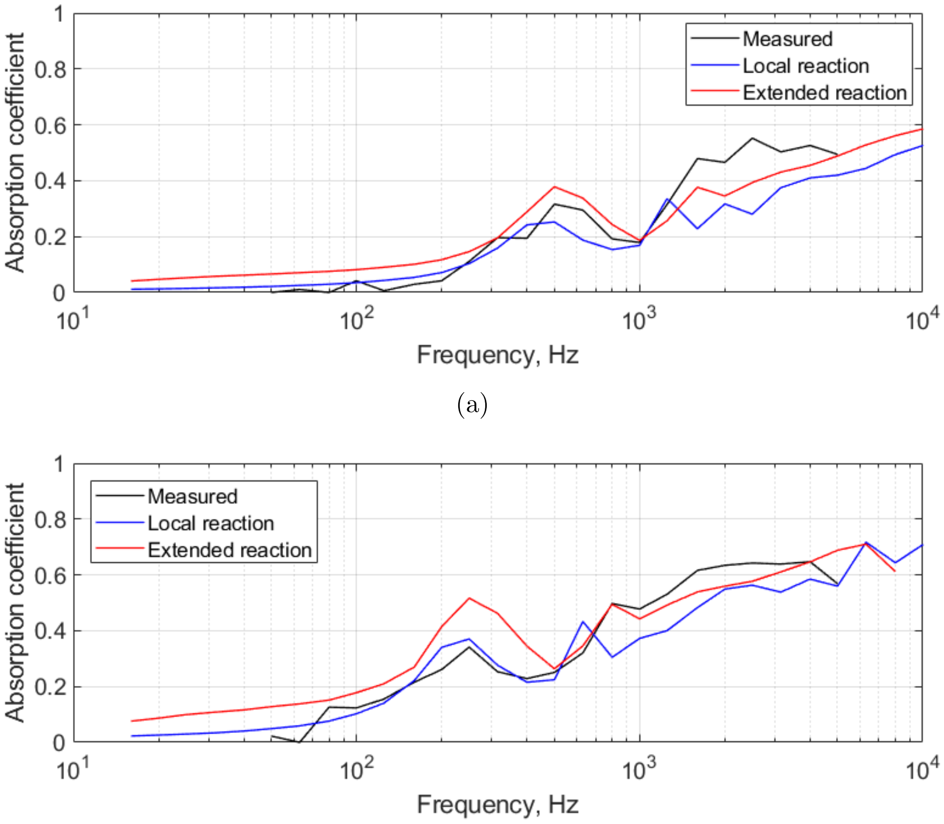

(a)

(b)

Figure 5.2. Absorption coefficient of ballast in diffuse field in 1/3 octave bands: (a) 0.17 m thick full scale ballast and (b) 0.33 m thick full scale ballast; ▬ measured, ▬ predicted with local reaction model (analytical solution), ▬ predicted with extended reaction model (TMM with JAC model)

The effect of manipulating the adjusted parameters is shown in Figure 5.3, relative to the reference case of 0.17 m thickness. Different from the characterisation process in

Chapter 3, here the characteristic lengths play an important role (Figure 5.3(a)). This is mainly because of the low flow resistivity. As mentioned in the beginning of the chapter, the low flow resistivity allows more air to flow through the pores, so that the acoustic energy loss relies more on the viscous dissipation. The thermal dissipation contributes little compared to the viscous one (Figure 5.3(b)). It should be noted that the thermal characteristic length should be no shorter than the viscous one by definition. The definitions of the two characteristic lengths (see Equations (2.9) and (2.10)) indicate that the two parameters only depend on the geometry of the pores. The weighting factors in the viscous characteristic length always lead to a smaller value than the thermal characteristic length ($\Lambda \leq \Lambda'$). They become identical in the case of nonintersecting uniform pores, as there is no weighting effect. This would be the upper limit of the viscous characteristic length (or the lower limit of the thermal characteristic length). Thus in Figure 5.3(a) the thermal characteristic length has been set to the same value as the viscous characteristic length. For the same reason the value of the thermal characteristic length Λ' could not be taken below 2800 μm. The effect of tortuosity is shown in Figure 5.3(c). It shifts peaks or dips of the absorption curve, introducing additional fluctuation when increased.

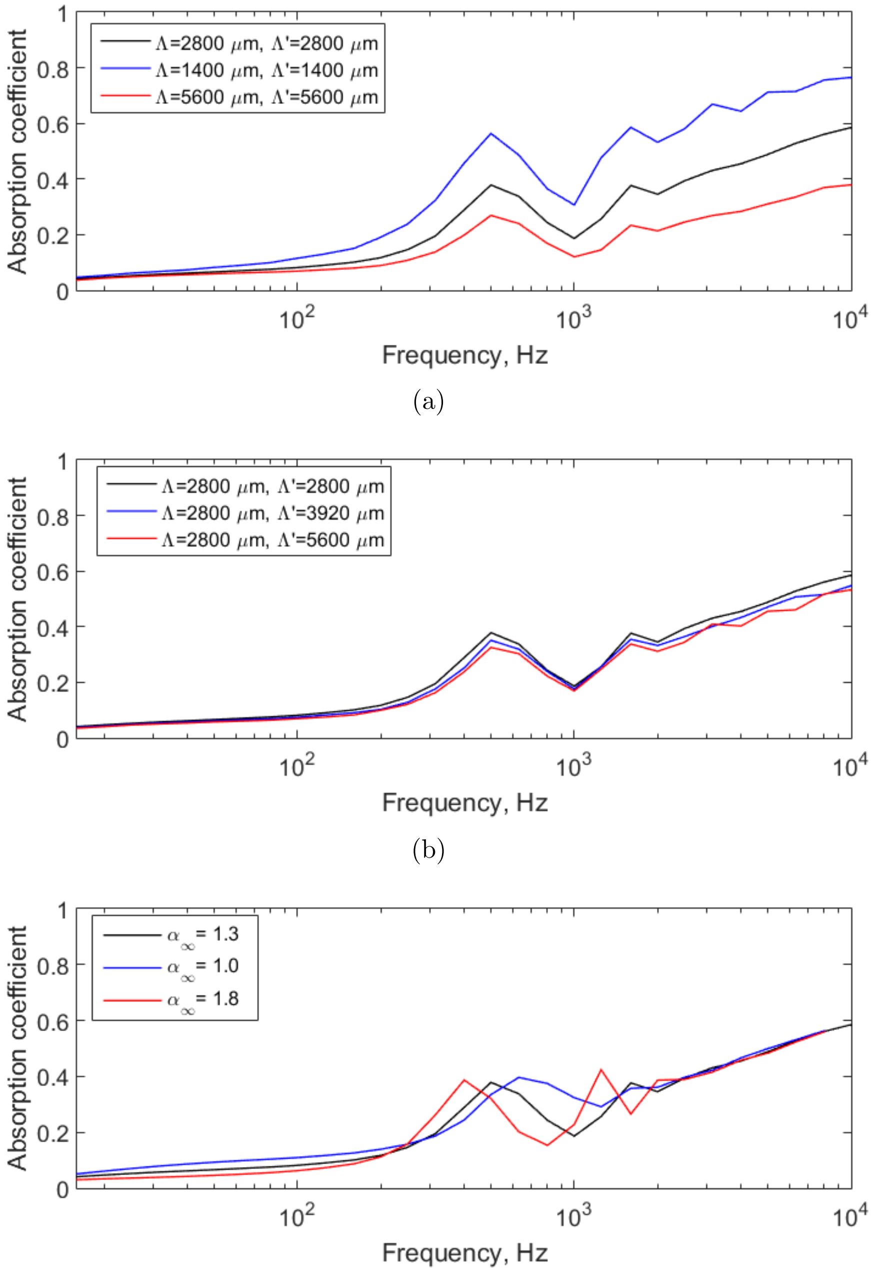

(a)

(b)

(c)

Figure 5.3. Sensitivity of the absorption coefficient of ballast from the extended reaction model to adjustable parameters: (a) viscous characteristic length, (b) thermal characteristic length and (c) tortuosity; — reference, — lower bound, — upper bound

5.2 Sound radiation of a sleeper embedded in ballast

The second example considered is the radiation of a sleeper when it is embedded in ballast. Measured data for a single sleeper embedded in ballast at scale 1:5 has been used for comparison in terms of radiation ratio of the sleeper. The measurement was carried out by Zhang [13] using a reciprocal method in a reverberant chamber [101]. A layer of 1:5 scaled ballast was placed on the floor of a reverberant chamber and a loudspeaker and a rotating microphone were installed. An accelerometer was attached to the sleeper to measure the acceleration of the structure and the microphone was used to measure the spatially-averaged mean-square pressure in the chamber after the diffuse field had fully developed. Also, the spatially-averaged transfer mobility of the sleeper was measured with an impact hammer and an accelerometer. The measurement setup and the dimensions of the sleeper cross–section are shown in Figure 5.4. The dimensions of the ballast were 2.1 m × 1.25 m × 60 mm and the length of the sleeper was 0.50 m. The top surface of the sleeper was flush with that of the ballast. The method to obtain the radiation ratio of the sleeper in the reverberant chamber is briefly described in Appendix D, and more details about the method can be found in [101].

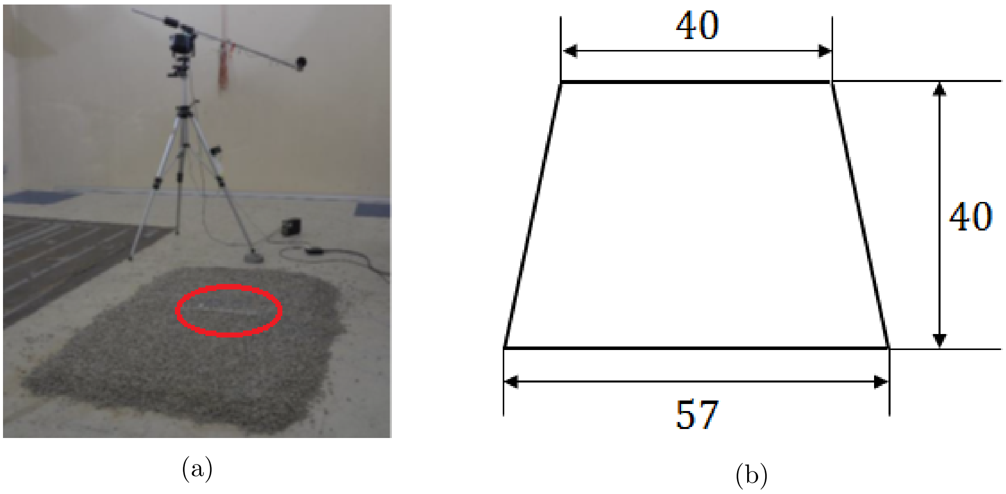

(a) (b)

Figure 5.4. Sound radiation of sleeper embedded in ballast: (a) measurement setup (sleeper marked red) [13] and (b) sleeper cross–section dimensions (in mm, not to scale)

In [13], a comparison was made between the measurement and a 3D acoustic boundary element model, which showed large discrepancies. One of the reasons was the fact that in the 3D boundary element model only the ballast surface can be modelled using an impedance, while the interior of it is not included in the domain. Also, due to the limitation of the boundary element model, it was not possible to make the embedded part of the sleeper vibrate inside the ballast.

To overcome these limitations, the sleeper embedded in ballast has been modelled in 2D using the developed FE/BE model. As the elastic properties for the ballast were unknown, the equivalent fluid model has been used for the ballast (see Section 4.1.1). The corresponding mesh is shown in Figure 5.5. The red line is the acoustic boundary elements to calculate sound radiation and the green region is the equivalent fluid finite elements with the modified density ρ_e and bulk modulus K_e, which are the ballast. The hollow region in the middle of the ballast represents sleeper cross–section, as shown in Figure 5.4. The rigid ground has been modelled using a modified Green's function in the boundary element model. A unit vertical velocity amplitude is given around the sleeper. Therefore the simulation does not consider structural modes of the sleeper.

For the ballast properties, the porosity, flow resistivity and tortuosity of the ballast are the same as those in Table 5.1. For the characteristic lengths, $\Lambda = 482$ μm and $\Lambda' = 964$ μm were taken for the scaled ballast, as in [13]. These were obtained by curve fitting the result from the local reaction model to a diffuse field absorption coefficient. It should be noted that the relation between the characteristic lengths $\Lambda' = 2\Lambda$ was used in Zhang's work, whereas $\Lambda' = \Lambda$ was used in Section 5.1. This would not make a large difference to the results, as they are all in a reasonable range. As the purpose of this study is the comparison between the models, the properties used in [13] have been used, which are shown in Table 5.2.

TABLE 5.2: Properties of saturated fluid used for the scaled ballast

α_∞	ϕ	σ (Ns/m^4)	Λ (μm)	Λ' (μm)
1.3	0.46	280	482	964

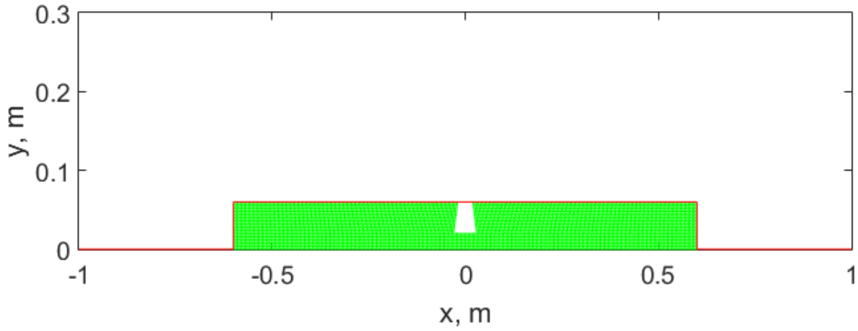

Figure 5.5. Reduced scale sleeper embedded in ballast; 🟥 boundary elements, 🟩 poro–elastic finite elements

The radiation ratio from the simulation is plotted in Figure 5.6 and compared with the measured data. A result from a 3D acoustic boundary element model with the ballast modelled using the local reaction model is also plotted (dashed black line), which is reproduced from [13]. In addition, a case with the porous 2D FE model where the velocity is only given on the top surface of the sleeper has been considered to see whether the sleeper vibration inside the ballast has an influence on the radiation.

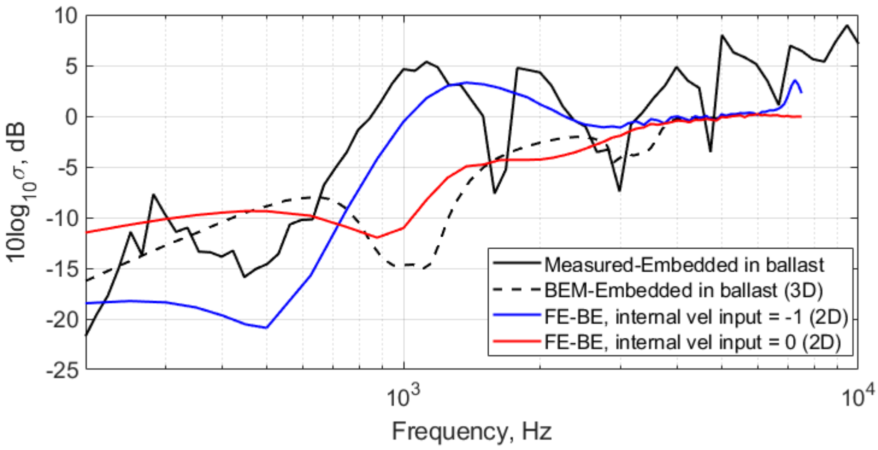

Figure 5.6. Radiation ratio of the 1:5 scale sleeper; — measured, - - - predicted using 3D BEs, — predicted using 2D BEs and poro–elastic FEs (velocity on the top of the sleeper), — predicted using 2D BEs and poro–elastic FEs (velocity around the sleeper)

The red line in Figure 5.6 represents the result when the velocity is given only on the top surface of the sleeper. It has a dip at 900 Hz, similar to the boundary element model with an impedance for the ballast. The blue line, which is the result for a unit velocity around the sleeper, shows much better agreement with the measurement. The dip at around 500 Hz and the broad peak around 900 Hz are predicted from the model although the magnitude differs. At high frequency, fluctuating behaviour is seen in the measurement but not in the simulations. This is because of the flexural behaviour of the sleeper, which could not be modelled in the simulations. To consider the sleeper modes, a 3D model would be required including the structural vibration of the sleeper. The dips in the measurement correspond to modes of the sleeper, for which the resonance frequencies in free space are 1500 Hz, 2800 Hz, 4400 Hz, etc [13]. The first peak at 300 Hz is thought to be due an artefact present in the reverberant room (or the type of the loudspeaker), which was reduced by repeating the measurement [13].

The RMS error of each prediction is 8.0 dB, 4.3 dB and 5.7 dB for the 3D BE prediction, 2D prediction with the internal velocity and 2D prediction without the internal velocity, respectively. From this it can be said that the extended reaction model gives better results, although some important differences are still visible. It is clear that when the sleeper radiates noise into the field, the vibration of the embedded part of the sleeper also contributes to the result. This feature can only be captured by the extended reaction model.

The 3D effects on the radiation are expected to be small in this case, as the 2D extended reaction model (solid blue line) yields better agreement than the 3D local reaction model (dashed black line) in Figure 5.6. A separate investigation has been carried out comparing 2D and 3D models of a sleeper, as follows. Consider a baffled surface with the same size as the top surface of the reduced scale sleeper, as shown in Figure 5.7.

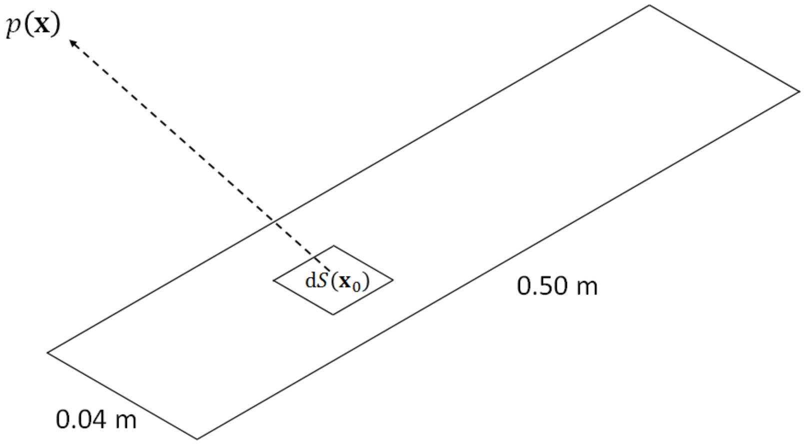

Figure 5.7. Sound radiation from a baffled surface

The pressure $p(\mathbf{x})$ at field point $\mathbf{x}$ can be calculated by the Rayleigh integral:

$$p(\mathbf{x}) = \mathrm{i}\rho_0\omega \int_S v_n(\mathbf{x_0}) \frac{e^{-\mathrm{i}k_0 r}}{2\pi r} \mathrm{d}S \tag{5.5}$$

where ρ_0 is the density of air, ω is the angular frequency, v_n is the normal velocity of the baffled surface of area S, k_0 is the acoustic wavenumber and $r = |\mathbf{x} - \mathbf{x}_0|$ is the distance from the surface element to the field point. For simplicity, a unit normal velocity with constant phase has been applied to the whole surface. The sound power in the far field can be calculated by integrating the sound intensity around a hemisphere with radius a.

$$W = \int_0^{2\pi} \int_0^{\pi/2} \frac{|p(a, \theta, \psi)|^2}{2\rho_0 c_0} a^2 \sin\theta \mathrm{d}\theta \mathrm{d}\psi \tag{5.6}$$

where c_0 is the speed of sound in air. The radiation ratio is calculated by

$$\sigma_{textrmrad} = \frac{W}{W_{ref}} \tag{5.7}$$

where $W_{ref} = \frac{1}{2}\rho_0 c_0 S$ is the reference power. Note that Equation (5.6) assumes a plane wave propagation in the far field ($p = \rho_0 c_0 v_n$). The result is shown in Figure 5.8. Results from different sleeper lengths are also shown; as the length increases this tends towards the 2D case. However, above 400 Hz, the differences in the radiation ratio are negligible.

Therefore it can be said that the 3D effects may not be important on the radiation above 400 Hz (or 80 Hz at full scale), apart from the structural modes of the sleeper.

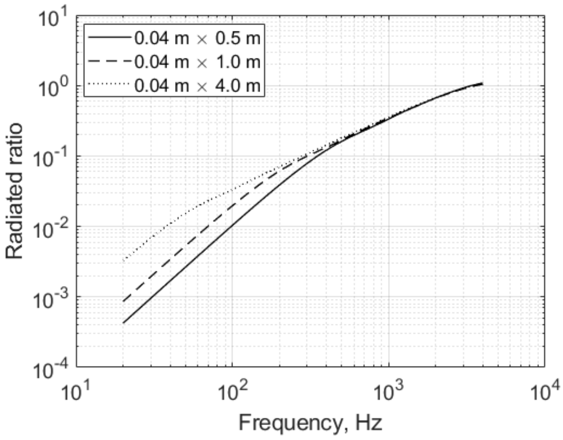

Figure 5.8. Radiation ratio of baffled plates of different lengths representing a reduced scale sleeper; ━━ 0.5 m, - - - 1.0 m, ····· 4.0 m

5.3 Sound radiation of a rail above ballast

The third case considered is the radiation from a rail located above a layer of ballast. With the same measurement setup as the sleeper case, the sound radiation of a 1:5 scale rail above the ballast was also measured and compared with the local reaction model [13]. Note that the same reciprocal method was used in the measurement (see Appendix D). A 2 m long rail was used and the cross-section is shown in Figure 5.9. It was hung by elastic cord 20 mm above the ballast. The ballast layer had a thickness of 60 mm. A comparison is made here between the result from the local reaction model and a result from the extended reaction model. Figure 5.10 shows the measurement setup and the numerical mesh used for the extended reaction model simulation. Both models are two–dimensional.

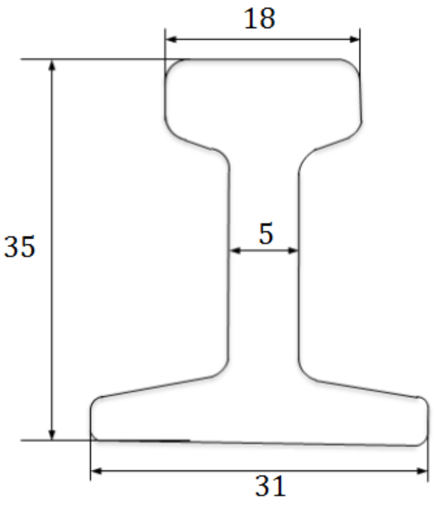

Figure 5.9. Dimensions of the rail (in mm, not to scale) [13]

Two cases are considered in which the rail vibrates vertically and laterally. As the rail is modelled using boundary elements, it is assumed to move rigidly. The results are plotted in Figure 5.11, normalised with respect to the case of rail radiation in free space. The dip at 1500 Hz from the local reaction model is due to the thickness of the ballast. It occurs when a quarter of the acoustic wavelength is equal to the thickness, i.e., $f_{\text{dip}} = 343/4/0.06 = 1429$ Hz. The corresponding dip is observed at a higher frequency in the measurement and the extended reaction model, because the propagating wavelength in the medium is increased by the presence of the transverse wave component. The other dips seem to be related to other factors such as the lateral size of the ballast region and the distance between the rail and the ballast. The general tendency of the two numerical models is quite similar, with a slight improvement at the dips when the extended model is included.

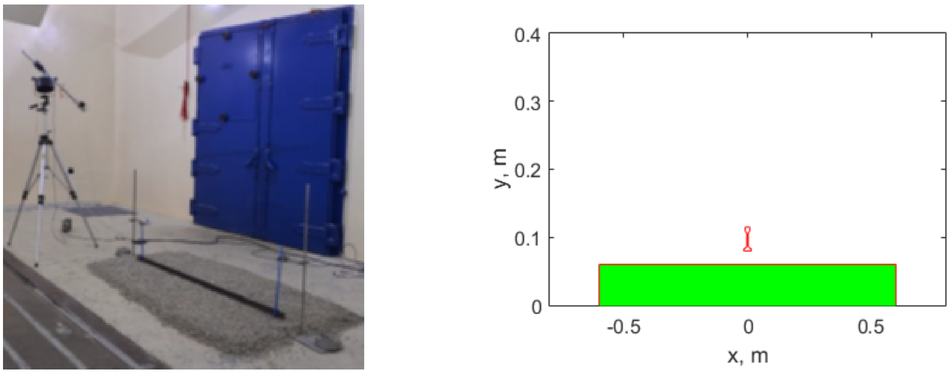

(a) (b)

Figure 5.10. Sound radiation of rail over ballast: (a) measurement setup in reverberant chamber [13] and (b) numerical mesh for the simulation

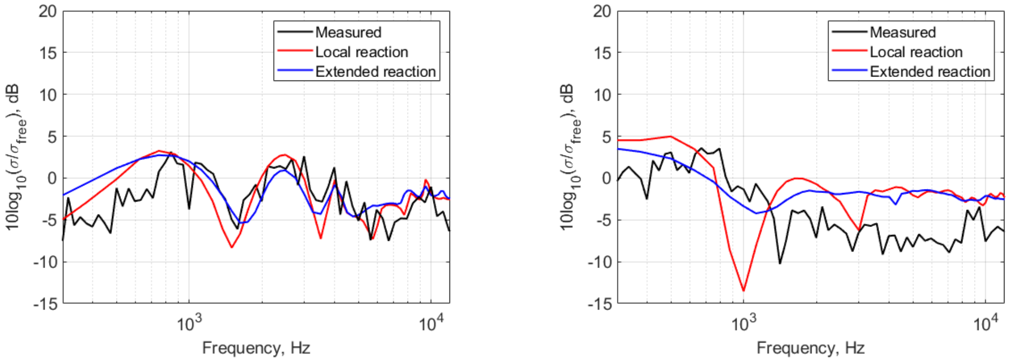

(a) (b)

Figure 5.11. Normalised radiation ratio of the rail over the ballast: (a) vertical motion and (b) lateral motion; — measured, — predicted using 2D boundary elements with JAC model for the ballast surface, — predicted using 2D boundary elements and poro–elastic finite elements

The disparity between the local reaction model and the measurement appears to be larger in the case of lateral motion, as more oblique incidence waves are expected in the ballast. Above 1.5 kHz a 6 dB level difference is seen between the measured result and the two numerical models. The reason for this is unclear, but the fact the results from the two 2D numerical models are similar may indicate that the disparity comes from waves in the third direction. Also, different from the simulations, the rail section does not move rigidly in the lateral direction. This could be the reason why the agreement between the measurement and the simulations is worse compared to the case of vertical motion. The result may also have been affected by the slope at the edges of the ballast in the measurement. This could be investigated by changing the geometry in the simulation.

5.4 Sound radiation of railway ballast

The ballast itself has not been highlighted as a noise source, and is usually ignored in the rolling noise calculation. This is true at high frequencies, because the rail vibration is isolated from the sleepers. In the software TWINS the ballast (including the ground) is only included as a spring in the track dynamics. However, it might also have an effect on the rolling noise at low frequencies where its response is comparable to that of the sleepers. This section will address how much the noise radiation from the ballast contributes to the rolling noise.

There are practical problems with using 2D or 2.5D numerical models for the ballasted track. For example, sleepers laid periodically on the ballast cannot be represented in such a model. One may consider a cross–section in the direction of the track, but this cannot model the decay of vibration in 3D properly. For these reasons, a 3D model has been created using the software COMSOL. From the model the structural response of the track has been obtained, and the sound radiation is calculated based on the structural response. To simplify the problem, the noise radiation has been assumed to be the noise radiation of a vibrating surface set in a rigid ground, which can be calculated using the Rayleigh integral (see Equation (5.5)).

Figure 5.12 shows the geometry and the mesh of the COMSOL model. The properties of the rail, rail pad and sleepers are listed in Table 5.3. These have been modelled using solid finite elements. The ground has also been modelled using solid finite elements. However, the ballast has been modelled using poro–elastic finite elements, as they were recently added to COMSOL 5.3. It should be noted that the sides of the sleepers are not in contact with the ballast. This is because it is thought that the outer surfaces of the ballast would not behave as a fully continuous medium. Thus the sleepers are coupled with the ballast only at the bottom surface. A core region has been set, with radius 2 m around the centre point of the ground, to obtain a good mesh resolution where the force is applied.

The boundaries at the symmetry planes have been set to be symmetric, the outer surface of the ground (the quarter hemisphere) has been set to be low–reflecting and the rest has been set to be free. This means, on the ballast surfaces, the pressure of the interstitial fluid in the pores is set to be zero. Therefore it should be noted that the zero fluid pressure on the surface will lead to overestimation of the radiated sound power as the pores will cause some absorption, i.e., negative power. A non–zero pressure can be considered, if the ballast is coupled with fluid finite elements (air). However, this will require a great amount of computational resources due to an increased model size and hence it has not been considered. This would be feasible if coupling between a fluid boundary element model and the poro–elastic model is made.

The total number of elements is 631586, and the total number of degrees of freedom is 2878602. This takes around 22 minutes to calculate the case at one frequency, with 128 cores running at 2.60 GHz on the Iridis 4 super computer.

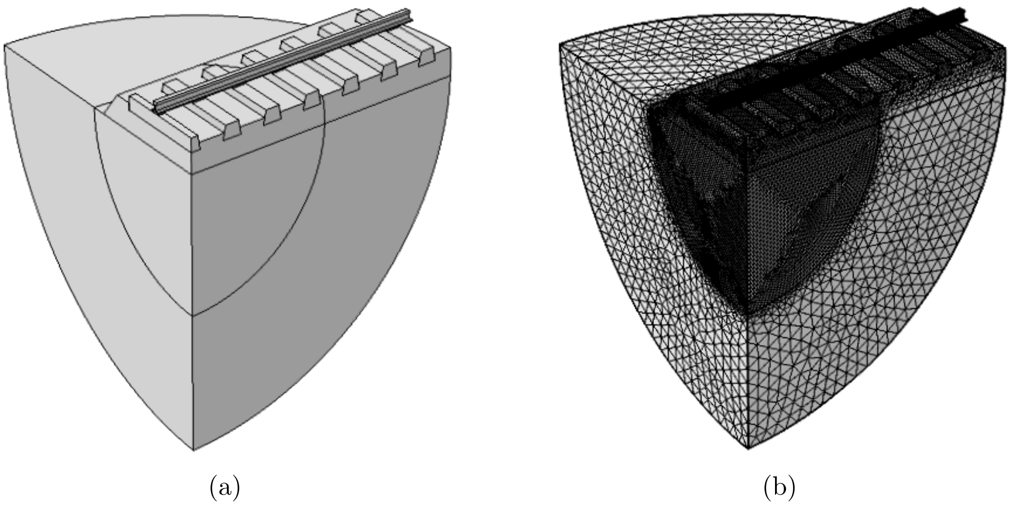

Figure 5.12. FE model used for ballast radiation: (a) geometry and (b) mesh for the numerical prediction

Table 5.3: Properties of the rail, rail pad and sleepers

	E (GPa)	ν	ρ (kg/m^3)	η
Rail	210	0.30	7850	0.02
Rail pad	0.03	0.45	10	0.25
Sleeper	41.3	0.15	2750	0.02

5.4.1 Elastic properties of ballast and ground

In Section 5.1, only the properties of saturated fluid of ballast are determined. However, the elastic properties are not fully known. The frame density ρ_1 can be measured easily, using a container of a known volume. In fact it is known to be around 1800 kg/m^3. The Young's modulus and the Poisson's ratio are, however, not easy to measure. In terms of the order of magnitude, the Young's modulus is known to be around 10^8 Pa with prestress, as given for example in [103]. This data is usually obtained from compression tests; thus little information is given for the Poisson's ratio. It is only mentioned in the so–called frustum model as a "stress distribution angle". Obviously the ballast is stiff in compression, as many studies suggest. However, this might not be the case for shear. Initially, a value of 0.35 has been chosen for the Poisson's ratio with the Young's modulus of 1.1×10^8 N/m^2. This corresponds to a shear wave speed of 150 m/s. Also, to take account of a reduced shear stiffness of the ballast, a shear wave speed of 100 m/s has been chosen together with the Poisson's ratio of 0.45. Two different Young's moduli for the underlying ground have been used, to see the effects of the rigidity of the ground. The elastic properties are listed in Table 5.4. Note that the properties are frequency–independent.

Table 5.4: Assumed elastic properties of the ballast and the ground with variations

	E (MPa)	ν	ρ (kg/m^3)	η	c_p (m/s)	c_s (m/s)
Ballast	110	0.35	1800	0.1	313	150
	52.2	0.45	1800	0.1	331	100
Ground	107	0.30	1835	0.04	280	150
	428	0.30	1835	0.04	560	300

5.4.1.1 Measurement of ballast surface vibration

To find an appropriate set of the elastic properties of the ballast, a simple measurement was carried out at a test track in Chilworth, which belongs to the University of Southampton. The track is 32 m long, and the rail pads between the rail and the sleeper have a stiffness of 120 MN/m. The measurement was conducted in the middle of the track. The purpose of the experiment was to find the frequency–dependent ratio between the ballast vibration and the sleeper vibration for excitation of the sleeper. The surface vibration of the ballast was measured by an accelerometer attached to a stone on the ballast surface. The measurement setup is shown in Figure 5.13. A B&K accelerometer type 4514–001 of which the mass is 8.7 gram was attached to a stone on the ballast surface (red circle in Figure 5.13(b)) and a PCB accelerometer type 353B32 was attached to the sleeper close to the rail seat. The large accelerometer, next to the one attached to the stone, was used as a reference to check the sensitivity of the accelerometer on the stone. A PCB instrumented hammer type 086C05 with a nylon tip was used to excite the sleeper close to the accelorometer. Each measurement was repeated six times and the frequency response was averaged.

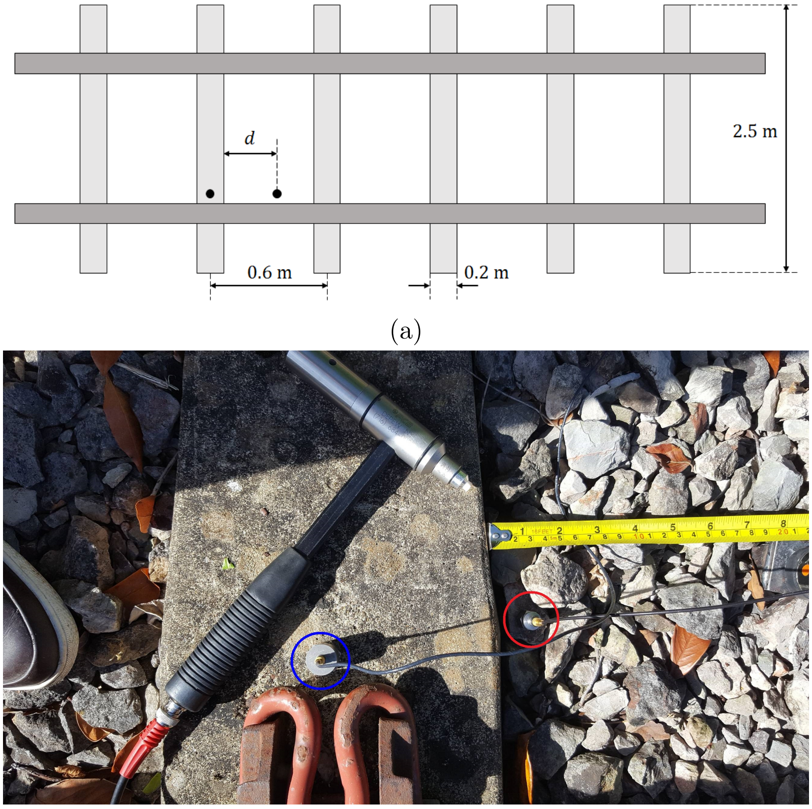

(a)

(b)

Figure 5.13. Measurement setup for the track vibration test: (a) top view of the track and the accelerometers and (b) the actual setup; ○ accelerometer on the sleeper, ○ accelerometer on the ballast

The measurement can only give a rough estimate of the vibration ratio, as there were many uncertainties. For example the accelerometer on the stone only measured in a single axis, which means the vertical alignment would be very important. The choice of the stone might affect the result as well, as it may tend to bounce on the surface. By the same token, the placement of the stone on the ballast surface could also change the result. To check the variability due to the stone size, the vibration on four different stones (see Figure 5.14) was measured and the results are shown in Figure 5.15. Similar behaviour is seen at low frequencies, and the results diverge at around 300 Hz. It should be noted that the placement could not be exactly the same in these measurements, which would have caused further differences. The stone in Figure 5.14(a) was used throughout the measurements. One reason was that its surface was relatively flatter than the others, which made it easier to attach the accelerometer. The other reason was that it could easily be placed within the ballast. However, the variability of the stone has been considered as a range, which is included in the result.

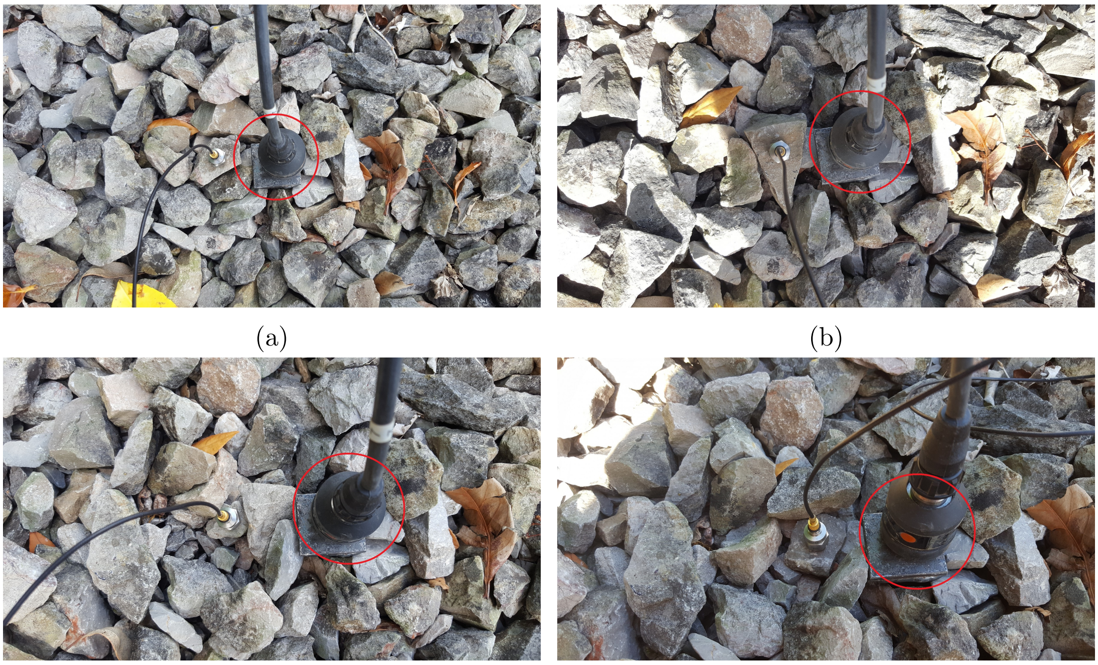

(a) (b) (c) (d)

Figure 5.14. Accelerometer attached to four different stones: (a) stone 1, (b) stone 2, (c) stone 3 and (d) stone 4; ○ reference accelerometer (not shown in the result)

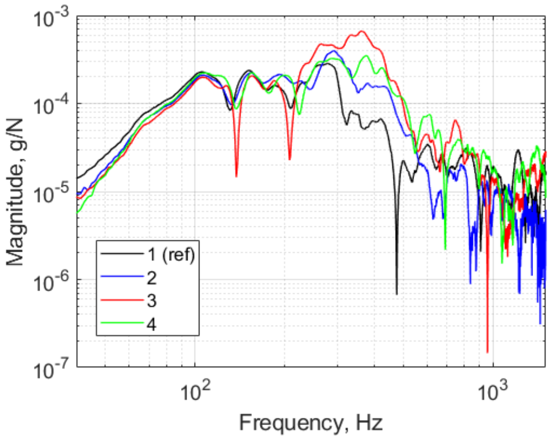

Figure 5.15. Magnitude of accelerance measured on different stones (shown in Figure 5.14); — stone 1 (reference), — stone 2, — stone 3, — stone 4

The vibration of the ballast was measured at 230 mm and 375 mm from the edge of the sleeper, which is denoted by d in Figure 5.13(a). The coherence corresponding to the accelerances is shown in Figure 5.16. The coherence of the sleeper vibration is good below 1 kHz, while the ballast transfer function shows good coherence below 200 Hz. Above that some dips are observed, but overall it is acceptable up to 500 Hz.

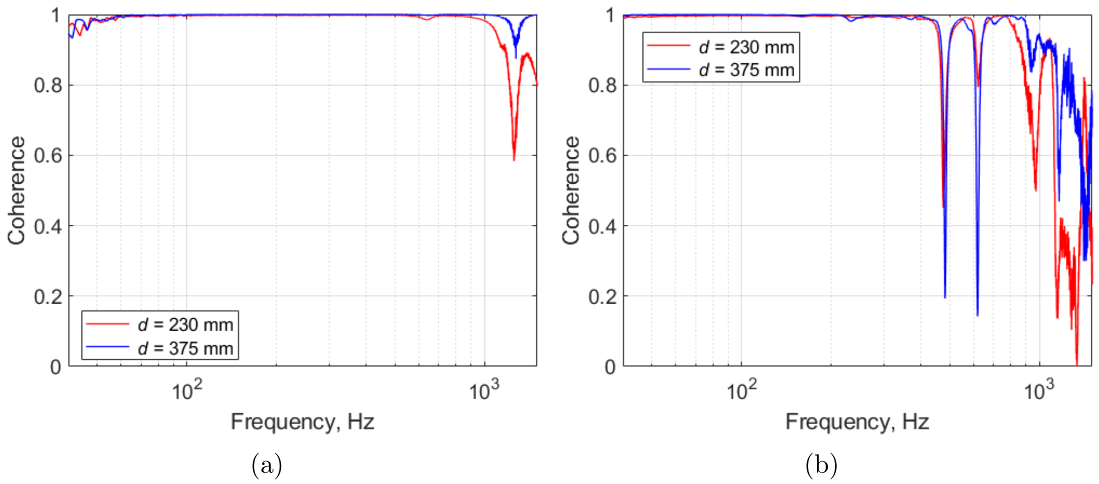

Figure 5.16. Coherence between the excitation and the response: (a) sleeper and (b) ballast; ▬ response measured at 230 mm away from the edge of the sleeper, ▬ response measured at 375 mm away from the edge of the sleeper

Simulations have been made using the COMSOL model in Figure 5.12 to replicate the measurements. A point unit force has been given on the top of the sleeper next to the rail at the symmetry plane, and the vertical displacements of the sleeper and the ballast have been obtained at the same positions as in the measurements. The results are compared in terms of the ratio of the ballast displacement to the sleeper displacement. Figure 5.17 shows the comparison between the simulations and the measured data, for the properties given in Table 5.4. Note that the ballast displacement is averaged from the results at the two distances. The variability due to different stones in Figure 5.15 has been taken into account, which is shown as a grey area. It is seen that the softer ground overestimates the ballast vibration at low frequencies, compared with the ones with the stiffer ground. The blue lines show better agreement than the red lines, although the difference is not very significant. Therefore the Young's modulus of 110 MPa and the Poisson's ratio of 0.35 have been chosen for the calculation of the sound radiation. The two Young's moduli for the ground have been used to see the effects of the ground stiffness.

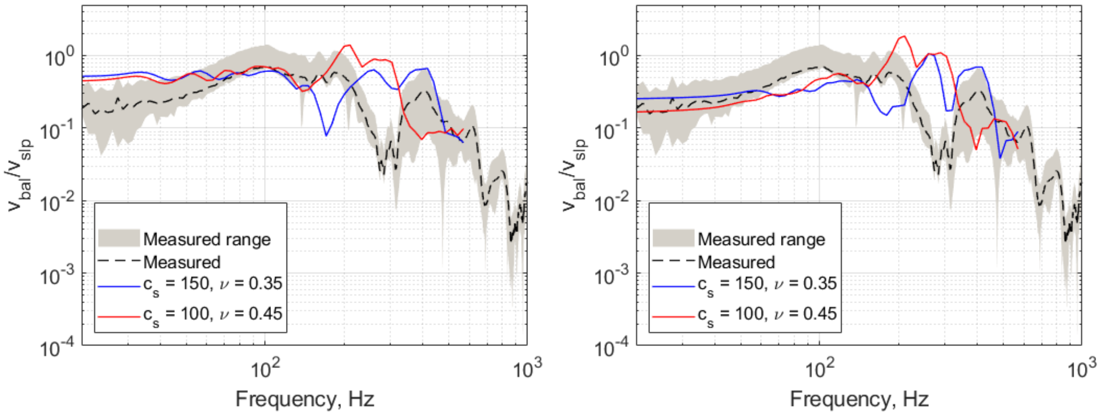

(a) (b)

Figure 5.17. Comparison of vibration ratio of ballast and sleeper with (a) soft ground and (b) stiff ground; ▨ variance due to the stone (see Figure 5.15), - - - measured, ▬ predicted with c_s=150 m/s and ν=0.35, ▬ predicted with c_s=100 m/s and ν=0.45

5.4.2 Ballast noise radiation

Using the properties obtained, the sound radiation of the ballast has been calculated, with a point excitation given on the top of the rail. The configuration in Section 5.4.1 has been used. The radiated power has been calculated using the Rayleigh integral, with an assumption of a baffled surface for the radiating surfaces. The sleeper noise has also been calculated for comparison, in order to estimate the relative contribution of the ballast noise radiation to the sleeper noise radiation. The radiating areas for the ballast and the sleepers used in the calculation are shown in Figure 5.18.

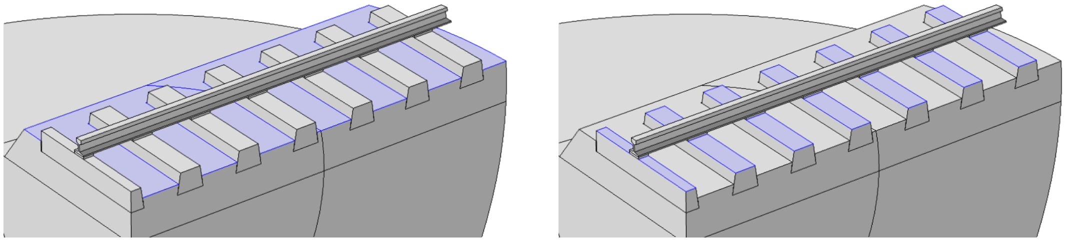

(a) (b)

Figure 5.18. Surfaces for calculating sound radiation (highlighted in blue): (a) ballast and (b) sleepers

The Rayleigh integral for a baffled surface is given by

$$p(\mathbf{x}) = \mathrm{i}\rho_0\omega \int_S v_n(\mathbf{x_0}) \frac{e^{-\mathrm{i}k_0 r}}{2\pi r}(1-\phi)\mathrm{d}S \tag{5.8}$$

where ρ_0 is the density of air, ω is the angular frequency, v_n is the normal velocity of the baffled surface of area S, k_0 is the acoustic wavenumber and $r = |\mathbf{x} - \mathbf{x}_0|$ is the distance from the surface element to the field point. A correction for the porosity has been made $(1 - \phi)$, to consider the structural vibration only. For the sleepers the porosity is zero, hence the result is not affected by this factor. The sound power can be calculated by integrating the sound intensity around a hemisphere with the radius a.

$$W = 4\int_0^{2\pi} \int_0^{\pi/2} \frac{|p(a,\theta,\psi)|^2}{2\rho c} a^2 \sin\theta \mathrm{d}\theta \mathrm{d}\psi \tag{5.9}$$

The factor 4 in Equation (5.9) takes account of the two symmetry planes (2 for each symmetry plane). The results are shown in Figure 5.19, in terms of sound power per unit force. The blue and red lines are the radiation of the sleepers and the ballast, respectively. The black line is the total radiation from the ballast and the sleepers. The total power has been calculated from the combination of the ballast and sleeper vibration. In both figures, a similar sound power is seen from the ballast and the sleepers below 200 Hz. In this frequency region, the ballast and the sleepers vibrate almost in phase, making constructive interference. Thus the total power is increased by 6 dB. Above 200 Hz, there are regions where the total noise radiation is less than the sleeper noise radiation. This is because the sleepers and the ballast vibrate out of phase, leading to destructive interference. However, as the sleeper noise radiation is generally stronger in magnitude, the overall sound power is mostly determined by the sleepers above 200 Hz. Also, the stiffness of the ground has an effect on the level and the trend at low frequencies, below 250 Hz. In this case the soft ground shows a higher noise level by around 9.3 dB below 40 Hz whereas the stiff ground shows a higher level of up to 4.6 dB between 50 Hz and 250 Hz.

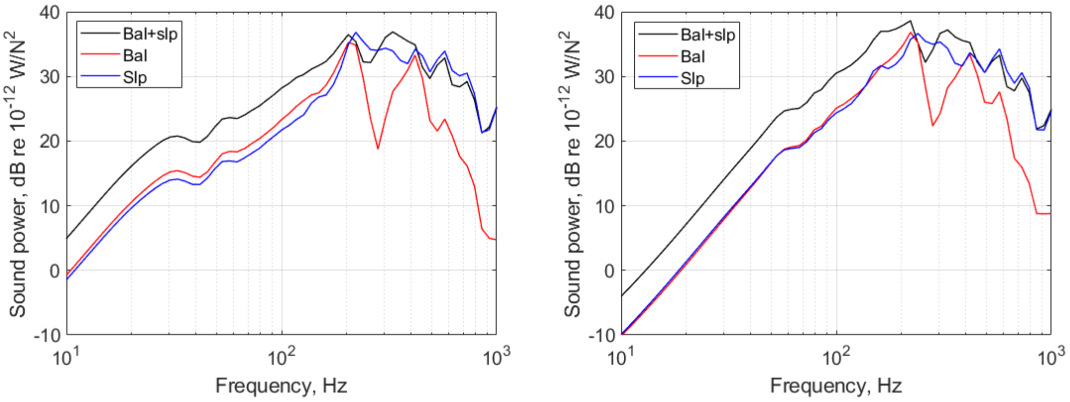

(a) (b)

Figure 5.19. Comparison of radiated sound power from ballast and sleepers with (a) soft ground and (b) stiff ground; ▬ total radiated power (ballast+sleepers), ▬ radiated sound power from ballast, ▬ radiated sound power from sleepers

Figure 5.20 shows the relative contribution of the ballast noise to the total noise, which is reproduced from Figure 5.19. The result is plotted in terms of the level difference between the total noise and the sleeper noise. With a little deviation, the two cases show similar trends, with a constant difference below 100 Hz. Figure 5.19 shows that the ground stiffness changes the overall level at low frequencies, but from Figure 5.20 it is clear that the effect of the ballast on the sleeper noise radiation does not change much.

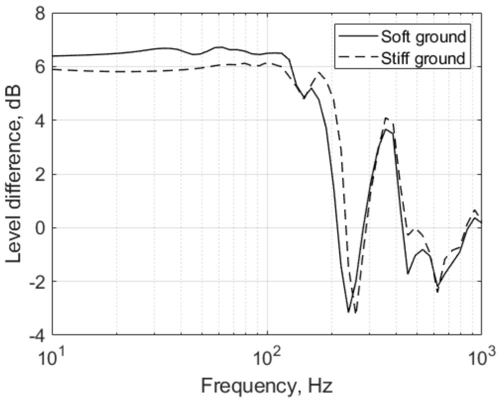

Figure 5.20. Effect of the ballast on the sleeper noise radiation: ▬ on soft ground - - - on stiff ground

5.5 Dynamic stiffness of railway ballast

Using the elastic properties obtained in Section 5.4, the stiffness of the ballast used in the track model for rolling noise has been reviewed. The track model used for rolling noise predictions is a beam on two-layer foundation system, where the ballast and sub-foundation is modelled as a damped spring [1]. In this model, the stiffness of the ballast (and ground) affects the vibration level of the whole system, and hence the radiated noise from the rail and the sleeper. A stiffness measurement carried out by Frémion et al. [100] showed that the stiffness of the ballast is dependent on frequency, above about 100 Hz. This has a great impact on the sleeper vibration, as it changes resonance frequencies of the sleeper and also reduces the amplitude of higher modes of the sleeper. It has been used in TWINS for calculating noise from ballasted tracks [104]. However, this relies on a single measurement and no physical explanation has been given for this effect. In this section, a numerical prediction for the ballast stiffness has been made to check the validity of the measurement. The numerical model does not represent the measurement exactly, as the properties of the ballast and the ground in the measurement were unknown. Nonetheless, one would expect to see a similar trend from the numerical prediction.

Figure 5.21 shows the stiffness measured by Frémion et al. [100]. Note that the units are N/m^2, because the stiffness is normalised by the length of the sleeper (2.5 m). In the measurement an indirect method was used for high frequencies, so the mass effect of the sleeper was compensated. The magnitude and the phase were assumed to be constant below 100 Hz.

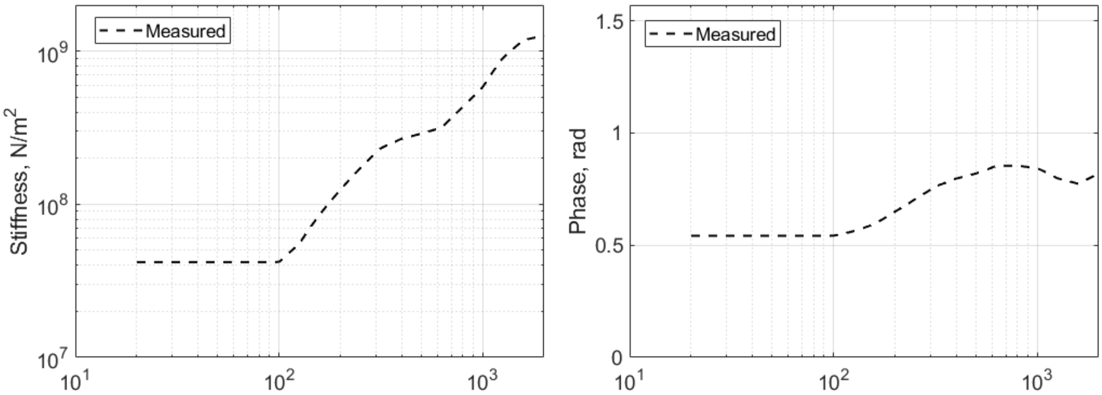

(a) (b)

Figure 5.21. Measured ballast stiffness [100]: (a) magnitude and (b) phase

Again, COMSOL has been employed to calculate the structural response of the ballast. A quarter domain of ballast and ground has been modelled, for which the configuration and the mesh are shown in Figure 5.22. As the ballast stiffness seen from the sleeper includes the ground stiffness, the ground should be included. The radius of the ground region is 6.4 m, which would correspond to a shear wavelength at 23 Hz. On the top of the ground is the ballast, of which the width is 3.6 m at the bottom and 3.0 m at the top and the height is 0.4 m. For excitation, a prescribed displacement is given to an area where the sleeper would be placed. The excitation area is marked blue in Figure 5.22(a). A core region has been set, with radius 2 m around the centre point of the ground, to obtain a good mesh resolution where the force is applied. In total, 724936 tetrahedral elements have been used for the calculation.

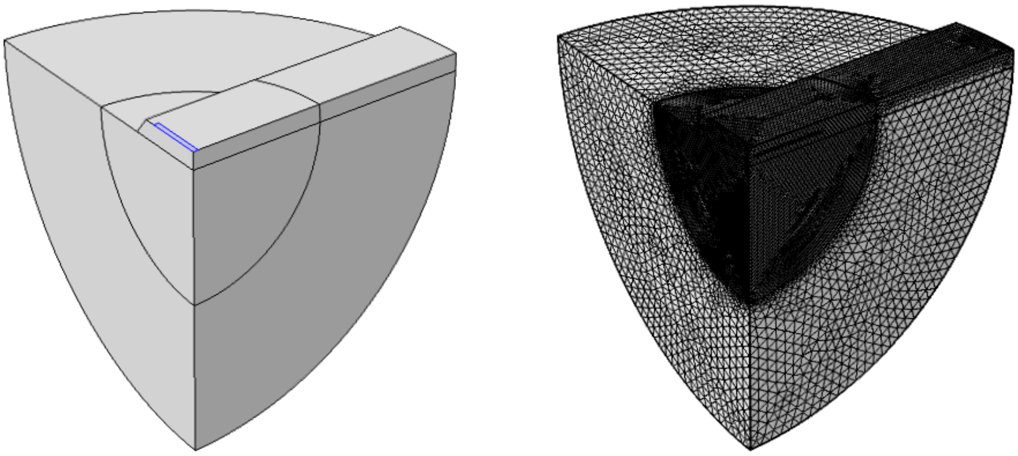

(a) (b)

Figure 5.22. FE model used for the calculation of ballast stiffness: (a) geometry and (b) mesh for the numerical prediction

The ground has been modelled using solid finite elements and the ballast has been modelled using poro–elastic finite elements as in the previous section. The boundaries at the symmetry planes have been set to be symmetric, the outer surface of the ground (the quarter hemisphere) has been set to be low–reflecting and the rest has been set to be free. Again, the fluid in the pores at the ballast surface has zero pressure due to the free boundary condition. Nonetheless the mesh should give reasonable results because the stiffness is mostly affected by the structural response of the ballast. The properties of the ground are listed in the first row of Table 5.5 and those of the ballast are given in Table 5.6. The second row in Table 5.5 will be used for comparison. Note that the properties are frequency–independent.

Table 5.5: Properties of the ground

	E (MPa)	ν	ρ (kg/m^3)	η	c_p (m/s)	c_s (m/s)
Stiff ground	428	0.30	1835	0.04	560	300
Soft ground	107	0.30	1835	0.04	280	150

Table 5.6: Properties of the ballast

ϕ	α_∞	σ (Ns/m^4)	Λ (μm)	Λ' (μm)	E (MPa)	ν	ρ_1 (kg/m^3)	η
0.46	1.3	280	2800	2800	110	0.35	1800	0.1

A prescribed displacement is given on the top surface of the sleeper, and the stiffness normalised by the sleeper length has been calculated using the following equation:

$$K = \frac{F_z}{w_{\mathrm{mean}} L} \tag{5.10}$$

where L (=2.5 m) is the length of the sleeper and the force in $z-$direction F_z and the mean displacement $z-$direction w_{mean} are defined as

$$F_z = 4 \int_S \sigma_{zz} \mathrm{d}S \tag{5.11}$$

$$w_{\mathrm{mean}} = \frac{1}{S} \int_S w \mathrm{d}S. \tag{5.12}$$

Here, σ_{zz} is the normal stress and w is the displacement in the z–direction. S is the interface of the excited sleeper and the ballast. The factor 4 in F (Equation (5.11)) is introduced due to the two symmetry planes (2 for each symmetry plane). Also, the sleeper length L is introduced in Equation (5.10) to be compared with the measured result in Figure 5.21.

Figure 5.23 shows a comparison between the measured stiffness and the predicted stiffness. In terms of magnitude, the predicted stiffness is similar to the measured one above 100 Hz. The measured stiffness was assumed to be constant below 100 Hz, which is also found in the prediction. In the numerical prediction, the phase is close to $\pi/2$ above 200 Hz, which is similar to that of a damper and greater than the value found from the measurement. The reason for the discrepancies is unclear, as the details of the measurement are not provided.

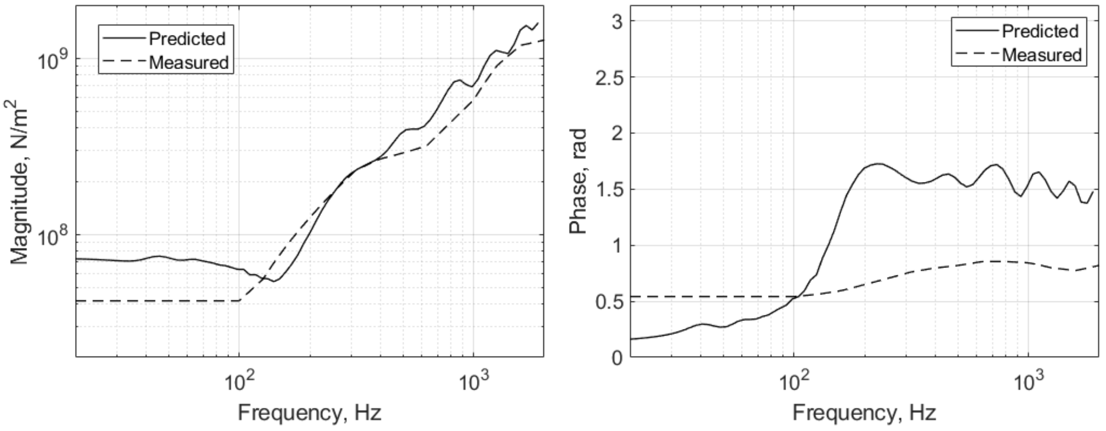

(a) (b)

Figure 5.23. Comparison of the measured stiffness and the predicted stiffness of ballast (normalised by the sleeper length): (a) magnitude and (b) phase; —— predicted, - - - measured

The asymptotic behaviour in Figure 5.23 can be seen as a spring–damper system. The region below 150 Hz is stiffness–controlled and above that is damping–controlled. In this context, the stiffness–like behaviour of the ballast and ground below 100 Hz will be affected by the stiffness of the underlying ground. For the current properties, the shear wave speed of the ground in the first row of Table 5.5 is 300 m/s, which is relatively stiff. To check this effect, the case with a soft ground has been considered. The properties of the ground are shown in the second row of Table 5.5. Compared with the properties in the first row, only the Young's modulus is quartered. This corresponds to the shear wave speed of 150 m/s, which is the same as the shear wave speed of the ballast (150 m/s).

Figure 5.24 shows the corresponding result. It is seen that the transition occurs at a lower frequency (around 40 Hz), due to the lowered stiffness. Also, the magnitude below 100 Hz becomes smaller, and closer to the measured stiffness. The damping–controlled region is not affected significantly, either in magnitude or phase. The results from the two different Young's moduli imply that the Young's modulus of the ground for the measurement would be in between these two values. Also, these results confirm that the measured data are reasonable.

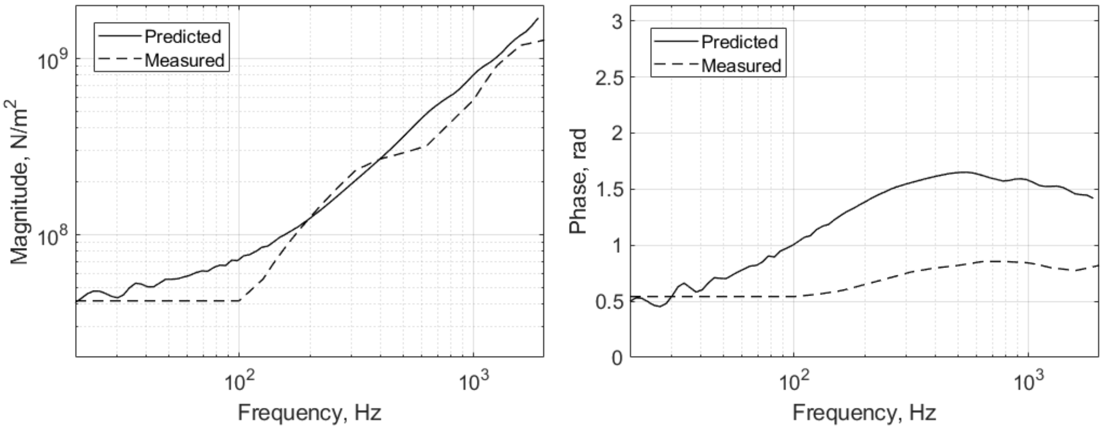

(a) (b)

Figure 5.24. Comparison of the measured stiffness and the predicted stiffness of ballast on soft ground: (a) magnitude and (b) phase; ━━ predicted, - - - measured

5.6 Summary

In this chapter, the behaviour of railway ballast has been studied using porous finite element models. In the first three sections it was shown that the extended reaction model is more appropriate to describe the behaviour of the ballast than a local reaction model, although the differences were quite modest. No clear difference was seen in the absorption of the ballast, compared with the measured data. The difference was more noticeable in the sleeper radiation case, where the extended reaction model showed better agreement with the measured data. Discrepancies still existed, including the effects of the sleeper modes. In the rail vertical vibration case, a slightly better agreement was found from the extended reaction model. The comparison for the lateral vibration case showed better agreement below 1 kHz. However, the overall comparison was inconclusive as neither numerical model showed a clear agreement with the measurement over the entire frequency range. This might be due to the conditions of the measurement.

An estimate of the sound radiation of the ballast has been calculated and compared with the sleeper noise. As it was not appropriate to use a 2.5D model, a 3D model in COMSOL has been used. Due to the limitation of the numerical model, the radiation from the air in the ballast pores has been neglected. A measurement was carried out in an attempt to determine the ballast properties, particularly the Poisson's ratio. From the comparison a value of 0.35 was determined for the Poisson's ratio, with the Young's modulus of 110 MPa. The sound radiation was calculated from the Rayleigh integral, using the surface vibration from the ballast and sleeper surfaces. The results showed that the ballast and the sleeper would vibrate in phase below 200 Hz. The stiffness of the ground affects the sound power radiated. However, the effect of the ballast on the sleeper noise radiation remains almost independent of the ground stiffness.

With the elastic properties obtained for the ballast, the ballast stiffness has been calculated, and compared with a measured frequency–dependent stiffness used in TWINS. A 3D COMSOL model has been used for calculating the stiffness. The model showed good agreement with the measured data in terms of magnitude. The predicted phase was different from the measured one, for which the reason is unclear. From the numerical result it was found that the ballast and ground behave as a damper above 100 Hz, showing the phase of around $\pi/2$.

Chapter 6

Experimental study of absorptive panels

Measurements in a laboratory have been carried out to study the effects of noise mitigation measures on the track noise radiation. Two measures are compared: a low–height noise barrier and absorptive panels. For the absorptive panels, porous rubber panels for which the absorption coefficients were measured were used in the measurement. The effects of individual measures are compared, and the effects of the combination of the two measures are also presented. A realistic overall insertion loss at full scale is estimated using a rolling noise spectrum calculated using TWINS. Also, the measured data are compared with results from the developed model.

6.1 Measurements

For the measurement, a 1:5 scale ballasted track was installed in an anechoic chamber (see Figure 6.1). A box–shaped car body made of foam and sealed with varnish has been set up above the track using wooden supports. The scale ballasted track and the car body were constructed by Lawrence [105] and Ratkevicius [106], respectively. Because the car body did not have bogies or wheels, the track and the car body were not in contact. Thus the car body is expected to introduce only geometrical effects. Wooden panels were laid on the floor to represent the ground, which is assumed to be acoustically rigid. The panels around the track were covered by tarpaulin sheets, to protect the floor of the chamber from the gravels and dust. The track is 2 m long and 0.8 m wide, and the train body is 2.5 m long with cross–sectional dimensions 0.56 × 0.45 m (width × height). The rail head is 0.26 m above the floor. The distance between the train floor and the rail head was set to 19 cm.

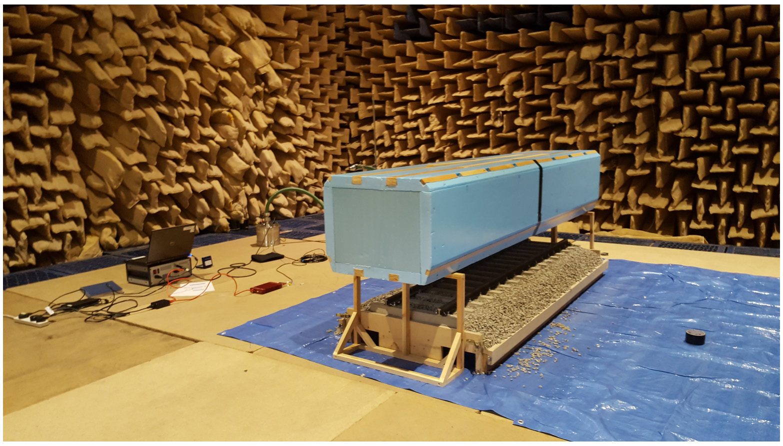

Figure 6.1. 1:5 scale track with train body set up in anechoic chamber

It was foreseen that direct excitation methods (impact hammer/shaker) would present some practical problems. A shaker is likely to radiate more noise than the rail itself as the scaled track is a relatively light structure. In addition to that, it might change the dynamic characteristics of the track. On the other hand, using an impact hammer would affect the sound propagation because the person who uses it is in close proximity to the track. For these reasons, a reciprocal approach has been used in the tests. This is shown schematically in Figure 6.2. The principle of reciprocity states that the transfer function between a point force $\tilde{F}$ acting on a structure at A and the resulting sound pressure $\tilde{p}$ at B is identical to the transfer function between the volume velocity $\tilde{Q}$ of a point monopole at B and the resulting vibration velocity $\tilde{v}$ at point A. The details about the method are given in [107].

In summary, if $\tilde{v}$ and $\tilde{Q}$ are measured, the ratio $\tilde{p}/\tilde{F}$ can be estimated from the measured data. However, as the measurement will be compared in terms of insertion loss, the measured velocity $\tilde{v}$ can be used alone provided that the source strength $\tilde{Q}$ does not change during the measurement. Figure 6.3 shows a diagram of the measurement setup. Three miniature PCB accelerometers were attached on the rail head, the web and the top surface of the sleeper to measure the vibration levels excited by the noise source, and the signals were collected by an FFT analyser. By the principle of reciprocity, this would be equivalent to measuring the sound pressure at the noise source position, which is caused by the vibration of the rail.

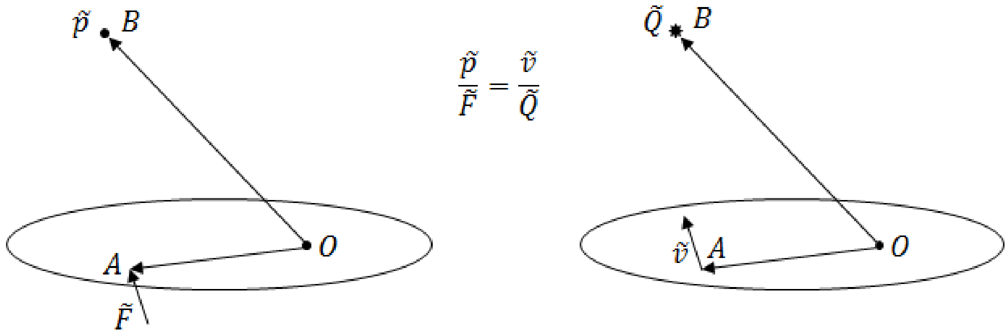

Figure 6.2. Principle of reciprocity used in the measurement

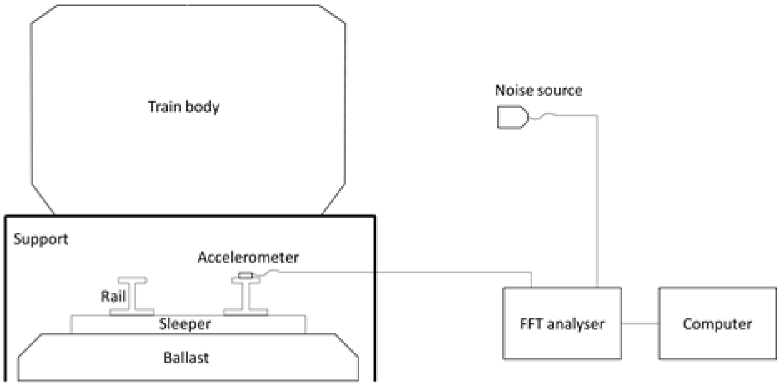

Figure 6.3. Diagram for reciprocal measurement in anechoic chamber

In the measurement a monopole–like loudspeaker consisting of a driver connected to a stiff hose has been used as the source (see Figure 6.4). The directivity of the loudspeaker has first been checked to ensure that the source acts as a monopole in the angles of interest. To verify its directivity the nozzle of the speaker was set 1.2 m above the floor, and the microphone (marked red in Figure 6.4(b)) was 1 m away from the speaker, at the same height. The angle was varied in the horizontal plane from $-90°$ to $90°$, in steps of $30°$. The angle is defined as in Figure 6.5(a). Figure 6.5(b) shows the sound pressure level measured by the microphone at each angle, in 1/3 octave bands. The background noise was also measured, and found to be below 20 dB re 2×10^{-5} Pa in all frequency bands. Below 5 kHz the results at different angles are quite close to each other to within 2 dB, whereas some deviations are observed at higher frequencies. Excluding $-90°$ and $90°$ shows differences of at most 2 dB between the signals over the whole frequency range. Thus the assumption that it behaves as a monopole is acceptable in the range from $-60°$ to $60°$.

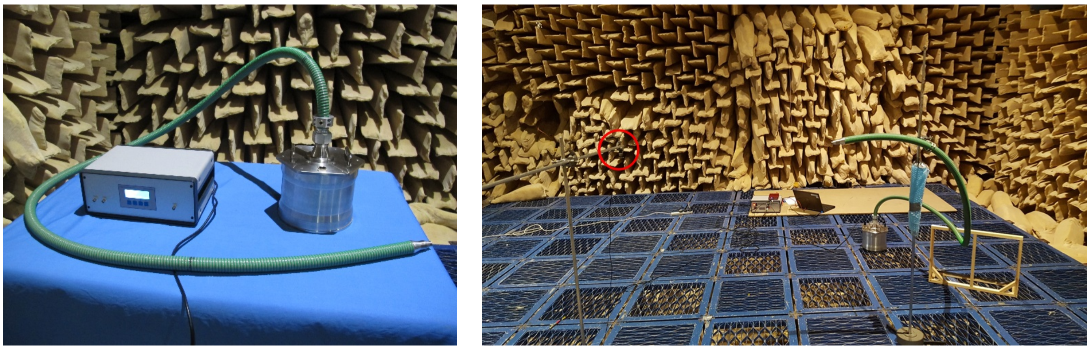

(a) (b)

Figure 6.4. Sound source directivity measurement: (a) loudspeaker and signal generator and (b) measurement setup (microphone marked with the red circle)

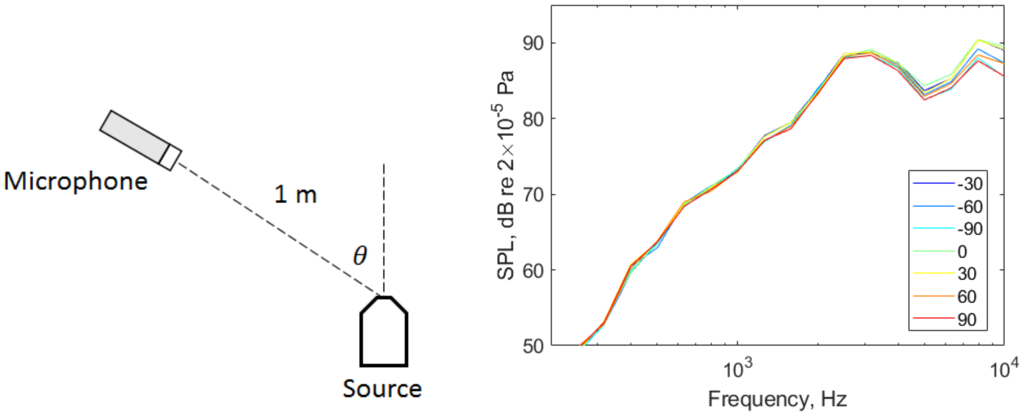

(a) (b)

Figure 6.5. Directivity measurement: (a) angle definition and (b) sound pressure level spectra at different angles

The source strength of the speaker has been measured to check if it is constant. This has been measured using an internal microphone installed inside the end of the hose. The results are shown in Figure 6.6. The legends are the angles of the microphone in Figure 6.5(a), hence irrelevant to the internal microphone. It is clearly seen that the source level is almost constant for each measurement. The source level was measured in all the subsequent measurements with the track and other materials, and was found to remain the same. It should be noted that the sound pressure level measured with the internal microphone is uncalibrated as the sensitivity was unknown and therefore not applied. However it is not necessary for the comparison.

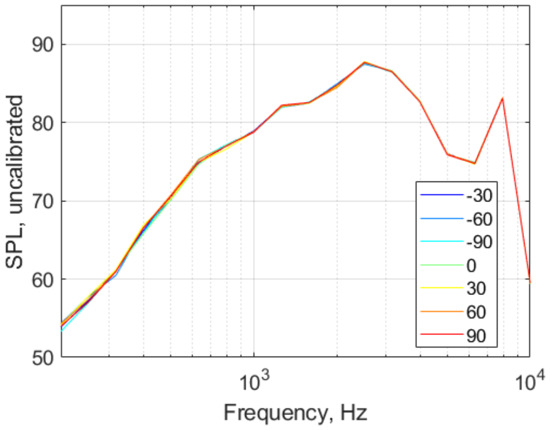

Figure 6.6. Sound pressure level measured by internal microphone (uncalibrated)

Figure 6.7 shows the accelerometers used in the measurement. The two accelerometers on the rail measure the vertical and lateral vibration of the rail, and the one on the sleeper near the rail seat measures the sleeper vertical vibration.

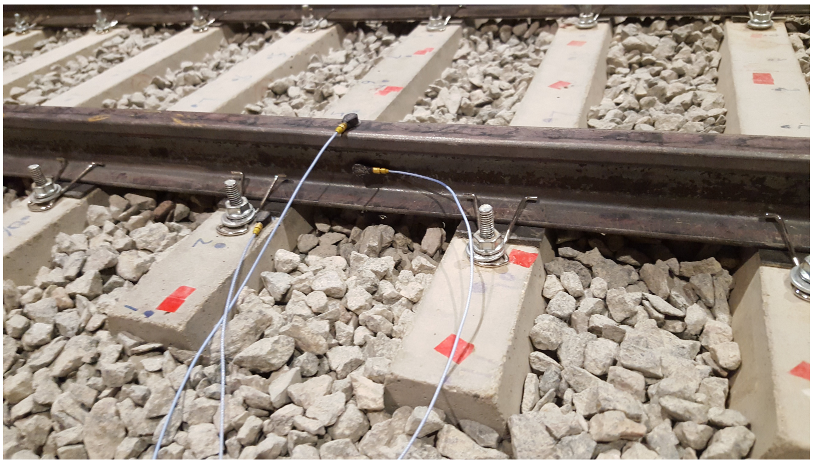

Figure 6.7. Accelerometer configuration

Some of the measurement configurations are shown in Figure 6.8. Figure 6.8(a) shows 2.2 cm thick absorptive rubber panels installed both between the rails and on the outer part of the sleepers. A low–height noise barrier made of pressed wood was installed alongside the enclosing wooden box (see Figure 6.8(b)). The thickness of the barrier is 0.5 cm, and the barrier top edge is 8 cm above the rail head and 40 cm away from the centre of the track. A close–up view of the rubber panel is shown in Figure 6.9. The dimensions of the measurement setup with the rubber panels and with the low height barrier are shown in Figure 6.10(a) and Figure 6.10(b), respectively. Note that in Figure 6.10(b) the repeated dimensions are omitted. The dimensions of the rail is given in Figure 5.9.

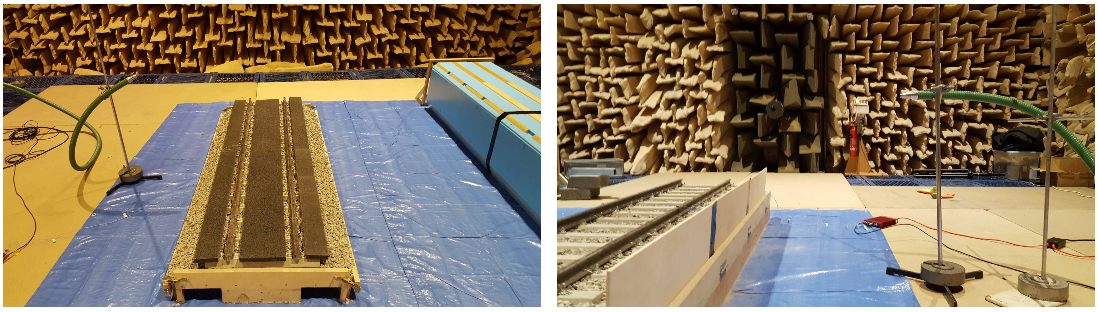

(a) (b)

Figure 6.8. Measurement setup with (a) absorptive panels and (b) low–height noise barrier

Figure 6.9. Close–up view of the rubber panel

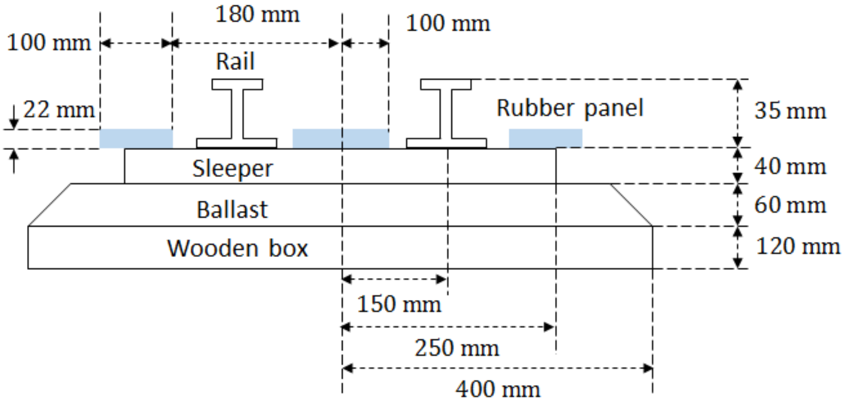

(a)

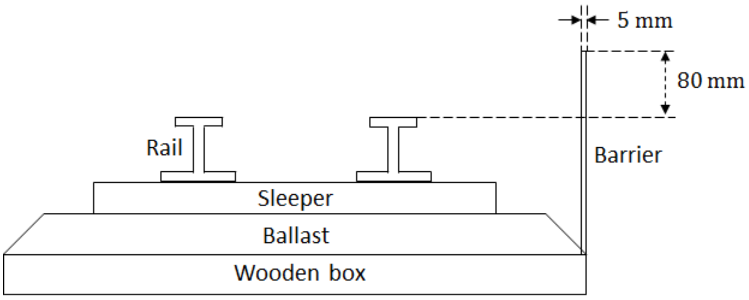

(b)

Figure 6.10. Dimensions of the measurement setups in Figure 6.8 (not to scale): setup with (a) absorptive panels and (b) low–height noise barrier

Again, to check the signal–to–noise ratio of measured signals from the accelerometers, the measured vibration levels were compared with the background noise level. Figure 6.11 shows the vibration levels when the source was 1 m from the centre of the track and 51 cm above the floor, in the presence of the car body. Here “T” means the track, “B” means the barrier, “R” means the rubber panels and “C” means the car body. For example, “TR” means the track with the rubber panels, which corresponds to Figure 6.8(b) although the car body was also present in Figure 6.11.

Clearly, the sleeper vibration level is close to the background noise level. Therefore it could not be measured reliably. In fact the sleeper vibration is expected to be low, due to the low rail pad stiffness, 8 MN/m [13]. This isolates the rail vibration from the sleepers from low frequencies. The results for the vertical and lateral vibration of the rail show that below 300 Hz the signals are almost the same as the background noise, but the signal–to–noise ratio increases as frequency increases. It can be said that the results are acceptable for frequencies above 1000 Hz with a signal–to–noise ratio of at least 2 dB. At full scale this corresponds to 200 Hz.

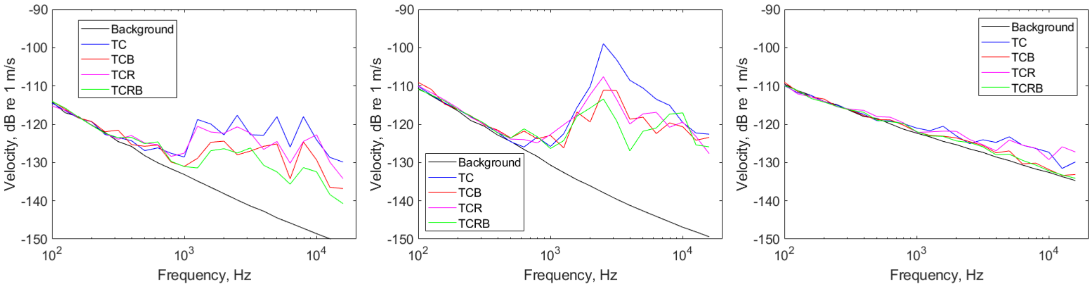

(a) (b) (c)

Figure 6.11. Signal–to–noise ratio of the measured vibration signals: (a) rail vertical, (b) rail lateral and (c) sleeper

6.2 Insertion loss of low–height noise barrier and absorptive panel

The insertion loss is calculated as

$$\mathrm{IL} = 20 \log_{10} \frac{p_0}{p_1} \tag{6.1}$$

where p_0 is the sound pressure at the receiver without the treatment and p_1 is the sound pressure in with the treatment. As in each case the source (rail vibration) is assumed to be the same, Equation (6.1) can be rewritten as

$$\mathrm{IL} = 20 \log_{10} \frac{p_0/F}{p_1/F} \tag{6.2}$$

where F is the force acting on the rail. By the principle of reciprocity (see Figure 6.2), this can be written as

$$\mathrm{IL} = 20 \log_{10} \frac{\tilde{v}_0/Q}{\tilde{v}_1/Q} \tag{6.3}$$

where $\tilde{v}_0$ is the reference velocity measured on the rail without the treatment and $\tilde{v}_1$ is the corresponding velocity with the treatment, in each case excited by the same acoustic source with source strength Q. Therefore the insertion loss can be obtained from the vibration level of the rail, with and without the treatment. As the source spectrum does not represent rolling noise, a sound pressure spectrum calculated using TWINS has been combined with the insertion loss spectrum to obtain an overall insertion loss. For this the parameters listed in Table 6.1 have been used the TWINS calculation. In other words, the measured insertion loss in 1/3 octave bands is subtracted from the TWINS sound pressure level (after applying the scaling factor to shift the frequencies). The resulting sound pressure spectrum is then summed. This would be the broadband sound pressure level with the treatment, and the difference between this and the original overall level is the overall insertion loss. In TWINS the rail radiation can be divided into vertical and lateral components. In this study they have been considered separately to obtain the overall insertion loss for each direction. As mentioned previously, the sleeper vibration was not included due to its low signal–to–noise ratio.

Table 6.1: Track parameters for vibration

Wheel parameters	
Wheel load (kN)	50
Wheel type	Korean metro wheel
Wheel radius (m)	0.43
Train speed (km/h)	101
Rail parameters	
Vertical bending stiffness (MNm^2)	4.32
Lateral bending stiffness (MNm^2)	0.73
Density (kg/m^3)	7850
Rail mass per unit length (kg/m)	50
Vertical and lateral shear coefficient	0.34
Rail vertical and lateral loss factor	0.02
Pad paramters	
Pad vertical stiffnesss (MN/m)	300
Pad lateral stiffness (MN/m)	50
Pad vertical and lateral loss factor	0.02
Sleeper parameters	
Sleeper mass (kg)	340
Sleeper Young's modulus (GPa)	41.3
Sleeper Poisson's ratio	0.15
Sleeper shear coefficient	0.83
Sleeper density (kg/m^3)	2750
Sleeper loss factor	0.02
Sleeper length (m)	2.4
Sleeper spacing (m)	0.6
Ballast parameters (per sleeper end)	
Ballast vertical stiffness (MN/m)	Measured (Figure 5.21(a))
Ballast lateral stiffness (MN/m)	40
Ballast vertical loss factor	Measured (phase shown in Figure 5.21(b))
Ballast lateral loss factor	0.5
Roughness	Measured (Figure 6.12)

In TWINS ballast stiffness can be set to be frequency–dependent, as dicussed in Chapter 5. The measured ballast vertical stiffness and loss factor in Section 5.5 have been used. Figure 6.12 shows the roughness measured on a ballasted track in Anyang, South Korea supplied by KRRI. This was combined with the roughness of a typical metro wheel with disc brakes. The combined roughness has been used as input to the TWINS calculation (see Figure 1.1). The ISO 3095:2013 limit for the rail roughness is also shown for reference (dotted line).

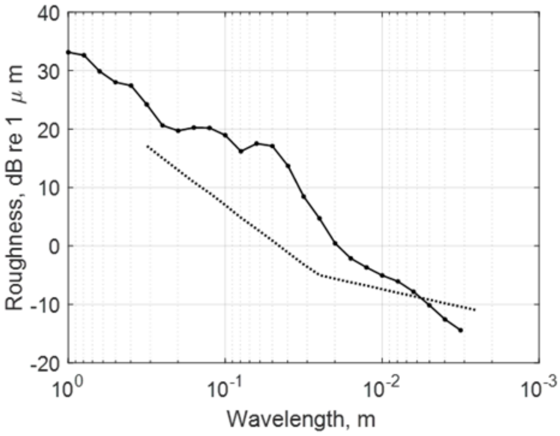

Figure 6.12. Roughness: (···) ISO 3095 limit for rail roughness, (–·–) measured rail roughness combined with wheel roughness

Four different source heights (or equivalent receiver heights) have been considered in the measurement: 30 cm, 43 cm, 51 cm and 70 cm above the floor (see Figure 6.13) which correspond to 4 cm, 17 cm, 25 cm and 44 cm. These are denoted by position 1, 2, 3 and 4 correspondingly. The equivalent positions at the full scale are also shown in Table 6.2. The lateral distance from the centre of the track is fixed to 1 m. The 43 cm position is on the same line as the ISO standard measured point (7.5 m, 1.2 m). It is also in the shadow zone when the barrier is included. On the other hand, the 51 cm and 70 cm positions are in the illuminated zone. In the TWINS calculations, the positions at full scale have been used. The corresponding lateral distance from the centre of the track is 5 m. The flow resistivity for the ground has been set to 100 MNs/m^4 to represent rigid ground and the height from the ground to the rail head has been set to 1.3 m, which is the height of the rail head in the measurement multiplied by the scale (0.26 m×5). The sound pressure level spectra for these positions are shown in Figure 6.14. Rail vertical and lateral noise components from the TWINS calculation have been considered separately, to obtain the insertion loss for both directions.

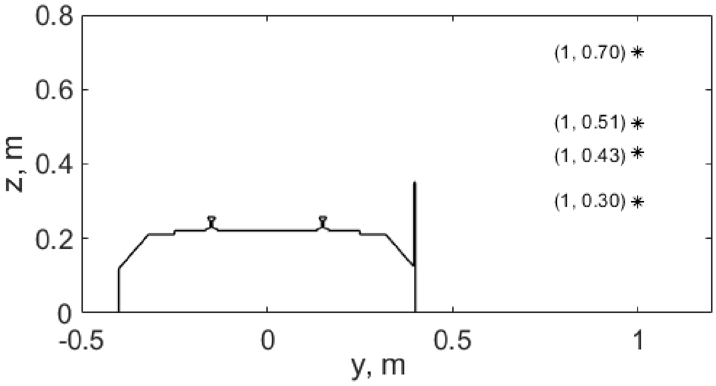

Figure 6.13. Equivalent receiver positions (positions of the loudspeaker in the measurement)

Table 6.2: Distance from the rail head to the receiver

Position	Measurement (cm)	Full scale (cm)
1	4	20
2	17	85
3	25	125
4	44	220

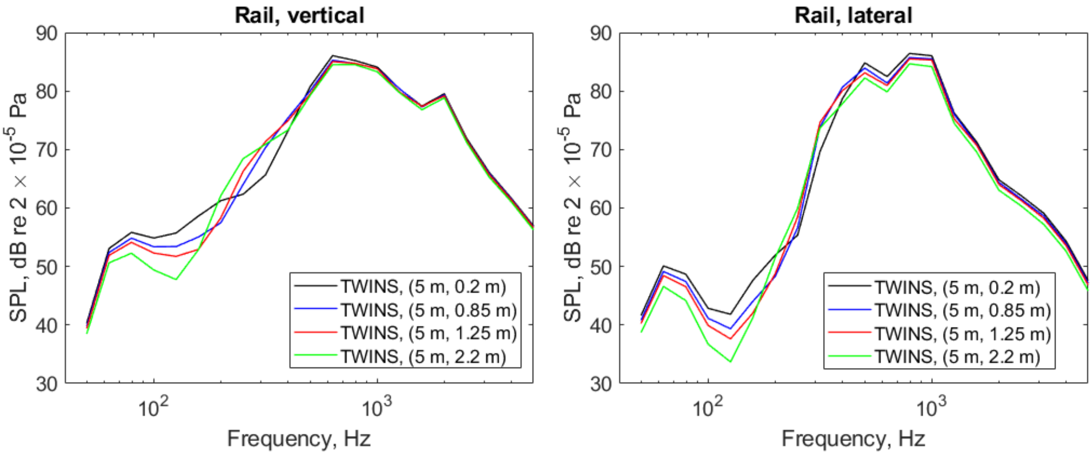

(a) (b)

Figure 6.14. Reference sound pressure level at different positions at full scale: rail (a) vertical and (b) lateral components from TWINS calculation; ▬ position 1 (5 m, 0.2 m), ▬ position 2 (5 m, 0.85 m), ▬ position 3 (5 m, 1.25 m), ▬ position 4 (5 m, 2.2 m)

The insertion loss for the vertical direction is calculated and plotted in Figure 6.15. These results are plotted against full scale frequencies. The overall insertion losses calculated using the above results are listed in the figure legend. Note that the TWINS results are used only for the calculation of the overall insertion loss, thus the shape of the insertion loss graphs in this section are not affected. The values are unweighted, but these will not be significantly different from A–weighted values as the rail noise is already very small at low frequencies. In all the results the barrier is more effective than the rubber panel. At position 1 (30 cm), the rubber panel has almost no effect when combined with the barrier, as the overall effect of it is −0.2 dB relative to that of the barrier only (see Figure 6.15(a)). On the other hand, at the other positions, the combination of the two measures leads to a larger insertion loss than either separately. No general tendency can be found from the graphs, due to various factors including the geometry and the floor condition. For example, the result at position 1 could have been affected by the ground reflection. Moreover the source was moved manually between each measurement, so a small change in the source position could have occured leading to differences in the spectrum. It was checked that the response of the middle of the rail is almost same as that of the next mid span.

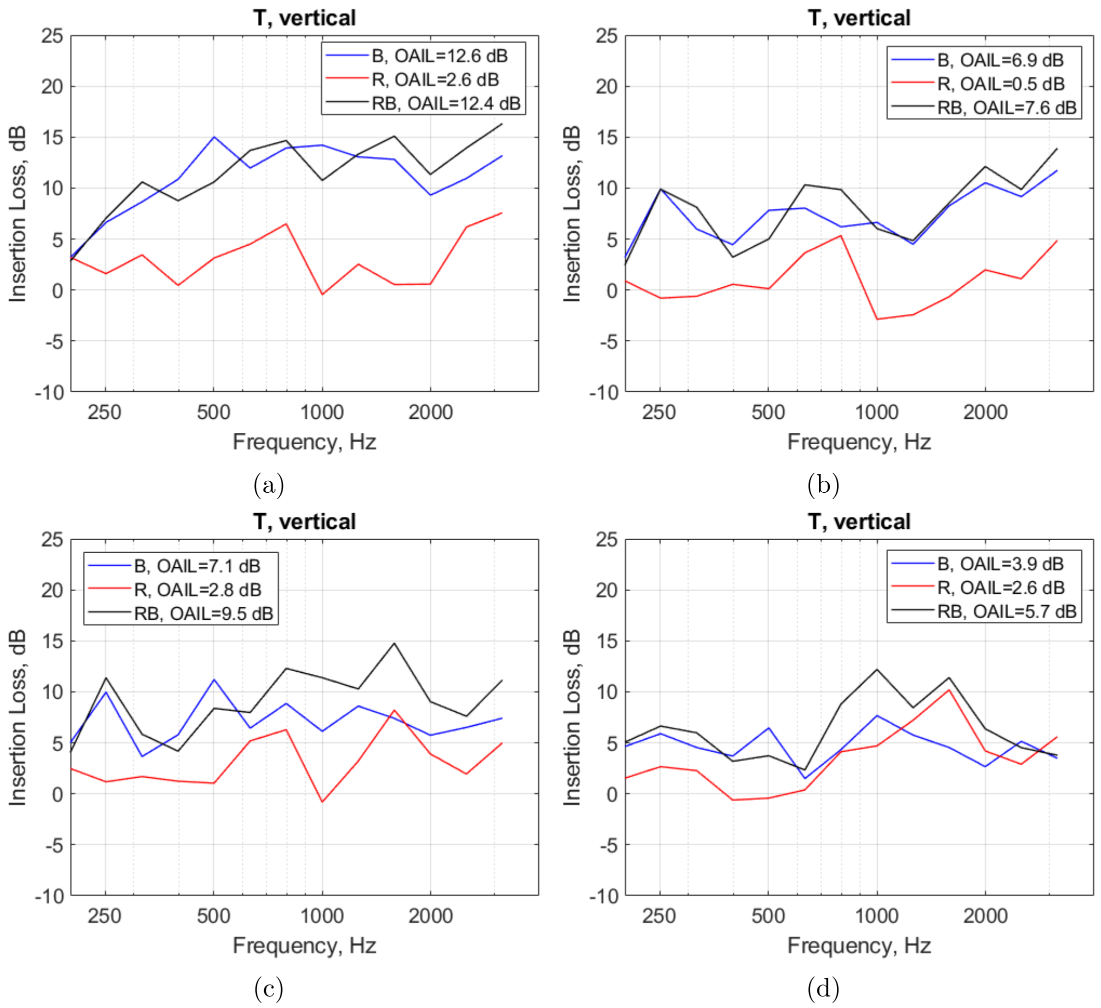

(a) (b)

(c) (d)

Figure 6.15. Insertion loss of different measures for vertical vibration of the rail without car body at different receiver heights: (a) 30 cm, (b) 43 cm, (c) 51 cm and (d) 70 cm (full scale frequencies); — barrier, — rubber panel, — barrier and rubber panel

The corresponding results for the lateral direction are shown in Figure 6.16. Different from the vertical direction, the case with the barrier and the rubber panels combined shows a higher insertion loss than with the barrier alone by 1–3 dB. Compared with the results for the vertical direction, it is observed that the insertion loss of the two measures is similar when the receiver position is higher. The rubber panel gives higher insertion losses than for the vertical direction.

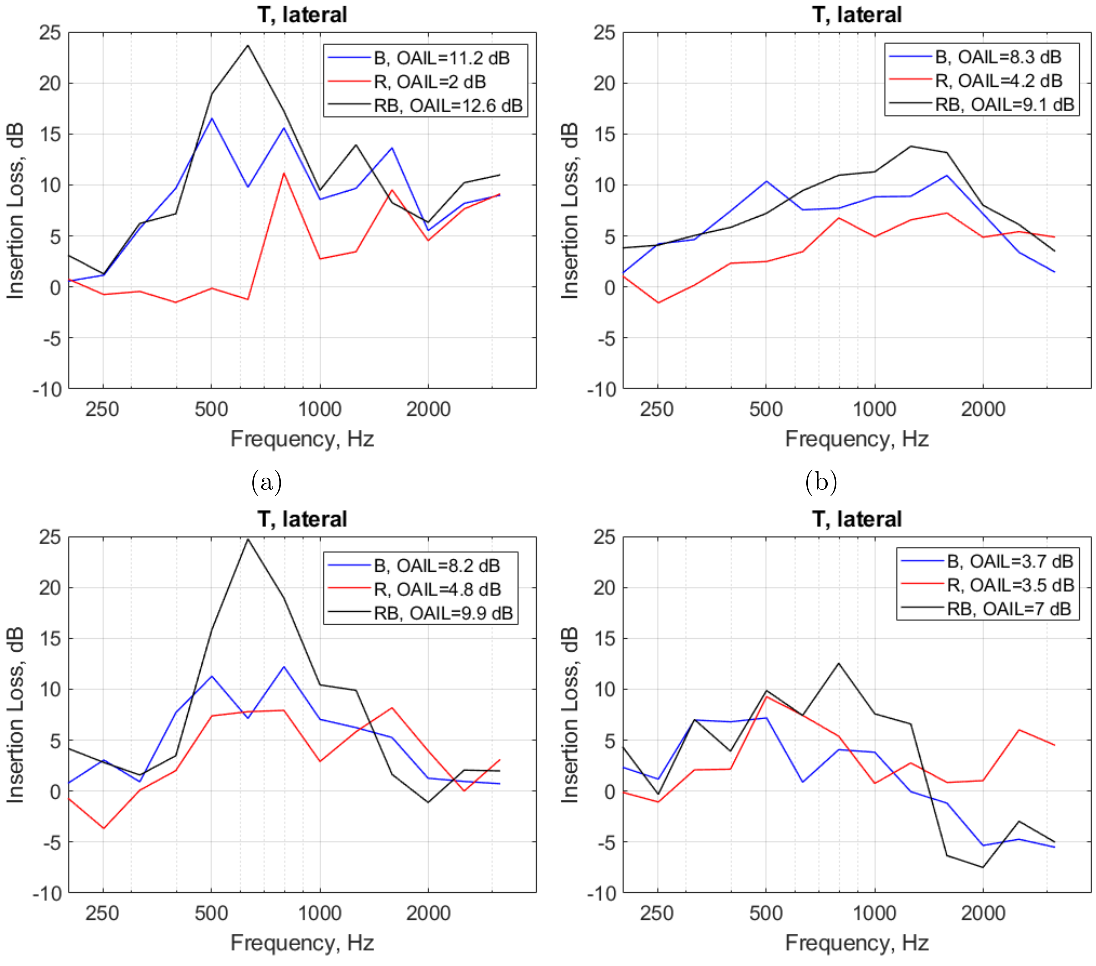

(a) (b) (c) (d)

Figure 6.16. Insertion loss of different measures for lateral vibration of the rail without car body at different receiver heights: (a) 30 cm, (b) 43 cm, (c) 51 cm and (d) 70 cm (full scale frequencies); — barrier, — rubber panel, — barrier and rubber panel

Figure 6.17 shows the results with the car body present at a height of 19 cm above the rail head. Again, the barrier is more effective than the rubber panel. Different from Figure 6.15, the overall insertion loss of the combination is always greater than that of the individual components. However, the overall insertion loss is smaller than that in Figure 6.15. This is due to increased reflections due to the presence of the car body.

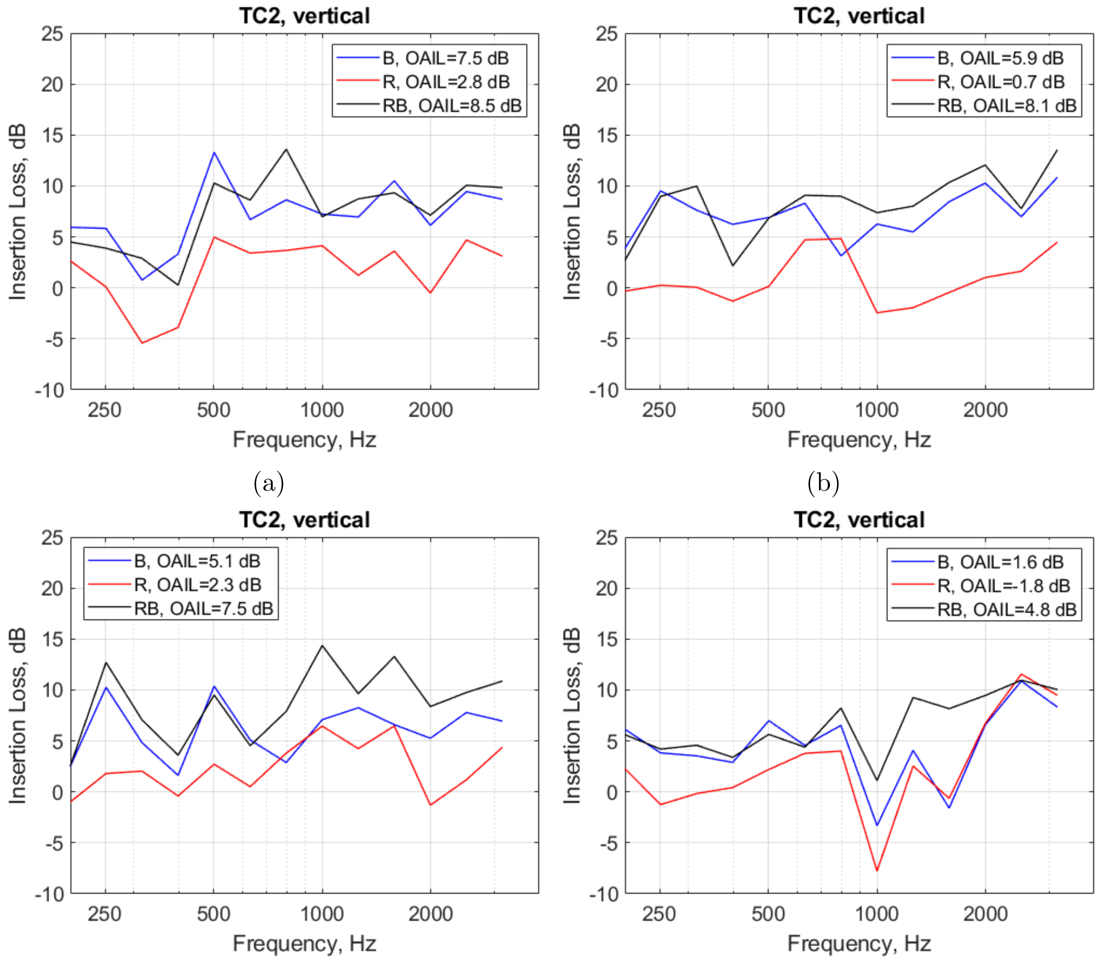

(a) (b)

(c) (d)

Figure 6.17. Insertion loss of different measures for vertical vibration of the rail in the presence of car body at different receiver heights: (a) 30 cm, (b) 43 cm, (c) 51 cm and (d) 70 cm (full scale frequencies); ━ barrier, ━ rubber panel, ━ barrier and rubber panel

The corresponding results for the lateral direction are plotted in Figure 6.18. Except for position 2 the overall insertion loss increases when the two measures are used together. At position 4 (70 cm) the overall insertion loss of each is negative, due to the negative values between 500 Hz and 1000 Hz where the sound pressure from TWINS is largest.

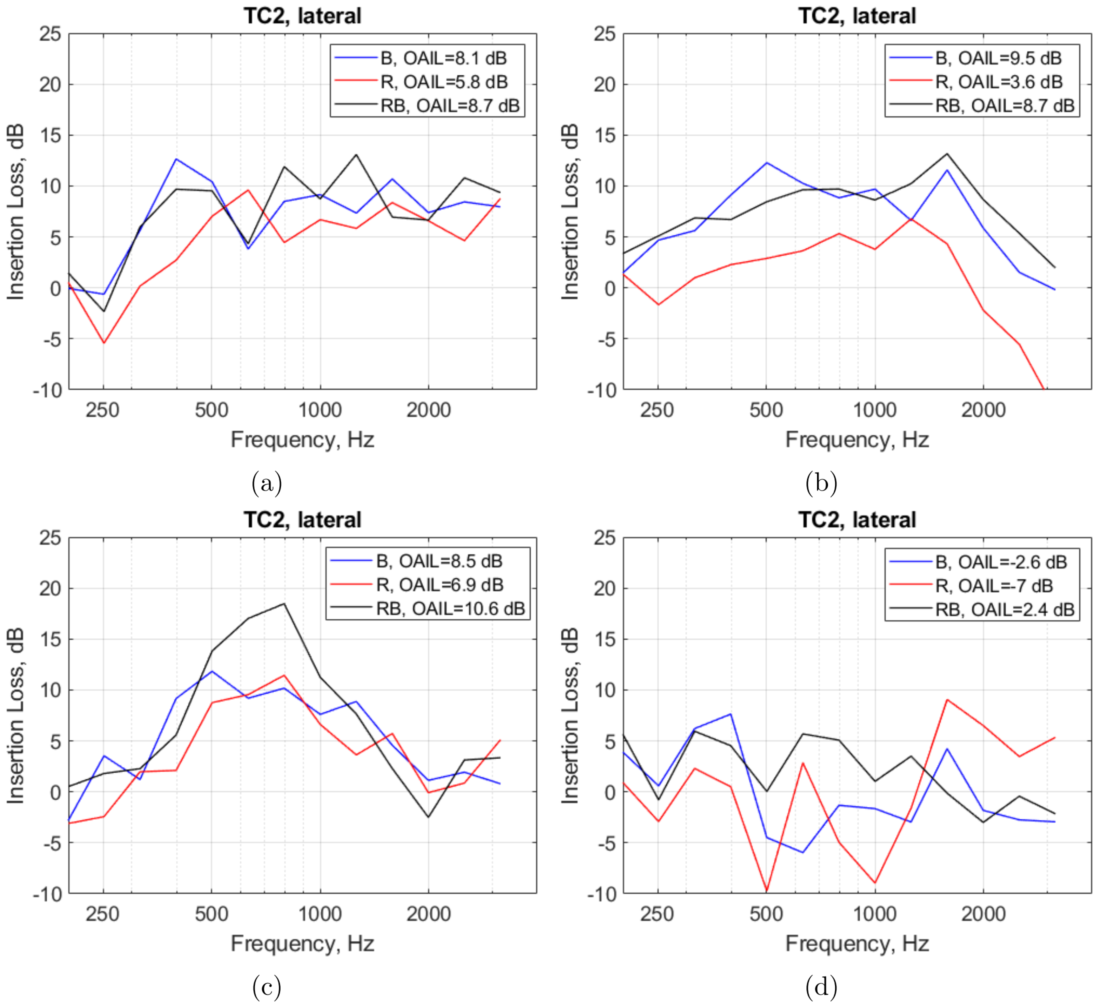

(a) (b)

(c) (d)

Figure 6.18. Insertion loss of different measures for lateral vibration of the rail in the presence of car body at different receiver heights: (a) 30 cm, (b) 43 cm, (c) 51 cm and (d) 70 cm (full scale frequencies); ▬ barrier, ▬ rubber panel, ▬ barrier and rubber panel

Although it is not easy to reach a general conclusion, one can say that the use of both absorptive panels and low–height barriers will help to reduce noise in most circumstances. It can also be said that the low–height noise barrier is more effective than the absorptive panels in the measurement. Note that it was applied to a ballast track which was already absorptive to some extent. Application on a slab track is expected to be more effective. In addition, this will be affected by their geometry as well as material properties. This may be explained by a parametric study.

6.3 Numerical model set-up

Geometries replicating the cases in the measurement have been made for numerical calculations using the boundary element method in 2.5D (see Figure 6.19). As the track has a periodic characteristic due to the sleepers, a 2.5D model cannot describe the exact sound radiation of the track. As a way of taking the periodicity into account, the simulation has been divided into two parts (see Figure 6.19(a) and (b), for example). One represents the track with sleepers (left column in Figure 6.19), and the other without them. Considering the sleeper spacing it was determined that 1/3 of the radiation is from the case with the sleeper section and the rest is from the case without it. Later it was found that at least for the insertion loss the ratio was not a critical factor, thus the suggested ratio has been used throughout. The ballast is modelled as an impedance surface using the Delany–Bazley–Miki model, having the flow resistivity of 280 Ns/m^4 [13]. The reason for using the local reaction model was to reduce the calculation time, thus it should be noted that the ballast absorption would be overestimated due to neglection of the porosity in the DBM model. The use of the DBM model was because the boundary element model did not have the JAC model. For the rubber panels, however, poro–elastic finite elements have been used (see Figure 6.19(e) and (f)) to study their effects accurately. The two vertical lines at the left and right ends ($y = -0.4$ m and $y = 0.4$ m) represent the enclosing box, which is rigid. The ground is rigid and modelled using a half space formulation in the boundary element model.

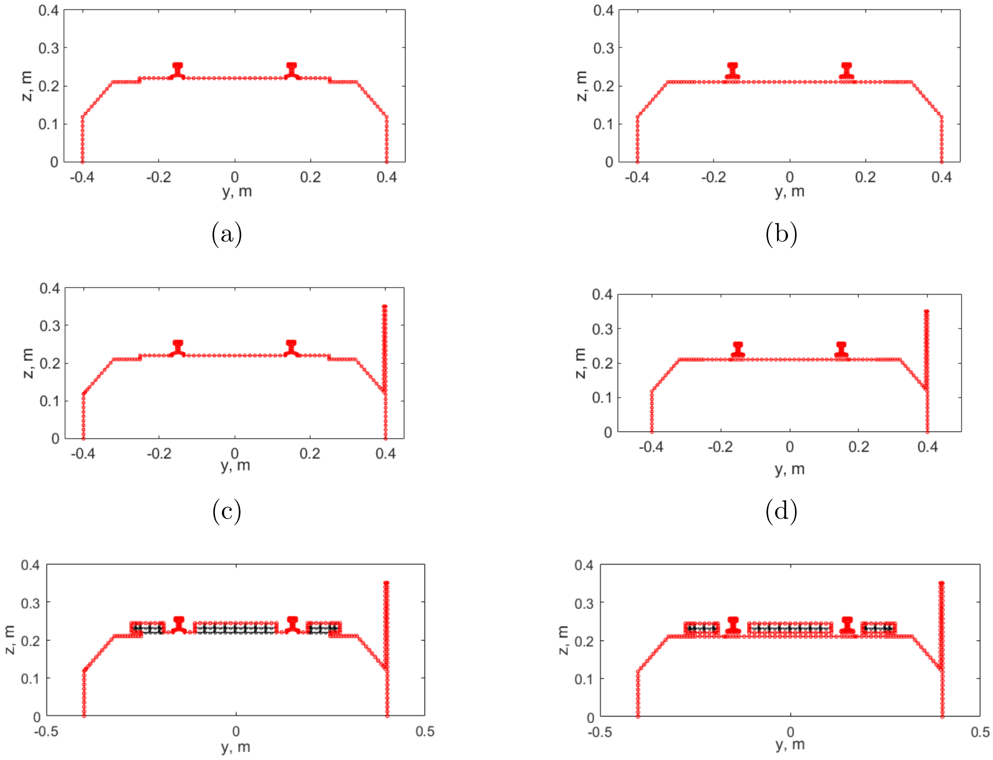

(a) (b)

(c) (d)

(e) (f)

Figure 6.19. Geometries for numerical calculation: (a) track, (c) track with barrier and (e) track with absorptive panel ((b), (d) and (f) represent the same case respectively without the sleeper); — boundary elements, — poro–elastic finite elements

For the excitation, the rail vertical mobility has been used as a boundary condition at the top in the middle of the right–hand rail. The mobility has been calculated using the track model in TWINS, with the parameters in Table 6.1. This will provide results corresponding to a point force excitation. Figure 6.20 shows the mobility at 2000 Hz, for example. The receiver positions are set to be the same as those in Figure 6.13. Note that the wavenumber range considered is from $-1.4k_0$ to $1.4k_0$ where k_0 is the acoustic wavenumber. Outside this range the contribution can be considered negligible in the sound radiation to the far field.

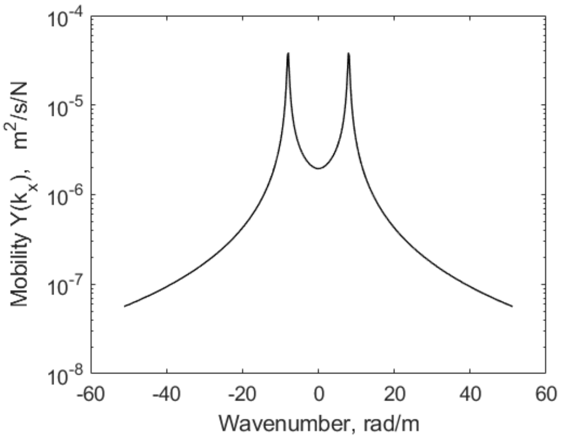

Figure 6.20. Magnitude of rail mobility in the wavenumber domain at 2000 Hz

6.3.1 Characterisation of the rubber panel

In Figure 6.19(e) and (f) the absorptive panel has been modelled using poro–elastic finite elements. As its properties were unknown, the absorption coefficient previously measured from an impedance tube has been used to inversely characterise the properties of saturated fluid. Figure 6.21 shows the measured absorption coefficients of the rubber panel for three different thicknesses[1]: 46 mm, 63 mm and 73 mm. The 73 mm result has been used for curve fitting, as the thickest sample is expected to give the most reliable result. For the optimisation the Matlab routine “lsqnonlin” has been used, combined with the transfer matrix method to obtain the absorption coefficient. The initial parameters and their range are shown in Table 6.3. ϕ is the porosity, σ is the flow resistivity, α_∞ is the tortuosity, Λ is the viscous characteristic length and Λ' is the thermal characteristic length.

---

[1] The measured data was provided by Martin Toward, ISVR Consulting

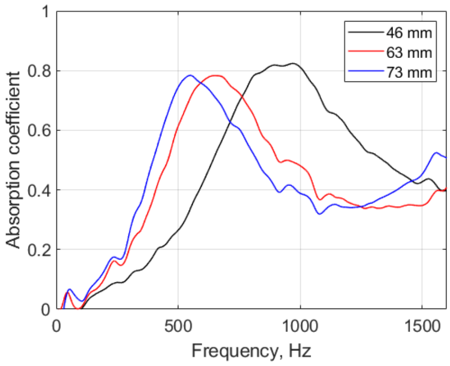

Figure 6.21. Measured absorption coefficient of rubber panel for normal incidence, for different thicknesses: ▬ 46 mm, ▬ 63 mm, ▬ 73 mm (data provided by Martin Toward, ISVR Consulting)

TABLE 6.3: Parameters used for optimisation of absorption coefficient of 73 mm thick rubber sample

Property	ϕ	σ (Ns/m^4)	α_∞	Λ (mm)	Λ' (mm)
Base (q_0)	0.5	5000	3.2	0.24	0.36
Min ($q_{\min}$)	0.1	2000	1.0	0.01	0.15
Max ($q_{\max}$)	0.8	80000	4.8	3.00	4.50

The result is shown in Figure 6.22. The blue line is the measured value, the thick pink line is the initial result and the thin pink line is the optimised result. It is observed that the optimised curve agrees well with the measured data. The optimised parameters are given in Table 6.4.

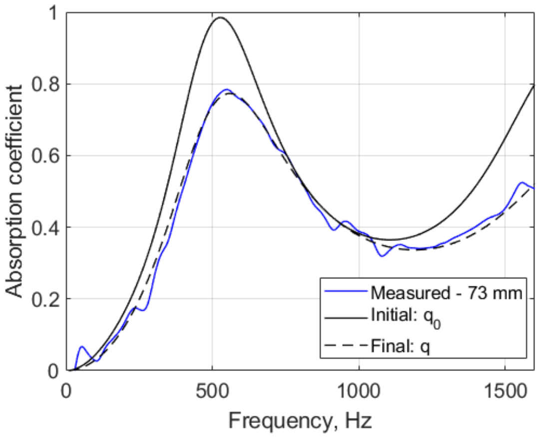

Figure 6.22. Comparison of absorption coefficient of for 73 mm thick rubber sample: ▬ predicted with initial parameters, ▬ measured, - - - predicted with optimised parameters

Table 6.4: Optimised parameters of saturated fluid of porous rubber

Property	ϕ	σ (Ns/m^4)	α_∞	Λ (mm)	Λ' (mm)
Optimised (q)	0.31	22650	2.6	0.17	0.21

Using the optimised parameters, the absorption coefficient for the other thicknesses has been predicted and compared with the measured data, as shown in Figure 6.23. The calculated results agree well with the measured values. From these results it can be said that the obtained parameters are valid.

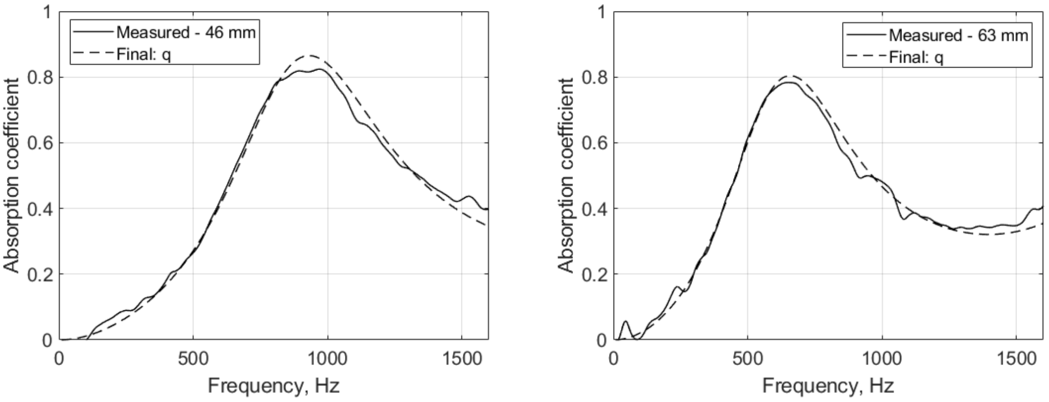

(a) (b)

Figure 6.23. Comparison of absorption coefficient for other thicknesses with the optimised parameters: (a) 46 mm and (b) 63 mm (reduced scale frequencies); — measured, - - - predicted with the optimised parameters

The elastic properties have not been determined. Therefore the frame of the material is assumed to be rigid and the model used here should rather be called poro–rigid.

6.4 Comparison results

6.4.1 Insertion loss of the barrier

Figure 6.24 shows the insertion loss of the barrier for the track in the presence of the rigid ground, in 1/12 octave bands. Results are shown from a 2D BE model as well as the 2.5D model. For the cases (a)–(d), the RMS errors of the 2.5D prediction are 5.7 dB, 3.2 dB, 4.1 dB and 3.4 dB. The discrepancies could be due to small changes in the measurement positions. Also, the result at point 1 might have been affected more by the floor, which is another uncertainty in the measurement. The results from the 2D calculation have a slightly bigger magnitude than the 2.5D results.

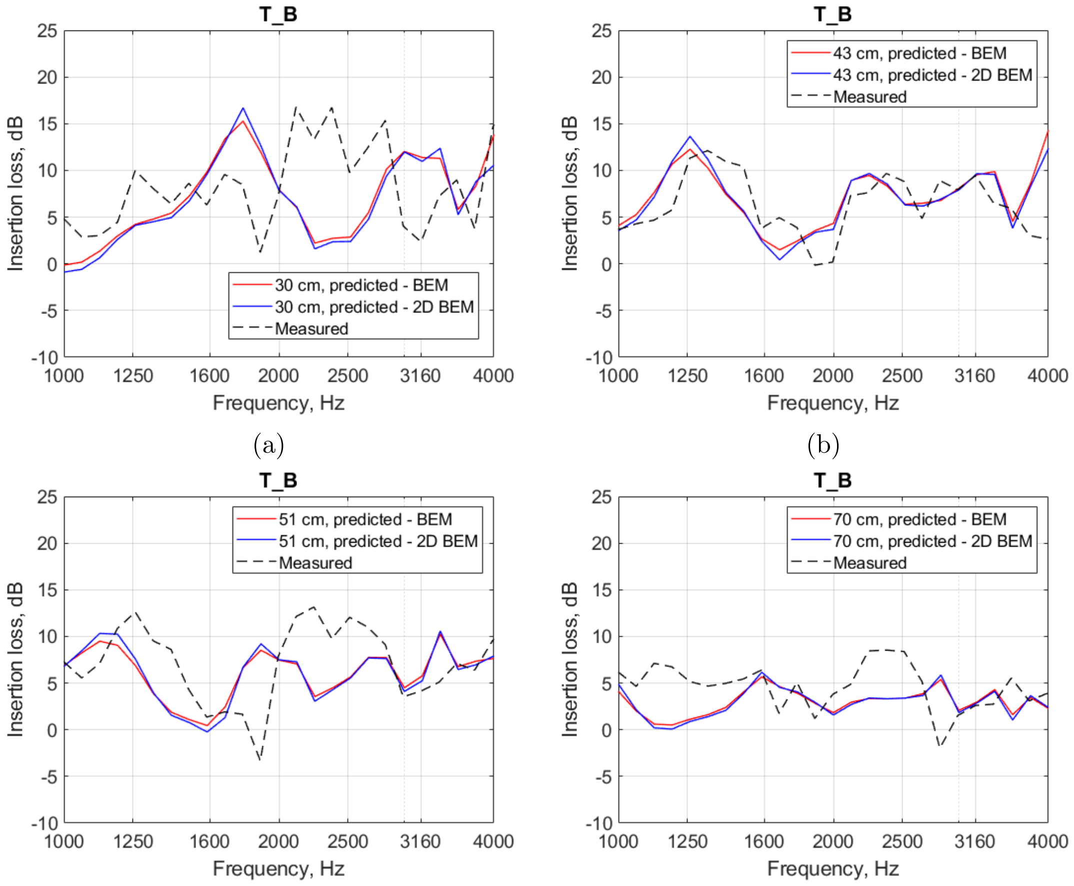

(a) (b)

(c) (d)

Figure 6.24. Comparison of the insertion loss of the low–height barrier for vertical vibration of the rail at different receiver heights: (a) 30 cm, (b) 43 cm, (c) 51 cm and (d) 70 cm (reduced scale frequencies); — calculated (2.5D, boundary element model), — calculated (2D, boundary element model), - - - measured

The case with the car body has also been considered and the results are shown in Figure 6.25. In this case, the RMS errors are of the 2.5D prediction are 8.7 dB, 3.4 dB, 5.7 dB and 4.5 dB for the cases (a)–(d). At position 1 a large discrepancy is found in the location of the peak, for which the reason is unclear.

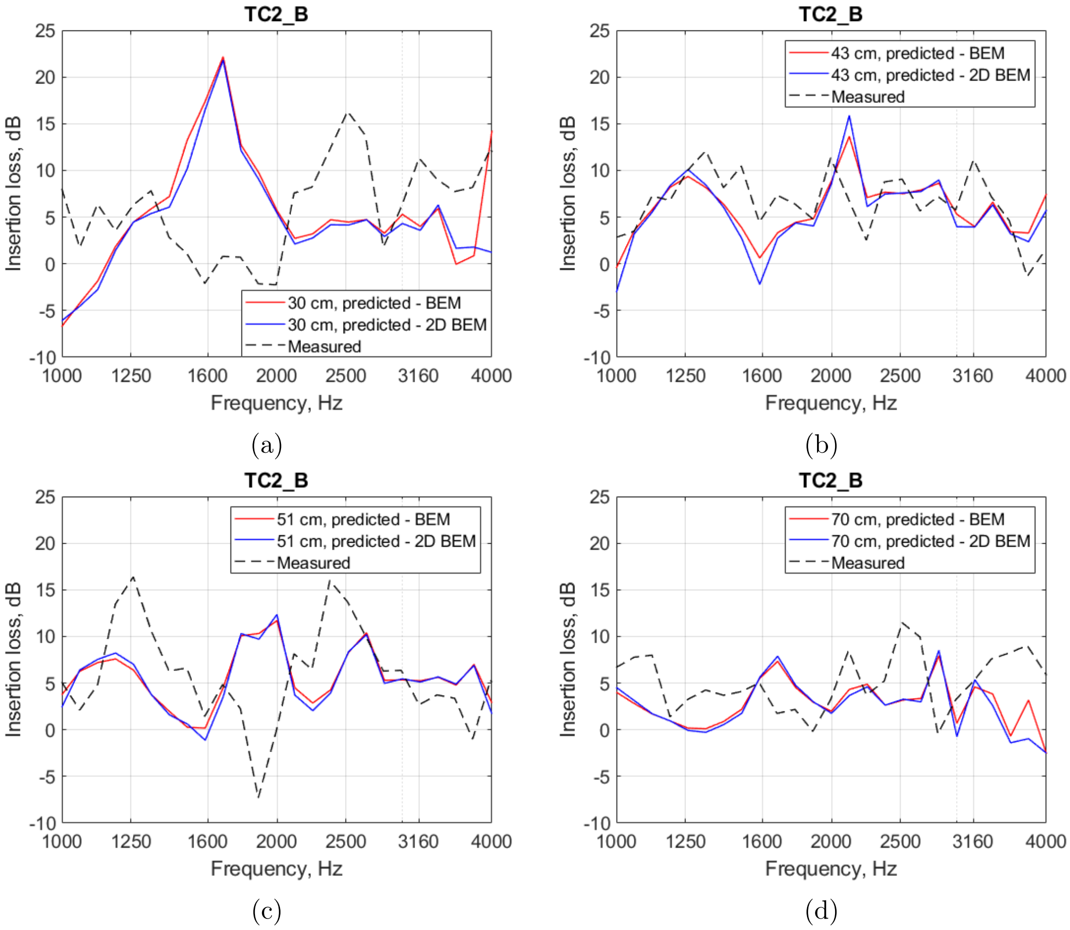

(a) (b)

(c) (d)

Figure 6.25. Comparison of the insertion loss of the low–height barrier for vertical vibration of the rail in the presence of car body at different receiver heights: (a) 30 cm, (b) 43 cm, (c) 51 cm and (d) 70 cm (reduced scale frequencies); ▬ calculated (2.5D boundary element model), ▬ calculated (2D boundary element model), - - - measured

6.4.2 Insertion loss of the absorptive rubber panel

The insertion loss of the rubber panel on the noise from the rail at different receiver positions is shown in Figure 6.26 for the same receiver locations. Overall, the calculated values are smaller than the measured ones. Also, the simulation shows that the insertion loss is often negative for this rubber panel. The RMS errors of the 2.5D prediction are 4 dB, 2.4 dB, 3.6 dB and 3.7 dB for the cases (a)–(d). Figure 6.27 shows the results with the inclusion of the car body, which gives the RMS errors of 4.4 dB, 3.0 dB, 3.5 dB and 4.3 dB for the cases (a)–(d). Still, the insertion loss is around 0 dB at all frequencies.

As a way of investigating why the inclusion of the rubber panel resulted in a negative insertion loss, the absorption coefficients of the ballast and the rubber panel have been compared. The properties for the 1:5 scale ballast in Chapter 5 have been used. The results are shown in Figure 6.28. For the calculation of the absorption coefficient the transfer matrix method has been used with the JAC model. In this case the layer thicknesses are 92 mm for the ballast and 22 mm for the rubber panel.

From Figure 6.28(a) it is clear that the ballast is more absorptive than the rubber panels, except at frequencies around 2 kHz. Similar behaviour is observed in Figure 6.28(b), which is for oblique incidence at 71°. This angle is chosen to correspond to receiver 3. However, the angle could vary with the positions of the source and the absorbing surface. The oblique incidence result shows that the rubber panel is less effective than the ballast at most frequencies. As the oblique incidence is mostly applicable in the calculation, this is expected to cause a broad decrease in the insertion loss. On the other hand the rubber panels can provide some shielding, at least for lateral vibration of the rail.

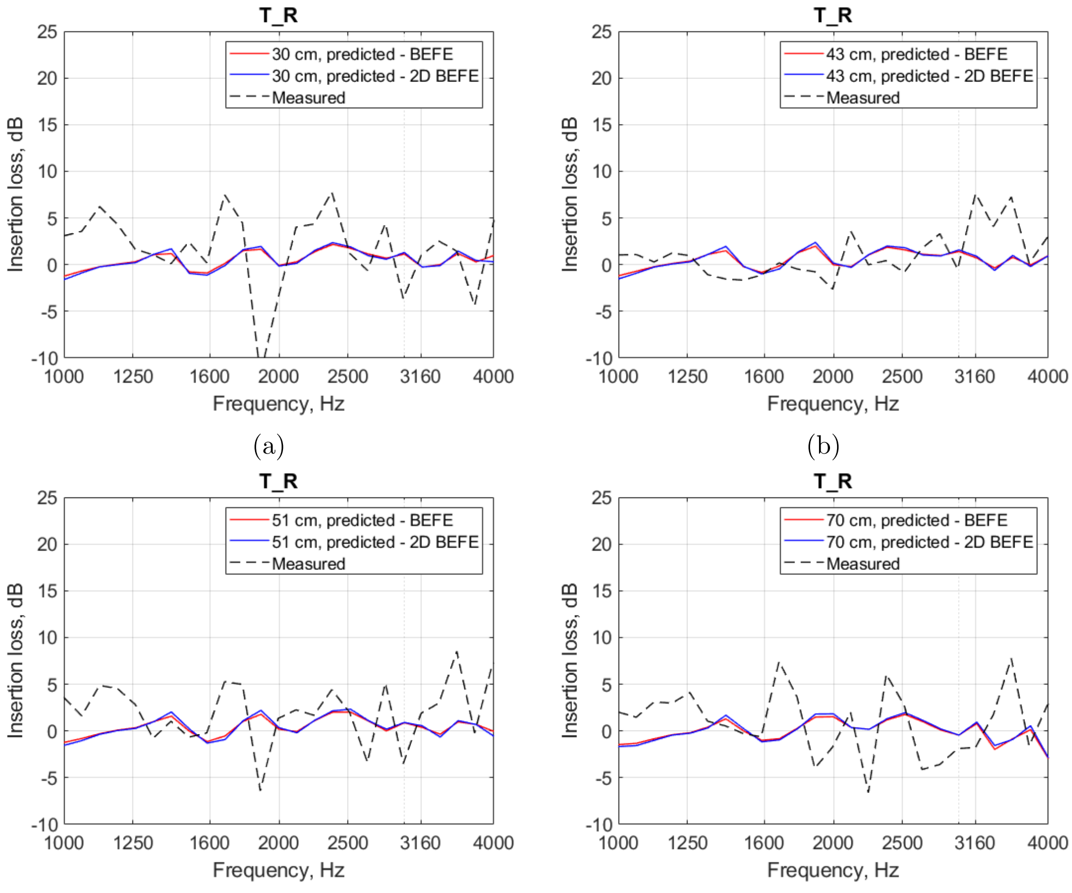

(a) (b)

(c) (d)

Figure 6.26. Comparison of the insertion loss of the absorptive rubber panel for vertical vibration of the rail at different receiver heights: (a) 30 cm, (b) 43 cm, (c) 51 cm and (d) 70 cm (reduced scale frequencies); ▬ calculated (2.5D boundary element and poro–elastic finite element model), ▬ calculated (2D boundary element and poro–elastic finite element model), - - - measured

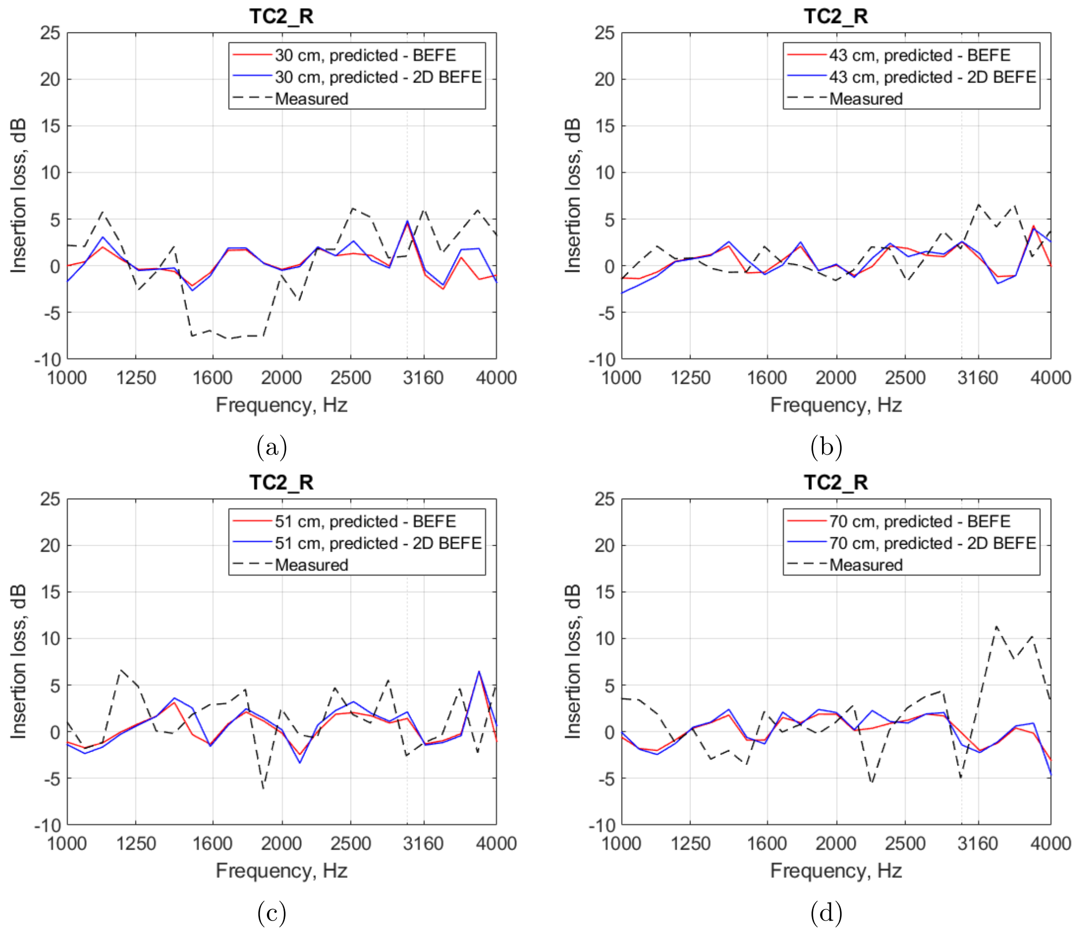

(a) (b)

(c) (d)

Figure 6.27. Comparison of the insertion loss of the absorptive rubber panel for vertical vibration of the rail in the presence of car body at different receiver heights: (a) 30 cm, (b) 43 cm, (c) 51 cm and (d) 70 cm (reduced scale frequencies); ▬ calculated (2.5D boundary element and poro–elastic finite element model), ▬ calculated (2D boundary element and poro–elastic finite element model), - - - measured

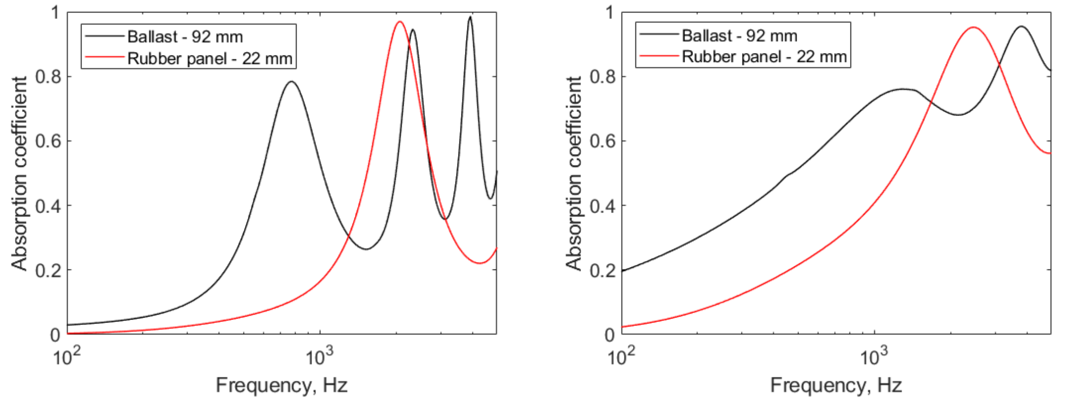

(a) (b)

Figure 6.28. Comparison of predicted absorption coefficients of ballast and rubber panel calculated using the JAC model (TMM, extended reaction): (a) normal incidence and (b) oblique incidence at 71°; ▬ ballast, ▬ rubber panel

6.4.3 Insertion loss of the barrier and absorptive rubber panel

Figures 6.29 and 6.30 show the insertion loss of the two measures combined. The values are mostly underestimated compared with the measurement. These results are also smaller than the insertion loss of the barrier alone, suggesting that the rubber panel lessens the effect of the barrier. The RMS errors are 5.9 dB, 4.0 dB, 5.1 dB and 4.5 dB for the cases (a)–(d). Again the simulation results seem to be valid particularly for the position close to the line where the ISO standard position lies (see Figure 6.29(b)).

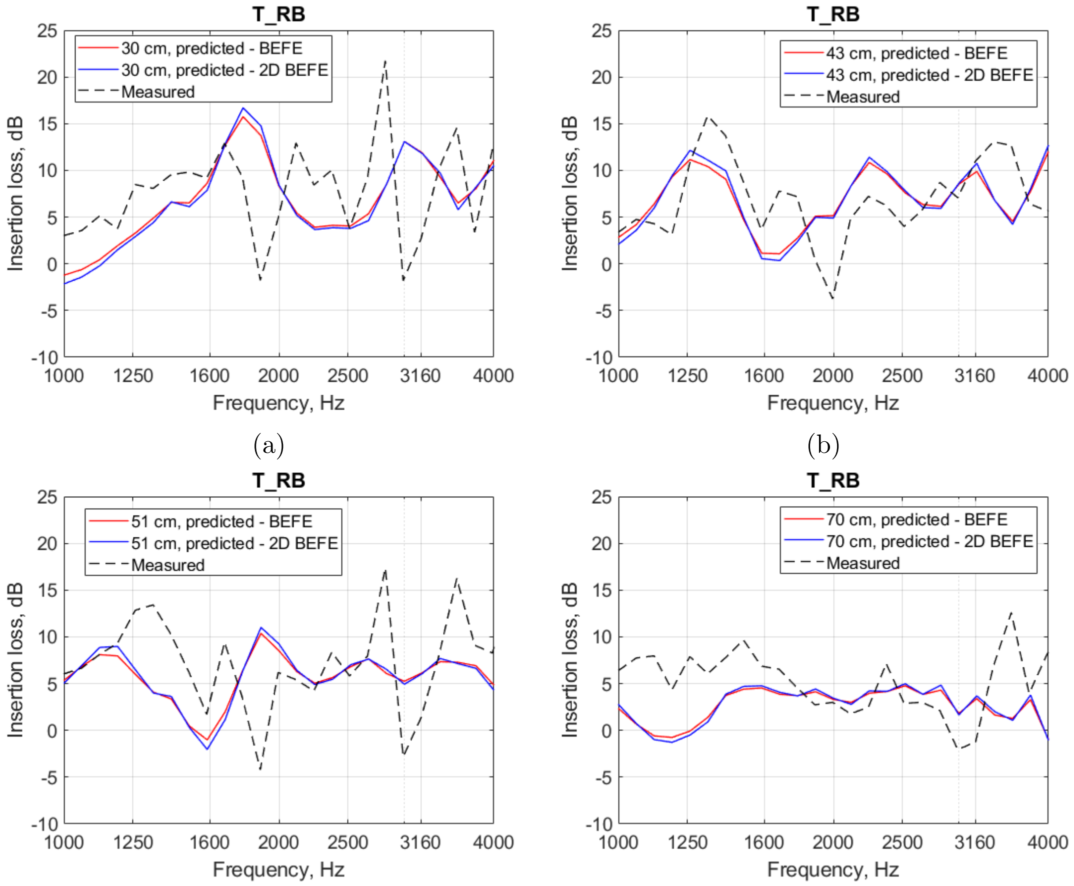

(a) (b)

(c) (d)

Figure 6.29. Comparison of the insertion loss of the barrier and absorptive rubber panel for vertical vibration of the rail at different receiver heights: (a) 30 cm, (b) 43 cm, (c) 51 cm and (d) 70 cm (reduced scale frequencies); — calculated (2.5D boundary element and poro–elastic finite element model), — calculated (2D boundary element and poro–elastic finite element model), - - - measured

Figure 6.30 shows the case with the car body. Again a large peak at around 1700 Hz is seen. This might be due to the barrier and the car body (see also Figure 6.25(a)). The RMS errors for the cases (a)–(d) are 8.2 dB, 4.5 dB, 6.2 dB and 4.7 dB.

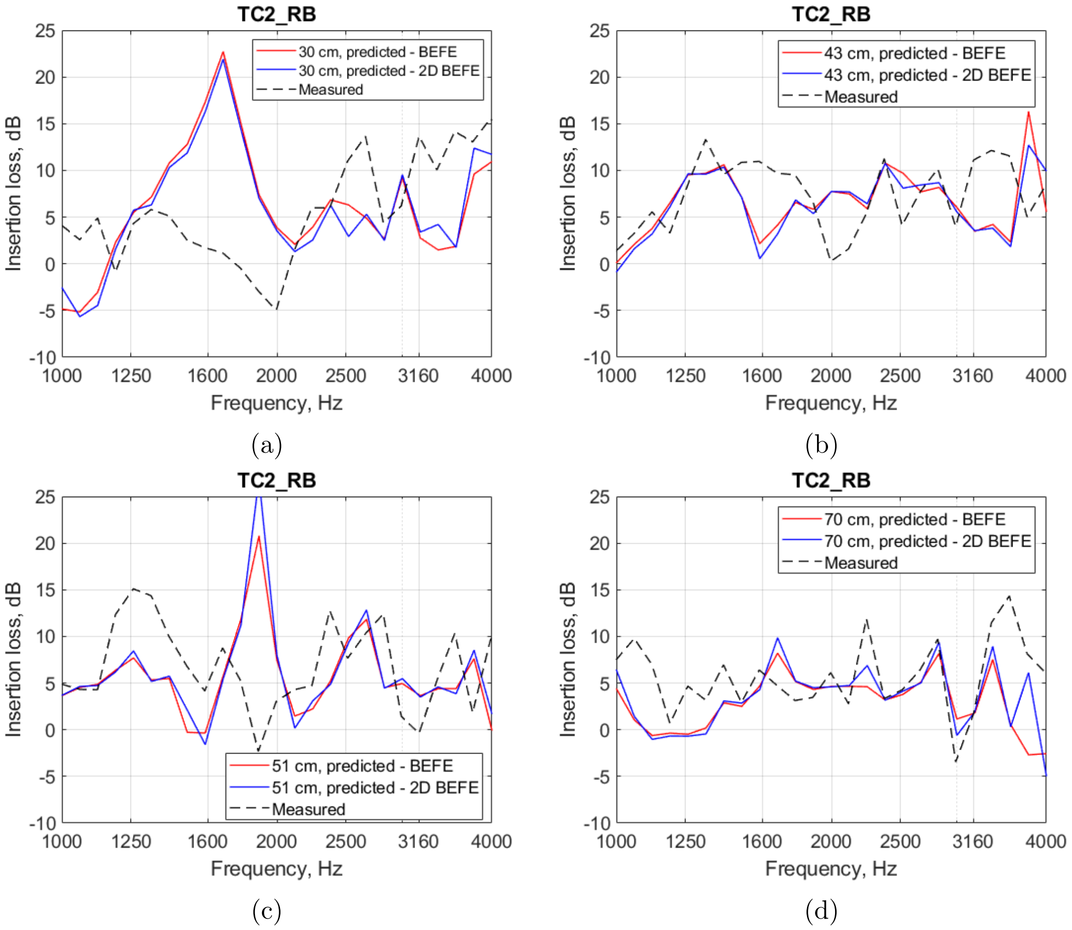

(a) (b)

(c) (d)

Figure 6.30. Comparison of the insertion loss of the barrier and absorptive rubber panel for vertical vibration of the rail in the presence of car body at different receiver heights: (a) 30 cm, (b) 43 cm, (c) 51 cm and (d) 70 cm (reduced scale frequencies); — calculated (2.5D boundary element and poro–elastic finite element model), — calculated (2D boundary element and poro–elastic finite element model), - - - measured

6.5 Summary

A laboratory measurement has been conducted to validate the numerical model and to study the effect of low–height noise barriers and absorptive panels on the track noise radiation. The measurements showed that the low–height barrier is much more effective than the absorptive panel, and the combination of the two gives the best result in most cases. The effect is decreased when the car body is included, because the car body itself reflects sound over the barrier. The simulation results showed moderate agreement with the measurements, with an RMS error ranging from 3 dB to 9 dB. The absorptive panel used in the measurement was found not to be effective from the simulation. It should be noted that the ballasted track was already absorptive to some extent. Thus the absorptive panel would be more effective when applied on a slab track. This would also be improved by increasing the thickness of the panel.

Chapter 7

Performance of absorptive treatments at full scale

As stated in the literature review, noise barriers are a relatively simple solution to implement in reality to reduce railway noise. They can be more cost–effective when installed in close proximity to the track, or by adding a layer of porous material. This study is focused on the latter; therefore it will investigate how effective porous materials can be when installed on low–height barriers.

Another type of absorptive treatment is the use of absorptive blocks on slab track (see Figure 1.2). They have advantages over noise barriers because they are easier to install on the track and are not visually intrusive. Absorptive blocks can potentially be more cost–effective than noise barriers as they are installed much closer to the source, although the shielding effect will be limited due to a limited height of the blocks. These effects will be quantified and discussed.

7.1 Barrier and materials

An example geometry of a low-height barrier is shown in Figure 7.1 and the porous materials used in the barrier are shown in Figure 7.2. The materials were chosen and provided by Korea Railroad Research Institute. The number on the top in the pictures indicates the bulk density of the material. For example, '40K' means the bulk density of 40 kg/m^3. They are both made of polyester. The red arrows in Figure 7.1 represent the direction of sound waves propagating from a sound source to show in which order the barrier layers should be installed.

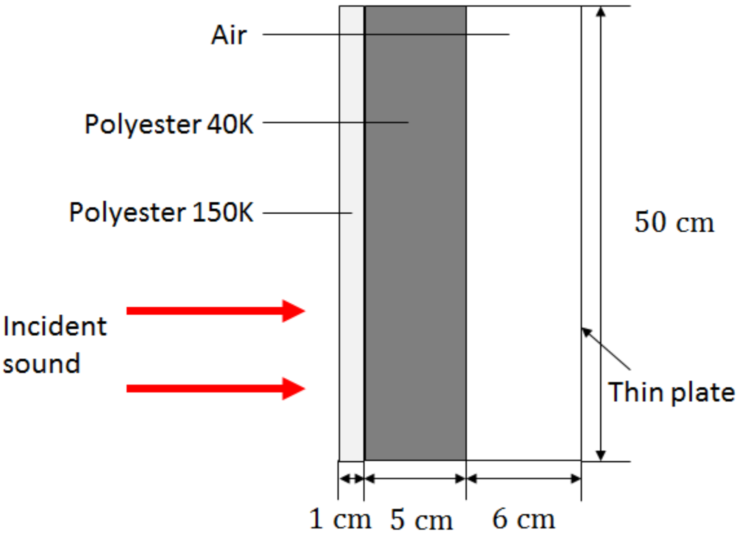

Figure 7.1. Barrier configuration

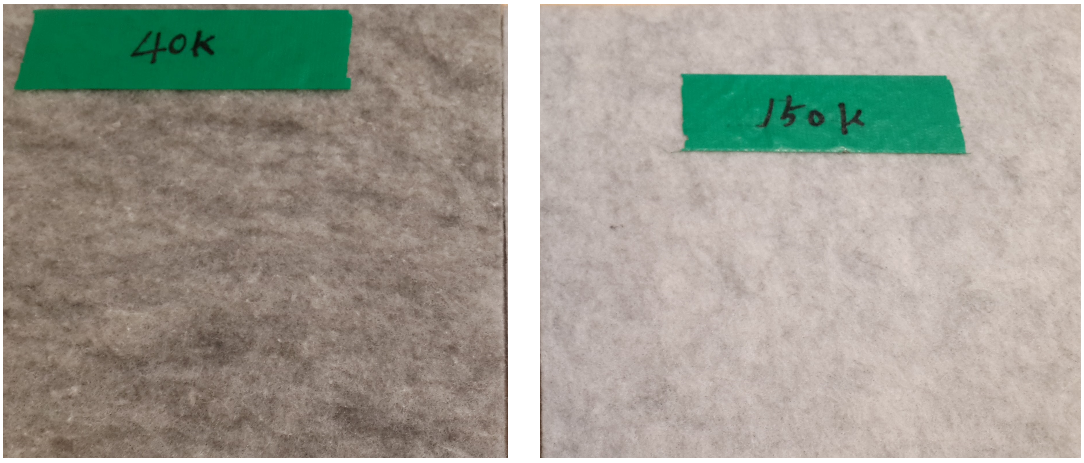

(a) (b)

Figure 7.2. Porous materials used in the barrier: polyester materials with density of (a) 40 kg/m^3 and (b) 150 kg/m^3

The properties of saturated fluid of the materials have been identified from impedance tube measurements and by directly measuring the flow resistivity using the method and equipment shown in Chapter 3. The flow resistivity has been measured with three different flow rates (see Table 7.1). Note that higher flow rates have been used than the ISO standard values (0.5–4 mm/s). The compressed air could not generate a reliable air flow at lower flow rates, which led to a fluctuation in the pressure drop. For the 40K sample different thicknesses have been used, while for the 150K sample as supplied it was impossible to make it thicker. A mean value of these measured results has been taken for the flow resistivity: 2500 Ns/m^4 for the 40K sample and 22000 Ns/m^4 for the 150K sample.

Table 7.1: Measured results

(a) 40K sample

v (mm/s)	Δp (N/m^2)	h (m)	σ (Ns/m^4)
8.49	0.62	0.030	2430
6.37	0.34	0.020	2670
8.70	0.48	0.020	2760

(b) 150K sample

v (mm/s)	Δp (N/m^2)	h (m)	σ (Ns/m^4)
8.59	1.87	0.010	21800
6.26	1.38	0.010	22000
4.03	0.88	0.010	22800

Having fixed the flow resistivity, the other properties have been inversely characterised from the impedance tube measurement, as in Chapter 3. To do this the absorption coefficient of both materials has been measured in an impedance tube. In the measurement the supplied thicknesses have been used (50 mm for the 40K sample and 10 mm for the 150K sample). The absorption coefficient has been calculated using the transfer matrix method, with the JAC model for poro–elastic layers. The results in one third octave bands are shown in Figure 7.3 and the fitted properties are listed in Table 7.2. Good agreement is found between the measured results and the predicted results for both materials. The RMS error is found to be 0.06 for both cases.

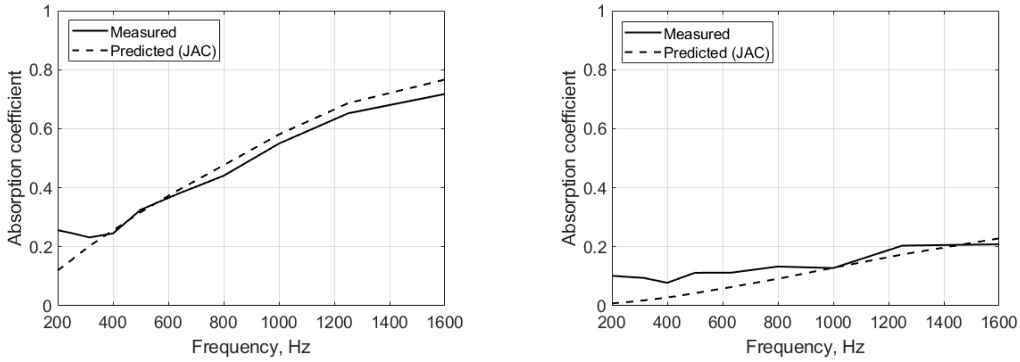

(a) (b)

Figure 7.3. Absorption coefficient of the samples: (a) 40K and (b) 150K; — measured, - - - predicted using Johnson-Allard-Champoux model

Table 7.2: Properties of saturated fluid of the porous materials

Material	ϕ	σ (Ns/m^4)	α_∞	$\Lambda(\mu\text{m})$	$\Lambda'(\mu\text{m})$
40K	0.95	2500	1.02	180	250
150K	0.90	22000	1.06	50	120

Other cases have also been examined in the impedance tube where both samples are used together. Figure 7.4 and Figure 7.5 show the cross-sections of the two configurations in the impedance tube; acoustic waves are incident from the left and the right end is rigidly terminated. The dark grey part represents the 40K material and the light grey part is the 150K material. The predicted results have been obtained with the parameters in Table 7.2, using the JAC model and the transfer matrix method.

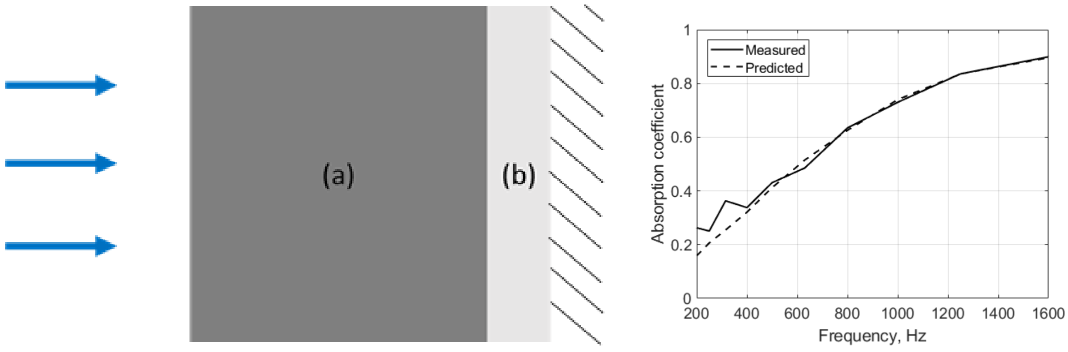

(a) (b)

Figure 7.4. Absorption coefficient of the samples: (a) configuration and (b) comparison between the measurement and the calculation

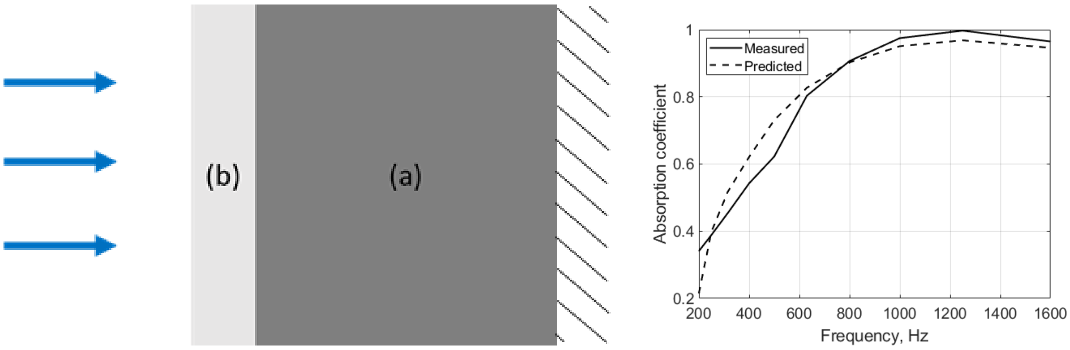

(a) (b)

Figure 7.5. Absorption coefficient of the samples: (a) configuration and (b) comparison between the measurement and the calculation; ━━ measured, - - - predicted using poro–elastic model

The RMS errors in Figures 7.4 and 7.5 are 0.05 and 0.06, respectively. The good agreement between the prediction and the measurement confirms the validity of the material properties selected in Table 7.2. The elastic properties have not been obtained for these materials. Thus they will be treated as porous materials with a rigid frame.

7.2 Performance of the barrier

7.2.1 Case without car body

Initially, a 2D FE/BE model of a single rail and the barrier in Figure 7.1 has been set up as shown in Figure 7.6. Here, (0 m, 0 m) is set as the centre of the track and the barrier is located 1.8 m away from the centre (1.05 m from the nearest rail) as indicated by KRRI. The blue lines represent the porous materials, which are modelled with the poro–rigid FE model (or equivalent fluid model), and the red lines are the acoustic boundary elements. The air gap in the barrier (see Figure 7.1) has not been considered, and the right end of the porous linings has been set to be free. This means that the displacement at the right end boundary is free and the pressure is set to be zero. The ground is assumed to be rigid by introducing a symmetric geometry with respect to $z = 0$. The maximum size of the elements is 0.01 m for the rail and 0.02 m for the sides of the barrier. On the top surface of the barrier the element length is 0.001 m where the 150K sample is used and 0.005 m for the 40K sample.

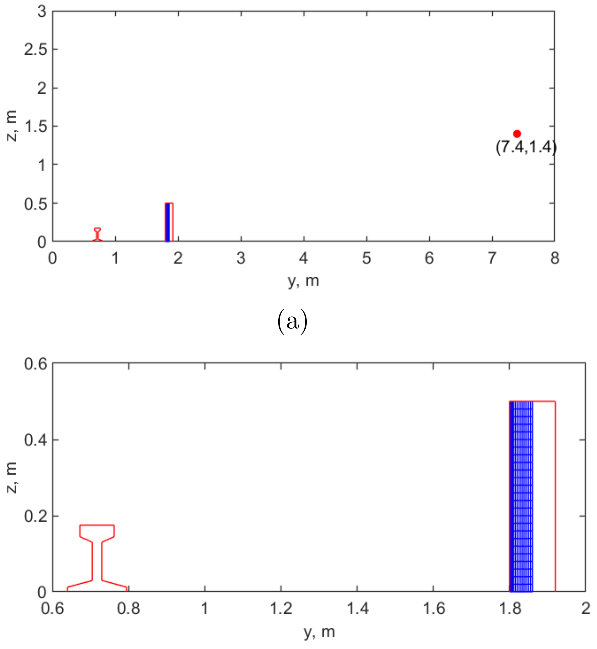

(a)

(b)

Figure 7.6. FE/BE mesh of a single rail with a barrier lined with porous materials: (a) mesh and the receiver position at (7.4 m, 1.4 m) and (b) close–up view of the mesh; — boundary elements, — poro–elastic finite elements

The input is given as a unit vertical and lateral velocity around the rail. Separate calculations have been performed for vertical and for lateral motion of the rail. The rail is assumed to be attached to the ground, so the bottom of the rail has zero velocity. A rigid barrier is considered for comparison with the same geometry of the boundary element mesh. The frequency range has been set from 100 Hz to 6000 Hz, with 60 logarithmically spaced frequencies. This will give at least 3 frequency component in each octave band. Results have been plotted in 1/3 octave bands from 125 Hz to 4000 Hz but are based three frequencies per band. This range will be enough to cover the frequency region where the track noise is dominant.

A comparison of the effects of the barrier is made for a position near one of the reference measurement positions used in ISO 3095 [108]. Figure 7.7 shows the sound pressure level at (7.4 m, 1.4 m) for the cases of vertical and lateral motion of the rail. A significant reduction from the barrier is found in both cases, with the addition of the porous materials showing a small further reduction of the noise. In the vertical vibration case, a dip is seen at around 1600 Hz without the barrier. This, however, turns into a peak in the presence of the barrier, which is even higher than that without the barrier. The reason for this would be related to the ground reflections. This will be investigated in more detail below.

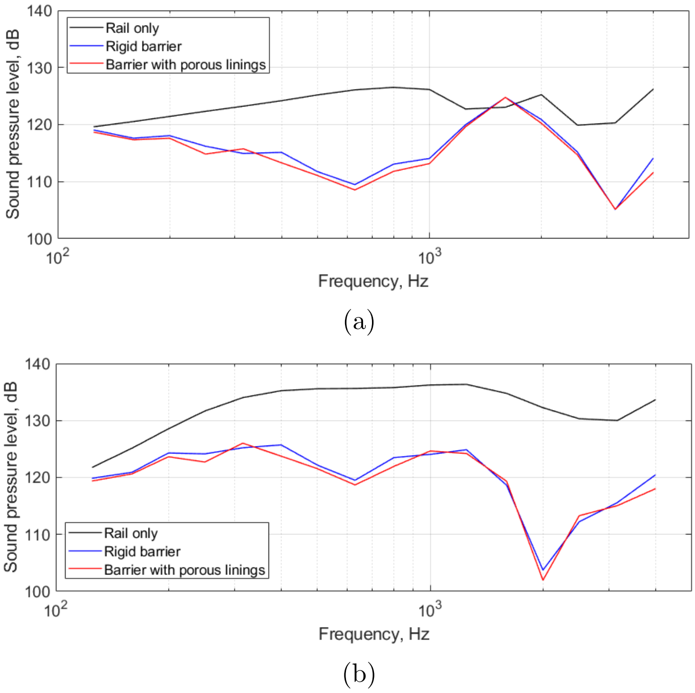

(a)

(b)

Figure 7.7. Comparison of sound pressure level at (7.4 m, 1.4 m): (a) vertical motion and (b) lateral motion of the rail; — rail, — rail with rigid barrier, — rail with barrier with porous linings

The results are also shown in terms of insertion loss in Figure 7.8. The insertion loss is defined by the difference between the sound pressure level with and without the barrier. It is given by

$$\mathrm{IL} = 20\log_{10}\frac{p_0}{p_1} \tag{7.1}$$

where p_0 is the sound pressure without the barrier and p_1 is the sound pressure in the presence of the barrier. In Figure 7.8, a positive insertion loss is seen for both directions apart from the dip at 1.6 kHz for the vertical direction. Also, the trend is similar below 1 kHz, with a large insertion loss for the lateral direction. This is mainly due to the directivity pattern of the rail, which interacts with the barrier. For example, the directivity of the lateral motion of the rail has a relatively strong component sideways up to 2000 Hz band, then the pattern changes to have a comparable component in the 60° right–upward direction. To investigate and understand more about how the sound pressure level and the insertion loss change due to the barrier and the porous materials, a contour analysis of the SPL has been conducted.

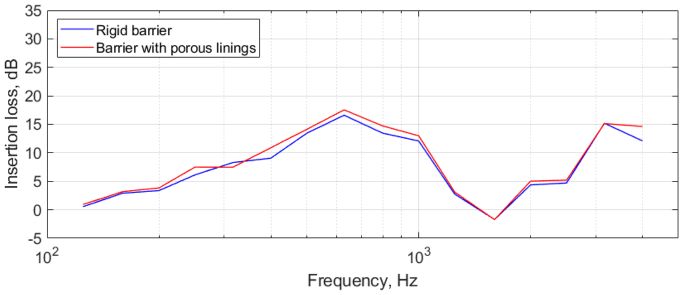

(a)

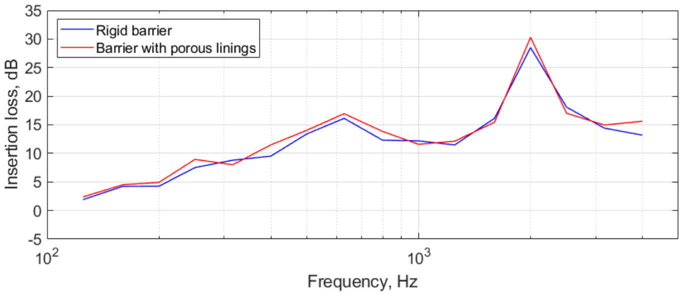

(b)

Figure 7.8. Comparison of insertion loss at (7.4 m, 1.4 m): (a) vertical motion and (b) lateral motion of the rail; ▬ rigid barrier, ▬ rigid barrier with porous linings

First the radiation of the rail without the barrier has been calculated and plotted as a reference in Figure 7.9. This shows the broadband SPL over the frequency range 125 Hz to 4000 Hz for a unit velocity excitation. It is seen that for the vertical motion there are three preferential directions in which the noise is radiated. Also, near the ground there is amplification of the noise due to the ground reflection. In the lateral case the noise is mostly radiated sideways, which would make the barrier more effective.

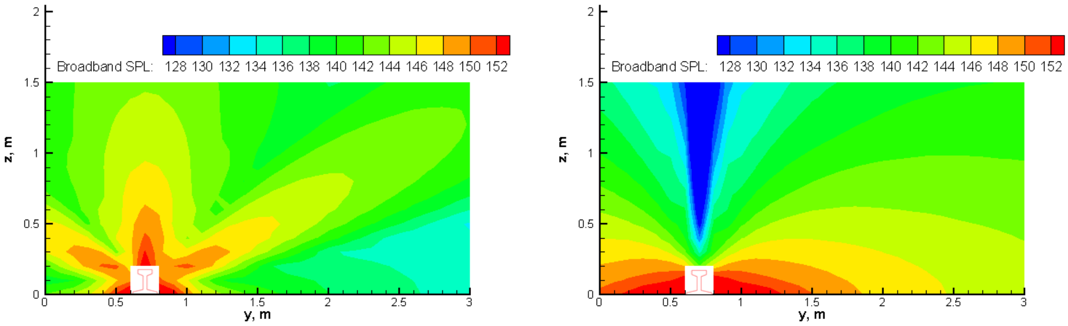

(a) (b)

Figure 7.9. Broadband SPL of the rail noise radiation on rigid ground: (a) vertical motion and (b) lateral motion

Next, the broadband sound pressure level has been plotted around the rail and barrier and the insertion loss has been plotted on a receiver grid behind the barrier. Results for the vertical excitation are shown in Figure 7.10. Note that two different legends are used for the sound pressure level close to the rail and the insertion loss in the far field.

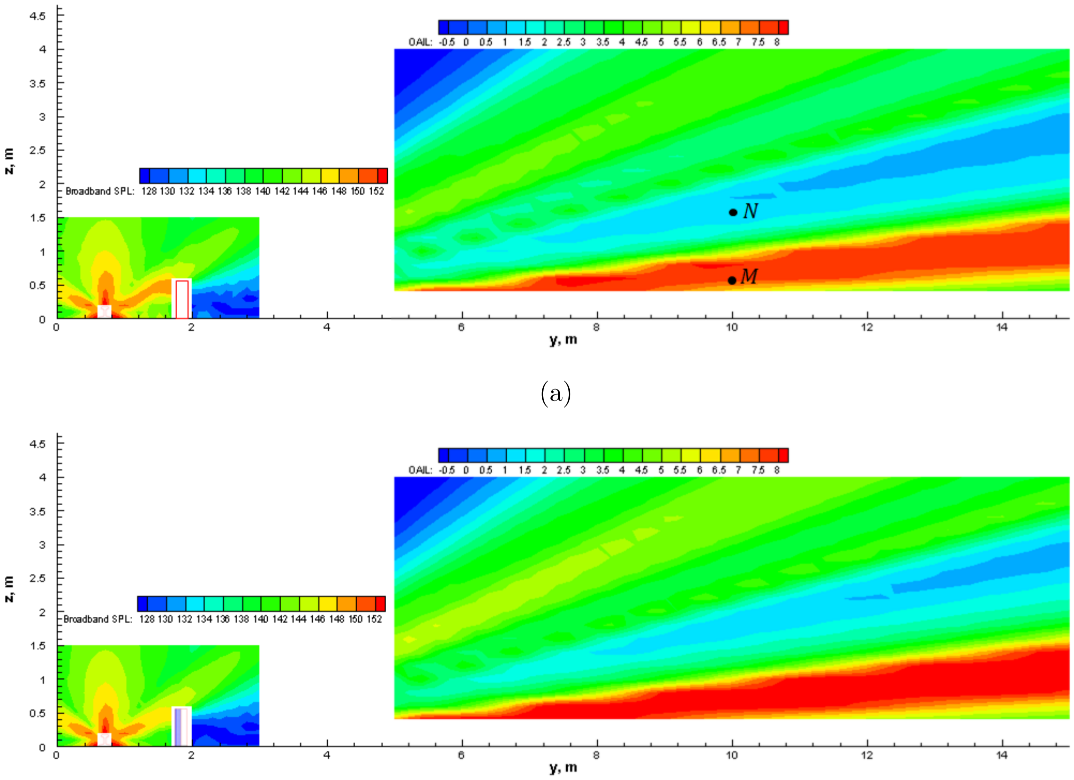

(a)

(b)

Figure 7.10. Broadband SPL and overall IL for vertical motion of rail with (a) rigid barrier and (b) barrier with porous linings; M=(10 m, 0.6 m), N=(10 m, 1.6 m)

Generally a positive noise reduction is seen behind the barrier. The difference in the insertion loss between the rigid barrier and the barrier with porous linings is very small. In terms of magnitude, the difference is about 1 dB. There is a light blue zone where the insertion loss is close to zero, while the largest reduction of noise is found near the ground. To see whether this is due to the ground reflection, the same configuration without the ground (i.e., in free space) has been investigated and the result is plotted in Figure 7.11. In this case the barrier geometry is extended down to 5 m below the ground level, so as to minimise the effect of waves diffracting at the bottom edge of the barrier.

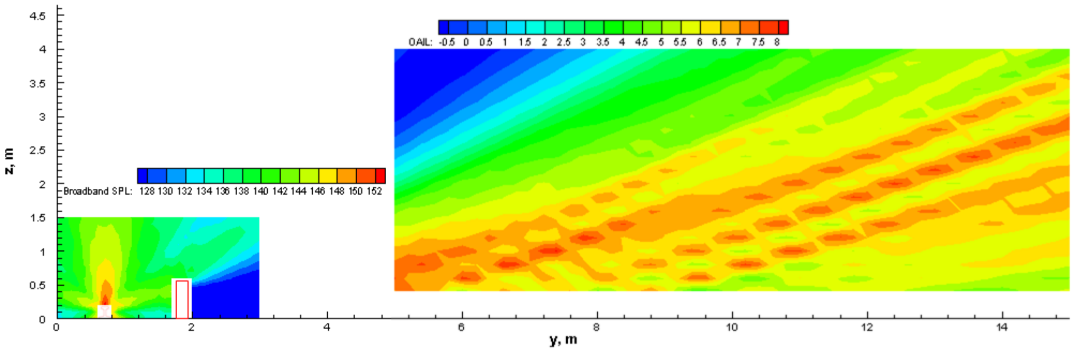

Figure 7.11. Broadband SPL and overall IL for vertical motion of rail without ground

Compared with Figure 7.10, the sound pressure in the source region is decreased, particularly in both sides of the rail. From the comparison it can be said that the ground intensifies the sound pressure in the source region. In this case the whole shadow zone shows a positive noise reduction. The relatively large insertion loss in Figure 7.11 is found in the right-upward direction, the reason for which is quite straightforward from the directivity of the noise source. It was found that while the case without the ground shows a consistent noise reduction in the 30° direction (right–upward, with respect to the ground) in every 1/3 octave band, some frequency components have increased sound pressure level in the case with the ground. This can be found in Figure 7.7, in the 1600 Hz band. To see this characteristic, the insertion loss fields at 1600 Hz and 2000 Hz, for example, are shown in Figure 7.12.

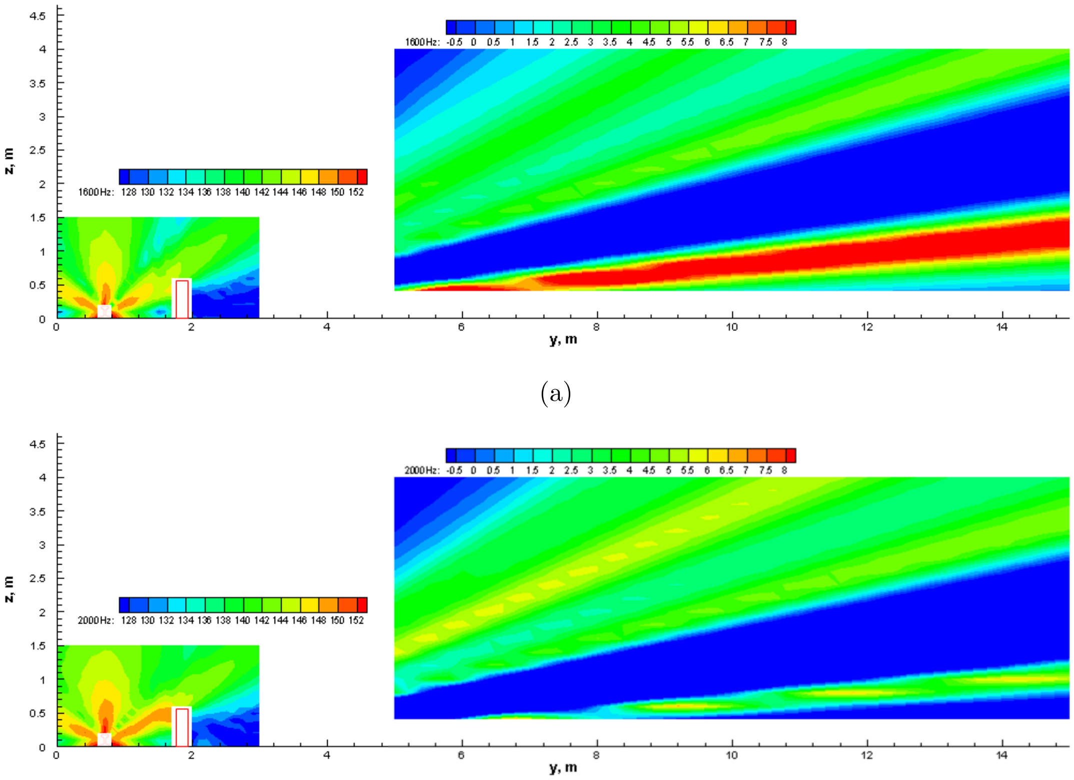

(a)

(b)

Figure 7.12. SPL and IL for vertical motion in 1/3 octave bands: (a) 1600 Hz band and (b) 2000 Hz band

The sound pressure level spectrum has been compared at points within the first red and the blue zones above the ground in Figure 7.10(a) to see how each frequency component has affected the result. Two points at (10 m, 0.6 m) and (10 m, 1.6 m) have been chosen (M and N in Figure 7.10(a)) to represent positive and negative insertion loss zones. The corresponding sound pressure levels are shown in Figure 7.13. The black line represents the sound pressure level when only the rail is considered, the blue line represents the SPL with the rigid barrier and the red line represents the case when the ground is removed. For the cases without the ground, similar trends are found in both figures. Compared to the cases with the ground, reduction of the noise is seen at low frequencies. In other words, the presence of the ground increases the SPL. At (10 m, 0.6 m) it is seen that in the presence of the ground, the barrier reduces the noise most at 1 kHz. A similar effect can be found at (10 m, 1.6 m) around 800 Hz. However, there is a large increase in the level at 1600–2000 Hz, which is enough to increase the broadband sound pressure level. This would be affected by a combination of the source directivity, source height, barrier height, ground and the distance between the source and the barrier.

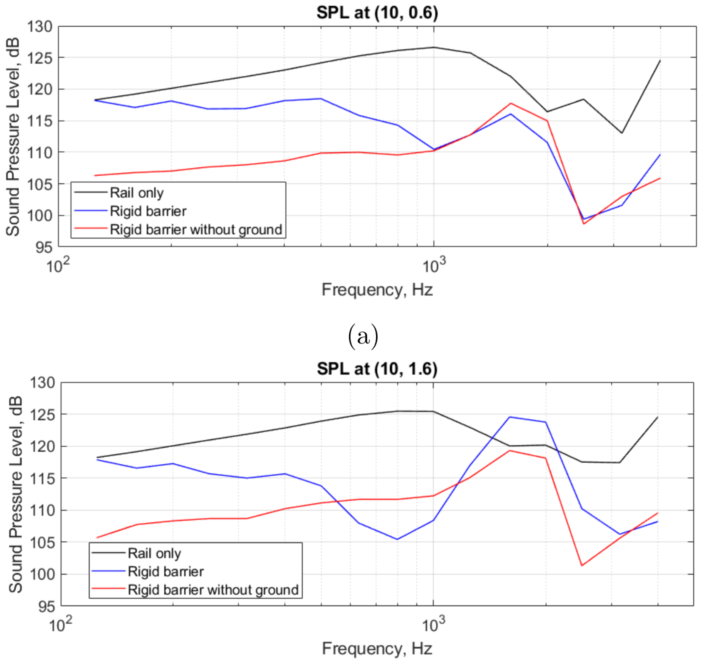

(a)

(b)

Figure 7.13. Sound pressure level spectra at two different points in Figure 7.10(a): (a) at (10 m, 0.6 m) and (b) at (10 m, 1.6 m); — rail only, — rail with rigid barrier, — rail with rigid barrier without ground

Results for lateral vibration are shown in Figure 7.14. The ground effect appears to be small in this case. The region where the insertion loss is the largest is more similar to that of the vertical excitation case without the ground. From the noise radiation pattern it is expected that more noise would be radiated in the lateral direction, which leads to a larger insertion loss on the receiver grid. The porous materials seem to have a similar effect as for the vertical case on the receiver grid, with an additional noise reduction of up to around 1 dB. However, compared with the vertical case, the change in the radiation pattern is more prominent. This is largely due to increased interaction between the rail and the barrier as seen in the small inserts in Figure 7.14.

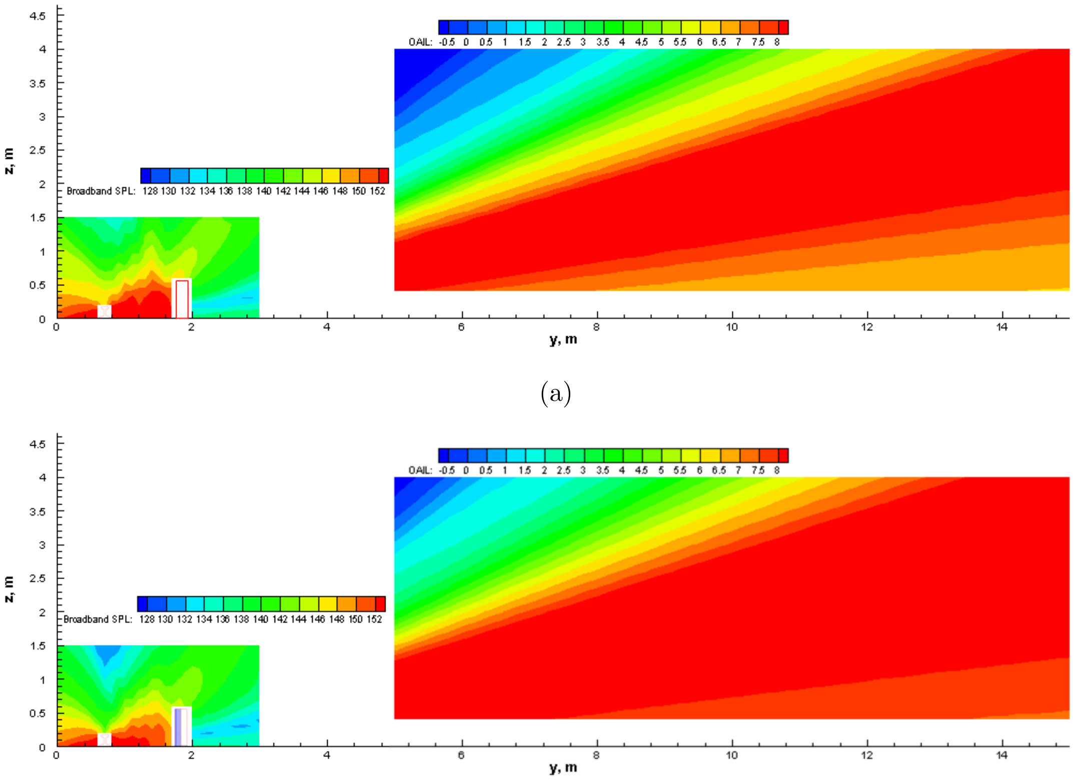

(a)

(b)

Figure 7.14. Broadband SPL and overall IL for lateral motion with (a) rigid barrier and (b) barrier with porous linings

7.2.2 Case with car body

Another feature that would significantly affect the insertion loss of the barrier is the presence of the car body, as it blocks a large area around the source. The same simulations have been conducted with a car body modelled as a rigid box above the rail. The car body has been set to be 1.2 m wide, 0.6 m high and 0.6 m above the ground. Again, there is no symmetry with respect to $x = 0$. Although the width of the car body is smaller than it should be, the sound radiation on the right hand side will not be affected significantly. The sound pressure level around the rail for each case without the barrier is shown in Figure 7.15. Increased sound pressure level is observed in the source region compared with Figure 7.9. Due to the different characteristics of the directivity of the rail, the increase and the change in the radiation pattern are more noticeable for the vertical vibration case. However, the changed radiation does not contribute much to the increase of the noise beside the track, as there is already a strong radiation in the 30° right-upward direction from the rail (with respect to the ground, see Figure 7.9).

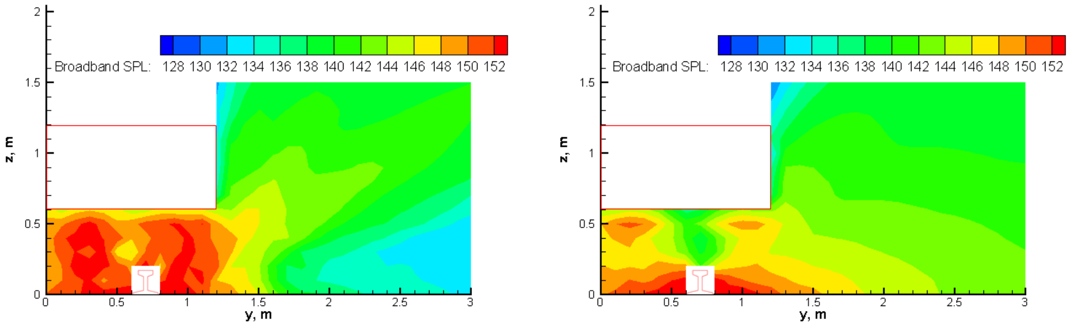

(a) (b)

Figure 7.15. Broadband SPL the rail radiation in the presence of car body, without barrier: (a) vertical motion and (b) lateral motion

Figure 7.16 and Figure 7.17 show the results with the barrier for both directions. The general trend of the insertion loss is similar to the cases without the car body, with smaller values. In both directions, the barrier increases the reflections below the car body compared to the case without the barrier (see Figure 7.15), resulting in an increase of the sound pressure level at the exit between the barrier and the car body. Thus the sound pressure level at the receiver grid also increases in the case with the barrier. In the vertical vibration case, there is a region with negative insertion loss as a consequence of the increased reflections (see Figure 7.16). In the lateral vibration case the insertion loss is always positive in the shadow zone, as the most of the reflected waves would propagate leftward (see Figure 7.17). These reflected waves do not affect the insertion loss on the right hand side of the barrier. The porous materials alleviate the sound pressure in the area below the car body, making the insertion loss larger than that of the rigid barrier (see Figure 7.16(b) and Figure 7.17(b)). In this case the insertion loss becomes positive throughout the entire shadow zone. Therefore it can be said that in the presence of the car body the barrier with porous linings shows a better performance than the rigid barrier, by around 2 dB in terms of broadband SPL. The significant decrease of noise in the source region in the case of using porous materials will also have beneficial consequences for the interior noise in the vehicle.

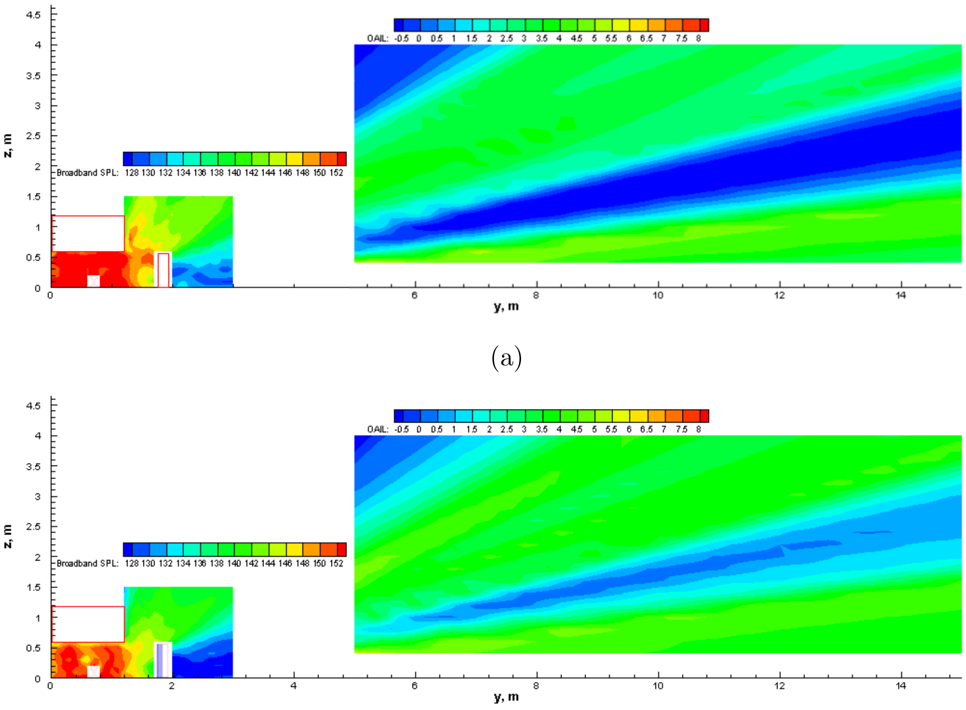

(a)

(b)

Figure 7.16. Broadband SPL and overall IL for vertical motion in the presence of car body with (a) rigid barrier and (b) barrier with porous linings

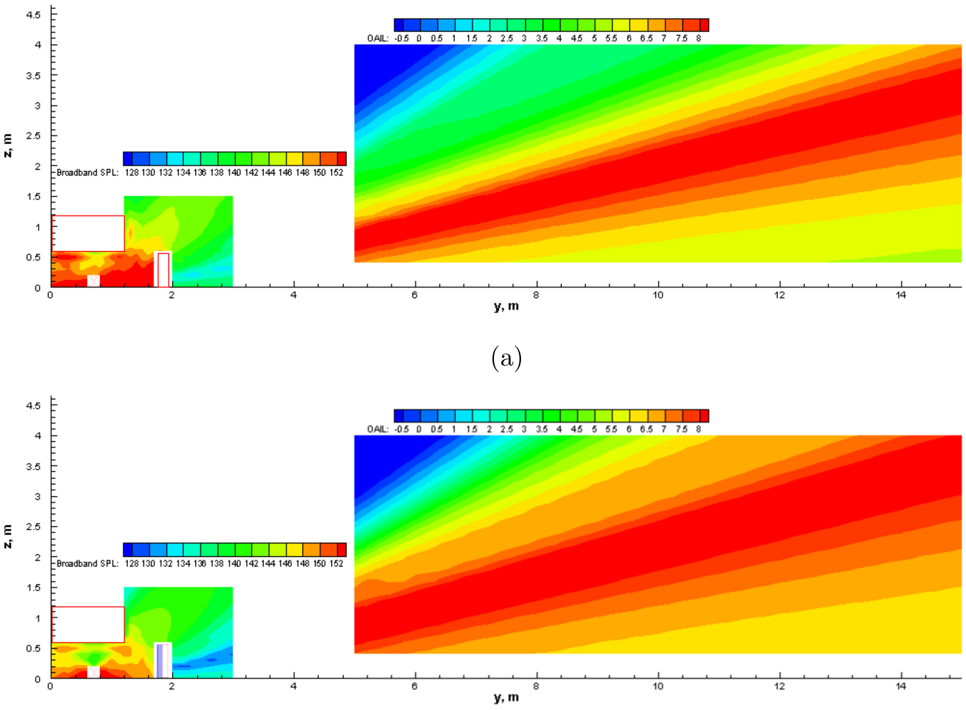

(a)

(b)

Figure 7.17. Broadband SPL and overall IL for lateral motion in the presence of car body with (a) rigid barrier and (b) barrier with porous linings

Comparisons of sound pressure level and insertion loss are made at (7.4 m, 1.4 m), and are shown in Figure 7.18 and Figure 7.19 respectively. The barrier with porous linings shows better performance above 500 Hz, except for at 1 kHz. Despite this, the difference in the overall insertion loss is not as large as it is in the frequency spectra. The overall insertion losses for the vertical case are 0.1 dB for the rigid barrier and 1.4 dB for the barrier with porous linings (9.1 dB and 9.3 dB for the lateral case, respectively). It should be noted that these values are for a unit velocity excitation. The spectra will change if the wheel is included, as it modifies the propagation path and the reflections.

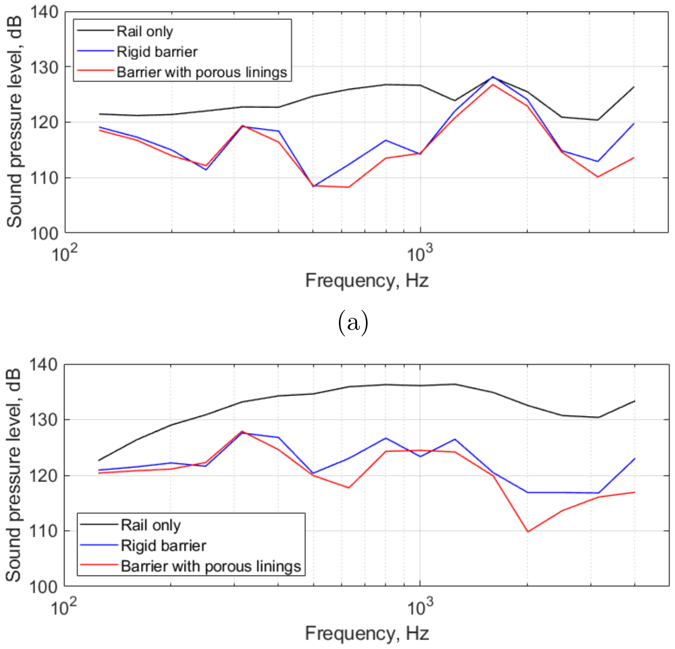

(a)

(b)

Figure 7.18. Sound pressure level at (7.4 m, 1.4 m) in the presence of car body: (a) vertical motion and (b) lateral motion; — rail, — rail with rigid barrier, — rail with barrier with porous linings

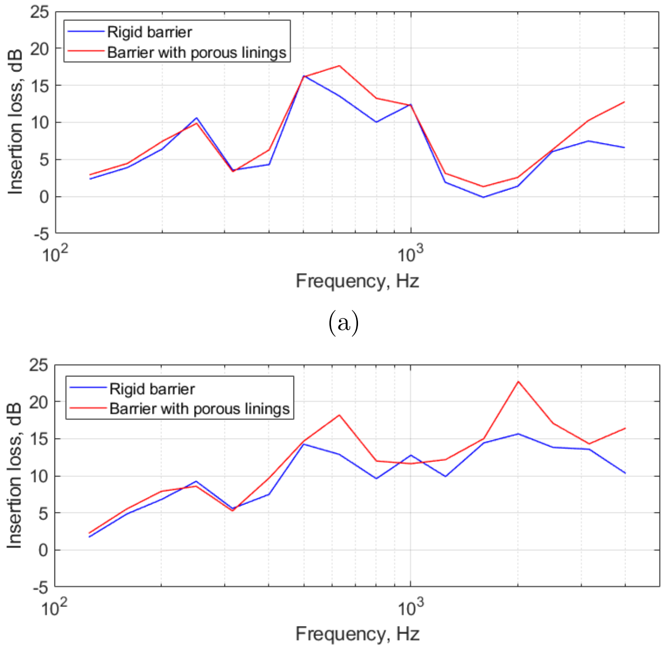

(a)

(b)

Figure 7.19. Insertion loss at (7.4 m, 1.4 m) in the presence of car body: (a) vertical motion and (b) lateral motion; — rigid barrier, — barrier with porous linings

Using the insertion losses from Figure 7.19, the overall insertion loss of the barrier on the rail noise has been calculated. The rail noise has been calculated using TWINS, for which the properties of the track are given in Table 7.3. These parameters represent a slab track with a double layer fastening system, and were provided by the KRRI. The roughness was also given, and is shown in Figure 7.20. It was measured at a high speed line in South Korea. This is combined with the roughness of a typical wheel with disk brakes, which is embedded in TWINS. The ISO 3095 limit for the rail roughness [108] is also plotted for comparison (dashed line).

Table 7.3: Parameters for slab track

Wheel parameters	
Wheel load (kN)	50
Wheel type	Korean metro wheel
Wheel radius (m)	0.43
Train speed (km/h)	101
Rail parameters	
Vertical bending stiffness (MNm^2)	6.42
Lateral bending stiffness (MNm^2)	1.07
Density (kg/m^3)	7850
Rail mass per length (kg/m)	60
Vertical and lateral shear coefficient	0.40
Vertical and lateral loss factor	0.02
Upper pad parameters	
Vertical stiffness (MN/m)	1400
Lateral stiffness (MN/m)	50
Vertical loss factor	0.4
Lateral loss factor	0.4
Baseplate parameters	
Mass (kg)	6.0
Spacing (m)	0.65
Lower pad parameters	
Vertical stiffness (MN/m)	47
Lateral stiffness (MN/m)	30
Vertical loss factor	0.30
Lateral loss factor	0.30
Roughness	Figure 7.20

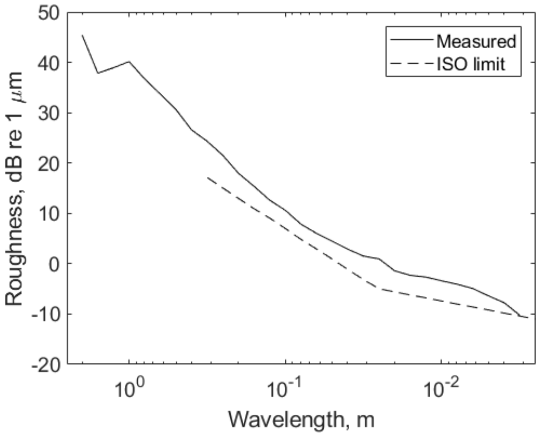

Figure 7.20. Roughness measured on the Honam line combined with wheel roughness; ▬ measured, - - - ISO limit for rail roughness

Comparisons have been made between the sound pressure level spectra of rail noise with and without the barrier, for the cases of the rigid barrier and the barrier with porous linings. These are shown in Figure 7.21. The dashed blue lines represent the noise from vertical vibration of the rail without the barrier and the solid blue lines are the cases with the barrier. The red lines correspond to the same for lateral vibration of the rail. A significant reduction is seen in both figures, for both directions. In terms of the broadband sound pressure level of the rail noise, the rigid barrier showed an overall insertion loss of 9.8 dB(A) and the barrier with porous linings showed 11.4 dB(A). Thus the effect of the porous linings on the barrier is 1.6 dB(A). Note that this is constrained to the rail noise only, as the wheel noise is not considered. The inclusion of the wheel would result in an increased insertion loss mainly due to increased reflections. The reason that these overall values are much greater than found in Figure 7.18 is that the noise is dominated by the region below 1 kHz for which the insertion loss is large.

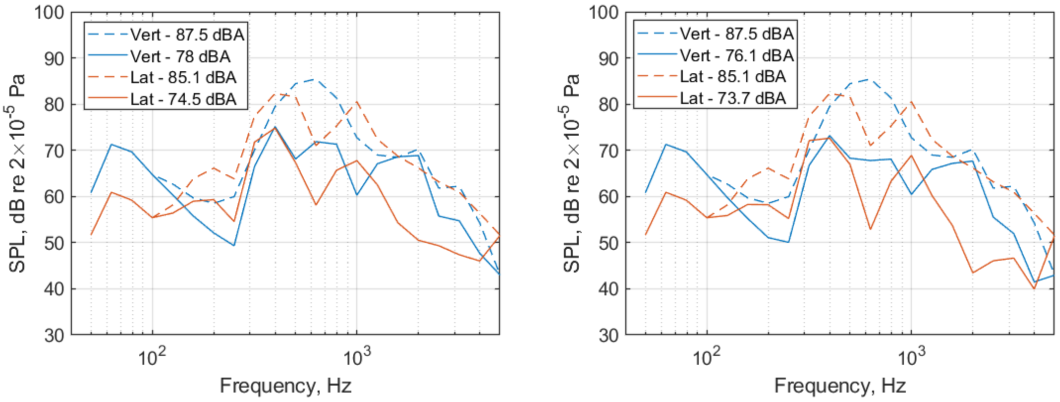

(a) (b)

Figure 7.21. Comparison of sound pressure at (7.4 m, 1.4 m) in the presence of car body: (a) rigid barrier and (b) barrier with porous linings; dashed lines – without barrier, solid lines – with barrier

7.3 Absorptive blocks on slab track

Absorptive blocks are also a potentially useful method for reducing the noise of a slab track. Not only do they absorb noise from the rail, they also have a shielding effect. At the same time, there is a possibility that the vibration transmitted from the rail to the blocks causes another source of noise radiation, which may contribute to the overall noise. These aspects are quantified in the following sections. The noise radiation from the slab is studied first, followed by the effect of absorptive blocks.

7.3.1 Application of TWINS to slab noise radiation

The developed 2.5D numerical model can be directly used to calculate the track component of rolling noise if a full structure is considered. However, this would require a very long calculation time. In fact, the calculation of the full track radiation is not necessary, as TWINS [11, 12] already provides accurate results for the rail, sleeper and wheel noise. However, it does not calculate sound radiation from the substructure, which is ballast or slab. The contribution from these can be calculated using the developed model combined with WANDS [20, 21], with consideration of a proper excitation. The combination of the two calculations will yield a more complete prediction, including the noise radiation from absorptive treatments. This can also provide the results for noise radiation from the sub–structure.

Figure 7.22 shows a dynamic system of a railway track as it is implemented in TWINS [1]. For a ballasted track, the beam on the top represents the rail with mass per unit length m'_r and bending stiffness EI. The intermediate layer of mass represents the sleepers that are continuously distributed with a mass per unit length m'_s. u_r and u_s are the displacements of the rail and the sleepers. The springs between the beam and mass layer are the rail pads, and s_p is its complex stiffness per unit length. The other spring here represents the ballast, with complex stiffness per unit length s_b. The whole structure is supported by a rigid foundation. For a slab track, the same system can be used for the track with a double layer fastening system. In this case the two springs represent the upper and lower pads, and the mass between them is the baseplate. Here, the slab is assumed to be rigid, which is represented as the rigid foundation in Figure 7.22. This means that in the TWINS calculation it is assumed that the slab vibration is negligible. However, the slab can vibrate as a part of the whole structure. This might also contribute to the overall noise, particularly at low frequencies, where the rail vibration is not isolated from the substructure. This can be calculated using WANDS. In this case the excitation is the force transmitted to the bottom (rigid) in Figure 7.22. Therefore, only the slab response is affected by the transmitted force from the track. In other words, the vibration of the slab does not affect the response of the track. This is called one–way coupling, and in this case the direction of the coupling is from the TWINS track model to the WANDS slab model. The effect of the coupling from the slab to the track will not be significant, as the vibration of the slab is much smaller than that of the other track components.

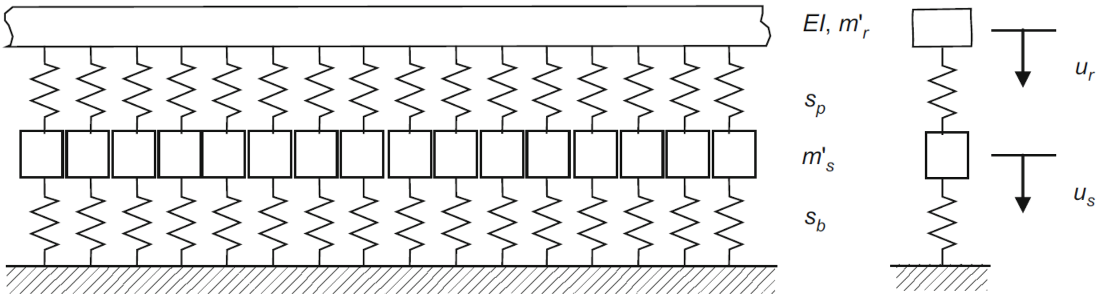

(a) (b)

Figure 7.22. (a) Beam on a two-layer foundation and (b) equivalent mass-spring system [1]

The excitation for the rolling noise is the interaction force between the wheel and the rail, caused by the wheel–rail roughness. A schematic diagram of the wheel–rail interaction is shown in Figure 7.23. In the figure the circle represents the wheel, and the spring between the wheel and the track is a Hertzian contact spring with stiffness K_H and the roughness with magnitude r [1]. F_0 is a nominal static load from the train and is typically set to 50 kN for passenger vehicles. v_w, v_c and v_r are the vibration velocities of the wheel, contact spring and rail. The dynamic force F at the wheel–rail contact is calculated from the following equation:

$$F = \frac{\mathrm{i}\omega r}{Y_r + Y_w + Y_c} \tag{7.2}$$

where ω is angular frequency and Y_r, Y_w and Y_c are the mobilities of the rail, wheel and contact spring in the vertical direction. From this, the rail velocity can be obtained as follows:

$$v_r = \frac{\mathrm{i}\omega r Y_r}{Y_r + Y_w + Y_c} \tag{7.3}$$

More details can be found in [1].

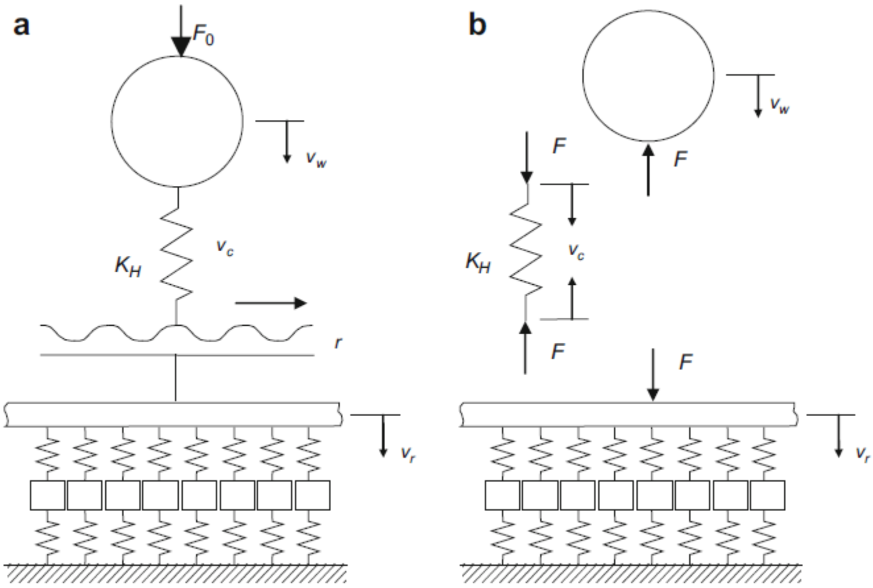

Figure 7.23. Force diagram of the wheel/rail system [1]: (a) roughness excitation and (b) forces appled to the track and the wheel

The force transmitted to the rigid foundation can be extracted from TWINS; the displacement of the mass layer u_s can be obtained from TWINS and the transmitted force F_T is then given by

$$F_T = s_b u_s \tag{7.4}$$

Note that F_T is a function of x (along the track). This will be the excitation force applied to the slab. As the slab is modelled using solid finite elements in WANDS, the input is a force applied on a node. In terms of numerical implementation, this can be applied as follows. WANDS solves the following linear equation for each frequency and wavenumber:

$$\mathbf{A}\mathbf{x} = \mathbf{F} \tag{7.5}$$

where $\mathbf{A} = \mathbf{A}(f, \kappa)$ is the system matrix of a FE/BE model, $\mathbf{x} = \mathbf{x}(f, \kappa)$ is the solution vector at frequency f and wavenumber κ and $\mathbf{F} = \mathbf{F}(f, \kappa)$ is the force vector. κ is the wavenumber in the x–direction. If $\mathbf{F}$ is a point force vector, it can be factorized as

$$\mathbf{F} = c_f \mathbf{b} \tag{7.6}$$

where $c_f = c_f(f, \kappa)$ is the magnitude of the excitation and $\mathbf{b}$ is the vector in which the component is 1 at the excitation degree of freedom and 0 elsewhere. The solution of Equation (7.5) can be expressed as

$$\mathbf{x} = \mathbf{A}^{-1} c_f \mathbf{b} = c_f \mathbf{A}^{-1} \mathbf{b} \tag{7.7}$$

Equation (7.7) shows that one can obtain the solution for a unit force vector and apply the actual magnitude of the force in the post processing. This is possible when the non-zero values are all identical in $\mathbf{F}$ (or $\mathbf{b}$). As a point force excitation has been used throughout the study, the problem of different magnitudes at different degrees of freedom will not appear. In the following section a way to obtain c_f is presented.

7.3.1.1 Input for WANDS calculation

To obtain the transmitted force, the stiffness of the bottom spring and the displacement of the intermediate mass (sleeper or baseplate) are required. The stiffness of the bottom spring (ballast or lower pad) is given and the displacement can be calculated from the response of the track.

The rail in the track dynamics model is represented as a Timoshenko beam. Thus there is one propagating wave and one decaying wave in the rail at an excitation point, for the positive and negative directions [1]. Without losing generality, the excitation point can be set to $x = 0$. The rail velocity for a unit roughness can be written as [1]

$$\frac{v_r(x)}{r} = A_p e^{-\mathrm{i}k_p|x|} + A_d e^{-k_d|x|}, \quad x \in \mathbb{R} \tag{7.8}$$

where A_p and A_d and k_p and k_d are the rail response magnitudes and the wavenumbers for the propagating and decaying waves, respectively. v_r is the rail vibration at location x. These are obtained from TWINS along with the interaction force and mobility. The ratio of the velocities of the intermediate mass (representing the sleeper or the baseplate) and the rail is given by [1]

$$v_s = \tau v_r, \qquad \tau = \frac{s_p}{s_p + s_b - \omega^2 m'_s} \tag{7.9}$$

where v_s is the velocity of the mass, τ is the ratio of the displacement of the intermediate mass to the displacement of the rail, s_p is the upper spring complex stiffness per unit length, s_b is the lower spring complex stiffness per unit length, ω is angular frequency and m'_s is the baseplate (or sleeper) mass per unit length. To apply this in the wavenumber domain, Equation (7.8) is converted into the wavenumber domain using the Fourier transform. This gives

$$\frac{\bar{v}_s(\kappa)}{r} = \tau \left(\frac{A_p}{\mathrm{i}(k_p - \kappa)} + \frac{A_d}{k_d - \mathrm{i}\kappa} + \frac{A_p}{\mathrm{i}(k_p + \kappa)} + \frac{A_d}{k_d + \mathrm{i}\kappa} \right) \tag{7.10}$$

where $\bar{v}_s(\kappa)$ is the velocity of the baseplate in the wavenumber domain. Note that the roughness r is not affected, as it is not a function of x. The force $\bar{F}(\kappa)$ acting on the slab in the wavenumber domain can be determined by

$$\frac{\bar{F}(\kappa)}{r} = s_b \frac{\bar{v}_s(\kappa)}{\mathrm{i}\omega r} \tag{7.11}$$

The force $\bar{F}(\kappa)$ is obtained by multiplying by the roughness r. This force acts as a filter to the solution in the wavenumber domain. For example, the far field pressure $p(x, y, z)$ is obtained from the wavenumber solution $\bar{p}(\kappa, y, z)$ and the force $\bar{F}(\kappa)$:

$$p(x, y, z) = \frac{1}{2\pi} \int_{-\infty}^{\infty} \bar{p}(\kappa, y, z) \bar{F}(\kappa) e^{\mathrm{i}\kappa x} \mathrm{d}\kappa \tag{7.12}$$

If a velocity input on the rail is needed, Equation (7.10) can be used instead.

7.3.2 TWINS model of slab track

As mentioned in Section 7.3.1, a double pad slab track is similar to a ballasted track from a dynamic point of view. In this model the foundation (slab) is assumed to be rigid; thus from TWINS one can only predict the rail and wheel noise. Noise from the base plate can be neglected, as in reality it is often encased by the upper and lower pads.

The parameters in Table 7.3 have been used, with the roughness shown in Figure 7.20. A comparison of predicted and measured track decay rates is shown in Figure 7.24. The peaks at 1 kHz and 5 kHz in the measured result are due to the pinned–pinned mode and the rail foot flapping, respectively. This cannot be seen from the prediction because in the TWINS model the baseplate is assumed to be continuous along the track. The peaks in the prediction are the resonances of the track model. These can be shifted in frequency by adjusting the pad stiffnesses. The magnitude will also decrease by reducing the mass of the baseplate. However, the adjustment has not been made as the properties were provided and thus should be known variables. In the calculation, a combination of the predicted (below 160 Hz) and measured (above 160 Hz) track decay rate has been used. For the lateral direction, the predicted one has been used because measured data was not available.

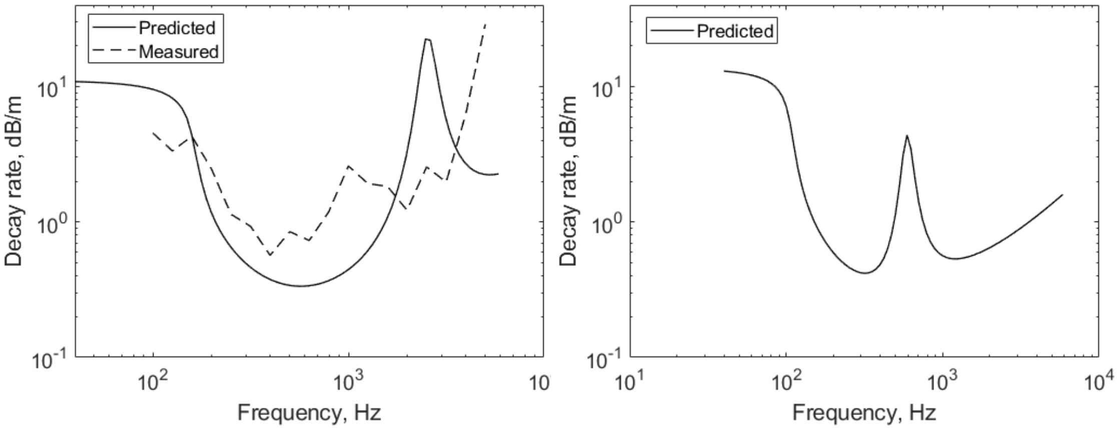

(a) (b)

Figure 7.24. Track decay rates: (a) vertical and (b) lateral direction; — predicted, - - -measured

With this information, the noise at 7.5 m from the centre of the track and 1.2 m above the rail head has been predicted using TWINS and WANDS. The following section describes the procedure to calculate the noise from the slab and shows the noise spectra for the case given.

7.3.3 Noise radiation of slab

A 2.5D numerical mesh has been created for slab, as shown in Figure 7.25. The slab consists of two layers: a hydraulically bonded layer (HBL) of 300 mm thickness at the bottom and the reinforced concrete slab of 200 mm thickness at the top. The width is set to be 2.6 m. These are modelled using solid finite elements. The ground is modelled using solid boundary elements (blue line with circles), to consider the interaction between the foundation and the ground. The slab and HBL are enclosed with fluid boundary elements to consider the interaction between the slab and the air as well as to calculate sound radiation from the slab. The properties of the slab and the ground are listed in Table 7.4. The ground corresponds to a soil with a shear wavespeed of 152 m/s, which is relatively soft. The excitation is given as a point force at 0.75 m from the centre on the top surface, where the rail would be located.

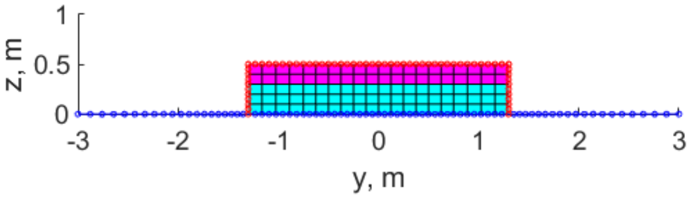

Figure 7.25. Finite element/boundary element mesh for slab

TABLE 7.4: Properties of slab and ground

	E (GPa)	ν	ρ (kg/m^3)	η	Thickness (mm)
Slab	38.00	0.15	2400	0.01	200
HBL	17.00	0.15	2400	0.01	300
Ground	0.11	0.30	1835	0.04	–

Figure 7.26 shows the sound pressure level at 7.5 m from the centre of the track and 1.2 m above the rail head. The slab noise is comparable to the rail noise below 100 Hz, but it rapidly becomes negligible at higher frequencies. The low frequency noise also has negligible contribution to the overall A–weighted level, so that the slab contribution is 40 dB(A) lower than the overall level.

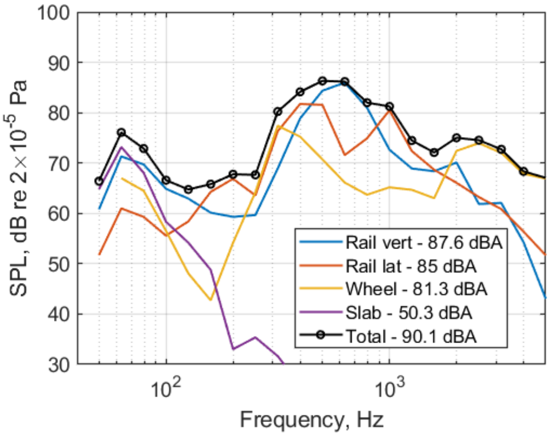

Figure 7.26. Noise spectrum for slab track at 7.5 m from the centre of the track and 1.2 m above the rail head

As pointed out previously, the whole procedure is based on one–way coupling: only changes in the TWINS calculation affect the WANDS calculation and not vice versa. This may not be the case if the slab does not act approximately as a rigid foundation to the track. One way to check this is to compare the mobility of the track from the TWINS model and that of the slab from the WANDS model. This is shown in Figure 7.27(a), in terms of the velocities for a unit roughness at $x = 0$. The corresponding force spectrum at $x = 0$ to obtain the velocity is also shown in Figure 7.27(b). Note that the force is for a unit roughness and a unit length. From the vibration, it is seen that the rail and the baseplate move together at all frequencies in this range, which means that they are coupled strongly by the upper pad which had a high pad stiffness. The vibration amplitude of the slab is much smaller than that of the track, which means that the slab is isolated from the track. This is also due to the low pad stiffness of the lower pad and the high mass of the slab.

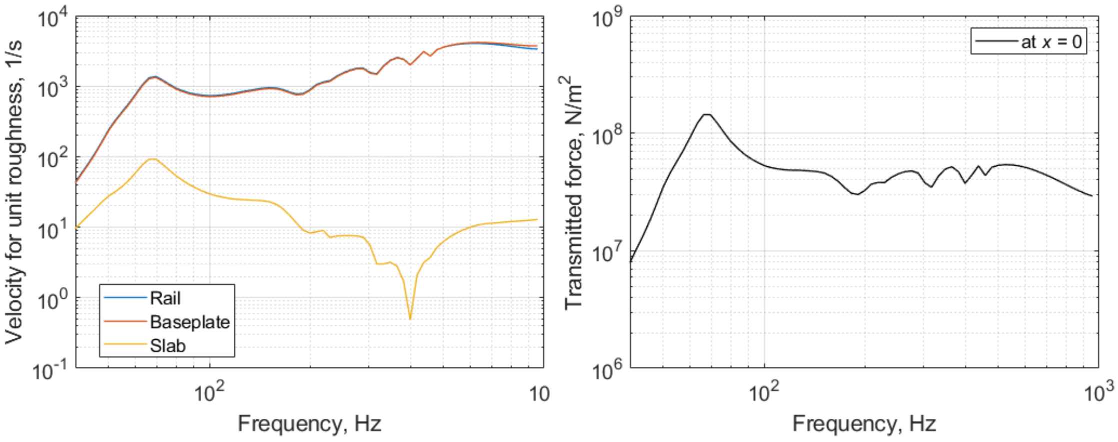

(a) (b)

Figure 7.27. Slab track response at $x = 0$: (a) velocity of each component and (b) transmitted force spectrum for unit roughness

The force spectrum in Figure 7.27(b) is the blocked force, which is obtained when the slab is assumed to be rigid. The interaction force F_i when the track and the slab are coupled can be obtained by using the following equation:

$$F_\mathrm{i} = \left(\frac{Y_\mathrm{t}}{Y_\mathrm{t} + Y_\mathrm{s}}\right) F \tag{7.13}$$

where Y_t and Y_s are the mobilities of the track and the slab at the contact point $(x = 0)$. Note that the variables are all complex. In this equation, the ratio F_i/F is a measure of how much the slab is isolated from the track. The magnitude of the ratio is shown in Figure 7.28 for the present case. It is seen that all values are close to 1 to within 1%. Therefore it can be said the one–way coupling is acceptable for this case. The force that is transmitted from the track to the slab could be considered by including the whole track into the WANDS calculation. However for this track the above assumption gives a reasonable result, and hence the full interaction has not been considered.

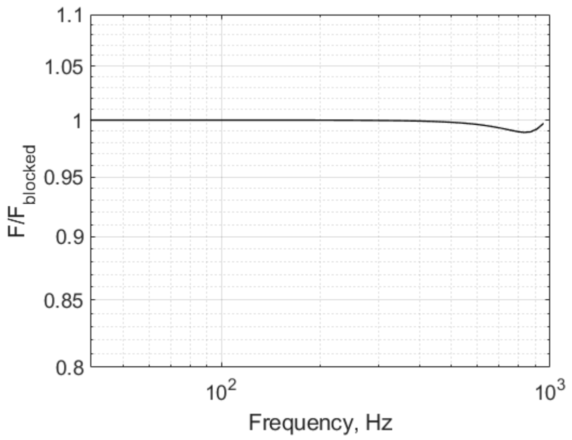

Figure 7.28. Ratio of interaction force and blocked force

The slab still radiates more noise than the rail at low frequencies, due to its large radiating area. With the increase of frequency the noise radiated by the slab becomes insignificant above 160 Hz. The noise spectrum in Figure 7.26 will be used in the following section to study the effect of absorptive blocks on the slab track.

7.3.4 Effect of absorptive blocks

7.3.4.1 Effects on rail noise

As mentioned at the beginning of the section, absorptive blocks have shielding effects as well as absorbing effects. To see these effects separately, different types of geometry have been made, as shown in Figure 7.29. The black lines are solid finite elements, the red lines are fluid boundary elements and the blue lines are poro–elastic finite elements. Figure 7.29(a) is the reference case, a rail supported by a rail pad. The rail pad is represented by the finite elements at the bottom, where z–coordinate is negative. Note that the boundary elements only cover the rail. Thus the boundary elements have been used to calculate the rail noise radiation only.

Figure 7.29(b) is the rail with the blocks. In this case, the blocks can be modelled as a rigid surface (shielding) or an absorbing surface depending on the boundary condition. In Figure 7.29(c), the blocks are modelled using poro–elastic finite elements. Thus the last case allows for wave propagation inside the blocks. The insertion loss has been calculated from the sound pressure levels with and without the blocks, at 7.5 m from the centre of the track and 1.2 m above the rail head.

The slab has been replaced with a rigid ground, as a rigid ground would have a similar effect to that of the slab and including the slab would increase the computation time significantly. Therefore, slab vibration is not included at this stage. In the model a half–space formulation is used in the fluid boundary element model. For the boundaries of the blocks in Figure 7.29(b) rigid or impedance boundary coditions have been applied to represent rigid or absorptive blocks. For the impedance boundary condition the Delany–Bazley–Miki model has been used. Note that the DBM model has been used instead of the JAC model, due to the lack of the JAC model in the boundary element model (see also Section 6.3). The use of the DBM model will show the effect of the absorptive blocks modelled with a local reaction model. A vertical or lateral unit force is given at the middle of the top surface of the rail.

The properties of the rail and rail pad are given in Table 7.5 and those of the absorptive rubber panel are given in Table 7.6. From these cases, the insertion loss of the blocks has been calculated and applied to the rail vertical and lateral noise components calculated using TWINS. The result was compared in terms of the changes in the rail vertical and lateral noise components, for which the reference values are shown in Figure 7.26.

Table 7.5: Properties of the rail and rail pad

	ρ (kg/m^3)	E	ν	η
Rail	7850	210.0 GPa	0.3	0.02
Pad	10	4.8 MPa	0.45	0.25

Table 7.6: Properties of the absorptive block

ϕ	σ (Ns/m^4)	α_∞	Λ (mm)	Λ' (mm)	ρ_1 (kg/m^3)	E (MPa)	ν	η
0.31	22650	2.6	0.17	0.21	1300	710	0.4	0.1

The maximum size of the elements is 0.0318 m, which leads to the maximum frequency of about 4.2 kHz. Therefore the mesh is expected to give a reliable result in the frequency range where the track noise is considered to be important (up to 2 kHz). The wavenumber range is shown in Figure 7.30. The acoustic wavenumber $k_0 = \omega/c_0$ and the dispersion curves for the rail and pad are also plotted for comparison. From the dispersion curves it is seen that the lowest cut–on frequency of the FE system is 40 Hz. As the wavenumber range covers all the propagating waves, the model should be able to capture all the acoustic radiation. The spacing in the wavenumber domain has been set to 0.05 rad/m.

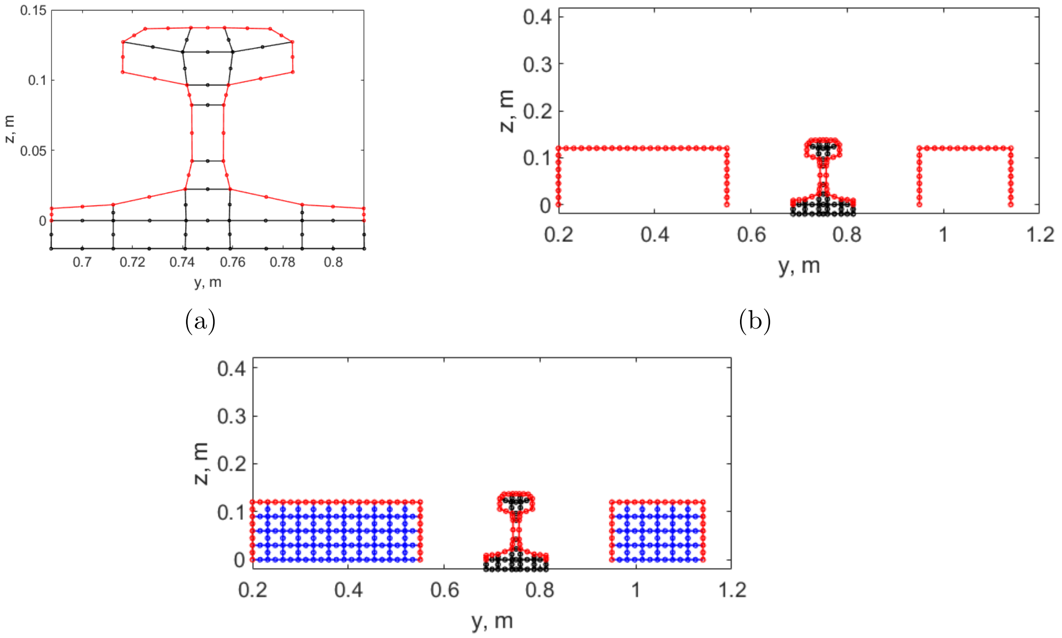

(a) (b)

(c)

Figure 7.29. Geometries for calculation: (a) rail, (b) rail with rigid blocks and (c) rail with porous blocks in each case on rigid ground (not to scale)

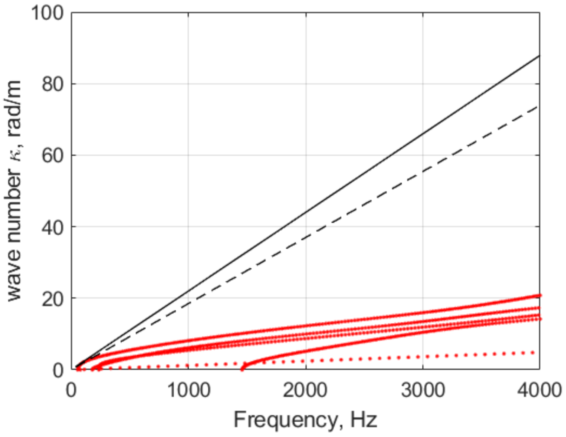

Figure 7.30. Wavenumber range used for calculation; ···· dispersion curves for the FE model of rail and rail pad, - - - acoustic wavenumber k_0, —— wavenumber range used for the calculation

Figure 7.31 shows the changes of the rail noise components at 7.5 m from the centre of the track and 1.2 m above the rail head. The dashed black line is the rail noise spectrum from the TWINS calculation using Table 7.3 and the data in Figures 7.20 and 7.24. The coloured lines represent the rail noise spectra including the effects of the absorptive blocks; the blue line is the changed rail noise spectrum when the blocks are rigid (Figure 7.29(b)), the red line is when the surfaces of the blocks are locally–reacting (impedance) (Figure 7.29(b)) and the yellow line is when the blocks are poro–elastic

(Figure 7.29(c)). It is seen that the three cases show similar trends in general. The overall level with the blocks does not differ very much from the rigid block case; thus it can be said that the shielding effect is dominant in both directions.

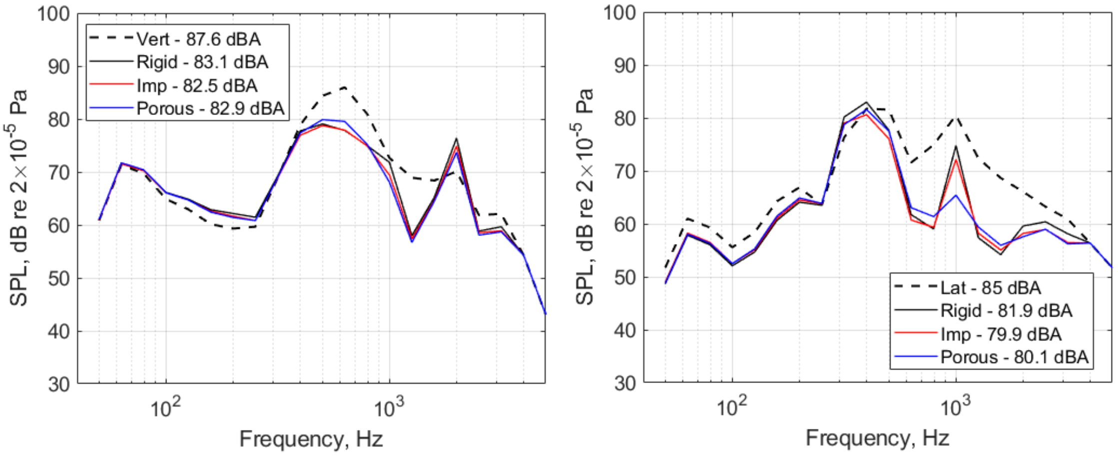

(a) (b)

Figure 7.31. Effect of the absorptive block on the rail noise: (a) vertical and (b) lateral components; - - - TWINS spectrum, — blocks modelled using BEs (rigid), — blocks modelled using BEs (impedance), — blocks modelled using poro–elastic FEs

The lowest level is observed when the surface is modelled as an impedance. This is because the impedance model overestimates the absorption. The Delany–Bazley–Miki model usually works well for materials with a high porosity (close to 1), which is not the case for the rubber block. To check the difference, the normal absorption coefficient of a layer of the porous rubber is compared between the JAC model (poro–elastic, extended reaction) and the DBM model (impedance, local reaction). The absorption coefficient for the empirical formula has been calculated from the following equation:

$$\alpha_{\mathrm{DBM}} = 1 - \left| \frac{Z_s - \rho_0 c_0}{Z_s + \rho_0 c_0} \right|^2 \tag{7.14}$$

where the surface impedance Z_s is given by

$$Z_s = -\mathrm{i} Z_c \cot\left(k_{\mathrm{DBM}} h\right) \tag{7.15}$$

where Z_c and k_{DBM} are the characteristic impedance and the modified wavenumber by the Delany–Bazley–Miki model and h is the thickness of the layer. In the calculation, 0.12 m has been used for the thickness, which is the height of the block. The absorption coefficient for the porous case has been calculated using the transfer matrix method.

Figure 7.32 shows the absorption coefficients obtained using these two models. It should be noted that the TMM result is reliable as results with the current properties showed very good agreement with measurements (see Figures 6.22 and 6.23). From the result it can be said that the empirical model overestimates the absorption, especially at high frequencies. This explains why the local reaction model showed better performance in Figure 7.31 than the extended reaction model.

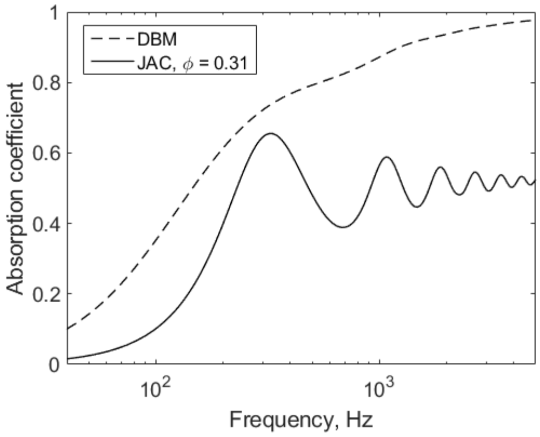

Figure 7.32. Comparison of absorption coefficient of the block with the JAC model (extended reaction) and with the DBM model (local reaction); - - - DBM model, —— JAC model

Because of the overestimation from the empirical model, the difference between the local reaction and the extended reaction models cannot be evaluated clearly. However, this can be compared if one is made to be similar to the other in in terms of the absorption characteristics. As the discrepancy is mainly due to a low porosity, the porosity has been set to 0.91 with the other parameters unchanged. The results are shown in Figure 7.33. The two absorption coefficients are now comparable to each other up to 1 kHz, with small difference aboves that.

With the modified porosity, the results in Figure 7.31 were recalculated with the modified porous block case, and these are shown in Figure 7.34. Clearly the extended reaction model shows greater insertion losses in both directions, due to the increased absorption. Compared with the previous case the sound pressure level with the extended reaction model is decreased by 1.2 dB(A) and 2.7 dB(A) in the vertical and lateral cases, due to the increased absorption. The overall differences between the local reaction model and the extended reaction model are 0.8 dB(A) and 2.5 dB(A) in the vertical and lateral directions for this configuration. The vertical component is still similar, whereas the lateral component has a slightly larger difference. This can be explained by the directivity of the rail noise radiation (see Figure 7.9). The noise radiation of the rail for vertical motion is dominant in three upward directions, which will not be much affected by the presence of the block. On the other hand, the lateral vibration of the rail radiates noise mostly sideways, which will be directly affected by the absorptive blocks.

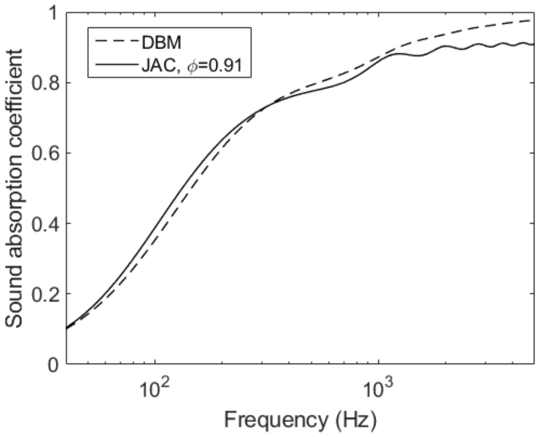

Figure 7.33. Comparison of absorption coefficient of the absorptive block with a modified porosity; - - - DBM model, ― JAC model

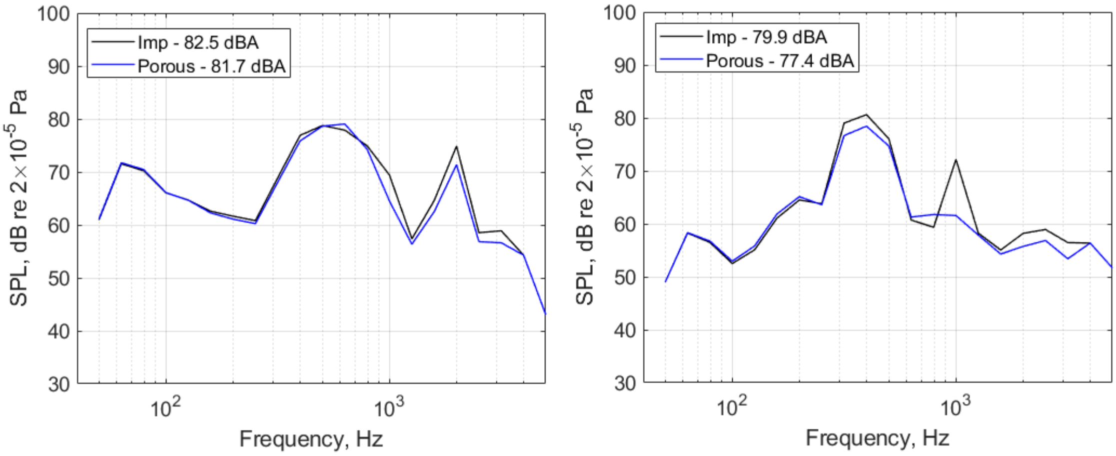

(a) (b)

Figure 7.34. Comparison of sound pressure level at (7.5 m, 1.2 m), using different models for the absorptive blocks: (a) vertical and (b) lateral components of the rail noise; ― DBM model (local reaction), ― JAC model (extended reaction) with a modified porosity

A large decrease in the 1 kHz band from the porous block case in the rail lateral component is due to the dissipation inside the block, for which the distance between the rail and the block corresponds to a half acoustic wavelength. The corresponding frequency f_1 is

$$f_1 = \frac{c_0}{2l} \simeq \frac{343}{2 \cdot 0.175} = 980 \text{ Hz} \tag{7.16}$$

where c_0 is the speed of sound in air and l is the distance between the rail and the block. It varies as the rail surface is not a straight line, but the frequency f_1 will be in the 1 kHz band.

7.3.4.2 Effects on slab noise

The absorptive blocks also reduce the noise radiated by the slab, although its contribution is only limited to the low frequency range. A geometry of the slab with the absorptive blocks has been made to quantify this effect. The numerical mesh is shown in Figure 7.35. Apart from the absorptive blocks, the geometry is same as in Figure 7.25. The red line represents the ground and is modelled using solid boundary elements. The rectangle represents the slab with two layers, i.e., the hydraulically bonded layer (bottom) and the slab (top). On the top of the slab are the blocks (blue), which are modelled using poro–elastic finite elements. The slab and the blocks are bounded by acoustic boundary elements to calculate the sound pressure at (7.5 m, 1.85 m). The material properties are the same as those in the previous sections.

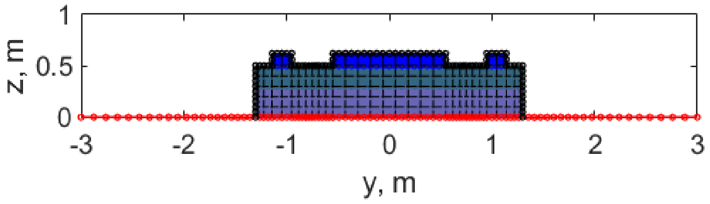

Figure 7.35. FE/BE mesh of slab with absorptive blocks

Figure 7.36(a) shows the SPL from the slab at 7.5 m from the centre of the track and 1.2 m above the rail head with and without the blocks. It is observed the noise is almost unaffected by the presence of the blocks, particularly below 100 Hz. The difference is negligible at higher frequencies, and the overall insertion loss is 0.2 dB(A). As a result, the total noise remains unchanged.

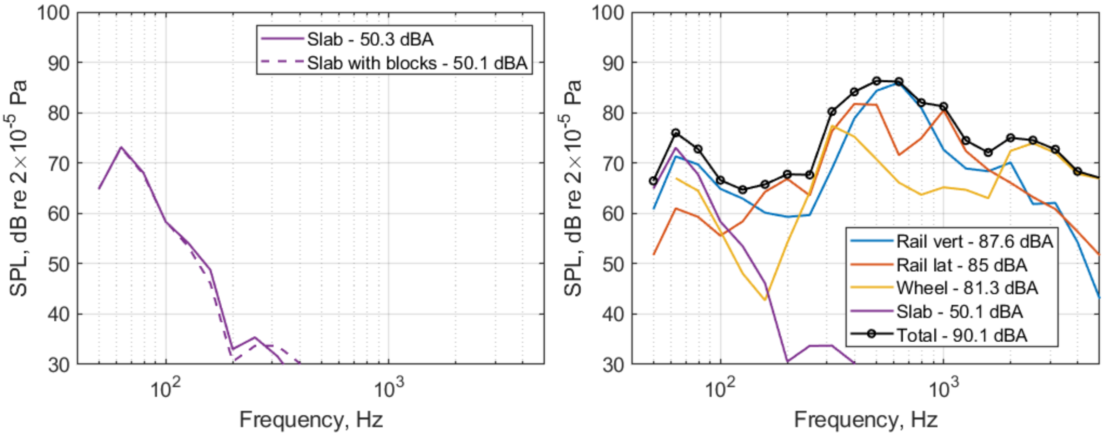

(a) (b)

Figure 7.36. Effects of absorptive blocks on slab noise at (7.5 m, 1.85 m): (a) slab noise with and without the blocks and (b) rolling noise spectrum with the slab and blocks (IL only applied to the slab noise)

The combined effect of the blocks on the rail noise and the slab noise is shown in Figure 7.37. The overall noise spectrum from the reference case is also plotted for comparison (dashed black line). The reduction is seen below 100 Hz and between 400 Hz and 2 kHz, resulting in a decrease of the overall noise by 3.8 dB(A). This is mainly due to the reduction by the shielding and absorbing effects of the blocks on the rail noise.

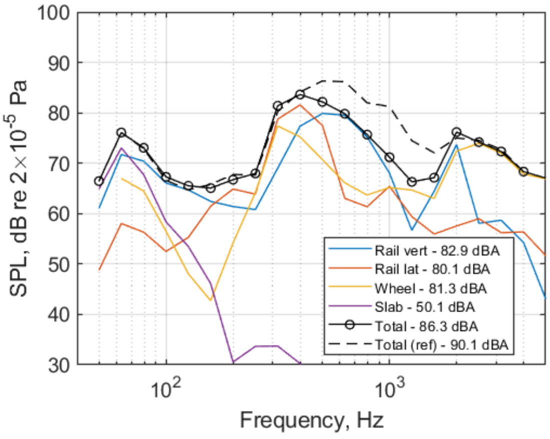

Figure 7.37. Overall effect of the absorptive blocks on rolling noise

7.4 Summary

It has been shown how much a noise barrier or absorptive blocks with absorptive treatments can reduce the noise radiated by the track. From the barrier cases a further reduction of up to 1 dB was seen with the porous linings, compared to the level with the rigid barrier. The presence of the car body led to an increase of noise in the source region, due to increased reflections. The level was decreased by the barrier with porous linings, whereas it was intensified with the rigid barrier. This implies that the use of porous linings may help reduce the noise transmitted into the car body.

Effects of absorptive blocks on the track have also been investigated. The noise from the slab was calculated first, which had a big influence below 100 Hz. The overall level of noise from the slab was estimated to be around 50 dB(A) for a 0.2 m thick slab with a hydraulically bonded layer of 0.3 m thickness and for a train speed of 101 km/h. This was 40 dB lower than the overall noise when A–weighted. The effect of the absorptive blocks on the slab noise was found to be negligible, for which an overall insertion loss of 0.2 dB(A) was obtained.

The shielding effect of the blocks on the rail vertical and lateral noise was 4.5 dB(A) and 3.1 dB(A), for the given configuration and receiver point. Having the blocks filled with a porous rubber leads to a slightly greater noise reduction, i.e., 0.2 dB(A) for the rail vertical motion and 1.8 dB(A) for the lateral motion. The Delany–Bazley–Miki model overestimated the noise reduction, because the model was developed based on high porosity materials. The total noise reduction from the absorptive blocks was found to be 3.8 dB(A).

Chapter 8

Conclusions and future work

8.1 Conclusions

In this thesis, the effects of absorptive treatments on the noise radiation of a railway track have been investigated using numerical simulations and scale model experiments. A 2.5D finite element model has been developed for modelling sound propagation in porous media. Using the developed model, and from experiments, the performance of absorptive treatments for the track have been investigated. The effects of ballast as a porous material have also been studied.

Ways to obtain the properties of porous materials have been reviewed and a melamine foam has been characterised by the presented methods. From a sensitivity analysis with known properties of glass wool, it was shown that the flow resistivity and the porosity have the largest effect on the acoustic properties. For the elastic properties, it was shown that different sets of elastic parameters can give the same characteristics in the absorption spectrum of the material. From the comparison with a case in a previous study, the properties that were directly measured using ISO standards as well as the indirectly characterised properties were found to be in a reasonable range.

A numerical model to evaluate the noise radiation from a railway track with absorptive treatments has been developed. Based on the Biot-Allard model and the $\mathbf{u} - p$ formulation, a 2.5D finite element model for sound propagation in poro–elastic media has been developed and implemented in a software code. The developed code has been validated in 2D. It has been coupled with an existing multi–domain 2.5D finite element and boundary element software. The coupled code has also been validated in 2D for poro–elastic and acoustic coupled domains. From the validation cases, it was shown that, for a foam with high porosity, the poro–elastic model and the poro–rigid model have almost the same characteristics apart from frequencies close to structural resonance frequencies.

Using the developed model, the effects of ballast as a porous material were studied. Three different example cases, where the ballast was previously modelled using a local reaction model, were revisited with the developed model (extended reaction model). For the diffuse field absorption coefficient, the extended reaction model did not show a clear improvement, compared with measured data. For the case of the radiation from a sleeper embedded in ballast, however, the new model showed better agreement with the measured data. It was shown that when the sleeper radiates noise, the vibration of the embedded part of the sleeper also contributes to the radiation. In the third case of the rail radiation above ballast, a better agreement was found with the new model for the vertical vibration of the rail, whereas for the lateral vibration case differences of up to 6 dB were found above 1 kHz.

The radiation of sound from the ballast has been calculated and its relative contribution to the sleeper noise has been studied. For this a 3D COMSOL model has been used to calculate the structural response of the ballast and the sleepers. The properties used for the ballast were determined by comparison with vibration data measured at a test track. The results showed that the ballast and the sleepers would vibrate in phase below 200 Hz, giving an increase in the sound power of about 6 dB. The stiffness of the ground had some effect on the noise levels but not on the relative contribution of the ballast to the sound power of the sleepers. With the properties obtained, the ballast stiffness seen by the sleepers has also been calculated and compared with a previously measured result used in the TWINS model. Good agreement was found with the measured data. From the numerical result it was found that the ballast and ground behave as a damper above 100 Hz, with the phase of the dynamic stiffness around $\pi/2$ and a magnitude increasing in proportion to frequency.

An experimental study with a 1:5 scale track was carried out to study the effect of absorptive panels. A low–height noise barrier was also studied to compare the performance. The results were compared in terms of their insertion loss, and the overall effect was calculated using the insertion loss spectrum combined with a TWINS rolling noise spectrum for a ballasted track. From these results it was shown that the noise barrier gave better noise reduction than the absorptive panels, by up to 9 dB depending on the receiver position and the configuration. The combination of the two measures led to an improved performance in most cases. Comparisons have been made with numerical simulations, which showed moderate agreement with the measurements.

Finally the effects of absorptive treatments on a slab track have been investigated. First, a low–height noise barrier with porous linings was considered. From the numerical results it was shown that the addition of the porous linings increased the noise reduction by up to 1 dB, compared with the rigid barrier. The results with a car body present showed that the porous linings help to reduce the noise level around the source region, which may also reduce the noise transmitted into the car body. The effects of absorptive blocks on rolling noise were also presented, these results being combined with the TWINS model. The noise from the slab was calculated first, which contributed significantly only below 100 Hz. The overall level from the slab was around 50 dB(A) at 7.5 m from the centre of the track and 1.2 m above the rail head, compared with 90 dB(A) for the overall rolling noise for a train speed of 101 km/h. The effect of the blocks on the slab noise was found to be negligible, for which an overall insertion loss of 0.2 dB(A) was obtained. The blocks had a shielding effect on the rail vertical and lateral noise of 4.5 dB(A) and 3.1 dB(A) at the receiver point. Including the absorption of the blocks showed a further reduction for each direction, i.e., 0.2 dB(A) and 1.8 dB(A). The total noise reduction due to the absorptive blocks was found to be 3.8 dB(A).

8.2 Recommended future work

Through this work a 2.5D poro–elastic finite element model has been developed and coupled with other finite element/boundary element models. The developed model has been used for studying the effects of low–height noise barriers with a porous lining and absorptive blocks. Still, there can be improvements on some parts of the developed model. For example, an absorptive ground can be introduced in the simulation by using acoustic boundary elements of a large box–shaped structure with impedance boundary conditions. As this would increase the computational cost, a modified Green's function may be implemented in the developed model (see for example, [109]). In addition, implementing source terms within the model would make it possible to represent noise sources such as rails or wheels in a simplified form, which would lead to reduction of the computational cost.

The COMSOL model used for the ballast noise radiation had the limitation that it could not consider the interaction between acoustic boundary elements and poro–elastic finite elements. In the calculation the boundary condition was given as "free", which means the fluid pressure at the surface is zero. Therefore the sound power radiated from the fluid was zero and hence could not be taken into account. This could be considered, if coupling between the acoustic boundary element model and the poro–elastic finite element model is added, or a model of a reduced size is coupled with the acoustic finite element model. Also, the measurement of the ballast vibration had many uncertainties, such as the variability between different stones or the vertical alignment. A more robust measurement and a model for the vibration of the ballast could provide more reliable properties.

The discrepancies between the measurements and the simulations for the reduced scale track may need to be investigated further. The absorption of the car body has been reduced as much as possible but it should still be measured and considered in the simulation. Also, an investigation of the ground reflection can help the simulation have better agreement with the measurement. For simplicity, one may consider only a single rail in combination with the absorptive rubber panels.

The properties of porous concrete blocks have not yet been measured. In Chapter 7, only the abosprtion coefficient for the porous rubber was available, from which the properties were obtained. The properties of porous concrete blocks will be required for an accurate assessment of their effect on track noise.

There are other mitigation methods that can be considered using the developed model. A rail shield would be a good example, which covers a part of the rail (see for example, [110]). In this case internal resonances of the fluid inside the shield may occur. This may be alleviated by introducing a porous lining on the inside of the shielding panel, which will effectively increase the damping of the fluid.

Another example is the effect of absorptive linings on the sound transmission through the outer surfaces of a train. This would consist of two regions of acoustic boundary elements and plate and poro–elastic finite elements in between. In this case the frame resonances can be more important. This can also be studied using the transfer matrix method.

The developed model is rather a general model, thus it can be used in different areas for which the 2.5D assumption holds. Straight pipes, bridges and tunnels would be good examples.

Appendices

Appendix A

Transfer matrix method

A.1 Introduction

A multi–layered system that is laterally infinite can be described by the transfer matrix method. It can include all types of media. Here fluid media and poro–elastic media are considered, which have been used throughout the thesis. The transfer matrices are introduced and assembled into the global matrix. A hard wall termination is used to calculate the surface impedance of a multilayer system. This appendix is based on [49], in which a detailed description of the method can be found.

A.2 Principle of the method

The basic concept of the transfer matrix method is to divide a system into parallel layers and to link the properties at both ends of each layer. This is illustrated in Figure A.1 for a plane oblique wave impinging on a medium layer of thickness h. As the geometry of the problem is bidimensional, considering two directions (x_1 and x_3) is sufficient to derive the equations. The tangential component of the wavenumber in the finite medium is the same as that in the free air:

$$k_t = k_0 \sin\theta \tag{A.1}$$

where k_t is the tangential component of the wavenumber in the finite medium and k_0 is the wavenumber in the free air. The sound propagation in the medium can be written as

$$\mathbf{V}(M) = \mathbf{T}\mathbf{V}(M') \tag{A.2}$$

where M and M' are the points close to the front and the back, and $\mathbf{V}(M)$ is a vector that describes the acoustic field at point M. The transfer matrix, denoted by $\mathbf{T}$, links the acoustic field between the two ends.

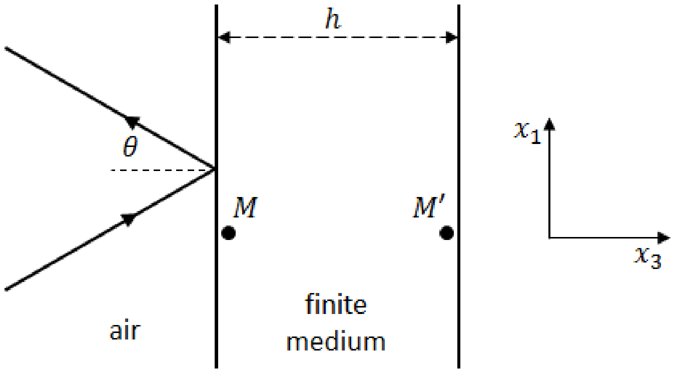

Figure A.1. Plane wave impinging on a medium layer of thickness h

A.3 Transfer matrices for acoustic and poro–elastic media

A.3.1 Fluid layer

The acoustic field in a fluid medium is defined by pressure and particle velocity. At any point M, the vector is given as

$$\mathbf{V}(M) = \begin{bmatrix} p(M) & v_3^f \end{bmatrix}^{\mathrm{T}} \tag{A.3}$$

where p and v_3^f are the pressure and the x_3 component of the particle velocity, respectively. Let ρ^f and k^f be the density and the wavenumber of the fluid medium. For propagating waves, the pressure and the velocity can be written as

$$p(x_3) = A_1 \exp\left(-\mathrm{i}k_3^f x_3\right) + A_2 \exp\left(\mathrm{i}k_3^f x_3\right) \tag{A.4}$$

$$v_3^f(x_3) = \frac{k_3^f}{\omega\rho^f}\left[A_1 \exp\left(-\mathrm{i}k_3^f x_3\right) + A_2 \exp\left(\mathrm{i}k_3^f x_3\right)\right] \tag{A.5}$$

where $k_3^f = k\sqrt{1-\sin^2\theta}$ is the x_3 component of the wavenumber and ω is the angular frequency. Setting x_3 to be zero at M yields the acoustic field $\mathbf{V}^f(M)$:

$$\mathbf{V}^f(M) = \left[\begin{array}{cc} A_1 + A_2 & \frac{k_3^f}{\rho^f \omega}(A_1 - A_2) \end{array}\right]^{\mathrm{T}} \tag{A.6}$$

Similarly, the other vector $\mathbf{V}^f(M')$ can be obtained at $x_3 = h$. The relation between the two vectors can be written as in equation (A.2), with the following transfer matrix:

$$\mathbf{T}^f = \left[\begin{array}{cc} \cos k_3^f h & \frac{\mathrm{i}\omega\rho^f}{k_3^f} \sin k_3^f h \\ \frac{\mathrm{i}k_3^f}{\omega\rho^f} \sin k_3^f h & \cos k_3^f h \end{array}\right] \tag{A.7}$$

As porous materials with a rigid frame can be described as an equivalent fluid, the fluid layer formulation can be applied to them with modified density and bulk modulus (or speed of sound in the medium).

A.3.2 poro–elastic layer

A poro–elastic medium is modelled with the Biot theory, in which two compressional waves and a shear wave can propagate. They can be described by wavenumber vectors, $\mathbf{k}_1, \mathbf{k}_2, \mathbf{k}_3$ and $\mathbf{k}_1', \mathbf{k}_2', \mathbf{k}_3'$. Here 1, 2 are for the compressional waves and 3 is for the shear wave. The prime denotes the backward wave, while the other wave is the forward wave. The x_3 components of the wavenumber vectors are

$$\begin{cases} k_{i3} = \left(\delta_i^2 - k_t^2\right)^{1/2} \\ k_{i3}' = -k_{i3} \end{cases} \qquad i = 1, 2, 3 \tag{A.8}$$

where δ_i^2 is the squared wavenumber. It is given by

$$\delta_1^2 = \frac{\omega^2}{2(PR - Q^2)} \left[P\tilde{\rho}_{22} + R\tilde{\rho}_{11} - 2Q\tilde{\rho}_{12} - \sqrt{\Delta_c}\right] \tag{A.9}$$

$$\delta_2^2 = \frac{\omega^2}{2(PR - Q^2)} \left[P\tilde{\rho}_{22} + R\tilde{\rho}_{11} - 2Q\tilde{\rho}_{12} + \sqrt{\Delta_c}\right] \tag{A.10}$$

$$\delta_3^2 = \frac{\omega^2}{N} \left(\frac{\tilde{\rho}_{11}\tilde{\rho}_{22} - \tilde{\rho}_{12}^2}{\tilde{\rho}_{22}}\right) \tag{A.11}$$

$$\Delta_c = \left[P\tilde{\rho}_{22} + R\tilde{\rho}_{11} - 2Q\tilde{\rho}_{12}\right]^2 - 4(PR - Q^2)\left(\tilde{\rho}_{11}\tilde{\rho}_{22} - \tilde{\rho}_{12}^2\right) \tag{A.12}$$

The frame displacement potentials of the compressional waves are written as

$$\phi_i^s = A_i \exp\left(\mathrm{i}(\omega t - k_{i3}x_3 - k_t x_1)\right) + A_i' \exp\left(\mathrm{i}(\omega t + k_{i3}x_3 - k_t x_1)\right) \tag{A.13}$$

where the superscript 's' means solid. The displacement potentials from the rotational waves are all zero in the $x_1 - x_3$ plane except for the x_2 component:

$$\psi_2^s = A_3 \exp\left(\mathrm{i}(\omega t - k_{33}x_3 - k_t x_1)\right) + A_3' \exp\left(\mathrm{i}(\omega t + k_{33}x_3 - k_t x_1)\right) \tag{A.14}$$

The potentials for the air displacement in the pores are given by

$$\phi_i^f = \mu_i \phi_i^s \quad i = 1, 2 \tag{A.15}$$

$$\psi_2^f = \mu_3 \psi_2^s \tag{A.16}$$

where the superscript 'f' represent the air in the pores and μ_i is the ratio of the velocity of the air and the velocity of the frame. These are given by

$$\mu_i = \frac{P\delta_i^2 - \omega^2\tilde{\rho}_{11}}{\omega^2\tilde{\rho}_{12} - Q\delta_i^2} \quad i = 1, 2 \tag{A.17}$$

$$\mu_3 = \frac{N\delta_3^2 - \omega^2\tilde{\rho}_{11}}{\omega^2\tilde{\rho}_{22}} \tag{A.18}$$

The acoustic field at point M is defined by six independent quantities:

$$\mathbf{V}^p(M) = \left[\begin{array}{cccccc} v_1^s(M) & v_3^s(M) & v_3^f(M) & \sigma_{33}^s(M) & \sigma_{13}^s(M) & \sigma_{33}^f(M) \end{array}\right]^{\mathrm{T}} \tag{A.19}$$

where v_i is the velocity in i–direction, σ_{ij} is (i,j) component of the stress tensor. Expressing $\mathbf{V}^p(M)$ and $\mathbf{V}^p(M')$ using the displacement potentials of the three waves for the solid gives the relation between the points M and M':

$$\mathbf{V}^p(M) = \mathbf{T}^p\mathbf{V}^p(M') \tag{A.20}$$

A way of deriving the transfer matrix is given in [49]. Here all the components of the 6×6 matrix are given:

$$T_{11}^p = \frac{2N\beta^2(p_2D_1 - p_1D_2) - (p_3(C_1D_2 - C_2D_1))}{\Delta} \tag{A.21}$$

$$T_{12}^p = \mathrm{i}\beta\frac{\alpha_2 q_1\left[\mu_2\left(\alpha_3^2 - \beta^2\right) + 2\beta\mu_3\right] - \alpha_1 q_2\left[\mu_1\left(\alpha_3^2 - \beta^2\right) + 2\beta\mu_3\right] + 2\alpha_3 q_3\alpha_1\alpha_2\left(\mu_1 - \mu_2\right)}{\alpha_1\alpha_2\left(\mu_1 - \mu_2\right)\left(\beta^2 + \alpha_3^2\right)} \tag{A.22}$$

$$T_{13}^p = \mathrm{i}\beta\frac{(\alpha_1 q_2 - \alpha_2 q_1)}{\alpha_1\alpha_2\left(\mu_1 - \mu_2\right)} \tag{A.23}$$

$$T_{14}^{p} = \beta\omega\frac{[p_1 D_2 - p_2 D_1 - p_3(D_2 - D_1)]}{\Delta} \tag{A.24}$$

$$T_{15}^{p} = \frac{\mathrm{i}\omega}{N(\beta^2 + \alpha_3^2)}\left(\frac{\beta^2 q_1(\mu_2 - \mu_3)}{\alpha_3(\mu_2 - \mu_1)} + \frac{\beta^2 q_2(\mu_1 - \mu_3)}{\alpha_2(\mu_1 - \mu_2)} + \alpha_3 q_3\right) \tag{A.25}$$

$$T_{16}^{p} = \beta\omega\frac{p_2 C_1 - p_1 C_2 - p_3(C_1 - C_2) + 2N\beta^2(p_2 - p_1)}{\Delta} \tag{A.26}$$

$$T_{21}^{p} = \frac{\mathrm{i}\beta}{\Delta}\left(2N(\alpha_1 q_1 D_2 - \alpha_2 q_2 D_1) - \frac{q_3}{\alpha_3}(C_1 D_2 - C_2 D_1)\right) \tag{A.27}$$

$$T_{22}^{p} = \frac{p_2\left[\mu_1(\alpha_3^2 - \beta^2) + 2\beta^2\mu_3\right] - p_1\left[\mu_2(\alpha_3^2 - \beta^2) + 2\beta^2\mu_3\right] + 2\beta^2 p_3(\mu_1 - \mu_2)}{(\mu_1 - \mu_2)(\beta^2 + \alpha_3^2)} \tag{A.28}$$

$$T_{23}^{p} = \frac{p_1 - p_3}{\mu_1 - \mu_2} \tag{A.29}$$

$$T_{24}^{p} = -\frac{\mathrm{i}\omega}{\Delta}\left(\alpha_1 q_1 D_2 - \alpha_2 q_2 D_1 + \frac{\beta^2 q_3}{\alpha_3}(D_2 - D_1)\right) \tag{A.30}$$

$$T_{25}^{p} = -\frac{\omega\beta}{N(\beta^2 + \alpha_3^2)}\left(p_1\frac{\mu_2 - \mu_3}{\mu_2 - \mu_1} + p_2\frac{\mu_1 - \mu_3}{\mu_1 - \mu_2} - p_3\right) \tag{A.31}$$

$$T_{26}^{p} = \frac{\mathrm{i}\omega}{\Delta}\left(\alpha_1 q_1(C_2 + 2N\beta^2) - \alpha_2 q_2(C_1 2N\beta^2) - \frac{q_3\beta^2}{\alpha_3}(C_1 - C_2)\right) \tag{A.32}$$

$$T_{31}^{p} = \frac{\mathrm{i}\beta}{\Delta}\left(2N(\alpha_1\mu_1 q_1 D_2 - \alpha_2\mu_2 q_2 D_1) - \frac{\mu_3 q_3}{\alpha_3}(C_1 D_2 - C_2 D_1)\right) \tag{A.33}$$

$$T_{32}^{p} = \frac{-\mu_1 p_1\left[\mu_2(\alpha_3^2 - \beta^2) + 2\beta^2\mu_3\right] + \mu_2 p_2\left[\mu_1(\alpha_3^2 - \beta^2) + 2\beta^2\mu_3\right] + 2\beta^2\mu_3 p_3(\mu_1 - \mu_2)}{(\mu_1 - \mu_2)(\alpha_3^2 + \beta^2)} \tag{A.34}$$

$$T_{33}^{p} = \frac{\mu_1 p_1 - \mu_2 p_2}{\mu_1 - \mu_2} \tag{A.35}$$

$$T_{34}^{p} = \frac{\mathrm{i}\omega}{\Delta}\left(-\alpha_1\mu_1 q_1 D_2 + \alpha_2\mu_2 q_2 D_1 + \frac{\beta^2\mu_3 q_3}{\alpha_3}(D_1 - D_2)\right) \tag{A.36}$$

$$T_{35}^{p} = \frac{-\beta\omega}{N(\alpha_3^2 + \beta^2)}\left(p_1\mu_1\frac{\mu_2 - \mu_3}{\mu_2 - \mu_1} + p_2\mu_2\frac{\mu_1 - \mu_3}{\mu_1 - \mu_2} - p_3\mu_3\right) \tag{A.37}$$

$$T_{36}^{p} = \frac{\mathrm{i}\omega}{\Delta}\left(\mu_1\alpha_1 q_1(C_2 + 2N\beta^2) - \mu_2\alpha_2 q_2(C_1 + 2N\beta^2) - \frac{\beta^2}{\alpha_3}\mu_3 q_3(C_1 - C_2)\right) \tag{A.38}$$

$$T_{41}^{p} = \frac{2N\beta}{\omega\Delta}\left[C_1 p_1 D_2 - C_2 p_2 D_1 - p_3(C_1 D_2 - C_2 D_1)\right] \tag{A.39}$$

$$T_{42}^{p} = -\mathrm{i}\frac{C_1 q_1\alpha_2\left[\mu_2(\alpha_3^2 - \beta^2)\right] - C_2 q_2\alpha_1\left[\mu_1(\alpha_3^2 - \beta^2) + 2\beta^2\mu_3\right] - 4N\alpha_3\beta^2\alpha_1\alpha_2(\mu_1 - \mu_2)q_3}{\alpha_1\alpha_2\omega(\beta^2 + \alpha_3^2)(\mu_1 - \mu_2)} \tag{A.40}$$

$$T_{43}^{p} = \mathrm{i}\frac{\alpha_2 C_1 q_1 - \alpha_1 C_2 q_2}{\omega\alpha_1\alpha_2(\mu_1 - \mu_2)} \tag{A.41}$$

$$T_{44}^{p} = \frac{-p_1 C_2 D_2 + p_2 C_2 D_1 - 2N\beta^2 p_3(D_2 - D_1)}{\Delta} \tag{A.42}$$

$$T_{45}^{p} = \frac{-\mathrm{i}\beta}{\beta^2+\alpha_3^2}\left(\frac{C_1 q_1}{N\alpha_1}\frac{\mu_2-\mu_3}{\mu_2-\mu_1} + \frac{C_2 q_2}{N\alpha_2}\frac{\mu_1-\mu_3}{\mu_1-\mu_2} - 2q_3\alpha_3\right) \tag{A.43}$$

$$T_{46}^{p} = \frac{p_1 C_1(C_2+2N\beta^2) - p_2 C_2(C_1+2N\beta^2) - 2N\beta^2 p_3(C_1-C_2)}{\Delta} \tag{A.44}$$

$$T_{51}^{p} = \frac{\mathrm{i}N\beta^2}{\Delta\omega}\left(4N\alpha_1 q_1 D_2 - 4N\alpha_2 q_2 D_1 - q_3\frac{\alpha_3^2-\beta^2}{\beta^2\alpha_3}(C_1D_2 - C_2D_1)\right) \tag{A.45}$$

$$T_{52}^{p} = \frac{2N\beta p_1\left[\mu_2(\alpha_3^2-\beta^2)+2\beta^2\mu_3\right] - 2N\beta p_2\left[\mu_1(\alpha_3^2-\beta^2)+2\beta^2\mu_3\right] + 2N\beta p_3(\alpha_3^2-\beta^2)(\mu_1-\mu_2)}{\omega(\mu_1-\mu_2)(\beta^2+\alpha_3^2)} \tag{A.46}$$

$$T_{53}^{p} = \frac{-2N\beta}{\omega(\mu_1-\mu_2)}(p_1-p_2) \tag{A.47}$$

$$T_{54}^{p} = \frac{2\mathrm{i}N\beta}{\Delta}\left(\alpha_1 q_1 D_2 - \alpha_2 q_2 D_1 - \frac{q_3}{2}\frac{\alpha_3^2-\beta^2}{\alpha_3}(D_2-D_1)\right) \tag{A.48}$$

$$T_{55}^{p} = \frac{2\beta^2}{\beta^2+\alpha_3^2}\left(p_1\frac{\mu_2-\mu_3}{\mu_2-\mu_1} + p_2\frac{\mu_1-\mu_3}{\mu_1-\mu_2} + p_3\frac{\alpha_3^2-\beta^2}{2\beta^2}\right) \tag{A.49}$$

$$T_{56}^{p} = \frac{-2\mathrm{i}N\beta}{\Delta}\left(\alpha_1 q_1(C_2+2N\beta^2) - \alpha_2 q_2(C_1+2N\beta^2) + \frac{q_3}{2}\frac{\alpha_3^2-\beta^2}{\alpha_3}(C_1-C_2)\right) \tag{A.50}$$

$$T_{61}^{p} = \frac{2N\beta D_1 D_2}{\omega\Delta}(p_1-p_2) \tag{A.51}$$

$$T_{62}^{p} = -\frac{\mathrm{i}}{\omega}\frac{\alpha_2 q_1 D_1\left[\mu_2(\alpha_3^2-\beta^2)+2\beta^2\mu_3\right] - \alpha_1 q_2 D_2\left[\mu_1(\alpha_3^2-\beta^2)+2\beta^2\mu_3\right]}{\alpha_1\alpha_2(\mu_1-\mu_2)(\beta^2+\alpha_3^2)} \tag{A.52}$$

$$T_{63}^{p} = \frac{\mathrm{i}}{\omega(\mu_1-\mu_2)}\left(\frac{q_1 D_1}{\alpha_1} - \frac{q_2 D_2}{\alpha_2}\right) \tag{A.53}$$

$$T_{64}^{p} = \frac{-D_1 D_2}{\Delta}(p_1-p_2) \tag{A.54}$$

$$T_{65}^{p} = -\frac{\mathrm{i}\beta}{N(\beta^2+\alpha_3^2)}\left(\frac{q_1 D_1}{\alpha_1}\frac{\mu_2-\mu_3}{\mu_2-\mu_1} + \frac{q_2 D_2}{\alpha_2}\frac{\mu_1-\mu_3}{\mu_1-\mu_2}\right) \tag{A.55}$$

$$T_{66}^{p} = \frac{p_1 D_1(C_2+2N\beta^2) - p_2 D_2(C_1+2N\beta^2)}{\Delta} \tag{A.56}$$

where the quantities $\alpha_i, \beta, C_i, D_i, p_i, q_i$ and Δ are given by

$$\alpha_i = k_{i3} \quad i = 1,2,3 \tag{A.57}$$

$$\beta = k_t \tag{A.58}$$

$$C_i = (P+Q\mu_i)(\beta^2+\alpha_i^2) - 2N\beta^2 \quad i = 1,2 \tag{A.59}$$

$$D_i = (R\mu_i+Q)(\beta^2+\alpha_i^2) \quad i = 1,2 \tag{A.60}$$

$$p_i = \cos\alpha_i h \quad i = 1,2,3 \tag{A.61}$$

$$q_i = \sin \alpha_i h \quad i = 1, 2, 3 \tag{A.62}$$

$$\Delta = D_1(2N\beta^2 + C_2) - D_2(2N\beta^2 + C_1) \tag{A.63}$$

A.4 Coupling two domains

The coupling between a poro–elastic layer and a fluid layer can be achieved by applying the continuity conditions between M_2 and M_3 in Figure A.2. This can be written as

$$\mathbf{I}_{pf}\mathbf{V}^p(M_2) + \mathbf{J}_{pf}\mathbf{V}^f(M_3) = 0 \tag{A.64}$$

where $\mathbf{I}_{pf}$ and $\mathbf{J}_{pf}$ represent the continuity conditions.

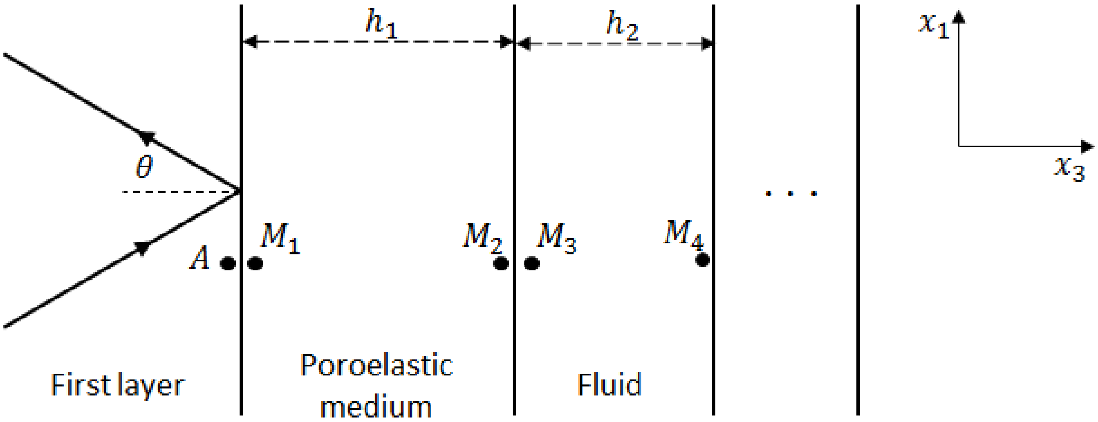

Figure A.2. Plane wave impinging on a poro–elastic medium – fluid system

The continuity conditions are

$$(1-\phi)v_3^s(M_2) + \phi v_3^f(M_2) = v_3^f(M_3) \tag{A.65}$$

$$\sigma_{33}^s(M_2) = -(1-\phi)p(M_3) \tag{A.66}$$

$$\sigma_{13}^s = 0 \tag{A.67}$$

$$\sigma_{33}^f(M_2) = -\phi p(M_3) \tag{A.68}$$

where ϕ is the porosity. The coupling matrices are given by

$$\mathbf{I}_{pf} = \begin{bmatrix} 0 & 1-\phi & \phi & 0 & 0 & 0 \\ 0 & 0 & 0 & 1 & 0 & 0 \\ 0 & 0 & 0 & 0 & 1 & 0 \\ 0 & 0 & 0 & 0 & 0 & 1 \end{bmatrix} \tag{A.69}$$

$$\mathbf{J}_{pf} = \begin{bmatrix} 0 & -1 \\ 1-\phi & 0 \\ 0 & 0 \\ \phi & 0 \end{bmatrix} \tag{A.70}$$

A.4.1 Global matrix

As a simple example, Figure A.2 is considered. From Equations (A.2) and (A.64) one can assemble the matrices for the layers. These are given by

$$\mathbf{I}_{ap}\mathbf{V}^a(A) + \mathbf{J}_{ap}\mathbf{T}^p\mathbf{V}^p(M_2) = 0 \tag{A.71}$$

$$\mathbf{I}_{pf}\mathbf{V}^p(M_2) + \mathbf{J}_{pf}\mathbf{T}^f\mathbf{V}^f(M_4) = 0 \tag{A.72}$$

These can be expressed in a form of $\mathbf{D}_0\mathbf{V}_0 = 0$, where

$$\mathbf{D}_0 = \begin{bmatrix} \mathbf{I}_{ap} & \mathbf{J}_{ap}\mathbf{T}^p & \mathbf{0} \\ \mathbf{0} & \mathbf{I}_{pf} & \mathbf{J}_{pf}\mathbf{T}^f \end{bmatrix} \tag{A.73}$$

$$\mathbf{V}_0 = \begin{bmatrix} \mathbf{V}^a(A) & \mathbf{V}^p(M_2) & \mathbf{V}^f(M_4) \end{bmatrix}^{\mathrm{T}} \tag{A.74}$$

The matrix contains insufficient equations to be well posed. Remaining equations are supplied by boundary conditions and the excitation. The excitation side (A) needs one impedance condition which relates the velocity to pressure, and the other side (M_4) needs equations depending on the type of the layer. For a porous layer three equations are needed, and one for a fluid layer. Thus in Figure A.2 the total number of equations needed is four.

A rigid termination can be given with zero velocity. For a porous layer and a fluid layer it is given by

$$\mathbf{Y}^p = \begin{bmatrix} 1 & 0 & 0 & 0 & 0 & 0 \\ 0 & 1 & 0 & 0 & 0 & 0 \\ 0 & 0 & 1 & 0 & 0 & 0 \end{bmatrix} \tag{A.75}$$

$$\mathbf{Y}^f = \begin{bmatrix} 1 & 0 & 0 & 0 \\ 0 & 1 & 0 & 0 \end{bmatrix} \tag{A.76}$$

Now a matrix with the boundary conditions at M_4 can be written as

$$\mathbf{D} = \begin{bmatrix} & \mathbf{D}_0 & \\ --- & --- & --- \\ \mathbf{0} & \cdots & \mathbf{Y}^f \end{bmatrix} \tag{A.77}$$

Still one more condition is needed from the excitation side. A case for calculating the surface impedance is given below as an example.

A.4.2 Surface impedance

If the surface impedance at A is $Z_s = p(A)/v_3^a(A)$, then $\mathbf{V}^a(A)$ can be expressed as

$$\begin{bmatrix} -1 & Z_s \end{bmatrix} \mathbf{V}^a(A) = 0 \tag{A.78}$$

Adding this equation to the top of the global matrix $\mathbf{D}$ completes the assembly process. It is written as

$$\begin{bmatrix} -1 & Z_s & 0 & \cdots & 0 \\ --- & --- & --- & --- & --- \\ & & \mathbf{D} & & \end{bmatrix} \mathbf{V}_0 = \mathbf{0} \tag{A.79}$$

The determinant of this matrix is zero, so the surface impedance can be calculated by

$$Z_s = -\frac{\det \mathbf{D_1}}{\det \mathbf{D_2}} \tag{A.80}$$

where $\det \mathbf{D_1}$ (or $\det \mathbf{D_2}$) is the determinant when the first column (or the second column) is removed from $\mathbf{D}$.

Appendix B

Finite element model for fluid

In this appendix a finite element formulation of sound propagation in fluid (air) is presented.

B.1 Outline of the theory

The steady–state governing equation for time–harmonic (with implicit variation $e^{\mathrm{i}\omega t}$ for circular frequency ω) linear acoustics is the Helmholtz equation and is given by

$$\boldsymbol{\nabla}^2 p + k^2 p = 0 \tag{B.1}$$

where $k = \omega/c$ is the wavenumber with c the speed of sound in the medium. For a given domain V that is bounded by a surface Ω, a weak formulation can be obtained by imposing an admissible pressure variation δp. Multiplying Equation (B.1) by δp and integrating over the domain V yields

$$\int_V \delta p \left(\boldsymbol{\nabla}^2 p + k^2 p\right) \mathrm{d}V = 0 \tag{B.2}$$

Using vector calculus identities, this is reformulated as

$$\int_V \left(\boldsymbol{\nabla} \cdot (\delta p \boldsymbol{\nabla} p) - \boldsymbol{\nabla} p \cdot \boldsymbol{\nabla} \delta p + k^2 p \delta p\right) \mathrm{d}V = 0 \tag{B.3}$$

where $\mathbf{n}$ is the outward normal vector. From Euler's equation (conservation of momentum),

$$\boldsymbol{\nabla} p \cdot \mathbf{n} = -\rho_0 \frac{\partial v}{\partial t} \cdot \mathbf{n} = -\rho_0 \mathrm{i}\omega v_n \tag{B.4}$$

Rearranging the terms yields

$$\int_V \boldsymbol{\nabla} p \cdot \boldsymbol{\nabla} \delta p \mathrm{d}V - \omega^2 \int_V \frac{1}{c^2} p \delta p \mathrm{d}V = -\int_\Omega \mathrm{i}\rho_0 \omega v_n \delta p \mathrm{d}\Omega \tag{B.5}$$

In this equation, the terms are associated, in order from left to right, with acoustic stiffness, acoustic mass, and boundary excitation, respectively. In the following section, each term will be discretized to allow numerical implementation.

B.2 Finite element discretization

In the finite element method, the whole fluid domain is discretized into smaller domains which are called elements. In each element, the pressure variable p is assumed to vary continuously depending on the shape functions of the element. The shape function is defined as having a value of 1 at one node, and 0 at the other nodes. Based on this concept, the pressure is also defined at each node. The pressure p in the domain can be given with the nodal pressures p_i, which is given by

$$p = \sum_{i=1}^{n} N_i p_i \tag{B.6}$$

where N_i is the shape function for the i^{th} node. The pressure gradient is given by

$$\boldsymbol{\nabla} p = \boldsymbol{\partial} \mathbf{N} \{p_i\} \tag{B.7}$$

where $\boldsymbol{\partial}$ is the gradient operator. With these, all terms in the equation can be discretized into element matrices and through the standard assembly process the global matrices of stiffness and mass can be obtained. In the same way, the source term can be discretized depending on a spatial distribution of the source. In summary, these terms are expressed as

$$\mathbf{K}_a = \int_V \mathbf{B}^{\mathrm{T}} \mathbf{B} \mathrm{d}V \tag{B.8}$$

$$\mathbf{M}_a = \int_V \frac{1}{c^2} \mathbf{N}^{\mathrm{T}} \mathbf{N} \mathrm{d}V \tag{B.9}$$

In most cases the boundaries of an uncoupled acoustic domain consist of imposed pressure, normal velocity, or normal boundary impedance depending on the situation. The following equations are used to calculate the boundary integral term in equation (B.5). On the boundary with imposed pressure ($\bar{p}$),

$$p = \bar{p} \tag{B.10}$$

On the boundary with imposed normal velocity ($\bar{v}_n$),

$$v_n = \frac{\mathrm{i}}{\rho_0 \omega} \frac{\partial p}{\partial n} = \bar{v}_n \tag{B.11}$$

On the boundary with defined impedance $\bar{Z}$,

$$p = \bar{Z} v_n = \frac{\mathrm{i}\bar{Z}}{\rho_0 \omega} \frac{\partial p}{\partial n} \tag{B.12}$$

After a few steps of manipulation, the full matrix equation is obtained.

$$\{\delta p\}^{\mathrm{T}} \left(\mathbf{K}_a + j\omega \mathbf{C}_a - \omega^2 \mathbf{M}_a \right) \{p\} = \{\delta p\}^{\mathrm{T}} \left(\mathbf{V}_{n,a} + \mathbf{P}_a \right) \tag{B.13}$$

Here, $\mathbf{C}_a$ and $\mathbf{V}_{n,a}$ represent the impedance boundary and the imposed velocity boundary and are given by

$$\mathbf{C}_a = \int_\Omega \frac{\rho_0}{\bar{Z}} \mathbf{N}^{\mathrm{T}} \mathbf{N} \mathrm{d}\Omega \tag{B.14}$$

$$\mathbf{V}_{n,a} = \int_\Omega -\mathrm{i} \rho_0 \omega \mathbf{N}^{\mathrm{T}} \bar{v}_n \mathrm{d}\Omega \tag{B.15}$$

For the imposed pressure $\mathbf{P}_a$, the prescribed pressure is directly imposed onto the global matrix or for zero pressure the rows and columns that represent the imposed pressure boundary are removed from the global matrix.

The following example is used for validation of the code against an analytical solution. Note that linear shape functions have been used.

B.3 Validation of the model

A rectangular duct of length $L_x = 1$ m and width $L_y = 0.1$ m with a rigid wall has been used for validation, see Figure B.1. An input harmonic velocity of amplitude $\mathrm{i}\omega X$ is given at the entrance of the duct.

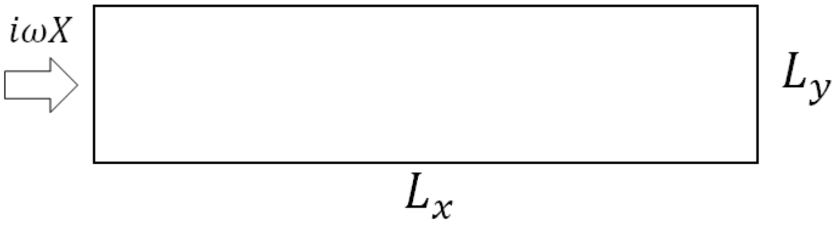

Figure B.1. Geometry of the problem (not to scale)

For a one-dimensional duct the exact solution for the steady state pressure amplitude in the duct can be obtained by solving the homogeneous Helmholtz equation with boundary conditions at both ends. The form of the solution is

$$p(x) = Ae^{-\mathrm{i}kx} + Be^{\mathrm{i}kx} \tag{B.16}$$

where the time dependence $e^{\mathrm{i}\omega t}$ is suppressed. The boundary conditions are

$$u(x) = \mathrm{i}\omega X \quad \text{at } x = 0 \tag{B.17}$$

$$u(x) = 0 \qquad \text{at } x = L_x \tag{B.18}$$

where $u(x)$ is the particle velocity in the x direction. Applying the boundary conditions the coefficients A and B can be determined. The solution is

$$p(x) = \rho_0 c\omega X \left[\sin\frac{\omega x}{c} + \frac{1}{\tan\frac{\omega L_x}{c}} \cos\frac{\omega x}{c} \right] \tag{B.19}$$

For a case with $L_x = 1$ m, $L_y = 0.1$ m, $X = 10^{-6}$ m, $f = 500$ Hz and 100 elements along the x–axis (20 elements along the y–axis), a comparison has been made between the finite element method and the analytical solution, as shown in Figure B.2. The results are compared in terms of the real part of the solution. Good agreement is found between the analytical solution and the finite element solution.

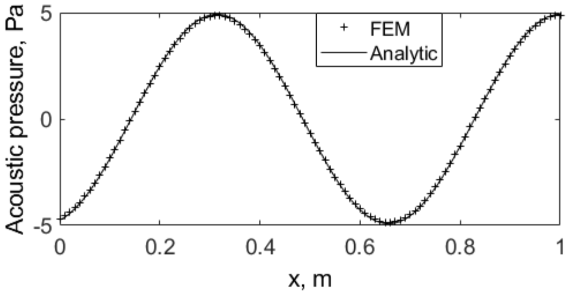

Figure B.2. Comparison of the real part of the sound pressure along the centre line of the tube at 500 Hz

As the accuracy depends on the frequency and the number of elements, this should be considered before the calculation. It is recommended to use at least 6 elements per wavelength [111]. As this case is used to validate the model itself, in this calculation, about 20 elements per wavelength are used.

Appendix C

Poro–elastic variables

The bulk modulus of the frame in vacuum is

$$K_b = \frac{2N(\nu+1)}{3(1-2\nu)} \tag{C.1}$$

where N is the shear modulus of the solid and ν is the Poisson's ratio. If the bulk modulus of the material from which the frame is made is K_s and the effective bulk modulus of the saturated fluid which can be obtained from the rigid frame model is K_f, the Biot coefficients become [49]

$$P = \frac{(1-\phi)(1-\phi-K_b/K_s)K_s + \phi(K_s/K_f)K_b}{1-\phi-K_b/K_s+\phi K_s/K_f} - \frac{2N}{3} \tag{C.2}$$

$$Q = \frac{(1-\phi-K_b/K_s)\phi K_s}{1-\phi-K_b/K_s+\phi K_s/K_f} \tag{C.3}$$

$$R = \frac{\phi^2 K_s}{1-\phi-K_b/K_s+\phi K_s/K_f} \tag{C.4}$$

Effective densities, the coupling coefficient and the modified stress tensor are given by

$$\rho_a = \phi\rho_0(\alpha_\infty - 1) \tag{C.5}$$

$$\tilde{\rho}_{11} = \rho_1 + \rho_a - \mathrm{i}\sigma\phi^2\frac{G(\omega)}{\omega} \tag{C.6}$$

$$\tilde{\rho}_{12} = -\rho_a + \mathrm{i}\sigma\phi^2\frac{G(\omega)}{\omega} \tag{C.7}$$

$$\tilde{\rho}_{11} = -\phi\rho_0 + \rho_a - \mathrm{i}\sigma\phi^2\frac{G(\omega)}{\omega} \tag{C.8}$$

$$\tilde{\rho} = \tilde{\rho}_{11} - \frac{\tilde{\rho}_{12}^2}{\tilde{\rho}_{22}} \tag{C.9}$$

$$\tilde{\gamma} = \phi \left(\frac{\tilde{\rho}_{12}}{\tilde{\rho}_{22}} - \frac{Q}{R} \right) \tag{C.10}$$

$$\hat{\boldsymbol{\sigma}}^s = \left(P - \frac{Q^2}{R} \right) \boldsymbol{\nabla} \cdot \mathbf{uI} + 2N \boldsymbol{\epsilon}^s \tag{C.11}$$

where ρ_1 is the density of the frame and ρ_0 is the density of the fluid in the pores.

Appendix D

Calculation of radiation ratio of a structure from a reverberant chamber measurement

The radiation ratio of a vibrating structure in Sections 5.2 and 5.3 was calculated by the following equation:

$$\sigma_{\text{rad}} = \frac{W/\overline{F^2}}{\rho c S \langle |Y_t|^2 \rangle} \tag{D.1}$$

where W is the radiated sound power from the structure, $\overline{F^2}$ is the mean-square force acting on the structure, ρ and c are the density of air and the speed of sound in air, S is the surface area of the structure and $\langle |Y_t|^2 \rangle = \langle \overline{v^2} \rangle / \overline{F^2}$ is the spatially–averaged transfer mobility with $\langle \overline{v^2} \rangle$ being the spatially–averaged mean-square normal vibration velocity.

The denominator in Equation (D.1) can be measured directly using a shaker or an instrumented hammer and an accelerometer. The numerator can be obtained from a reciprocal measurement in the reverberant chamber, which is given by

$$\frac{W}{\overline{F^2}} = \frac{S\bar{\alpha}}{4\rho c} \frac{\langle \overline{p^2} \rangle}{\overline{F^2}} \tag{D.2}$$

where $S\bar{\alpha}$ is the room absorption and $\langle \overline{p^2} \rangle$ is the spatially–averaged mean–sqaure pressure in the chamber. Applying the principle of reciprocity and using the sound power relation, the equation becomes [101]

$$W/\overline{F^2} = \frac{\overline{a_Q^2}}{\langle \overline{p_Q^2} \rangle} \frac{\rho}{4\pi c} \tag{D.3}$$

where a_Q is the acceleration response of the structure and $\langle \overline{p_Q^2} \rangle$ is the spatially–averaged mean–square acoustic pressure in the chamber due to the sound source Q. Excited by a loudspeaker, the accelerometer attached to the structure at the position where the force was applied in the transfer mobility measurement and a rotating microphone in the chamber meausre the acceleration a_Q and the mean pressure $\langle \overline{p_Q^2} \rangle$, respectively. From these the radiation ratio can be calculated.

References

[1] D. Thompson, Railway noise and vibration: mechanisms, modelling and means of control, Elsevier, 2008.

[2] P. J. Remington, Wheel/rail noise–part I: Characterization of the wheel/rail dynamic system, Journal of Sound and Vibration 46 (3) (1976) 359–379.

[3] P. J. Remington, Wheel/rail noise–part IV: Rolling noise, Journal of Sound and Vibration 46 (3) (1976) 419–436.

[4] P. J. Remington, Wheel/rail rolling noise, I: Theoretical analysis, The Journal of the Acoustical Society of America 81 (6) (1987) 1805–1823.

[5] P. J. Remington, Wheel/rail rolling noise, II: Validation of the theory, The Journal of the Acoustical Society of America 81 (6) (1987) 1824–1832.

[6] D. J. Thompson, Wheel-rail noise generation, part I: introduction and interaction model, Journal of Sound and Vibration 161 (3) (1993) 387–400.

[7] D. J. Thompson, Wheel-rail noise generation, part II: wheel vibration, Journal of Sound and Vibration 161 (3) (1993) 401–419.

[8] D. J. Thompson, Wheel-rail noise generation, part III: rail vibration, Journal of Sound and Vibration 161 (3) (1993) 421–446.

[9] D. J. Thompson, Wheel-rail noise generation, part IV: contact zone and results, Journal of Sound and Vibration 161 (3) (1993) 447–466.

[10] D. J. Thompson, Wheel-rail noise generation, part V: inclusion of wheel rotation, Journal of Sound and Vibration 161 (3) (1993) 467–482.

[11] D. J. Thompson, B. Hemsworth, N. Vincent, Experimental validation of the TWINS prediction program for rolling noise, part 1: description of the model and method, Journal of Sound and Vibration 193 (1) (1996) 123–135.

[12] D. J. Thompson, P. Fodiman, H. Mahé, Experimental validation of the TWINS prediction program for rolling noise, part 2: results, Journal of Sound and Vibration 193 (1) (1996) 137–147.

[13] X. Zhang, Modelling of track sound radiation, Ph.D. thesis, University of Southampton (2016).

[14] X. Sheng, C. J. C. Jones, D. J. Thompson, Modelling ground vibration from railways using wavenumber finite-and boundary-element methods, in: Proceedings of the Royal Society of London A: Mathematical, Physical and Engineering Sciences, Vol. 461, The Royal Society, 2005, pp. 2043–2070.

[15] X. Sheng, C. J. C. Jones, D. J. Thompson, Prediction of ground vibration from trains using the wavenumber finite and boundary element methods, Journal of Sound and Vibration 293 (3) (2006) 575–586.

[16] C.-M. Nilsson, C. J. C. Jones, D. J. Thompson, J. Ryue, A waveguide finite element and boundary element approach to calculating the sound radiated by railway and tram rails, Journal of Sound and Vibration 321 (3-5) (2009) 813–836.

[17] J. Ryue, S. Jang, D. J. Thompson, A wavenumber domain numerical analysis of rail noise including the surface impedance of the ground, Journal of Sound and Vibration 432 (2018) 173–191.

[18] ISO 9053:1001, Acoustics – Materials for acoustical applications – Determination of airflow resistance, Standard, International Organization for Standardization (Mar. 1993).

[19] ISO 18437-5:2011, Mechanical vibration and shock-Characterization of the dynamic mechanical properties of visco-elastic materials, Part 5: Poisson ratio based on comparison between measurements and finite element analysis, Standard, International Organization for Standardization (Apr. 2011).

[20] C. M. Nilsson, C. J. C. Jones, Theory manual for WANDS 2.1, ISVR Technical Memorandum University of Southampton.

[21] C. M. Nilsson, C. J. C. Jones, Manual for WANDS 2.1 wavenumber domain software for solids and fluids.

[22] J. Oertli, The STAIRRS project, work package 1: a cost-effectiveness analysis of railway noise reduction on a European scale, Journal of Sound and Vibration 267 (3) (2003) 431–437.

[23] A. Jolibois, J. Defrance, H. Koreneff, P. Jean, D. Duhamel, V. W. Sparrow, In situ measurement of the acoustic performance of a full scale tramway low height noise barrier prototype, Applied Acoustics 94 (2015) 57–68.

[24] F. Koussa, J. Defrance, P. Jean, P. Blanc-Benon, Acoustic performance of gabions noise barriers: numerical and experimental approaches, Applied Acoustics 74 (1) (2013) 189–197.

[25] C. J. C. Jones, A. E. J. Hardy, R. R. K. Jones, A. Wang, Bogie shrouds and low track-side barriers for the control of railway vehicle rolling noise, Journal of Sound and Vibration 193 (1) (1996) 427–431.

[26] C. J. C. Jones, D. J. Thompson, T. P. Waters, Application of numerical models to a system of train-and track-mounted acoustic shields, International Journal of Acoustics and Vibration 6 (4) (2001) 185–192.

[27] A. Frid, Skirts and barriers for reduction of wayside noise from railway vehiclesan experimental investigation with application to the BR185 locomotive, Journal of Sound and Vibration 267 (3) (2003) 709–719.

[28] H. G. Jonasson, Diffraction by wedges of finite acoustic impedance with applications to depressed roads, Journal of Sound and Vibration 25 (4) (1972) 577–585.

[29] H. G. Jonasson, Sound reduction by barriers on the ground, Journal of Sound and Vibration 22 (1) (1972) 113–126.

[30] P. Koers, Diffraction by an absorbing barrier or by an impedance transition, in: INTER-NOISE and NOISE-CON Congress and Conference Proceedings, Vol. 1983, Institute of Noise Control Engineering, 1983, pp. 311–314.

[31] A. D. Pierce, Diffraction of sound around corners and over wide barriers, The Journal of the Acoustical Society of America 55 (5) (1974) 941–955.

[32] W. J. Hadden Jr, A. D. Pierce, Sound diffraction around screens and wedges for arbitrary point source locations, The Journal of the Acoustical Society of America 69 (5) (1981) 1266–1276.

[33] R. Seznec, Diffraction of sound around barriers: use of the boundary elements technique, Journal of Sound and Vibration 73 (2) (1980) 195–209.

[34] P. A. Morgan, D. C. Hothersall, S. N. Chandler-Wilde, Influence of shape and absorbing surface–a numerical study of railway noise barriers, Journal of Sound and Vibration 217 (3) (1998) 405–417.

[35] P. Jean, A variational approach for the study of outdoor sound propagation and application to railway noise, Journal of Sound and Vibration 212 (2) (1998) 275–294.

[36] P. Jean, The effect of structural elasticity on the efficiency of noise barriers, Journal of Sound and Vibration 237 (1) (2000) 1–21.

[37] A. Daumas, Etude de la diffraction par un écran mince disposé sur le sol, Acta Acustica united with Acustica 40 (4) (1978) 213–222.

[38] D. Duhamel, Efficient calculation of the three-dimensional sound pressure field around a noise barrier, Journal of Sound and Vibration 197 (5) (1996) 547–571.

[39] S. M. Fard, H. Peters, N. Kessissoglou, S. Marburg, Three-dimensional analysis of a noise barrier using a quasi-periodic boundary element method, The Journal of the Acoustical Society of America 137 (6) (2015) 3107–3114.

[40] D. Shin, Y. Park, Analysis of noise reduction effect of concrete slab by the sound absorption block in urban railway, Vol. 1, The Korean Society For Railway, 2017, pp. 321–322.
URL `http://www.dbpia.co.kr/Article/NODE07266383`

[41] C. Zhao, P. Wang, L. Wang, D. Liu, Reducing railway noise with porous sound-absorbing concrete slabs, Advances in Materials Science and Engineering 2014.

[42] J. Kim, K. Kim, The properties of noise absorbing blocks and their applications for railway, in: INTER-NOISE and NOISE-CON Congress and Conference Proceedings, Vol. 2011, Institute of Noise Control Engineering, 2011, pp. 4708–4713.

[43] R. J. Diehl, R. Nowack, G. Hölzl, Solutions for acoustical problems with ballastless track, Journal of Sound and Vibration 231 (3) (2000) 899–906.

[44] B. Stephen, An assessment of the effectiveness of noise reduction systems on Dublin's light rail system (Luas), in: 11th European Conference on Noise Control 2018 (EURONOISE 2018), 2018, pp. 1337–1344.

[45] J. Defrance, E. Salomons, I. Noordhoek, D. Heimann, B. Plovsing, G. Watts, H. Jonasson, X. Zhang, E. Premat, I. Schmich, et al., Outdoor sound propagation reference model developed in the European Harmonoise project, Acta Acustica united with Acustica 93 (2) (2007) 213–227.

[46] K. Heutschi, Sound propagation over ballast surfaces, Acta Acustica united with Acustica 95 (6) (2009) 1006–1012.

[47] K. Attenborough, P. Boulanger, Q. Qin, R. Jones, Predicted influence of ballast and porous concrete on rail noise, in: INTER-NOISE and NOISE-CON Congress and Conference Proceedings, Vol. 2005, Institute of Noise Control Engineering, 2005, pp. 3547–3555.

[48] K. M. Li, T. Waters-Fuller, K. Attenborough, Sound propagation from a point source over extended-reaction ground, The Journal of the Acoustical Society of America 104 (2) (1998) 679–685.

[49] J. Allard, N. Atalla, Propagation of sound in porous media: modelling sound absorbing materials 2e, John Wiley & Sons, 2009.

[50] O. Umnova, K. Attenborough, K. M. Li, A cell model for the acoustical properties of packings of spheres, Acta Acustica united with Acustica 87 (2) (2001) 226–235.

[51] R. A. Broadbent, D. J. Thompson, C. J. C. Jones, The acoustic properties of railway ballast, in: 8th European Conference on Noise Control 2009 (EURONOISE 2009), 2009, pp. 3307–3316.

[52] X. Zhang, D. J. Thompson, H. Jeong, G. Squicciarini, The effects of ballast on the sound radiation from railway track, Journal of Sound and Vibration 399 (2017) 137–150.

[53] G. Hannema, H.-M. Tröbs, B. Van Damme, A. Zemp, K. Heutschi, B. Lechner, J. Zhang, M. Hecht, S. Sohr, J.-M. Wunderli, Validation of a FEM structure-borne sound radiation model for railway rolling noise, in: Noise and Vibration Emerging Methods, 2018.

[54] M. E. Delany, E. N. Bazley, Acoustical properties of fibrous absorbent materials, Applied Acoustics 3 (2) (1970) 105–116.

[55] Y. Miki, Acoustical properties of porous materials-Modifications of Delany-Bazley models, Journal of the Acoustical Society of Japan (E) 11 (1) (1990) 19–24.

[56] G. Taraldsen, The Delany-Bazley impedance model and Darcy's law, Acta Acustica united with Acustica 91 (1) (2005) 41–50.

[57] N. Voronina, K. Horoshenkov, A new empirical model for the acoustic properties of loose granular media, Applied Acoustics 64 (4) (2003) 415–432.

[58] C. Zwikker, C. W. Kosten, Sound absorbing materials, Elsevier, 1949.

[59] M. R. Stinson, The propagation of plane sound waves in narrow and wide circular tubes, and generalization to uniform tubes of arbitrary cross-sectional shape, The Journal of the Acoustical Society of America 89 (2) (1991) 550–558.

[60] M. C. Berengier, M. R. Stinson, G. A. Daigle, J. F. Hamet, Porous road pavements: Acoustical characterization and propagation effects, The Journal of the Acoustical Society of America 101 (1) (1997) 155–162.

[61] K. Attenborough, Acoustical characteristics of rigid fibrous absorbents and granular materials, The Journal of the Acoustical Society of America 73 (3) (1983) 785–799.

[62] D. K. Wilson, Relaxation-matched modeling of propagation through porous media, including fractal pore structure, The Journal of the Acoustical Society of America 94 (2) (1993) 1136–1145.

[63] K. Attenborough, I. Bashir, S. Taherzadeh, Outdoor ground impedance models, The Journal of the Acoustical Society of America 129 (5) (2011) 2806–2819.

[64] D. L. Johnson, J. Koplik, R. Dashen, Theory of dynamic permeability and tortuosity in fluid-saturated porous media, Journal of Fluid Mechanics 176 (1987) 379–402.

[65] Y. Champoux, J.-F. Allard, Dynamic tortuosity and bulk modulus in air-saturated porous media, Journal of Applied Physics 70 (4) (1991) 1975–1979.

[66] J.-F. Allard, Y. Champoux, New empirical equations for sound propagation in rigid frame fibrous materials, The Journal of the Acoustical Society of America 91 (6) (1992) 3346–3353.

[67] S. R. Pride, F. D. Morgan, A. F. Gangi, Drag forces of porous-medium acoustics, Physical Review B 47 (9) (1993) 4964.

[68] D. Lafarge, P. Lemarinier, J. F. Allard, V. Tarnow, Dynamic compressibility of air in porous structures at audible frequencies, The Journal of the Acoustical Society of America 102 (4) (1997) 1995–2006.

[69] M. A. Biot, Theory of propagation of elastic waves in a fluid-saturated porous solid. I. low-frequency range, The Journal of the Acoustical Society of America 28 (2) (1956) 168–178.

[70] M. A. Biot, Theory of propagation of elastic waves in a fluid-saturated porous solid. II. higher frequency range, The Journal of the Acoustical Society of America 28 (2) (1956) 179–191.

[71] Y. J. Kang, J. S. Bolton, Finite element modeling of isotropic elastic porous materials coupled with acoustical finite elements, The Journal of the Acoustical Society of America 98 (1) (1995) 635–643.

[72] N. Atalla, R. Panneton, P. Debergue, A mixed displacement-pressure formulation for poroelastic materials, The Journal of the Acoustical Society of America 104 (3) (1998) 1444–1452.

[73] P. Göransson, A 3-D, symmetric, finite element formulation of the Biot equations with application to acoustic wave propagation through an elastic porous medium, International Journal for Numerical Methods in Engineering 41 (1) (1998) 167–192.

[74] V. Easwaran, W. Lauriks, J. P. Coyette, Displacement-based finite element method for guided wave propagation problems: Application to poroelastic media, The Journal of the Acoustical Society of America 100 (5) (1996) 2989–3002.

[75] L. L. Beranek, Acoustic impedance of porous materials, The Journal of the Acoustical Society of America 13 (3) (1942) 248–260.

[76] R. W. Leonard, Simplified porosity measurements, The Journal of the Acoustical Society of America 20 (1) (1948) 39–41.

[77] Y. Champoux, M. R. Stinson, G. A. Daigle, Air-based system for the measurement of porosity, The Journal of the Acoustical Society of America 89 (2) (1991) 910–916.

[78] P. Leclaire, O. Umnova, K. Horoshenkov, L. Maillet, Porosity measurement by comparison of air volumes, Review of Scientific Instruments 74 (3) (2003) 1366–1370.

[79] Y. Salissou, R. Panneton, Pressure/mass method to measure open porosity of porous solids, Journal of Applied Physics 101 (12) (2007) 124913.

[80] J. Tao, P. Wang, X. Qiu, J. Pan, Static flow resistivity measurements based on the iso 10534.2 standard impedance tube, Building and Environment 94 (2015) 853–858.

[81] O. Doutres, Y. Salissou, N. Atalla, R. Panneton, Evaluation of the acoustic and non-acoustic properties of sound absorbing materials using a three-microphone impedance tube, Applied Acoustics 71 (6) (2010) 506–509.

[82] M. A. Picard, P. Solana, J. F. Urchueguia, A method of measuring the dynamic flow resistance and the acoustic measurement of the effective static flow resistance in stratified rockwool samples, Journal of Sound and Vibration 216 (3) (1998) 495–505.

[83] P. Leclaire, L. Kelders, W. Lauriks, M. Melon, N. Brown, B. Castagnede, Determination of the viscous and thermal characteristic lengths of plastic foams by ultrasonic measurements in helium and air, Journal of Applied Physics 80 (4) (1996) 2009–2012.

[84] M. Henry, P. Lemarinier, J. F. Allard, J. L. Bonardet, A. Gedeon, Evaluation of the characteristic dimensions for porous sound-absorbing materials, Journal of Applied Physics 77 (1) (1995) 17–20.

[85] Z. E. A. Fellah, S. Berger, W. Lauriks, C. Depollier, C. Aristegui, J.-Y. Chapelon, Measuring the porosity and the tortuosity of porous materials via reflected waves at oblique incidence, The Journal of the Acoustical Society of America 113 (5) (2003) 2424–2433.

[86] Y. Atalla, R. Panneton, Inverse acoustical characterization of open cell porous media using impedance tube measurements, Canadian Acoustics 33 (1) (2005) 11–24.

[87] K. V. Horoshenkov, A review of acoustical methods for porous material characterisation, International Journal of Acoustics and Vibration 22 (1) (2017) 92–103.

[88] L. Jaouen, A. Renault, M. Deverge, Elastic and damping characterizations of acoustical porous materials: Available experimental methods and applications to a melamine foam, Applied Acoustics 69 (12) (2008) 1129–1140.

[89] E. Mariez, S. Sahraoui, J. F. Allard, Elastic constants of polyurethane foam's skeleton for Biot model, in: International Congress on Noise Control Engineering, 1996, pp. 951–954.

[90] V. Tarnow, Dynamic measurements of the elastic constants of glass wool, The Journal of the Acoustical Society of America 118 (6) (2005) 3672–3678.

[91] C. Langlois, R. Panneton, N. Atalla, Polynomial relations for quasi-static mechanical characterization of isotropic poroelastic materials, The Journal of the Acoustical Society of America 110 (6) (2001) 3032–3040.

[92] M. Etchessahar, S. Sahraoui, L. Benyahia, J. F. Tassin, Frequency dependence of elastic properties of acoustic foams, The Journal of the Acoustical Society of America 117 (3) (2005) 1114–1121.

[93] J. F. Allard, M. Henry, L. Boeckx, P. Leclaire, W. Lauriks, Acoustical measurement of the shear modulus for thin porous layers, The Journal of the Acoustical Society of America 117 (4) (2005) 1737–1743.

[94] K. W. Hong, Acoustical estimation of macroscopic properties of poroelastic materials, Ph.D. thesis, Purdue University (2009).

[95] S. Sim, K. Kim, A method to determine the complex modulus and Poisson's ratio of viscoelastic materials for FEM applications, Journal of Sound and Vibration 141 (1) (1990) 71–82.

[96] J. Prisutova, K. Horoshenkov, J.-P. Groby, B. Brouard, A method to determine the acoustic reflection and absorption coefficients of porous media by using modal dispersion in a waveguide, The Journal of the Acoustical Society of America 136 (6) (2014) 2947–2958.

[97] X. Zhang, G. Squicciarini, D. J. Thompson, Sound radiation of a railway rail in close proximity to the ground, Journal of Sound and Vibration 362 (2016) 111–124.

[98] P. Debergue, R. Panneton, N. Atalla, Boundary conditions for the weak formulation of the mixed (u, p) poroelasticity problem, The Journal of the Acoustical Society of America 106 (5) (1999) 2383–2390.

[99] M. A. Biot, D. G. Willis, The elastic coefficients of the theory of consolidation, Journal of Applied Mechanics 15 (1957) 594–601.

[100] N. Frémion, J. Goudard, N. Vincent, Improvements of ballast and sleeper description in TWINS, Tech. rep., Technical report, VIBRATEC report ref. 072.028 a for the account of the ERRI C163 committee (1996).

[101] G. Squicciarini, A. Putra, D. J. Thompson, X. Zhang, M. A. Salim, Use of a reciprocity technique to measure the radiation efficiency of a vibrating structure, Applied Acoustics 89 (2015) 107–121.

[102] K. V. Horoshenkov, D. C. Hothersall, K. Attenborough, Porous materials for scale model experiments in outdoor sound propagation, Journal of Sound and Vibration 194 (5) (1996) 685–708.

[103] W. Zhai, K. Wang, J. Lin, Modelling and experiment of railway ballast vibrations, Journal of Sound and Vibration 270 (4-5) (2004) 673–683.

[104] D. J. Thompson, M. H. A. Janssens, TWINS–Track-Wheel Interaction Noise Software. Theoretical manual, version 2.4, TNO Institute of Applied Physics Report TPD-HAG-RPT (1997) 93–0214.

[105] B. Lawrence, Scale model facility for railway vibration and noise, ISVR MEng individual project (2014).

[106] L. Ratkevicius, Models of shielding of sound sources on railway vehicles, Master's thesis, University of Southampton (2017).

[107] F. J. Fahy, Some applications of the reciprocity principle in experimental vibroacoustics, Acoustical Physics 49 (2) (2003) 217–229.

[108] ISO 3095:2013, Acoustics – Railway applications – Measurement of noise emitted by railbound vehicles, Standard, International Organization for Standardization (Mar. 2013).

[109] D. Duhamel, P. Sergent, Sound propagation over noise barriers with absorbing ground, Journal of Sound and Vibration 218 (5) (1998) 799–823.

[110] X. Zhang, D. Thompson, J. Ryue, H. Jeong, G. Squicciarini, M. Stangle, The sound radiation of a railway rail fitted with acoustic shielding, in: International Congress on Sound and Vibration, 2018.

[111] S. Marburg, Six boundary elements per wavelength: is that enough?, Journal of Computational Acoustics 10 (01) (2002) 25–51.